A Modelling-Simulation-Analysis Workflow for Investigating Socket-Stump Interaction

Von der Fakultät Bau- und Umweltingenieurwissenschaften
der Universität Stuttgart zur Erlangung der Würde
eines Doktor-Ingenieurs (Dr.-Ing.)
genehmigte Abhandlung

vorgelegt von

Ellankavi Ramasamy, M.Sc.

aus

Chennai, Indien

Hauptberichter: Prof. Oliver Röhrle, PhD
Mitberichter: Prof. Can Yücesoy, PhD
Tag der mündlichen Prüfung: 12. April 2019

Institut für Modellierung und Simulation Biomechanischer Systeme
der Universität Stuttgart
2019

Report No.: CBM-03
Institute for Modelling and Simulation of Biomechanical Systems
Chair of Continuum Biomechanics and Mechanobiology
University of Stuttgart, Germany, 2019

Editor:
Prof. O. Röhrle, PhD

Fraunhofer Institute for Manufacturing Engineering and Automation IPA
Department of Biomechatronic Systems
Nobelstraße 12
70569 Stuttgart, Germany

ISBN 978-3-946412-02-1
D-93 – Dissertation, Universität Stuttgart

Declaration of authorship

Hiermit erkläre ich, dass ich die vorliegende Arbeit selbstständig verfasst habe, dass ich keine anderen als die angegebenen Quellen benutzt und alle wörtlich oder sinngemäß aus anderen Werken übernommen Aussagen als solche gekennzeichnet habe, dass die eingereichte Arbeit weder vollständig noch in wesentlichen Teilen Gegenstand eines anderen Prüfungsverfahrens gewesen ist, dass ich die Arbeit weder vollständig noch in Teilen bereits veröffentlicht habe und dass das elektronische Exemplar mit den anderen Exemplaren übereinstimmt.

I hereby declare that I have written the present work independently, that I have not used any sources other than those specified and that all statements taken verbatim or meaningfully from other works have been marked as such, that the submitted work has not been completely or partially the subject of another examination procedure, that I have not published the work either completely or in part, and that the electronic copy coincides exactly with the other copies.

Stuttgart, April 2019

Ellankavi Ramasamy

Dedication

To my wife, Vishnu Priya Kumar, for enduring and comforting me whenever I felt low, and to Beate Dorow, who insipred and supported me in more ways than I could have asked for.

Acknowledgements

The work presented in this thesis was carried out at the department of Biomechatronic Systems at Fraunhofer IPA, where I was working as a research assistant. Many people contributed to the realisation of this work, and their support is gratefully acknowledged.

Firstly, I would like to express my sincere gratitude to Prof. Oliver Röhrle not only for providing me the opportunity to undertake this work, but also for guiding me during all the difficult times at and outside of work. My equal gratitude goes to Dr. med. Urs Schneider, Head of the department of Biomechatronic Systems at Fraunhofer IPA, Stuttgart for believing in me, and for providing me with the necessary resources to conduct this research. I would like to extend my gratitude to Prof. Can Yücesoy for taking up the co-chair during my doctoral defence.

I will always remember my colleague, Beate Dorow. Through her eyes, I saw the world to be a much better place, and turned me into a better human being. I will always be indebted to her for making me believe in myself under all circumstances. I feel very blessed to have met such a strong and wonderful person in my life. You will never be forgotten. I would also like to thank her husband Bernd Woltermann, and their kids Anna and Mia for the good times together.

The wait for ethics approval for conducting medical experiments was one of the most anxious period during this work. Here, I would like to thank Sook-Yee Chong and Leonardo Gizzi for obtaining the ethics approval, and conducting the experiments. I would further like to thank them for the engaging discussions, clarifying my silliest questions, coffee, cakes and for extending a helpful hand whenever needed. My special thanks goes to Ekin Altan and Sergio Morales for helping me organise the defence and after-party, and to Andreas Hessenthaler and Mylena Mordhorst for assisting with several administrative questions.

I would like to thank all my colleagues at Fraunhofer IPA for the rather warm research atmosphere. In particular, I would like to thank Okan Avci for the innumerable brainstorming sessions, which proved very valuable to this work. In no particular order, I would like to thank my colleagues Christoph Giers, Christopher Riehs, Okan Avci, Beate Dorow, Mark Tröster, Christine Nitsche-Loske, Animesh Ranjan, Bernhard Kleiner, Oliver Schwarz, Florian Blab, Felix Müller-Graf, Marius Fabian, Amir Ebrahimi and Raphael Singer for the collegial atmosphere, and for the fun times together.

My friends helped me blow off steam when the going got tough. I am grateful to my friends Vivek Subramaniam Maiyappan, Meena Kannappan, Velusamy Kamaraj, Maheshwari Rajendran, Michael Sprenger, Cécile Lascaux, and Grzegorz Karch for all the good times that we spent together that helped me recharge my batteries.

I am indebted to my wife, Vishnu Priya Kumar for her constant support and understanding, which led to the successful completion of this work. I am also grateful to my parents and parents-in-law for believing in me and for their understanding.

Contents

List of Figures

List of Tables

Deutsche Zusammenfassung

Die vorliegende Thesis beschreibt die Entwicklung eines neuartigen Workflows zur patientenspezifischen Modellierung, Simulation und Analyse von Beinstümpfen. Daraus resultieren detaillierte Stumpfmodelle für Untersuchungen im Rahmen der Kontinuumsmechanik. Mit nur minimaler menschlicher Intervention werden detaillierte Stumpfmodelle aus medizinischen Bildern generiert und in Finite Elemente (FE) Simulationen verwendet, um dynamische Stumpf-Schaft-Interaktionen zu untersuchen. Im Gegensatz zu modernsten Modellen mit fusionierten Muskeln besteht der Stumpf in dieser Arbeit aus Knochen, individuellen Muskeln und Fett. Des Weiteren wird zusätzlich ein Modell mit den aktuellen Stumpfgeometrien als Vergleichsobjekt zu dem hier vorgestellten Modell erzeugt. Um die Notwendigkeit von detaillierten Stumpfmodellen aufzuzeigen, wird das Stand der Technik beschreibende bzw. aktuelle Modell mit dem detaillierten Modell in einer Simulation des zweibeinigen Stands verglichen. Hierzu wird ein nichtlinear hyperelastisches, transversal isotropes Werkstoffgesetz für den Skelettmuskel, welches ein Modell zu Schädigungen tiefer Gewebeschichten beinhaltet, im Rahmen der Kontinuums-Schädigungsmechanik in LS-DYNA implementiert. Interne Spannungen und Schädigungen tiefer Gewebeschichten während dynamischen Schaft-Stumpf-Interaktionen werden anhand von zweibeinigen Stand- und Gangsimulationen untersucht. Darüber hinaus werden das Potential von Vorwärtsdynamik mit aktiven Stumpfmodellen und die Möglichkeit von realitätsnahen Simulationen des Anziehens von Linern dargestellt. Zuletzt werden die Nutzungsmöglichkeiten des vorgeschlagenen Workflow bezüglich der Bestimmung von Schaftsitz und -komfort diskutiert.

Die Oberschenkel- bzw. transfemorale Amputation, auf welcher der Fokus dieser Thesis liegt, ist eine lebensverändernde und -beeinträchtigende Erfahrung. Erkrankte oder geschädigte Teile der unteren Gliedmaßen werden operativ entfernt. Um die Mobilität wiederherzustellen, wird transfemoral Amputierten häufig eine Prothese angepasst, welche aus einem Prothesenschaft, Kniegelenk, Rohradapter und einer Fuß-Knöchelprothese besteht. Unter diesen Komponenten ist der Prothesenschaft am wichtigsten. Ein idealer Prothesenschaft entspricht einer Einhängevorrichtung, die sowohl einen dichten Abschluss als auch eine effiziente Lastübertragung zwischen Stumpf und Prothese gewährleistet und zudem ein komfortables Tragen ermöglicht. Beim Entwickeln und Anpassen der Prothesen versuchen Orthopädie-Techniker stets, auf die spezifischen Wünsche und Bedürfnisse der Patienten einzugehen. Faktoren, die bei der Entwicklung einer prothetischen Komponente in Betracht gezogen werden, sind u.a. deren Sitz, Komfort, Stabilität, problemloses An- und Ausziehen, benötigte körperliche Energie, Gewicht, Fähigkeit zur Sicherstellung eines gesunden Stumpfes und ästhetische Aspekte. Unter den genannten Faktoren spielt der Schaftkomfort eine wichtige Rolle und wirkt sich somit auf die Gesamtakzeptanz einer Prothese aus. Nicht einmal eine technologisch weit entwickelte Prothese kann für ihren vorhergesehenen Nutzen eingesetzt werden, wenn sie unbequem zu tragen ist. Deshalb darf die Bedeutung der Orthopädie-Techniker als Ersteller von passgenauen Prothesen nicht unterschätzt werden. Leider sind die aktuellen Methoden für die Entwicklung unwissenschaftlich, was zu Schaftanpassungen führt, die sich nicht nur zwischen den Orthopädie-Technikern unterscheiden, sondern auch von Anpassung zu Anpassung ein und desselben Technikers. Dies ist ein Hinweis für suboptimale Schaftanpassungen, was Folgen wie eine erschwerte Akzeptanz einer Prothese, beeinträchtigtes Gehen und Schmerzen bzw. Verletzungen nach sich ziehen kann.

Viele rechnergestützte und experimentelle Studien betrachten den Anpressdruck zwischen Stumpf und Schaft als Hinweis für eine guten Passform und Komfort des Schafts, weshalb sie ihren Arbeitsaufwand auf dessen Optimierung fokussieren. Obwohl der Anpressdruck ein wichtiger Faktor für die Auswirkung auf den Gesundheitszustands des Stumpfes ist, ist er nicht die einzige Größe, die in Betracht gezogen werden muss. Kürzlich hob der "National Pressure Ulcer Advisory Panel" (NPUAP) die Wichtigkeit und Relevanz von Schädigungen tiefer Gewebeschichten durch die Nutzung von Prothesen hervor. Verletzungen tiefer Gewebe sind spannungsabhängige Verletzungen in subkutanen Geweben unter intakter Haut, die in der Nähe der Knochen entstehen. Bei Amputierten kann ein fortgeschrittenes Stadium von Tiefengewebe-Schädigungen zu Amputationen auf höheren Ebenen führen, um das verbleibende Stumpfvolumen zu retten. Obwohl die Ätiologie und Evolution von Tiefengewebe-Schädigungen noch unklar sind, weisen experimentelle Nachweise in Korrelation mit deren Vorkommen auf die Bedeutung von anhaltenden Spannungen und Dehnungen hin. Auch Prothesenschäfte belasten den Stumpf mit anhaltenden Spannungen, und Überbeanspruchungen der Tiefengewebe durch schlecht sitzende Schäfte machen die Patienten für Tiefengewebe-Schädigungen anfällig. Im Gegensatz zu vielen experimentellen Methoden bieten computergestützte Werkzeuge wie FE-Analysen eine praktische, nicht-invasive Alternative, um interne Weichgewebespannungen und Tiefengewebe-Schädigungen in dem Stumpf zu untersuchen. Die drei Grundpfeiler zur Erhaltung nützlicher Information von FE-Analysen sind, (i) detaillierte Geometrien, (ii) realistische Randbedingungen und (iii) Materialmodelle zur Erfassung der gewünschten Physik. Dennoch haben die modernsten *in silico* Modelle, die zur Erforschung des Weichgewebezustands im Stumpf verwendet werden, einfache Stumpfgeometrien und Randbedingungen und in manchen Fällen Annahmen von linear elastischen Materialien für Weichgewebe. Aktuell werden die Weichgewebe in der detailliertesten Stumpfgeometrie in Knochen, Muskelmasse, Fett und Haut unterteilt. Des Weiteren wird weder zwischen den Grenzen der einzelnen Muskeln unterschieden, noch werden Gewebeanisotropien berücksichtigt. Bei den FE-Analysen zur Untersuchung von Schaft-Stumpf-Interaktionen wird außerdem weitgehend die Rolle der Prothesen-Liner ignoriert, welche die Drücke auf den Stumpf reduzieren. Darüber hinaus sind die verwendeten Randbedingungen in den FE-Analysen nicht realistisch genug, um reale Bedingungen zu repräsentieren. Zum Beispiel wird der dynamische Prozess des Schaftanlegens nicht berücksichtigt, oder er wird durch das Anbringen von Verschiebungen stark vereinfacht; andere dynamische Bedingungen wie z.B. Laufen und Treppensteigen werden ebenfalls nicht in Betracht gezogen. Trotz der Notwendigkeit für detaillierte Stumpfmodelle, realistische Randbedingungen und realistische Weichgewebe-Materialmodelle sind in der FE-Analyse von Stumpf-Prothese-Interaktionen einfache Geometrien und unrealistische Randbedingungen und Gewebematerialien immer noch üblich.

Angesichts der Einschränkungen von bestehenden Stumpfgeometrien ist das hauptsächliche Ziel dieser Arbeit, einen Workflow zur Unterstützung der Erstellung von hochgenauen, dreidimensionalen, patientenspezifischen FE-Stumpfmodellen aus Diffusionstensor Magnetresonanztomographie (DT-MRI)-Aufnahmen zu entwickeln. Der vorgestellte Workflow zur Erstellung eines Stumpfmodells basiert auf MATLAB und Python, um das Pre- und Postprocessing der DT-MRI-Daten auszuführen, Datentransfer zwischen verschiedenen Software-Werkzeugen zu ermöglichen, die Erstellung von FE-Netzen des Stumpfes zu unterstützen und schließlich die Informationen der Muskelfasern aus den DT-MRI-Aufnahmen auf das erstellte FE-Mesh abzubilden. Das Potential des Modellbildungs-Simulations-Analyse-Workflows wird in vier Fallbeispielen angezeigt: (i) Simulation des Anziehens eines Liners, (ii) Vorwärtssimulation des *gluteus maximus*, (iii) zweibeinige Standsimulation und (iv) dynamische Gangsimulation. Zweck der FE Simulationen ist es, die Notwendigkeit von detaillierten Stumpfmodellen darzustellen, indem der interne Zustand der Weichgewebe und potentiell von Tiefengewebe-Schädigungen gefährdete Regionen des Stumpfes prognostiziert werden. Folglich sind geeignete Materialmodelle erforderlich, die Deformationen und Verletzungen von Weichgeweben charakterisieren. Zu diesem Zweck wird ein nichtlinear hyperelastisches, transversal isotropes Werkstoffgesetz für den Skelettmuskel im Rahmen der Kontinuumsmechanik entwickelt und in LS-DYNA implementiert. Für alle vier Fallbeispiele werden realistische Randbedingungen angewandt. Das dynamische Anziehen des Liners wird ähnlich einem realen Szenario simuliert, indem der Stumpf in den Liner invertiert und translatiert wird, während der Rand des Liners in allen translatorischen Freiheitsgraden eingeschränkt wird. Skelettmuskelfasern tragen zu sowohl aktiver als auch passiver Steifigkeit bei und beeinflussen dadurch die Muskelantwort. Dieser Effekt wird in einer Vorwärtssimulation des *gluteus maximus* dargestellt, in der die Muskelfasern (i) randomisiert werden und (ii) um die craniocaudale Achse um 20° und 40° rotiert werden. Der *gluteus maximus* wird für einen Zeitraum von 10 s aktiviert. Die Muskelaktivierung steigt in $t = 3\,\mathrm{s}$ linear von 0 auf 1 an und wird bis zum Ende der Simulation konstant gehalten. Um das hier vorgestellte Modell mit dem aktuellen Stumpfmodell zu vergleichen, bei dem die Muskeln fusioniert sind (fusionierte Muskelmodelle), wird ein zusätzliches Modell mit fusionierten Muskeln erstellt. Ferner wird der ursprüngliche Schaft isotropisch um 10 % herunterskaliert, um einen schlecht sitzenden Schaft zu simulieren, sodass dessen Effekt untersucht werden kann. Der zweibeinige Stand wird in zwei Phasen simuliert: (i) das Anziehen des Schaftes, bei dem die ursprünglichen und schlecht sitzenden Stümpfe in 10 s unter Verwendung von Dirichlet Randbedingungen in den Stumpf translatiert werden, gefolgt von (ii) dem zweibeinigen Stand, bei dem ca. die Hälfte des Patientengewichts (400 N) für 2 h aufgebracht wird. Die Spannungen in den Weichgeweben und Vorhersagen für Schädigungen der Tiefengewebe in dem Stumpf werden nach den FE-Simulationen des zweibeinigen Stands unter identischen Randbedingungen verglichen. Schließlich wird in der Gangsimulation die dynamische Interaktion zwischen Stumpf und ursprünglichem Schaft, der zu einer vollständigen transfemoralen Prothese mit einem kinematischen Kniegelenk angepasst wurde, analysiert. Die kinematischen Randbedingungen für einen Gangschritt, wie z.B. für die Translation und Rotation des Femurs, wird der experimentellen Bewegungserfassung (Motion Capture) entnommen. Um numerische Konvergenzprobleme zu reduzieren, wird die ursprüngliche Schrittdauer von 1.94 s auf 50 s hochgerechnet.Ähnlich der Analyse des zweibeinigen Stands wird die Gangsimulation ebenfalls in zwei Phasen durchgeführt: (i) das Anziehen des Schaftes, mit denselben Randbedingungen wie in der ersten Phase des zweibeinigen Stands, gefolgt von (ii) der Simulation des Gangschritts, bei dem Dirichlet Randbedingungen für den Femur übernommen werden. Die vollständige Dauer der Gangsimulation vom Anziehen des Schaftes bis zum Ende des Ganges beträgt hochskaliert 60 s.

Anhand des vorgestellten Workflows wurde eine detaillierte, patientenspezifische Stumpfgeometrie in ca. 20 min erstellt. Das FE-Stumpfmodell, bestehend aus Femur, elf Muskeln, Fett, Liner und Schaft wurde mit linearen, tetraedrischen Lagrange-Elementen vernetzt. Das FE-Netz des Stumpfes setzte sich aus 5416 Elementen im Femur, 35 257 Elementen in den Muskeln, 97 503 Elementen im Fett, 51 971 Elementen im Liner und 327 865 Elementen im Stumpf zusammen. Ausgenommen der Analyse des zweibeinigen Stands wurden dem Stumpf steifere Materialeigenschaften zugeordnet, um numerische Konvergenzprobleme zu umgehen. Der Spitzenwert der von-Mises-Spannung in dem Liner betrug nach der Liner-Anziehen-Simulation 3.78 MPa, während der maximale Druckdehungswert auf den Stumpf 0.816 % betrug, was einer Spannung von 317.91 kPa entspricht. Am Ende der Muskelaktivierungssimulation ($t = 10\,\mathrm{s}$) erzeugten die ursprünglichen Fasern im *gluteus maximus* in der sagittalen Ebene eine Verschiebung von 66 mm an der distalen Femurspitze. Die anderen Modelle, bei denen die Fasern um die craniocaudale Achse um 20° und 40° rotiert wurden, ergaben sich Verschiebungen von 60.02 mm bzw. 20.02 mm. Die Simulation des zweibeinigen Stands wurde mit vier Stumpf-Schaft-Modellen durchgeführt, nämlich mit (i) dem Muskelmodell mit individuellen Muskeln und dem urpsrünglichem Schaft, (ii) dem Muskelmodell mit fusionierten Muskeln und dem ursprünglichen Schaft, (iii) dem Muskelmodell mit individuellen Muskeln und dem kleineren, schlecht sitzenden Schaft, (iv) dem Muskelmodell mit fusionierten Muskeln und dem kleineren, schlecht sitzenden Schaft. Die Ergebnisse der Simulation des zweibeinigen Stands für die genannten vier Fälle beliefen sich auf 21.09 kPa, 10.83 kPa, 51.60 kPa bzw. 16.88 kPa. Die Volumennormalisierten Anpressdrücke betrugen 4.2 kPa, 4.1 kPa, 6.6 kPa bzw. 6.0 kPa. Bei der Ganganalyse betrugen die Maximalspannungen auf die Oberfläche und das Tiefengewebe des Stumpfes am Ende der Simulation 16.94 MPa bzw. 147.1 MPa. Das Volumen der verletzten Skelettmuskeln betrug in der Endphase des Schaft-Anziehens 0.24 %, als der ursprüngliche Schaft auf den Stumpf gezogen wurde. Der Wert stieg während des Fersenauftritts auf 1.85 %, blieb während der Standphase nahezu konstant und stieg bei dem Abheben der Zehen auf 2.83 %. Die maximale Relativverschiebung zwischen Femur und ursprünglichem Schaft wurde während des Aufsetzens der Ferse und des Abhebens der Zehen erfasst, mit einem Wert von 10.59 mm bzw. 16.06 mm.

Das Hauptergebnis des Workflows war eine automatisch erstellte, detaillierte, patientenspezifische Stumpfgeometrie mit integrierten Informationen zu Skelettmuskelfasern. Obwohl das erstellte Modell individuelle Muskeln beinhaltete, war es nicht möglich, Sehnen zu erzeugen. Diese Limitation ergibt sich nicht durch den Workflow, sondern durch die aktuelle medizinische Scannertechnologie. Um von DT-MRI-Scans Faserorientierungen entnehmen zu können, werden extrem hohe Magnetfeldstärken und hohe Pixelauflösungen benötigt. Dennoch können Sehnen von T_1- oder T_2-MRI-Scans segmentiert und mit dem Stumpfmodell verbunden werden. Die Parameter des kontinuumsmechanischen Modells, die zur Analyse von Spannungen, Dehnungen und potentiellen Gewebeschäden in dem Stumpf entwickelt wurden, wurden aus der Literatur entnommen. Die hohe Dynamik führte zu numerischen Konvergenzproblemen, die mit künstlicher Versteifung der isotropen Mooney-Rivlin-Parameter behoben werden konnten. Diese Probleme könnten aber auch mit Durchführungen von Experimenten zur Bestimmung von patientenspezifischen Materialparametern behoben werden, wodurch genauere Vorhersagen erhalten werden könnten. Die Kontraktion des *gluteus maximus* bei seiner Aktivierung wurde mittels Vorwärtsdynamik simuliert. Hier wurde gezeigt, dass die Verschiebung des *gluteus maximus* stark von der Ausrichtung der Muskelfasern abhängig ist. Bewegung im menschlichen

Körper entsteht als Folge von aktiver Muskelkontraktion. Die Größenordnung der Muskelaktivierung kann unter Einsatz von Oberflächen-Elektromyographie ermittelt werden. Somit kann eine vollständige Vorwärtssimulation des Stumpfes zusammen mit der Prothese simuliert werden. Solch eine Vorwärtssimulation stellt zwar eine Herausforderung dar, würde aber Potential für Erkenntnisse über realitätsnahe Dehungs- und Spannungszustände während dynamischer Bewegungen bieten. Bei dem Vergleich des aktuellen Modells und des vorgeschlagenen Modells in der Simulation des zweibeinigen Stands wurde zwischen den internen Spannungsspitzen eine Differenz des Dreifachen festgestellt. Die Differenz zwischen den Anpressdrücken der beiden Modelle war vernachlässigbar. Des Weiteren war das Gewebevolumen, das durch Tiefengewebeschäden beeinflusst wurde, in dem detaillierten Modell 1.71 Mal größer als in dem aktuellen Modell. Daher ist anzunehmen, dass die aktuellen Modelle- bei Nichtbeachtung der Heterogenität in den Stumpfgeweben- die Dehnungen und Verletzungen der Tiefengewebe untergraben. Da das experimentelle Protokoll keine Methoden zur Erfassung der Bewegungen des Femurs beinhaltete, wurde die Bewegung des Schafts, welche durch das Motion-Capture-System erfasst wurde, für den Femur eingesetzt. Mit dem Motion-Capture-System synchronisierte Ultraschallsensoren könnten jedoch bei der Erlangung der wahren Bewegungen des Femurs helfen. Die Approximation der Bewegungen des Femurs wird nicht als Einschränkung der vorgestellten Methode erachtet, da das Ziel des vorgestellten Workflows ausschließlich aus der Darstellung der Anwendbarkeit anhand der Messung von Schaftpassformen bestand. Mit diesem Workflow war es möglich, die Relativbewegungen zwischen der distalen Spitze des Femurs und dem Schaft zu analysieren, wodurch die dynamische Passform gemessen und quantifiziert werden konnte. Wie bereits erwähnt, wurden die Materialparameter in der Gangsimulation versteift, um Konvergenzprobleme zu verhindern. Obwohl die Anpassung der korrekten Materialparameter an den Patienten für die Behebung dieses Problems vielleicht geholfen hätte, lag dies außerhalb des Rahmens dieser Studie.

Das Modell, das in dieser Arbeit präsentiert wird, ist nur der erste Schritt zur Aufstellung einer wissenschaftlichen Methode, um Orthopädie-Techniker bei der Entwicklung und Evaluierung der Schaftpassform zu unterstützen. Das vorgestellte Modell kann unter verschiedenen Aspekten verbessert werden. Zum Beispiel können Sehnen anhand von T_1- oder T_2-MRI-Scans manuell segmentiert werden, um sie später mit dem Stumpfmodell zu verbinden, das in dem vorgeschlagenen Workflow mit DT-MRI-Scans generiert wurde. Diese Co-Registrierung von DT-MRI und T_1- oder T_2-MRI-Scans kann automatisiert werden. Darüber hinaus kann die Schaft-Stumpf-Interaktion durch Vorwärtsdynamik simuliert werden, bei der Multiskalenmethoden zur Überbrückung von mechanischen und makroskopischen Muskelkontraktionen verwendet werden. Das Modellieren des Zusammenspiels zwischen verschiedenen Muskelgruppen könnte in realistischeren Deformationen von Weichgewebe und Kinematiken des Stumpfes resultieren. Ähnlich dem vorgestellten geometrischen Modell des Stumpfes, das die Heterogenität von Weichgeweben modelliert, sollten die Materialparameter für verschiedene Gewebe im Stumpf durch bessere experimentelle Methoden bestimmt werden. Schließlich sollte der komplette Workflow als simples und klinisch anwendbares Werkzeug aufbereitet werden, so dass er von Orthopädie-Technikern verwendet werden kann.

Abstract

In this thesis, a novel subject-specific modelling-simulation-analysis workflow is developed, which generates detailed stump models for analysis in a continuum-mechanical framework. With minimal human intervention, detailed stump models are generated from medical images, and are used in Finite Element (FE) simulations to study dynamic stump-socket interactions. Herein, the stump is composed of bone, individual muscles and fat, as opposed to the state-of-the-art models with fused muscles. An additional model representing the state-of-the-art stump geometry is generated for comparison with the proposed model. To showcase the necessity of detailed stump models, the state-of-the-art model is compared with the detailed model in a bipedal stance simulation. For this purpose, a nonlinear hyperelastic, transversely isotropic skeletal muscle constitutive law containing a deep tissue injury model, using continuum damage mechanics, is implemented in LS-DYNA. Internal strains and deep tissue injury during dynamic socket-stump interaction are analysed with bipedal stance and gait simulations. Further, the potential of forward dynamics with active stump models, and the possibility of realistic liner donning simulations are presented. Finally, the possibilities of using the proposed workflow in the context of determining socket fit and comfort are discussed. A brief summary of the topic, methods, results and discussion follow.

Above-knee or transfemoral amputation, which is the focus of this thesis, is a life-changing and devastating experience, where diseased or damaged parts of the lower limbs are surgically removed. In order to restore mobility, transfemoral amputees are often fitted with a prosthetic device, which is composed of a prosthetic socket, knee joint, pylon and a foot-ankle prosthesis. Among these components, the role of the prosthetic socket is the most important. An ideal prosthetic socket is a suspension device, which forms a tight seal between a stump and prosthesis, facilitates efficient load transmission between them, and is comfortable to wear. When designing and fitting prosthetic devices, prosthetists try to cater to the unique needs and desires of a patient. Some factors considered in designing a prosthetic component are its fit, comfort, stability, ease of donning and doffing, energy required for its use, weight, ability to ensure healthy stump, and aesthetics. Of these, socket comfort plays an important role as it affects the overall acceptance of a prosthetic device. Even a technologically advanced prosthesis cannot be used as intended if it is uncomfortable to wear. Therefore, the importance of a prosthetist in creating a well-fitting prosthetic socket cannot be overstated. Unfortunately, the current methods of designing prosthetic sockets are non-scientific, and consequently, result in socket fits that vary not only from one prosthetist to another, but also within the same prosthetist. This is an indication of sub-optimal socket fits, which can impede the acceptance of prosthetic devices, affect gait, and lead to pain and injury.

Many computational and experimental studies consider socket-stump interface pressure as an indication of socket fit and comfort, and focus their effort towards optimising it. While interface pressure is an important factor affecting the health of the stump, it is not the only factor that needs consideration. Recently, the National Pressure Ulcer Advisory Panel (NPUAP) has raised the importance and relevance of deep tissue injury in prosthetic use. Deep tissue injuries are pressure-related injuries in subcutaneous tissues under intact skin, which originate close to the bones. In amputees, an advanced stage of deep tissue injury can lead to higher levels of amputation in order to salvage the remaining stump volume. While the aetiology and evolution of deep tissue injury are still unclear, experimental evidence indicates the role of sustained tissue pressure and strain in their occurrence. Prosthetic sockets also subject the residual limb to sustained pressure, and excessive tissue strains in the deep tissues of the stump, due to misfitting sockets, render the amputees susceptible to deep tissue injuries. Unlike many experimental methods, computational tools such as the FE analyses offer a convenient, non-invasive alternative to study internal soft tissue strains and deep tissue injuries in the stump. The three cornerstones for obtaining useful information from FE analyses are (i) detailed geometry, (ii) realistic boundary conditions, and (iii) material models to capture the desired physics. However, the state-of-the-art *in silico* models attempting to study the state of internal soft tissues in the stump have simple stump geometries, boundary conditions and, in some cases, have assumed linear elastic materials for soft tissues. Currently, in the most detailed state-of-the-art stump geometry, the tissues are characterised into bone, muscle lump, fat and skin. Further, no distinction is made between the boundaries of individual muscles, and tissue anisotropy is also not accounted for. The FE analyses investigating the socket-stump interaction have also largely ignored the role of prosthetic liners, which reduce the stresses on the stump. Further, the boundary conditions used in the FE analyses are not truly representative of the real world conditions. For example, the process of dynamically donning the socket are either not considered, or are oversimplified by applying nodal displacements on the surface of skin; other dynamic conditions such as walking and climbing stairs are not considered. Notwithstanding the need for detailed stump models, realistic boundary conditions and realistic tissue material models in the FE analysis of stump-prosthesis interaction, analyses with simple geometries, non-realistic boundary conditions and simple tissue materials are still common.

Given the limitations of existing stump geometries, the primary objective of this research is to develop a workflow to aid in the generation of a highly accurate 3D, patient-specific, FE stump model from diffusion tensor magnetic resonance imaging (DT-MRI) scans. The proposed workflow for generating the residual limb model is based on MATLAB and Python to orchestrate the pre- and post-processing of DT-MRI data, to enable data transfer between different software tools, to support the generation of FE mesh of the residuum, and to finally map the muscle fibre information present in the DT-MRI scans onto the generated FE mesh. The potential of the modelling-simulation-analysis workflow is exhibited with 4 case studies (i) liner-donning simulation, (ii) forward simulation of *gluteus maximus*, (iii) bipedal stance simulation, and (iv) dynamic gait simulation. The intent of the FE simulations are to demonstrate the necessity of the detailed stump model in predicting the internal state of soft tissues and to predict potential regions of the stump that will be affected by deep tissue injury. Therefore, appropriate constitutive material models characterising the deformation and injury of soft tissues are required. For this purpose, a nonlinear hyperelastic, transversely isotropic skeletal muscle constitutive law is developed in the framework of continuum damage mechanics, containing a deep tissue injury model, which is implemented in LS-DYNA. Realistic boundary conditions are applied for all the 4 case studies. Dynamic liner donning is

simulated by inverting and translating the stump into the liner while constraining the rim of the liner in all translational degrees of freedom, which resembles a realistic liner donning scenario. Skeletal muscle fibres contribute to both active and passive stiffness, affecting the muscle's response. This effect is demonstrated in a forward simulation of *gluteus maximus*, where the muscle fibres are (i) randomised, and (ii) rotated about the craniocaudal axis by 20° and 40°. The *gluteus maximus* is activated over a period of 10 s. Muscle activation is linearly ramped from 0 to 1 in $t = 3$ s and held constant until the end of the simulation. In order to compare the proposed model with the state-of-the-art stump model, where muscles are fused (fused-muscle models), an additional fused-muscle model is created. Further, to study the effect of misfitting sockets, the original socket is isotropically downscaled by 10 % to represent a misfitting socket. The bipedal stance is simulated in two stages: (i) socket donning, in which the original and misfitting sockets are translated into the stump in 10 s, using Dirichlet boundary conditions, followed by (ii) bipedal stance, in which approximately half the subject's body weight (400 N) is applied for 2 h. Under identical boundary conditions, stresses in the internal soft tissues and deep tissue injury predictions in the stump are compared after the FE simulations of bipedal stance. Finally, in the gait simulation, dynamic interaction between the stump and original socket, fitted to a complete transfemoral prosthesis with a kinematic knee joint, is analysed. The kinematic boundary conditions for one gait stride, i.e. translation and rotation of femur, are obtained from experimental motion capture. To reduce numerical convergence issues, the original stride duration of 1.94 s is upsampled to 50 s. Similar to the analysis of bipedal stance, the gait simulation is also performed in two stages: (i) socket donning, with boundary conditions identical to the first stage in bipedal stance, followed by (ii) simulation of gait stride, in which Dirichlet boundary conditions are applied to the femur. The total duration of the gait simulation, from socket-donning to end of gait, is 60 s.

Using the proposed workflow, a detailed subject-specific stump geometry was generated in approximately 20 min. The FE stump model consisting of femur, 11 muscles, fat, liner and socket was meshed with linear Lagrange tetrahedral elements. The FE mesh of the stump was made up of 5416 elements in the femur, 35 257 elements in the muscles, 97 503 elements in the fat, 51 791 elements in the liner, and 327 865 elements in the socket. Barring bipedal stance analysis, stiffer material properties were assigned to the stump in order to avoid numerical convergence problems. The peak von Mises stress in the liner after the liner-donning simulation was 3.78 MPa, and the maximum compressive strain on the surface of the stump was 0.816 %, corresponding to a stress of 317.91 kPa. At the end of muscle activation simulation ($t = 10$ s), the original fibres in *gluteus maximus* produced a displacement of 66 mm in the distal tip of the femur, in the sagittal plane. The other models, where the fibres were rotated about the craniocaudal axis by 20° and 40° produced displacements of 60.02 mm and 20.02 mm, respectively. The bipedal stance simulation was performed with 4 stump-socket models, namely (i) the individual-muscle model with original socket, (ii) the fused-muscle model with the original socket, (iii) the individual-muscle model with smaller, misfitting socket, and (iv) the fused-muscle model with the misfitting socket. The results of the bipedal stance simulation for the above 4 cases were 21.09 kPa, 10.83 kPa, 51.60 kPa and 16.88 kPa, respectively. The volume-normalised interface stresses were 4.2 kPa, 4.1 kPa, 6.6 kPa, and 6.0 kPa, respectively. In the case of gait analysis, the maximum stresses on the surface and deep tissues of stump, at the end of the simulation, were 16.94 MPa and 147.1 MPa, respectively. The volume of

skeletal muscles injured at the end of socket donning stage was 0.24 % when the residual limb was donned with the original socket. This value rose to 1.85 % during heel-strike, remained almost constant during the stance phase, and rose to 2.83 % during toe-off. The maximum relative displacement between the femur and original socket were observed during heel-strike and toe-off, which were 10.59 mm and 16.06 mm, respectively.

The primary outcome of the workflow was an automatically generated, detailed subject-specific stump geometry, containing skeletal muscle fibre information. While the generated model contained individual muscles, it was not possible to generate tendons that connect skeletal muscles to bones. This was not a limitation of the proposed workflow but of the current medical scanner technology. Extremely high magnetic field strength and high pixel resolution are required to obtain fibre orientation from DT-MRI scans. However, tendons can be manually segmented from T_1- or T_2-MRI scans, and attached to the stump model. The parameters of the continuum mechanical model, which were developed to analyse the stresses, strains and potential tissue damage in the stump, were obtained from already existing literature, and were not fitted to the subject. As a result, high dynamics led to numerical convergence problems, which were overcome by artificially stiffening the isotropic Mooney-Rivlin parameters. These issues can, however, be overcome by performing experiments to determine subject-specific material parameters with which more accurate predictions can be obtained. The contraction of *gluteus maximus* upon its activation was simulated using forward dynamics. Herein, the displacement of *gluteus maximus* was shown to strongly depend on the direction of muscle fibres. Movement in the human body occurs as a result of active muscle contraction. The magnitude of muscle activation can be obtained using surface electromyography (sEMG), and a complete forward simulation of the stump, together with the prosthesis, can be simulated. Such forward simulation is challenging but will provide insight into the realistic state of strains and stresses during dynamic movements. Upon comparing the state-of-the-art model with the proposed stump model in the bipedal stance simulation, a three-fold difference in the internal peak stresses was observed. However, there was negligible difference in the interface pressures between the two models. Further, the volume of tissues affected by deep tissue injury in the detailed model was 1.71 times more than that in the state-of-the-art model. Therefore, by ignoring the heterogeneity of tissues in the stump, the state-of-the-art models might be undermining the deep tissue strains and injury. Since the experimental protocol did not include methods to capture the movement of femur during gait, the motion of socket, which was captured by the motion capture system, was applied on the femur. However, ultrasound sensors, which are synchronised with the motion capture system, can help in obtaining the true motion of femur. The approximation of femur motion is not considered a limitation of the presented methodology since the goal of the presented workflow was only to demonstrate its applicability in quantifying socket fit. With this workflow, it was possible to analyse the relative motion between the distal tip of the femur and the socket with which the dynamic socket fit can be quantified. As mentioned earlier, the material parameters were stiffened in the gait simulation to avoid convergence issues. While fitting the correct material parameters to the subject might have helped overcome this issue, it was outside the scope for this study.

The model presented in this thesis is only the first step towards establishing a scientific method to assist prosthetists in designing and evaluating socket fit. The presented model can be improved in several aspects. For example, tendons can be manually segmented from T_1- or T_2-MRI scans, which can later be merged with the stump model generated

with the proposed workflow using DT-MRI scans. This co-registration of DT-MRI, and T_1- or T_2-MRI scans can be automated. Further, the socket-stump interaction can be simulated using forward dynamics, where multiscale methods are used to bridge cellular mechanics and macroscopic muscle contractions. Modelling the synergy between various muscle groups might result in more realistic soft tissue deformation and the observed stump kinematics. Similar to the proposed geometric model of the stump, which modelled soft tissue heterogeneity, the material parameters should be determined for the various tissues in the stump through better experimental methods. Finally, the complete workflow should be presented as a simple and clinically applicable tool such that it can be used by prosthetists.

Nomenclature

Operators

$\mathrm{d}(\bullet)$	Differential operator
$\partial(\bullet)$	Partial differential operator
$\mathrm{Grad}(\bullet) = \dfrac{\partial}{\partial \boldsymbol{X}}(\bullet)$	Gradient with respect to reference position vector
$\mathrm{grad}(\bullet) = \dfrac{\partial}{\partial \boldsymbol{x}}(\bullet)$	Gradient with respect to current position vector
$\mathrm{Div}(\bullet) = \dfrac{\partial}{\partial \boldsymbol{X}} \cdot (\bullet)$	Divergence with respect to reference position vector
$\mathrm{div}(\bullet) = \dfrac{\partial}{\partial \boldsymbol{x}} \cdot (\bullet)$	Divergence with respect to current position vector
$\mathrm{tr}\,(\bullet) = (\bullet) \cdot \mathbf{I}$	Trace operator
$\det(\bullet)$	Determinant operator
$(\bullet)^{-1}$	Inverse operator

Symbols

Scalars are represented by small-faced fonts, vectors by bold-faced fonts, 2^{nd} order tensors by bold-faced sans-serif font, and 4^{th} order tensors by bold, sans-serif calligraphic font.

Scalars

Symbol	**Unit**	**Description**
$\mathcal{B}$	[-]	Continuum body
$\mathcal{P}$	[-]	Particle in body $\mathcal{B}$
$\mathcal{B}_0$	[-]	$\mathcal{B}$ in the reference configuration ($t = 0$)
$\mathcal{B}$	[-]	$\mathcal{B}$ in the current configuration ($t > 0$)
$(\partial\mathcal{B})$	[-]	Boundary of $\mathcal{B}$
$(\partial\mathcal{B})_{\boldsymbol{t}}$	[-]	Traction boundary of $\mathcal{B}$
$(\partial\mathcal{B})_{\boldsymbol{u}}$	[-]	Dirichlet boundary of $\mathcal{B}$

Symbol	Unit	Description
dV	[mm^3]	Volume element in the reference configuration
dv	[mm^3]	Volume element in the current configuration
V	[mm^3]	Volume of $\mathcal{B}$ in the reference configuration
v	[mm^3]	Volume of $\mathcal{B}$ in the current configuration
Ψ	[MPa]	Volumetric strain energy
c_1	[MPa]	Isotropic material constant
c_2	[MPa]	Isotropic material constant
c_3	[MPa]	Anisotropic material constant
c_4	[-]	Anisotropic material constant
κ	[MPa]	Bulk modulus
ι	[MPa]	Shear modulus
$\sigma_{\mathrm{iso}}^{\mathrm{max}}$	[MPa]	Max isometric stress in muscle fibre
ν_{asc}	[-]	Skeletal muscle parameter
ν_{dsc}	[-]	Skeletal muscle parameter
ΔW_{asc}	[-]	Skeletal muscle parameter
ΔW_{dsc}	[-]	Skeletal muscle parameter
ω	[-]	Switch to toggle the anisotropy of muscle fibres
$I(\bullet)$	[-]	Invariant of $(\bullet)$
$\bar{I}_{(\bullet)}$	[-]	Deviatoric invariant of $(\bullet)$
J	[-]	Determinant of the deformation tensor
$\mathcal{K}$	[N mm]	Kinetic energy in $\mathcal{B}$
$\mathcal{E}$	[N mm]	Internal energy in $\mathcal{B}$
θ	[K]	Temperature of $\mathcal{B}$
$\mathcal{D}$	[N mm]	Internal dissipation
ϑ	[-]	Element damage flag
ζ	[-]	Phenomenological damage variable
η	[N^{-1} mm^{-1}]	Continuous damage variable
μ	[N^{-1} mm^{-1}]	Discontinuous damage variable
γ	[N mm]	Discontinuous damage offset
$\zeta_{\mathrm{c},\infty}$	[-]	Maximum permitted continuous damage
$\zeta_{\mathrm{d},\infty}$	[-]	Maximum permitted discontinuous damage
$\dot{\Psi}$	[mJ s^{-1}]	Rate of strain energy
$\hat{\zeta}$	[s^{-1}]	Rate of change of phenomenological damage
ϕ	[-]	Damage criteria
$\mathbb{E}$	[N mm]	Equivalent strain energy
f	[N]	Thermodynamic force
$\dot{f}$	[N s^{-1}]	Rate of change of f
β	[N mm]	Continuously accumulated discontinuous energy

Vectors

Symbol	Unit	Description
$\boldsymbol{U}$	[mm]	Displacement of $\mathcal{P}$ in the reference configuration
$\boldsymbol{u}$	[mm]	Displacement of $\mathcal{P}$ in the current configuration
$\boldsymbol{V}$	[mm s^{-1}]	Velocity of $\mathcal{P}$ in the reference configuration
$\boldsymbol{v}$	[mm s^{-1}]	Velocity of $\mathcal{P}$ in the current configuration
$\boldsymbol{A}$	[mm s^{-2}]	Acceleration of $\mathcal{P}$ in the reference configuration
$\boldsymbol{a}$	[mm s^{-2}]	Acceleration of $\mathcal{P}$ in the current configuration
$\boldsymbol{T}$	[N mm^{-2}]	Traction on a unit area of $\mathcal{B}$ in the reference configuration
$\boldsymbol{t}$	[N mm^{-2}]	Traction on a unit area of $\mathcal{B}$ in the current configuration
$\boldsymbol{L}$	[N mm]	Linear momentum of $\mathcal{P} \in \mathcal{B}$ in the reference configuration
$\boldsymbol{J}$	[N mm^2 s^{-1}]	Angular momentum of $\mathcal{P} \in \mathcal{B}$ in the reference configuration
$\boldsymbol{b}$	[N mm^{-3}]	Body force acting on $\mathcal{B}$ in the reference configuration
$\boldsymbol{a}_0$	[-]	Muscle fibre direction in the reference configuration
$\hat{\boldsymbol{e}}_1, \hat{\boldsymbol{e}}_2, \hat{\boldsymbol{e}}_3$	[-]	Basis vectors
$d\boldsymbol{S}$	[mm^2]	Infinitesimal area element in the reference configuration
$d\boldsymbol{s}$	[mm^2]	Infinitesimal area element in the current configuration
$\boldsymbol{N}$	[-]	Surface normal to $d\boldsymbol{S}$
$\boldsymbol{n}$	[-]	Surface normal to $d\boldsymbol{s}$

2$^{\text{nd}}$ order tensors

Symbol	Unit	Description
$\mathbf{I}$	[-]	Second-order identity
$\mathbf{F}$	[-]	Deformation gradient
$\mathbf{C}$	[-]	Right Cauchy-Green tensor
$\mathbf{b}$	[-]	Left Cauchy-Green tensor
$\mathbf{M}$	[-]	Material tensor
$\mathbf{d}$	[s^{-1}]	Rate of deformation tensor
$\mathbf{E}$	[-]	Green-Lagrange strain tensor
$\mathbf{e}$	[-]	Euler-Almansi strain tensor
$\boldsymbol{\sigma}$	[MPa]	Cauchy stress tensor
$\tilde{\boldsymbol{\sigma}}$	[MPa]	Volume-normalised Cauchy stress tensor
$\boldsymbol{\sigma}_{\text{ich}}$	[MPa]	Deviatoric Cauchy stress tensor
$\boldsymbol{\tau}$	[MPa]	Kirchhoff stress tensor
$\mathbf{P}$	[MPa]	First Piola-Kirchhoff stress tensor
$\mathbf{U}$	[-]	Right stretch tensor
$\mathbf{v}$	[-]	Left stretch tensor
$\mathbf{S}$	[MPa]	Second Piola-Kirchhoff stress tensor
$\boldsymbol{\sigma}^{\text{VM}}$	[MPa]	von Mises stress tensor

3rd order tensors

Symbol	Unit	Description
$\boldsymbol{\mathcal{E}}$	[-]	Ricci permutation tensor

4th order tensors

Symbol	Unit	Description
$\boldsymbol{\mathfrak{I}}$	[-]	Fourth-order identity
$\boldsymbol{\mathfrak{C}}$	[MPa]	Fourth-order material tangent
$\boldsymbol{\mathfrak{B}}$	[MPa]	Fourth-order spatial tangent

1 Introduction

1.1 Motivation

Above-knee or transfemoral amputation, which is the focus of this thesis, is a life-changing and devastating experience, where diseased or damaged parts of the lower limbs are surgically removed. After an above-knee amputation, the knee joint is removed, which is a severe disability in comparison to the transtibial or below-knee amputation. Therefore, this thesis focusses on the problems faced by a transfemoral amputee. Following a lower limb amputation, movement from one place to another becomes both physically and mentally challenging, which is exacerbated by the lack of knee joint in transfemoral amputees (cf. Dillingham et al., 2001). The goal of rehabilitation programs is to train amputees in overcoming these challenges, in order to try and restore normal mobility. In these programs, on the basis of individual requirements, e.g. activity level, age, health and other socio-economic factors, amputees are provided assistive devices such as crutches, wheelchairs, osseointegrated or socket prostheses to help in ambulation. The primary reason for prescribing mobility devices other than prosthetics, such as wheelchairs and crutches to transfemoral amputees, was short stumps (cf. Karmarkar et al., 2009). According to a National Health Interview Survey in the United States, about 80 % of lower limb amputees were fitted with socket prostheses (cf. Sondik et al., 1999). The reasons for amputees and prosthetists preferring prosthetics to other assistive devices are higher utility, better mobility, and ease of use and concealment (cf. Legro et al., 1999). An ideal prosthetic socket is a suspension device, which forms a tight seal between the prosthesis and stump, and efficiently transfers the loads between them. The job of a prosthetist is to design such sockets by identifying sensitive and load-bearing regions of the stump, and to ensure that loads in the socket-stump complex do not injure the residual limb.

In the order of importance, an ideal socket prosthesis, henceforth simply referred to as prosthesis, should be comfortable, functional and aesthetically acceptable. But a high correlation among these factors makes the art of designing an equally comfortable and functional prosthesis extremely challenging (cf. Radcliffe, 1955). For example, aesthetics will limit the functional complexity of a mechanical prosthesis that aims to achieve an efficient transfer of forces and moments between the residual limb and its surroundings. A prosthesis that is motivated by purely functional design might excessively load pressure-sensitive regions of the residual limb by favouring efficiency to comfort, which might lead to pain and disintegration of tissues in the residual limb. To mitigate pain and prevent tissue injury, compensatory mechanisms in our body try to shift some of these excessive loads to the healthy limb, which can ultimately result in degradation of the other (healthy) limb as well (cf. Underwood et al., 2004). Therefore, the task of a prosthetist in designing an optimal socket that relieves excessive loads at sensitive areas of the stump and loads those regions of the stump that are capable of withstanding high pressures, is paramount.

Despite the importance of socket design, no standardised scientific techniques exist to date with which the quality of a socket fit can be estimated. Moreover, the empirical nature of designing sockets renders the task of evaluating their fit rather difficult. This statement is corroborated by scientific studies that lend support to the fact that socket fits vary greatly, not only from one prosthetist to another but also within the same prosthetist, indicating that socket fits are mostly sub-optimal (cf. Boone et al., 2012, Kobayashi et al., 2015). Therefore, any means to clinically quantify a socket's fit would help a prosthetist in creating well-fitting sockets. As a result, the relationship between socket rectification and the resulting fit can be understood, which would ensure replicable socket designs. In this regard, a numerical scale for rating pain, developed by Downie et al. (1978), was employed by Hanspal et al. (2003) to quantify socket fit. Herein, pain was chosen as the prime indicator of socket fit.

Pain is an indication of discomfort and possible injury, and its threshold, if it can be quantified, can be used in estimating socket fits. This threshold is, however, difficult to compute since pain is subjective. Moreover, the threshold varies from one person to another. Taking cues from patient-reported sites of discomfort, pressure at the residual limb-socket interfaces was commonly used as means to quantify pain (cf. Appoldt et al., 1970, Beil et al., 2002). When pressure recordings were insufficient, skin temperature in the residual limb was additionally measured. High temperature resulting from excessive friction between the socket and limb was assumed to cause skin disintegration and pain (cf. Peery et al., 2006). Some researchers calculated the energy expended during gait by studying the volume and rate of oxygen intake, while others developed psychophysical models that accounted for the patient's psychological state when donning a prosthesis (cf. Detrembleur et al., 2005, Neumann, 2001).

Following a lower limb amputation, soft tissues in the residual limb are easily susceptible to pain and injury resulting from the altered biomechanics of the skeleton. As a result of donning a prosthetic socket, tissues in the residual limb are subjected to high normal and shear loads, which among other factors, play a significant role in the aetiology of injury. For example, deep tissue pressure injuries, which result from prolonged pressure and shear forces at the bone-muscle interface (cf. Edsberg et al., 2016), are fatal. When such deep tissue injuries in the residual limbs are not detected early, they often require higher levels of amputation. With recent advances in medical imaging, it is possible to monitor the health of tissues deep within the body (cf. Bader & Worsley, 2018, Vogl et al., 2010). Invasive scientific experiments such as those conducted by Linder-Ganz et al. (2006) on albino rats might help determine the aetiology of soft tissue injury. But human trials are ethically bound, and invasive tests cannot be performed. However, such an experiment might prove invaluable in understanding the relationship between soft tissue deformation and pain. Obtaining this valuable insight is possible through the use of computational tools such as the Finite Element Method (FEM), in addition to experimental methods. The FEM is a powerful technique for solving complex real world problems, which can also be employed to analyse the socket-stump interaction. Using 3D models of the residual limb, along with realistic boundary conditions, finite element (FE) analyses can provide deeper insights into the internal state of tissues in the stump, which might be expensive or difficult using contemporary experimental methods. Gefen et al. (2008), Linder-Ganz & Gefen (2004) and Oomens et al. (2010) have shown that the internal stress-strain state of soft tissues in the residual limb provide better means to identify deep tissue injuries. Since the concept of stresses and strains are intrinsic to FEM, whose meaning can be readily extrapolated to injury or pain, the FEM as a computational tool can prove useful to prosthetists in creating well-fitting sockets.

The success of using FEM for estimating the state of internal stress in the residual limb hinges on the details of the finite element model. A realistic residual limb model with individual muscles, tendons, fat and skin can aid in accurately predicting the location and type of tissue experiencing high stresses or strains. Likewise, an accurate prediction is only possible when the finite element material models of these layers can describe the desired behaviour. For example, if deep tissue injury prediction is desired, an appropriate damage model should be used; if active muscle contraction must be studied then activation parameters should be included in the material model. And finally, the boundary conditions used in the finite element simulations must represent the experimental, or real world conditions, which the residual limb-socket complex will be subjected to. Some examples of such realistic boundary conditions are normal and fast-spaced gait, walking up and down stairs, high and low temperatures.

It is possible to generate realistic, i.e. detailed and accurate 3D models of the residual limb from medical images using several open-source and commercial software. This task, however, involves intense manual labour. Reviews by Silver-Thorn et al. (1996), Mak et al. (2001) and Dickinson et al. (2017) state that there might be value in modelling within-tissue inhomogeneity and in simulating the stump-socket interaction with the complete prosthesis. However, the state-of-the-art stump models used in FE analyses are neither detailed nor analyse the dynamic full prosthesis-stump interaction. One possible reason for choosing simple stump models could be the labour-intensive task of converting the medical images to 3D models, which is required to obtain detailed stump models. There has been tremendous research in the development of FE material models to simulate the behaviour of biological soft tissues. With experimental technologies such as electromyography (EMG), ultrasound, Microsoft Kinect and motion capture, it is possible to obtain data, which can provide realistic boundary conditions for FE analyses. Despite these advancements, scientific research on lower limb amputees has not altered the fundamental clinical practice (cf. Mak et al., 2001). The status-quo of biomechanical models used in the FE analysis of socket-stump interactions must be challenged by more advanced geometric and continuum mechanical models that can help the prosthetists to design well-fitting and comfortable prosthetic sockets.

1.2 State of the art

The field of lower limb amputee care has a rich history replete with technological advancements in surgical, experimental, and computational methods. Although prosthetics, as a field of medicine, existed since the 16^{th} century, it was not until the Second World War (1940s) that the field evoked scientific interest. Beginning with simple cosmetic replacements for lost limbs, the field has undergone tremendous growth to the current state, where bionic limbs have neural interface with the body. Since the possibility of incorporating technology in every aspect of a prosthesis is endless, it is important not to lose focus of the core problem at hand, which is essentially to restore comfort while maintaining a functional prosthesis.

Relevant articles pertaining to lower limb amputation, transfemoral prosthetics, finite element analysis, and medical imaging were queried in the period 1914 to 2018. The purpose was to focus on the contribution of finite element analysis in the advancements made in lower limb prosthetics. Since the field of prosthetics is highly patient-specific, the database was queried for those articles where medical scans of patients were used to model residual limbs for the FE analyses. Finally, an overview of the current (at the point of writing) topics of interest are summarised in the form of a word cloud. And, in Section 1.3, a set of concrete research questions are drawn from the state-of-the-art, which provides the aim and scope of the work in this thesis.

1.2.1 History of lower limb prosthetics

Developments in the field of lower limb prosthetics are grouped into decades, starting from 1941 until 2018. The search queries are listed in Section 9.2. The most significant contributions are listed as keywords alongside the time period, followed by their detailed description.

1941 – 1950: Suction sockets

Early transfemoral sockets required suspension systems such as lanyard cables and waist belts. These suspension techniques posed a considerable challenge in comfortably attaching the socket with residual limb during gait due to pistoning, i.e. translation of the residual limb within the socket. Pistoning leads to loss of control, and also requires extra energy to ambulate. To counter this problem, suction sockets were introduced, which directly attached to the stump by creating a vacuum between the socket and residuum (cf. Brodbeck, 1947, Canty & Ware, 1949, Forten, 1947).

1951 – 1960: Patient-specific care, socket fitting techniques

The suction sockets were easier to don than lanyard cables but were time consuming for the prosthetists to create an adequate fit (cf. Klein, 1959, Thorndike, 1955). In 1955, Radcliffe, who is widely regarded by many as the father of prosthetic biomechanics, proposed three basic requirements of a prosthesis – comfort, function and appearance (cf. Radcliffe, 1955). On this basis, he designed the quadrilateral socket, which was one of the most successful and widely used transfemoral socket designs. These basic requirements of prosthesis, though seemingly simple, are highly interrelated, and still pose a considerable challenge till date. Radcliffe et al. (1957) was also the first to emphasise the uniqueness of each amputee, and therefore the necessity for patient-specific care.

1961 – 1970: Modular prostheses, Knee mechanisms, Interface pressure

A major development in this decade was the concept of modular transfemoral prostheses. Individual parts of a prosthesis, which used to be constructed in a prosthetist's workshop, were beginning to be pre-fabricated, and fitted to an amputee. A review by Wilson (1968), on the advancements being made in the field of transfemoral prosthetics, revealed significant research conducted towards designing knee mechanisms and pylons, and towards developing new fitting technologies (cf. Asrael & Leckitner, 1964, Hanger, 1964, Kay et al., 1966). Allende et al. (1963) documented the skin problems resulting from friction between the suction socket and residual limb. It was believed that the high vacuum required by suction sockets worsened the socket-stump interface, which was already burdened with excessive shear loads. In an attempt to quantify these shear loads at the residual limb-socket interface, Appoldt et al. (1970) designed the first experiment with strain gauges and pressure transducers to quantify horizontal and tangential pressure during gait.

1971 – 1980: Gait analyses, Socket design, Simulation, Knee control, Personal digital computers

The practicality of modular prostheses resulted in their popularity and mass adoption well into the 1970s and in the forthcoming decades. One challenge in using these modular prostheses was in obtaining an optimal alignment of individual prosthetic components, which would provide adequate balance and comfort to the subject. Taylor (1979a,b) addressed them by proposing alignment units or norms to help the prosthetist in aligning the individual components of a transfemoral prosthesis with the residual limb.

This period also saw the emergence of the first gait analyses. Leavitt et al. (1972) conducted dynamic interface pressure measurements to compare gait and interface pressures in amputees and non-amputees. They standardised the gait parameters and ensured repeatability of their proposed methodology, which marked the beginning of modern gait analysis. Based on photographic gait analysis, Hershler & Milner (1980), Hughes & Jacobs (1979), Murray et al. (1980) concluded that although gait abnormalities increase the energy cost of walking, they provided safety, balance, and compensated for problems related to the use of prostheses.

Substantial contributions were also being made in the field of prosthetic socket and knee joints. A significant outcome in socket research was the development of total surface bearing socket by Redhead (1979). Unlike the quadrilateral socket, which transferred loads from the ground to ischial tuberosity, this socket transferred loads directly to the soft tissues of the residuum. It was based on the hypothesis that soft tissues in the residuum, when adequately supported in a suitable socket, will behave as an elastic solid, and are therefore capable of load transmission. Mechanical constant-friction knee joints were commonly used in transfemoral prostheses. Here, mechanical friction between the components of the knee joint controlled the knee-locking mechanism. For example, in a manual-locking knee, the knee was locked during gait, which the patient released when sitting down; in a single-axis constant-friction knee, the flexion and extension of the knee was controlled by the subject's musculature. Cappozzo et al. (1980) proposed a passive polycentric knee-ankle mechanism to reduce the muscular effort that was required to control constant friction knee joint prostheses.

This period also witnessed the dawn of digital personal computers, and consequently, the first computer simulation in the field of prosthetics. Zarrugh & Radcliffe (1976) created a mathematical model of an above knee prosthesis to study swing phase dynamics, and offered performance assessments of knee joint control systems without the need for experimental prototypes. Electronically-controlled knee mechanisms were also developed during this period (cf. Dyck et al., 1975, Fernie et al., 1978, Flowers & Mann, 1977). The dynamic gait and interface pressure measurements by Leavitt et al. (1972) were performed on a PDP-8 digital computer, which was used to simultaneously measure knee motion and residual limb-socket pressures.

1981 – 1990: Surgical techniques, Gait analyses, Finite element simulations

The 1980s witnessed extensive research to salvage limb loss occurring due to peripheral vascular diseases. Surgical re-vascularisation of affected limbs were attempted using femoropopliteal grafts. An overview of the re-vascularisation techniques are provided in Taylor et al. (1990, 1986).

Following the quadrilateral and total surface bearing sockets, another transfemoral socket based on the principle of containing the ischial ramus within the socket was introduced. Interestingly, all three socket designs are variations of one another, and are based on the biomechanical principles laid out by Radcliffe (cf. Pritham, 1990). This socket design aimed to correct the excessive shear forces that was applied by quadrilateral sockets on the proximal medial tissues lying between the medial brim of the socket, and the medial bones of the pelvis.

In the gait analysis by Leavitt et al. (1972), photoelectric cells were used to record gait solely in the sagittal plane. With increasing computational power, three-dimensional tracking of human gait was made possible through light emitting diodes (LEDs). Stein & Flowers (1987) studied gait kinetics during stance phase, and established the inter-dependence of knee controllers and designs of foot-ankle prostheses. Most interestingly, they also determined that normal knee kinematics does not necessarily produce normal hip kinematics. Apart from experimental methods, mathematical models of the prostheses were also being used to study knee control mechanisms (cf. Hale, 1990, Oberg & Lanshammar, 1982, Tsai & Mansour, 1986). Computer simulations were employed by Ishai & Bar (1983) to determine the influence of alignment changes on the resulting socket comfort based on thigh axial torque thresholds. Zahedi et al. (1986) performed an experimental sensitivity study of the influence of inter-component alignment changes on the function and comfort of a transfemoral prosthesis. It was concluded from this study that although there might be a unique optimal alignment, the amputees are generally capable of accepting a wide range of possible alignments. Another interesting conclusion drawn from these experiments was that the prosthetists were unable to detect variations in geometrical configuration of the prosthesis, gait patterns and alignment parameters.

Krouskop et al. (1987) analysed internal soft tissue stresses when donning a socket using the finite element (FE) method. The novelty in this research was that it was the first comprehensive, patient-specific approach using a simulation-based study. Mechanical soft tissue properties of the thigh were determined from 4 regions of the stump using an ultrasound Doppler system, averaged and additionally validated against measurement data from an Instron machine (cf. Malinauskas et al., 1989). Moreover, geometry of the residual limb was obtained from shape-sensing surface scan data. The soft tissues were assumed to be homogeneous, linear elastic and isotropic. Finally, prosthetic sockets were fabricated and evaluated based on stress-strain results from the simulation.

1991 – 2000: Medical imaging, FE simulations, Gait analyses, Active knee, Grafts

Smith et al. (1996) showed that computed tomography (CT) scans were accurate for the purposes of modelling residual limbs, and that any change in the shape of residual limbs as a result of wearing a prosthesis can be accurately determined from these scans. Their experiments showed that the volumetric error in the residual limb model, which was reconstructed from the CT scans, was about 1 %. Commean et al. (1997) investigated residual limb-socket interactions using finite element models of the residual limb constructed from spiral X-ray computed tomography (SXCT) images of the subject. This was one of the earliest studies incorporating subject-specific models of the limb from anatomically accurate medical images for use in finite element analyses. They used linear elastic, homogeneous and isotropic model of the residual limb to analyse the slippage of skin relative to the internal wall of the socket under various loading conditions. Similarly, other imaging modalities, e.g. computed tomography (CT) and magnetic resonance imaging (MRI) were also used for modelling the residual limb. He et al. (1997) proposed the use of a compound ultrasound scanning technique with which several 2D slices of the scanned residual limb can be stitched together to create the 3D surface of the limb. Convery & Murray (2000) performed the first experiments in which they studied the motion of femur relative to the socket using ultrasound sensors during gait. They also proposed the combined use of ultrasound and pressure measurements to relate relative femur movements to changes in pressure distributions, which could then be used to quantify socket fit.

Knee controllers that rose to prominence in the 1980s were plagued with stability problems, often leading to gait instability and higher metabolic cost for walking. As a result, experiments and computational models were developed to detect gait phase for implementation in active knee controllers, and to identify optimal control strategies for active knee joints. Aeyels et al. (1992) developed a prototype of an adaptive microcomputer-controlled knee joint that detected the active gait phase, and adapted the knee angle accordingly. Results from field tests indicated that while it was possible to smoothly control knee flexion, its acceptance by the patient during the early stance phase was not readily obtained. They concluded that refinements in the control strategy might be required for patient acceptance. Around the same time, Popović et al. (1991) devised a hierarchical control method for one degree of freedom (DoF), powered above-knee prostheses. The proposed control strategy was meant to provide simulation-based information for designing the prosthesis, and to control the prosthesis in real-time. Later, Popović et al. (1995) extended the above model to two DoFs – the first degree of freedom being the flexion-extension rotational DoF, and the second being the lateral-medial rotation of the shank. They intended their research to be used for selecting an appropriate motor and actuator hardware for controlling active knees.

In the field of gait analysis, Jaegers et al. (1995) compared the kinematics of trunk, hip and knee joints of both legs in unilateral transfemoral amputees. Interesting compensatory patterns emerged and relationships were drawn between various gait parameters such as stride length, step rate, step width and gait symmetry. Jaegers et al. (1996) extended the previous study (cf. Jaegers et al., 1995) to include electromyographic activity of hip muscles after amputation, and determined their activation levels during different phases of gait. They found that hip muscles remained active longer in amputees than in healthy humans, and attributed the reason to the necessity of hip muscles to control the prosthesis.

One notable contribution in the field of surgical amputation of the lower limb was from Gottschalk & Stills (1994). They documented the importance of *adductor magnus* in stabilising the residual limb, and also emphasised the importance of myodesis in restoring functional muscular power in the residual limb. In order to emphasise the necessity and importance of myodesis, Gottschalk (1999) performed 30 such muscle preserving myodesis surgeries to show that the procedure results in correctly oriented femur, and that the muscles are capable of producing enough power to ambulate.

During this period, FE simulations were being extensively used to gain an understanding of the socket-stump interface. Zhang & Mak (1996) used FE simulations to analyse different distal-end loading conditions of a 2D residual limb model. Linear elastic models were chosen for the limb, soft tissues and socket. Zachariah & Sanders (1996) created, to the author's knowledge, one of the first methods to efficiently and automatically create FE mesh of residual limbs from CT scans, optical scanning and mechanical surface digitisation. Zhang & Roberts (2000) compared interface stresses in a below knee residual limb of an amputee with clinical experiments. Subject-specific 3D residual limb geometry was obtained by digitising biplanar X-ray views. The FE stance simulation was performed in two stages – a socket donning simulation, followed by a static simulation of unilateral stance. All materials, namely, soft tissues, bone and liner were modelled with linear elastic and isotropic materials. Based on the differences between experimentally observed and FE-predicted stresses, They concluded that non-linear material properties and dynamic analysis of the stance problem might be necessary to obtain better stress predictions. Several other researchers also focussed on the FE analysis of the residual limb-socket interface pressure to study the effect of friction at the interface, to estimate socket fit, and to perform parametric studies with anthropometric limb and socket models (cf. Reynolds & Lord, 1992, Silver-Thorn & Childress, 1996, Zachariah & Sanders, 1996, Zhang et al., 1995, 1998)

2001 – 2010: Simulations, Patient specific

In this decade, one can observe a shift from experimental studies towards simulation-based ones. A review of the state-of-the-art in prosthetic biomechanics can be, for example, found in Mak et al. (2001). They drew the conclusion that the field of prosthetics had not greatly benefitted from the recent scientific advancements, and more specifically that the idea of employing interface stress measurements did not have enough clinical consensus to alter clinical practice. Regarding computational models that were being used to study the residual limb-socket interface, they concluded that analyses should be performed using the whole prosthesis, and not just with the prosthetic socket. Further, the insufficiency of literature data on pain or skin breakdown thresholds, and the lack of understanding of tissue properties were found to undermine the discussion of optimal load distribution between the limb and prosthesis.

There was continued research in obtaining experimental residual limb-socket interface pressures during various physical activities such as walking up and down the stairs, slope and flat surfaces, and using various liner-socket combinations (cf. Beil et al., 2002, Dou et al., 2006, Dumbleton et al., 2009). Linder-Ganz & Gefen (2004) hypothesised that mechanical properties of muscle tissues change when subjected to prolonged loads, and performed mechanical compression experiments on the *gracilis* muscle of rats to validate this hypothesis. In this work, they emphasised the importance of internal muscle stresses to prevent catastrophic deep pressure sores, which are not obtained from interface pressure studies. This work was extended by Gefen et al. (2005) to simulate the development of pressure sores in the buttocks of wheelchair users using FE analyses. While recognising the importance of detailed muscle models, they cited the lack of detailed experimental data as reasons for modelling muscles as homogeneous, isotropic materials in their FE simulations. Linder-Ganz et al. (2006) repeated the mechanical indentation experiments on rats for histopathology experiments. The histopathology findings provided correlation between cell death, indentation pressure and its duration with which a sigmoidal curve for predicting pressure-time cell death was proposed. Gefen et al. (2008) proposed that deep tissue injuries, a problematic form of deep pressure sores, are induced by excessive strains. Using engineered bio-artificial muscles, they also provided a strain-based sigmoidal cell death curve that was similar to Linder-Ganz et al. (2006). Portnoy et al. (2008) applied these findings by Linder-Ganz & Gefen (2004), Gefen et al. (2005) and Linder-Ganz et al. (2006) to simulate the internal mechanical conditions in a transtibial amputee at the end of socket-loading phase. The residual limb model for the FE analysis was segmented from MRI scans, and consisted of tibia, fibula, muscle flap and socket. The muscle flap was modelled with nonlinear Mooney-Rivlin material, while the bones and socket were linear elastic. This was the first study that analysed the deep tissue injuries in amputees using an anatomically accurate 3D model of the residual limb in a nonlinear finite elasticity framework. Based on previous research (cf. Gefen et al., 2005, Linder-Ganz et al., 2006, Linder-Ganz & Gefen, 2004, Linder-Ganz et al., 2007, Portnoy et al., 2008), Oomens et al. (2010) proposed that interface pressure is not a sufficient parameter to define a damage threshold and that the internal conditions in the residual limb, especially the strains, play a crucial role in defining the thresholds for deep tissue injuries.

2011 – 2018: Active knee control, Gait analyses

Extensive research was conducted to understand the reasons behind gait pathology in amputees using 3D motion capturing systems. Klotz et al. (2011) analysed the influence of different types of transfemoral sockets on the kinematics of hip joint. Upon analysing the hip joint kinematics without a socket, with quadrilateral socket, ischial containment and ischial-ramal containment sockets, they concluded that all sockets barring the ischial-ramal containment socket had a negative influence on the correct functioning of the hip joint. Andersen et al. (2012) analysed the motion of subjects mounted with both bone-pins and reflective markers, and developed a linear model to predict the motion of skin markers, i.e. soft tissue artefacts based on the movement of bone. Although marker-based 3D motion capture systems provided the possibility to obtain gait kinematics, they were not repeatable. Kent & Franklyn-Miller (2011) published a review of the biomechanical models, which concluded that there was no single marker set that can be employed in all contexts. Chong et al. (2015) showed the presence errors when tracking the motion of rigid bodies with reflective markers, proving that tracking errors do not necessarily stem from soft tissue artefacts. Dumas et al. (2017) also quantified the errors arising from 3D motion capture systems by comparing the magnitudes of forces and moments at the knee joint using motion capture and from direct measurements. These studies confirm that inverse dynamics should be used cautiously. Despite these warnings about using motion capture for gait analyses, it still remains a popular tool for understanding amputee gait kinetics and kinematics. Hendershot et al. (2018), Hendershot & Wolf (2014, 2015), and Shojaei et al. (2016) analysed the effects of pathological kinematics and kinetics on the lumbar column in lower limb amputees, and concluded that gait pathology was the primary reason for lower back pain and injury in amputees. Russell Esposito et al. (2015) established that the risk of unilateral transfemoral amputees developing knee osteoarthritis, as a result of excessively loading the sound limb, was high. Gholizadeh et al. (2014) reviewed the state of transfemoral suspension systems, and based on the literature review, identified reasons for reluctance to prosthetic use. The primary socket-related problems were discomfort, perspiration and skin problems. They concluded that transfemoral suspension has received less attention compared to transtibial prostheses, and more importantly, clinical and expert opinions on prosthetic suspension systems, i.e. socket designs, are still open-ended.

Ha et al. (2011) and Hefferman et al. (2015) integrated surface electromyographs (sEMG) in prosthetic sockets. Using the sEMG signals from *quadriceps* and *hamstring* muscles, Ha et al. (2011) controlled flexion and extension of active knee prosthesis. The subject's intent was determined through a combination of sEMG signals, pattern classification and principal component projection to flex or extend the knee. Hefferman et al. (2015) tested four configurations of socket-sEMG sensor combinations to determine which combination resulted in a comfortable socket with the lowest number of large amplitude motion artefacts. Of the four different configurations, suction socket with wireless sEMG sensors was judged to be the best. Durandau et al. (2018) used EMG signals developed during muscle contractions to accurately determine the muscular forces and joint moments, which might be useful in designing neural interfaces to prosthetic sockets. Geng et al. (2018) investigated the feasibility of using sub-dermal electrical stimulations to provide sensory feedback from prosthetic devices.

Frillici & Rotini (2013) attempted to create a clinically applicable tool to design prosthetic sockets through shape optimisations. Although the tool used techniques similar to those used by prosthetists to create a socket, shape optimisation based on FE analyses required several design iterations to converge to an optimal result. They identified the use of FE simulations for socket-shape optimisation to be a limiting factor for clinical applicability. A trade-off between accuracy (highly detailed model) and speed is required to use this tool. Colombo et al. (2013) created a digital platform where different prostheses could be fitted to a virtual subject. Simulations performed in this study were clinically oriented, with reduced complexity in the models, and primarily focussing on speed rather than on accuracy.

Lacroix & Patiño (2011) analysed the residual limb-socket interface pressures when donning a transfemoral socket. The residuum was modelled from MRI scans, and was segmented into bone and skin/fat layers. The bone was linear elastic, and soft tissues were modelled with hyperelastic materials. They concluded that patient-specific models are necessary for FE analyses of the residuum, and for socket design studies. Zhang et al. (2013) also performed a transfemoral socket donning simulation but with sliding contact between the socket and limb. Zhang et al. (2013) also modelled the residual limb geometry with 2 layers – bone and soft tissues, and the soft tissues with hyperelastic materials. Ramírez & Vélez (2012) considered friction between bone and surrounding soft tissues in an FE simulation of bipedal static stance. The soft tissues were modelled from MRI scans, and were segmented into bone and fat/skin layers. Bone was modelled with linear elastic material model, and the soft tissues with viscoelastic material. By comparing tied and frictional contact between bone and surrounding soft tissues, they showed that interface stresses were higher when frictional contact was modelled. Sengeh & Herr (2013) employed CAD/CAM processes to manufacture a variable impedance socket for a transtibial amputee. For the FE analyses, the residual limb of the amputee was modelled from MRI scans. Both the residual limb and socket were modelled as linear elastic materials. The regions on the residual limb subjected to high interface stresses were identified from the FE analyses, based on which elastic stiffness of the socket was locally modified. Sengeh et al. (2016) and Cagle et al. (2017) used MRI scans of the residual limbs for generating detailed FE models. Sengeh et al. (2016) performed *in vivo* indentation tests

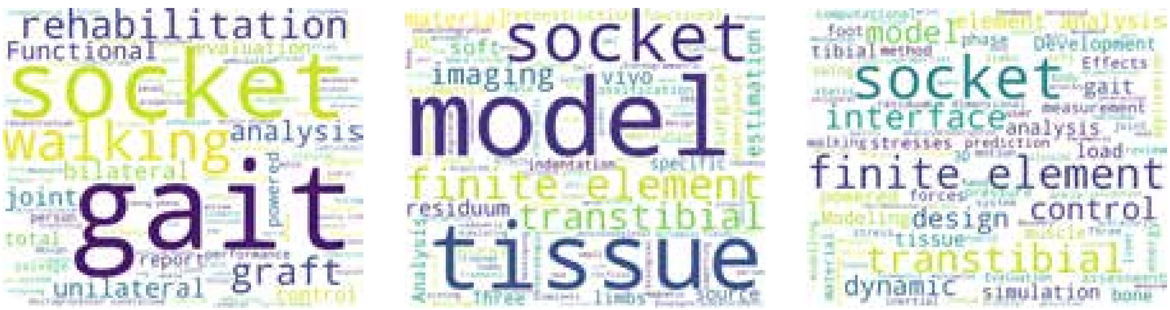

(a) *Transfemoral prosthetics* (b) *Medical imaging* (c) *Simulations*

Figure 1.1: *Word cloud illustrating the major topics of interest in transfemoral prosthetic development since* 1941 *until* 2018.

on the residual limbs of transtibial amputees to obtain viscoelastic material properties of the residuum, which was segmented into bone, fused muscle mass and skin. Cagle et al. (2017) studied the interaction between residual limbs and elastomeric liners in transtibial amputees. The FE models of the residual limbs were obtained from MRI scans, and were segmented into bone and skin/fat. Dickinson et al. (2017) provide an overview of the finite element analyses of the amputated lower limb.

Figure 1.1 shows the most frequently researched topics in the fields of transfemoral prosthesis, medical imaging and finite element simulations, in the form of a word cloud. This word cloud was generated from titles of the above reviewed articles, published over the last 78 years (1941 to 2018), using PubMed's Python API (Entrez Programming Utilities; cf. E. Sayers (2010)). In the next sections, the state of skeletal muscle and continuum mechanical models used in the FE analyses of socket-stump interactions are described.

1.2.2 FE Skeletal muscle models

As mentioned earlier, the success of employing FEM hinges on the details of the FE model. The FE models of the residual limb can be categorised broadly into generic and patient-specific models. Before the possibility of using medical imaging scanners for 3D modelling of residual limbs, generic stump models based on anthropometric data, were used. Steege et al. (1987) were the first to use the FEM for predicting the interface pressure at the limb-socket interface. A reference shape library for residual limbs for FE analyses was created by Torres-Moreno et al. (1989), which paved way for FE analyses with generic stump models. Silver-Thorn & Childress (1997) analysed the interface pressure between prosthetic socket and a generic limb, and concluded that capturing soft tissue anisotropy and heterogeneity are essential for FE analyses. Jia et al. (2004) constructed a 3D FE model of a transtibial stump from MRI scans to study the load transfer between the stump and socket. The stump was segmented into bones and soft tissues. Similar stump models were also constructed by many other researchers (cf. Cagle et al., 2017, Lee et al., 2004, Portnoy et al., 2007). However, detailed residual limb models with tissues segmented into, e.g. muscles, tendons and skin, are currently not used in the FE analyses.

Beyond the field of prosthetics, detailed biological models have been developed for studying skeletal muscles and other soft biological tissues. For example, Yucesoy et al.

(2002) modelled the skeletal muscle as two elastically linked intra- and extracellular domains. They showed that extracellular matrix is required to prevent muscle fibres from deforming beyond physiological limits. The effect of non-uniform shortening of active skeletal muscles was investigated by Chi et al. (2010) and Blemker et al. (2005). Here, the role of aponeuroses in generating experimentally-observed, complex and counter-intuitive strain distributions were analysed. Further, they identified the contribution of adjacent muscle fascicles to the force generated by a given muscle bundle. Röhrle et al. (2011) extracted single skeletal muscle fibres from stacked 2D micro-structural images of the *extensor digitorum longus* of a mouse. The micro-structural fibres could be used, e.g. to observe and numerically validate the musculoskeletal force transmission mechanism proposed by Yaman et al. (2013). With regard to modelling from MRI scans, Froeling et al. (2015) used diffusion tensor images to generate skeletal muscle fibres, and T_1- and T_2-weighted MRI scans to manually generate muscle geometries. The muscle geometries were used as regions of interest with which fibres of a given muscle were identified. Some multiscale models were also developed to couple large structural rigid body motions to deformations in the FE continuum mechanical models. Karajan et al. (2013) coupled multibody simulation of the deformation of a human lumbar segment with an FE analysis to study the stresses in an intervertebral disk, which was modelled as an inhomogeneous, biphasic and anisotropic material. Likewise, Röhrle et al. (2008) developed a framework for coupling electrophysiological cell model to a 3D continuum mechanical muscle model. The multiscale models provide the opportunity to drastically reduce the duration of simulations, to include physics from other fields of engineering such as chemistry, electromagnetics and fluid dynamics.

Scientific reviews of the FE models used in the field of prosthetics shed light on their shortcomings and provide focus for future research. Silver-Thorn et al. (1996) reviewed the methods employed to investigate socket-stump interface stresses and to identify their limitations. With regard to the state of FE models used in interface stress analyses, they identified two limitations. These were the representation of tissue properties across the entire limb and the interface condition between the residual limb and prosthesis, which were similar to the conclusions drawn by Sanders (1995). The review by Mak et al. (2001) pointed out two specific limitations in the FE analyses, namely (i) modelling of residual limb soft tissues, and (ii) effects of donning procedures with friction/slip interface conditions. They still pointed out the lack of accurate computational models to represent complex soft tissue deformation, and the lack of realistic boundary conditions in FE interface stress analyses. Further, they mention that FE studies on the stump-socket interaction must include the complete prosthesis, which can account for the effects of prosthetic alignment and joints. In the most recent review by Dickinson et al. (2017), it was mentioned that the state-of-the-art residual limb, capturing tissue inhomogeneity, was modelled in Portnoy et al. (2008), Portnoy et al. (2009b) and Portnoy et al. (2011). In these studies, the residuum was segmented into bone, fat, muscle lump and skin. Despite the emphasis on detailed human models by several authors, such models are currently not available as mentioned in the review by Dickinson et al. (2017). For example, Scheys et al. (2006) and Blemker et al. (2007) emphasise that image-based models and personalised biomechanical analyses are required to truly understand human movement, motion related disorders, or postoperative gait anomalies. Likewise, Fernandez & Pandy (2006) also place importance on realistic subject-specific, three-dimensional, individual-muscle FE models.

In the past decade, the residual limb models used in the FE analyses of stump-socket interaction have been extensively modelled with nonlinear materials. Lacroix & Patiño (2011) and Zhang et al. (2013) segmented the residuum into bone and soft tissue, and modelled the soft tissues with hyperelastic Mooney-Rivlin material. After performing a socket-donning simulation, Lacroix & Patiño (2011) analysed the stresses in the stump, while Zhang et al. (2013) studied the stresses at the socket-stump interface. Cagle et al. (2017) modelled the stump with hyperelastic Yeoh material to study the effect of liner in shielding the stump from high compressive and shear forces at the socket interface. Sengeh et al. (2016) modelled the elastic response of the stump with hyperelastic Ogden material, and the viscoelastic response using the quasi-linear theory of viscoelasticity, and fitted experimentally observed force-deformation response of the residuum to this model.

As early as 1980, the formation of pressure sores were identified in muscles of the residual limb, close to the bone, by Nola & Vistnes (1980). They observed the formation of pressure sores on Sprague-Dawley rats subjected to a pressure of 100 to 110 mmHg over an area of $1.5\,\mathrm{cm}^2$. Detecting the formation of pressure sores in amputees is extremely important when considering the higher levels of amputations they necessitate, which can also be life-threatening. However, it was not until 2006 when deep tissue injuries, in addition to interface pressures, were again considered a major factor in amputees. Linder-Ganz et al. (2006) performed an experiment, similar to Nola & Vistnes (1980), on albino rats to obtain a pressure-time cell death threshold for pressure sores. This study formed the basis for later studies, which analysed the potential occurrence of deep tissue injuries in amputees. Perhaps, the most significant contribution to the study of pressure sores was by Portnoy et al. (2008) and Portnoy et al. (2009a,b). They modelled the soft tissues in the residuum with hyperelastic materials, and used the strain-time cell death model proposed by Gefen et al. (2008) to identify potential regions of the residual limb that could be affected by deep tissue injury.

The tissue damage in the above models were based on lookup tables of strain- or pressure-time related cell death from experiments on rats and engineered tissues, and were not constitutively motivated. However, such damage models were developed for biological tissues in the framework of continuum damage mechanics, using the concept of internal variables. For example, Volokh (2008) proposed a strain-softening damage model for the prediction of arterial failure. They predicted soft tissue damage on a microstructural bi-layer fibre-matrix model. Ehret & Itskov (2009) predicted damage in anisotropic biological soft tissues, and showed the presence of Mullins effect from experiments on the skin of a mouse. Similarly, Peña et al. (2009) also predicted damage in soft tissues but extended the damage model to predict continuous and discontinuous damage, which was originally proposed by Miehe (1995) for rubber-like materials. Peña (2011) developed a rate-dependent soft-tissue damage model. Balzani et al. (2012), Waffenschmidt et al. (2014) and Ferreira et al. (2017) developed anisotropic damage models for biological soft tissues, and fitted their models to experimental data.

Apart from soft tissue models that describe damage, there are continuum mechanical models that capture the other aspects of a skeletal muscle. For instance, Odegard et al. (2008) and Röhrle et al. (2017) modelled the active and passive response of skeletal muscles with which the contractile property of muscles were simulated. Valentin et al. (2018) determined muscle activations in an upper limb based on a constrained optimisation problem, and showed the feasibility of using continuum 3D muscle models for muscle activation studies. Here, a surrogate model of a 2-muscle upper limb was developed to vastly reduce the computational effort. In the above models, the strain energy describing the state of skeletal muscles was additively split into an active and passive component. Here, the contraction was modelled through a single variable, which described the magnitude of muscle activation. Unlike the above models in which the active and passive responses of the muscles were additively split, Ehret et al. (2011) proposed an alternate activation model in which skeletal muscles changed their properties depending on their state of activation. Röhrle (2010) used a multi-scale, multi-physics skeletal muscle model to describe the skeletal muscle contraction. Herein, the cellular-level muscle physiology was coupled to the continuum electro-mechanical behaviour of the muscle. Similar to Odegard et al. (2008), he followed an additive split of the strain energy function into active and passive components. But the activation term was motivated by cellular parameters from an electro-physiological model proposed by Shorten et al. (2007). Yucesoy & Huijing (2012) developed the linked fibre-matrix FE model of skeletal muscles to account for the connectivity that exists between the muscle matrix and fibres, and to describe myofascial force transmission.

1.3 Research goals

To the author's knowledge, no previous study has developed a subject-specific modelling-simulation-analysis workflow in a continuum-mechanical framework, using continuum damage mechanics, to predict tissue injuries in amputees by modelling the dynamic interaction between the subject's residual limb and prosthesis. The purpose of this thesis is to fill that void.

This study specifically addresses three scientific challenges that currently hinder the clinical relevance and applicability of finite element methods in the field of prosthetics. The goals of the presented work are

1. to efficiently create automated subject-specific finite element models from medical imaging data,

2. to develop a modular workflow, which is extensible and clinically relevant, and

3. to check the sufficiency of minimally-segmented, fused-muscle models for studying the stump-socket interaction.

It is expected that the methodologies emerging from addressing the above three research goals, will provide the fundamentals for a scientific platform to analyse the fit of a prosthesis to an amputee, and therefore tremendously improve patient care.

1.4 Outline of the thesis

After this motivation (**Chapter 1**), a general background on a healthy human musculoskeletal system is provided in **Chapter 2**. The important role of bones and muscles in transferring forces within the skeletal system is discussed, which is followed by a discussion of the roles of a surgeon and prosthetist in pre-amputation planning and post-amputation care.

The workflow to efficiently generate subject-specific FE models from diffusion tensor MRI (DT-MRI) data is described in **Chapter 3**, and addresses the first and second research goals. This chapter forms the core of the thesis, and begins with a brief introduction to MRI and DT-MRI, which are necessary to understand the concepts and proposed workflow. The core idea behind this workflow was to use the embedded fibre information within the DT-MRI images to generate a finite element model of the residual limb with individual muscles. Methods to extract skeletal muscle fibres from DT-MRI images in order to reveal the architecture of soft tissues in the stump, are provided. This is followed by techniques to automatically generate a detailed finite element model of the residual limb consisting of individual muscles, fat and bone. Finally, a description of the mapping process, where the extracted fibres are mapped into the generated finite element mesh are given.

The material model with which stresses and damage in the soft tissues of residual limb were determined, are provided in **Chapter 4**. This chapter begins with the continuum-mechanical fundamentals and mechanical balance relations required to understand the proposed continuum damage model. The damage model is based on a continuous-discontinuous split of the damage variable, which is observed in fibred biological tissues. In addition to the continuum damage model, a strain-based experimentally-observed tissue damage, which models deep tissue injuries is introduced and implemented in the material model.

In **Chapter 5**, results of the proposed workflow are presented, namely the finite element residual limb model with embedded fibre distribution. In order to compare the proposed detailed model with the state-of-the-art models, an additional fused-muscle model is created. Finally, some case studies involving finite element simulations with the detailed residual limb model, are analysed.

Chapter 6 presents two analyses with the detailed stump model, namely liner donning simulation and forward dynamics simulation of *gluteus maximus* activation. In the liner donning simulation, stresses developed in the liner and in the deep tissues of the stump are presented.

In **Chapter 7** the residual limb is fitted with a full prosthesis with a kinematic knee joint, and a bipedal stance analysis is performed. This chapter addresses the third research goal concerning the sufficiency of the current state-of-the-art models. The prosthetic socket is first donned, and half the body weight is applied on the femur to simulate the bipedal stance situation. The stance condition is simulated for 2 h to detect potential regions of deep tissue injury.

The bipedal condition is extended to a fully dynamic gait simulation in **Chapter 8**. Boundary conditions on the femur are adapted from experimental motion capture analysis, and the stresses and potential regions of deep tissue injury are predicted. The evolution of deep tissue injury and relative femur-socket displacement are plotted, which could function as diagnostic tools in determining the quality of socket fit.

Chapter 9 presents an outlook and possible extensions of this work in the field of prosthetics, and possibilities of using the FEM to improving socket comfort.

1.5 List of publications

Research leading to the results presented in this thesis has previously been published in the following articles.

1.5.1 Peer-reviewed international journal articles

Ramasamy, E.; Avci, O.; Dorow, B.; Chong, SY.; Gizzi, L.; Steidle, G.; Schick, F.; Röhrle, O.: An Efficient Modelling-Simulation-Analysis Workflow to Investigate Stump-Socket Interaction Using Patient-Specific, Three-Dimensional, Continuum-Mechanical, Finite Element Residual Limb Models. *Frontiers in Bioengineering and Biotechnology* **6** (2018), 1–17, ISSN 2296-4185.

Chong, SY.; Dorow, B.; Ramasamy, E.; Dennerlein, F.; Röhrle, O.: The use of collision detection to infer multi-camera calibration quality. *Frontiers in bioengineering and biotechnology* **3** (2015), 1–6, ISSN 2296-4185.

1.5.2 Book chapters

Röhrle, O.; Sprenger, M.; Ramasamy, E.; Heidlauf, T.: Multi-Scale Skeletal Muscle Modelling: From Cellular Level to a Multi-Segment Skeletal Muscle Model of the Upper Limb, In: *Computer Models in Biomechanics. From Nano to Macro*, G.A. Holzapfel and E. Kuhl (Eds.): Springer Netherlands (2013) 63–75 ISBN 978-94-007-5464-5.

1.5.3 Conference proceedings and other non-peer reviewed publications

Dorow, B.; Ramasamy, E.; Röhrle, O.; and Schneider, U.: Entwicklung einer Simulationsumgebung für die Orthopädie: Virtual Orthopedic Lab. *Digital Engineering* **2** (2013) 28–29, ISSN 1435-9766.

Röhrle, O.; Ramasamy, E.; and Schmitt, S.: Forward Dynamics applied to a 3D continuum-mechanical model of the upper limb, *Proceedings in Applied Mathematics and Mechanics* **11** (2011), 115–116, ISSN 1617-7061.

Ramasamy, E.; Avci, O.; Dorow, B.; Röhrle, O.; Schneider, U.: There is more than just socket/stump interface pressure! An FE analysis of the stump-socket interaction, *OTWorld Congress Lecture*, May 15–18, Leipzig, Germany (2018).

Ramasamy, E.; Avci, O.; Dorow, B.; Gizzi, L.; Röhrle, O.: A workflow to investigate patient-specific prosthetic devices, *2nd International Symposium on Innovations in Amputation Surgery and Prosthetic Technologies*, May 10–12, Vienna, Austria (2018).

Saini, H.; Altan, E.; Ramasamy, E.; Ates, F.; Röhrle, O.: Predicting skeletal muscle force from motor unit activity using 3D FEM, *89th Annual Meeting of the GAMM*, March 19–23, Munich, Germany (2018).

Ramasamy, E.; Avci, O.; Dorow, B.; Schneider, U.; Röhrle, O.: Simulating Lower Extremity Amputee Dynamics using 3D Finite Element Simulations, *American Orthotics and Prosthetics Association*, September 6–9, Las Vegas, USA (2017).

Röhrle, O.; Ramasamy, E.: Principles of forward dynamics applied to a three-dimensional continuum-mechanical model of the upper limb, *82nd Annual Meeting of the GAMM*, April 18–21, Graz, Austria (2011).

2 The human musculoskeletal system

The human musculoskeletal system, as the name implies, is made up of the skeleton and muscles. The skeleton comprises of bones, which provide form, support and protection, and is responsible for transferring loads between the body and its surroundings. The muscles are responsible for generating force, which act upon the bones of the skeleton, that result in the overall movement of the musculoskeletal system. A detailed description of the roles played by various parts of the body that contribute to human movement is available in Tözeren (2000). The functions of a healthy skeletal system and musculotendon complex in facilitating movement and load transfer are discussed separately below. The description of the human anatomy and physiology is based on the books by Netter (2014), and Hall (2016), respectively. By the end of this section, it would be evident that an amputee would face a number of challenges as a result of an amputation.

2.1 Human skeletal system

The skeletal system comprises of bones, cartilages, ligaments and other connective tissues, which protect and hold the internal organs of the human body together, provide form, and transfer loads to and from the external environment. The skeleton can be broadly classified into the axial and appendicular skeleton. In an adult, the axial skeleton is made up of 80 bones, which are found in the head, chest and back, and forms the central axis of the body. The adult appendicular skeleton is made up of 126 bones that are found in the rest of the body, namely in the upper and lower limbs and pelvic bones, and is attached to the axial skeleton. These 206 bones in the adult skeleton are classified, based on their shape, into long, short, flat, sesamoid and irregular. Anatomically, long bones are cylindrical in shape, whose lengths are greater than their widths. Short bones have similar length, width and depth. Flat bones are thin and often curved; the sesamoid are small and round, and irregular bones have no characteristic shape. Physiologically, long bones function as ideal lever arms for transferring loads and help in movement. Short bones, e.g. the ones found in the human foot, provide limited mobility but greater stability. Sesamoid bones are typically found as a part of tendons, where large loads are experienced, and they help to protect the tendons from high tensile forces. The flat bones act as attachment points for other bones and muscles, and help to protect vital organs, while the functions of irregular bones vary for each individual case. Bones are connected to one another through joints, which enable humans to move efficiently. In the following sections, the joints that help in movement, and the anatomy and histology of femur, which are helpful in understanding the physical changes following its amputation are described in greater detail.

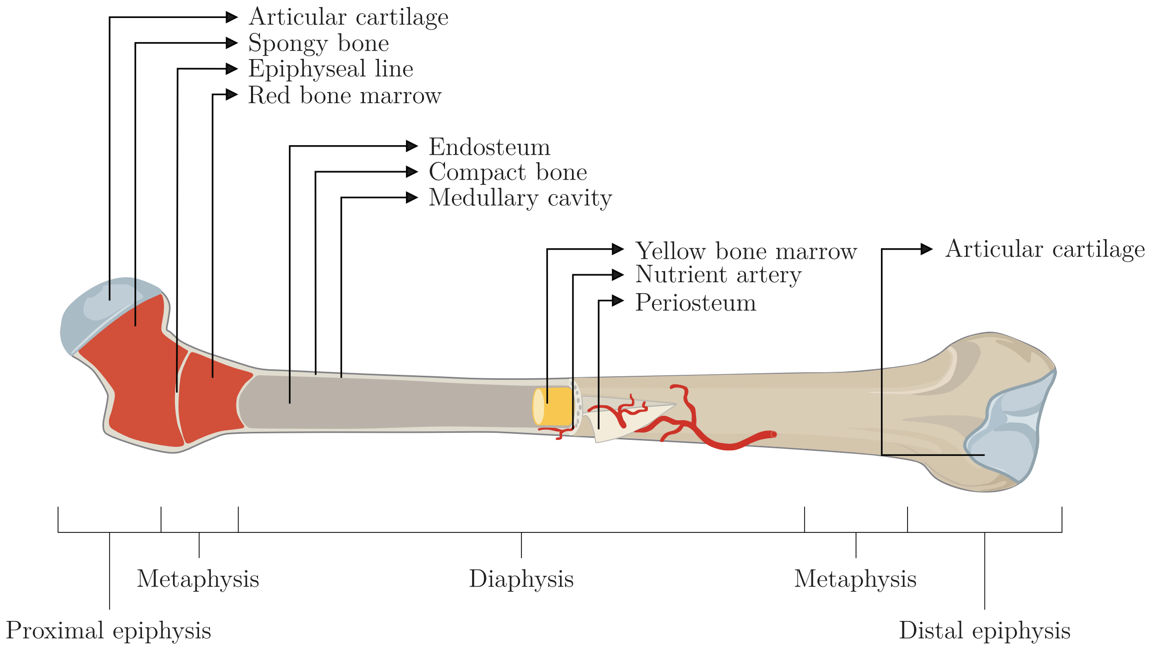

Figure 2.1: *Anatomy of an adult femur*[1]*. Source: A typical long bone shows the gross anatomical characteristics of bone by OpenStax, used under CC BY.*

2.1.1 Anatomy and histology of long bones

Anatomically, a long bone can be divided into diaphysis, metaphysis and epiphysis (cf. Figure 2.1). Epiphyses are the wide sections at either ends of a bone, which are filled with highly vascularised spongy or cancellous bone that contain red marrow. The red marrow performs the vital role of producing the red blood cells, white blood cells and blood platelets, which are required for oxygen transport, fighting infections, and for aiding blood clot, respectively. Over the life of an individual, the red marrow slowly transforms into the yellow marrow in the central tubular shaft of the bone, called the diaphysis. The diaphysis is hollow, and runs axially between the proximal and distal ends of the bone. The yellow marrow is contained in this hollow cavity, called the medullary cavity. While the outer walls of the diaphysis are dense and compact to protect the bone, its inner walls, i.e. the inner walls of the medullary cavity, are lined by membranous endosteum that promotes bone remodelling. Metaphyses are transitional zones between the diaphysis and epiphysis that contain the epiphyseal plate in a growing bone. As an individual attains maturity, the epiphyseal plate turns into an epiphyseal line. The outer surface of long bone, barring the articular cartilages, is enclosed by the periosteum. Apart from protecting the surface of the bone, the periosteum serves two main purposes – to provide nourishment through a rich supply of blood vessels, nerves and lymphatic vessels, and to provide attachment sites for tendons and other connective ligaments.

Bones are living tissues, which continuously adapt their shape to age and to the loads that they are subjected to. This continuous remodelling is made possible by the cells of endosteum, namely the osteocytes, osteoblasts, osteogenic and osteoclast cells (cf. Figure 2.2). The osteoblasts are responsible for forming the bone matrix by secreting collagen and calcium salts. As the bone grows, osteoblasts get trapped within the bone

[1]https://cnx.org/contents/FPtK1zmh@12.1:kwbeYj9S@6/Bone-Structure, retrieved on May 24, 2019

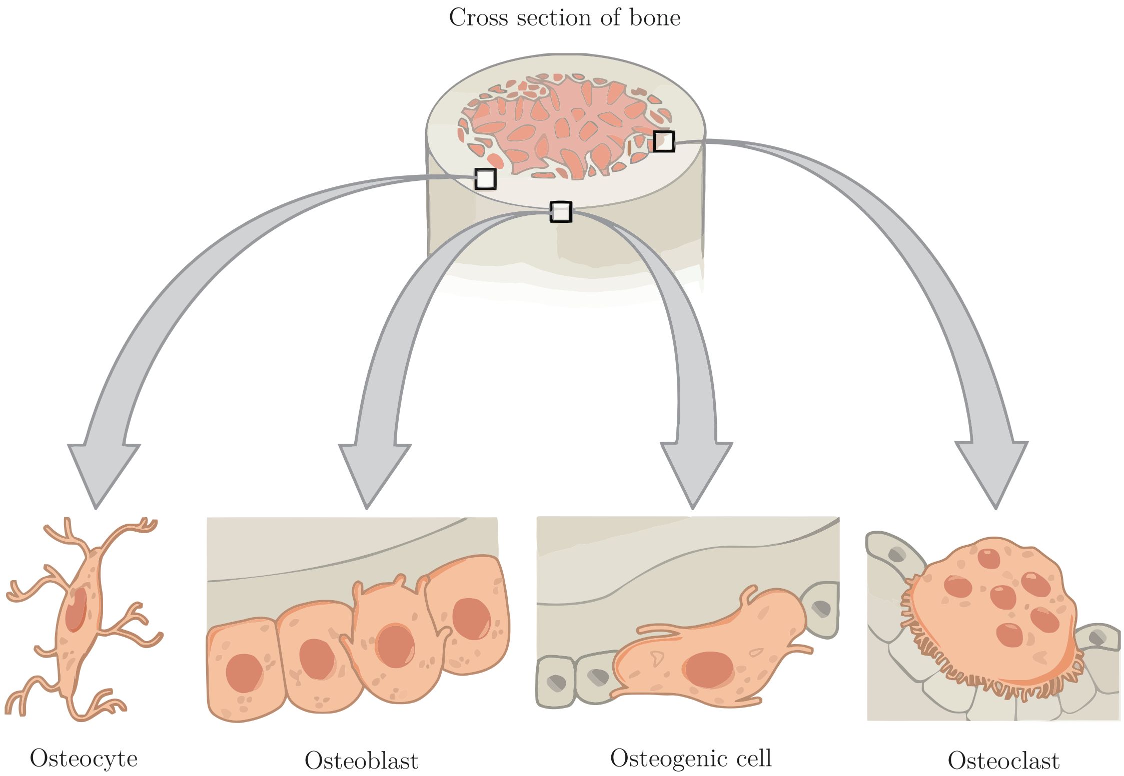

Figure 2.2: *Histology of cells in the cross-section of a long bone[2]. Source: Four types of cells are found within bone tissue by OpenStax, used under CC BY.*

cells and differentiate into osteocytes that become responsible for maintaining the mineral concentration in the bone matrix. Osteoclasts are bone-resorbing cells that repair or resorb old or damaged bone tissues, and release calcium in return. The osteogenic cells are the so-called stem cells, which produce the bone-forming osteoblasts. This subtle balance between bone-forming osteoblasts and bone-resorbing osteoclasts constantly remodels the structure of a long bone. On either ends of the epiphyses of a long bone, where it articulates with another bone, articular cartilages are present. These skeletal joints, which enable efficient transfer of loads that result in gross movement of the skeleton are described next.

2.1.2 Joints in the skeletal system

Joints in the human skeleton can be classified based on their structure into fibrous, cartilaginous and synovial joints, and based on their function into synarthrosis, amphiarthrosis and diarthrosis. A joint does not have to be mobile, e.g. fibrous and cartilaginous joints are examples of immobile joints, where bones are attached to one another by fibrous and fibrocartilage tissues, respectively. Some examples of immobile joints are fibrous joints between the bones of skull, and fibrocartilage joint found in the pubic symphsis. Unlike these joints, the synovial joint permits large range of motion, e.g. knee and hip joints (cf. Figure 2.3). The functional classification of joints into synarthrosis, amphiarthrosis and diarthrosis is based on the degree of motion permitted by the joints. Synarthrotic

[2]https://cnx.org/contents/FPtK1zmh@11.1:kwbeYj9S@6/Bone-Structure, retrieved on May 24, 2019

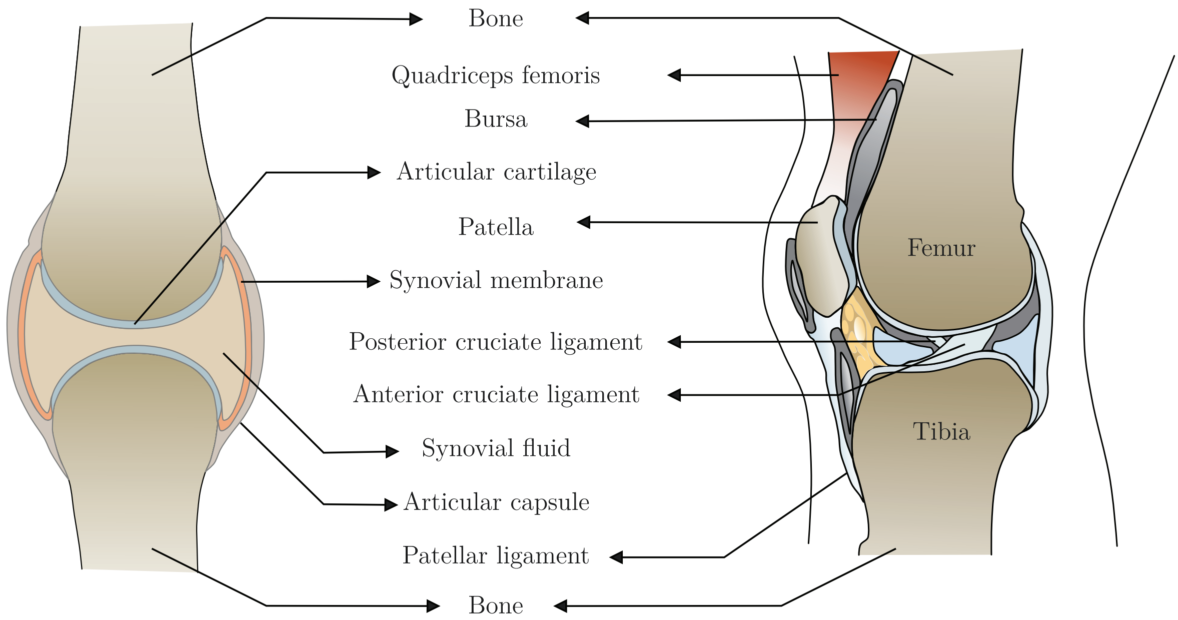

Figure 2.3: *Generic synovial joint (left) and the largest synovial joint in the human body, namely the knee joint (right)*[3]*, are illustrated here. Adapted from Synovial joints allow for smooth movements between the adjacent bones by OpenStax, used under CC BY, and Bursae are fluid-filled sacs that serve to prevent friction between skin, muscle, or tendon and an underlying bone by OpenStax, used under CC BY.*

joints, such as the sutures in human skull, are immobile. Amphiarthrotic joints are semi-mobile joints. An example of amphiarthrotic joint is the intervertebral disc (IVD) between two vertebrae. Each IVD individually permits limited degree of freedom but the sum of all their degrees of freedom results in a stable movement of the entire spinal cord. Diarthrotic joints are synovial joints that permit large degrees of freedom, and enable us to perform our daily physical tasks such as walking, writing, playing, and so on. Knee is the largest synovial joint in the body, which is removed during a transfemoral amputation. To understand the impact of removing the knee joint, the following discussion is focussed on the structure and function of the synovial knee joint.

For a synovial joint to function effectively, several structures are present that help in smooth articulation, to absorb shocks, and to reduce friction. For example, in the case of knee joint, articular surfaces of femur and tibia are encapsulated in a fluid-filled sac (cf. Figure 2.3). This fluid, called the synovial fluid, reduces friction between the cartilages of these bones, and ensures their smooth articulation. Shocks resulting from activities such as jumping and running are cushioned by articular discs in the knee joint, namely the menisci found on the proximal tibia. In other joints, e.g. the radioulnar joint, the articular discs serve to strongly unite the radius and ulna at the elbow joint, and in the temporomandibular joint, these discs help smooth the movements between mandible and temporal bone of the skull. The patella is a hard sesamoid bone that is embedded into the distal end of the *quadriceps femoris* tendon, and pulls the tibia over the knee joint to extend it. Any friction resulting from the translation of patella over the soft tissues in the knee are mitigated by fluid filled sacs called bursae. It is the

[3]https://cnx.org/contents/FPtK1zmh@11.1:bFtYymxt@5/Synovial-Joints, retrieved on May 24, 2019

presence of such structures, which are responsible for the flexibility provided by synovial joints. However, all diarthrotic synovial do not offer the same degrees of freedom. Some examples of the types of motion permitted by synovial joints are illustrated in Figure 2.4. The most common types of motion are flexion, extension, adduction, abduction and rotation. In addition to these, some joints allow special movements, e.g. the ankle joint can also perform dorsi- and plantar-flexion, and the elbow joint can perform pronation and supination. Flexion is the movement about a joint where the articulating bones come close to one another, while during an extension, they move away from each other. Abduction is the motion of the bone or any structure away from the midline of the body, while during adduction, the bone is pulled towards the midline of the body. Rotation is classified into medial and lateral rotation. During medial rotation of the thigh, the leg rotates towards the midline of the body, and it rotates away from this midline during lateral rotation. The range of motion permitted by diarthrotic synovial joints depends on the shapes of articulating surfaces.

It is simpler to understand the degrees of freedom permitted by various synovial joints by comparing them to their mechanical equivalents. Figure 2.5 illustrates the mechanical equivalents of some synovial joints. The entire weight of the human body is supported by three major joints in the lower limb, namely the hip, knee and ankle joints. The hip joint is formed between the femoral head and acetabulum of pelvis, and is similar to a ball-and-socket joint. This joint allows for rotations about all three axes, and yet remains stable under load. The iliofemoral, pubofemoral and ischiofemoral ligaments are responsible for this stability. These ligaments arise from the pelvis and attach to the femur, spiralling around its neck, thereby ensuring its stability. The knee joint is the largest joint in the human body. It has three articulations – the femoropatellar joint, medial tibiofemoral joint and lateral tibiofemoral joint. The combination of these joints result in a hinge-like knee joint that allows for flexion and extension of the leg. However, the knee joint is not a perfect hinge joint because, in reality, the femur rotates and slides over the tibia during flexion-extension movements. Similar to the hip joint, the knee is also stabilised by several ligaments. The patella serves to protect the tendon of *quadriceps femoris* from friction against the distal femur, and stabilises the knee by providing dynamic alignment by sliding over a groove in the distal femur. Lateral and medial movements are restricted by the fibular and tibial collateral ligaments, respectively. In addition to these supporting structures, the anterior and posterior cruciate ligaments increase joint stability by restricting the sliding motion of femur over the tibia. The leg is connected to foot at the ankle or talocrural joint. This is a hinge joint formed between the tibia and talus, and allows for plantar- and dorsiflexion. The deltoid ligament, anterior talofibular and posterior talofibular ligaments and the calceneofibular ligament are some ligaments in the foot that help stabilising it. Bones can only provide structural support; the forces required to articulate the bones about these joints are provided by skeletal muscles. The following section deals with the anatomy and physiology of the musculotendon complex, which are required to understand the forces generated by these muscles.

2.2 Musculotendon complex

Skeletal muscles that articulate synovial joints originate at a stationary bone, and insert into the articulating bone. Controlled rotation of bones about joints is possible as a result

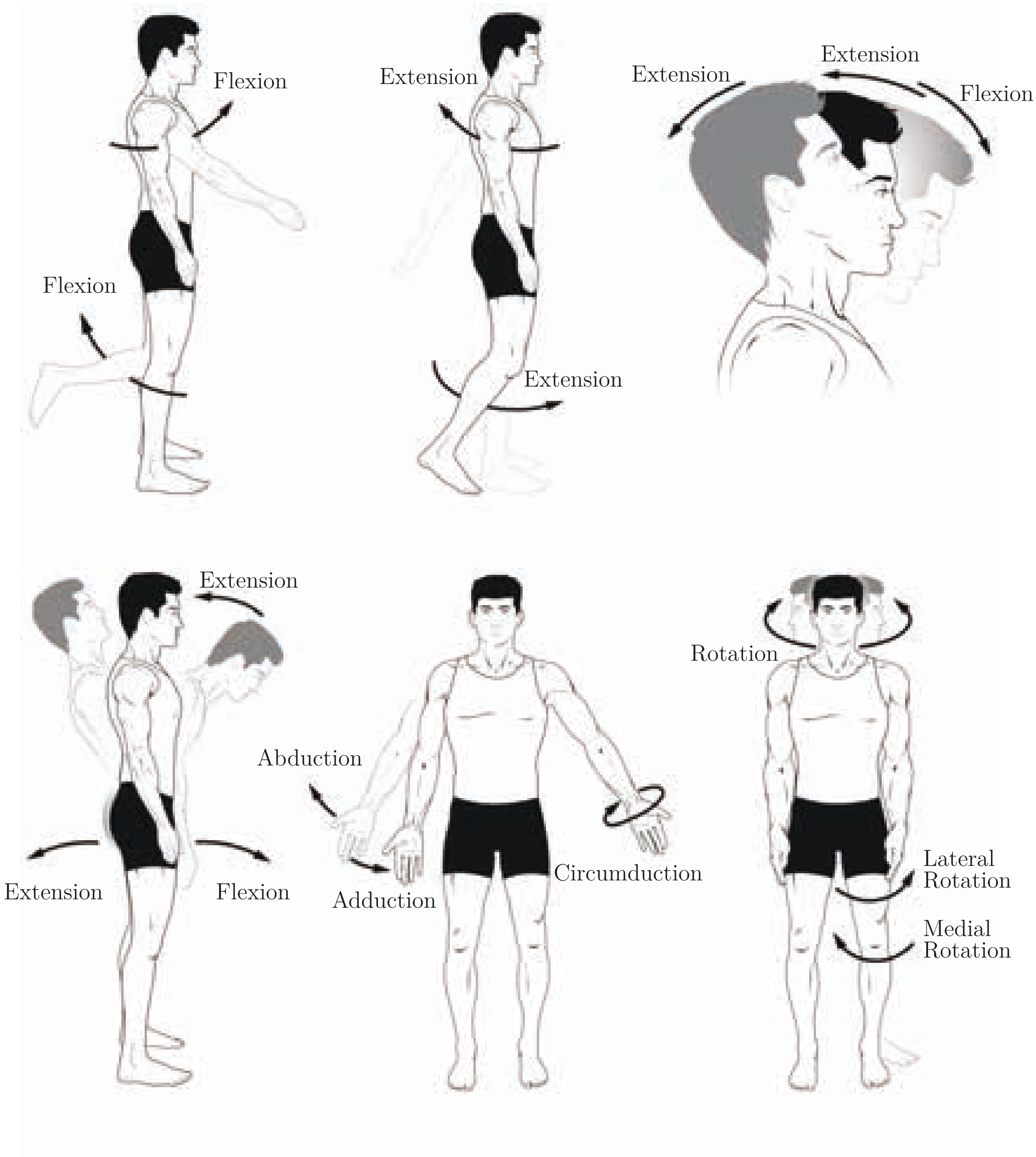

[a]https://cnx.org/contents/FPtK1zmh@11.1:qCnsYyus@4/Types-of-Body-Movements, retrieved on May 24, 2019

Figure 2.4: *Types of movements permitted by the synovial joints*[a]*. Source: Synovial joints give the body many ways in which to move by OpenStax, used under CC BY.*

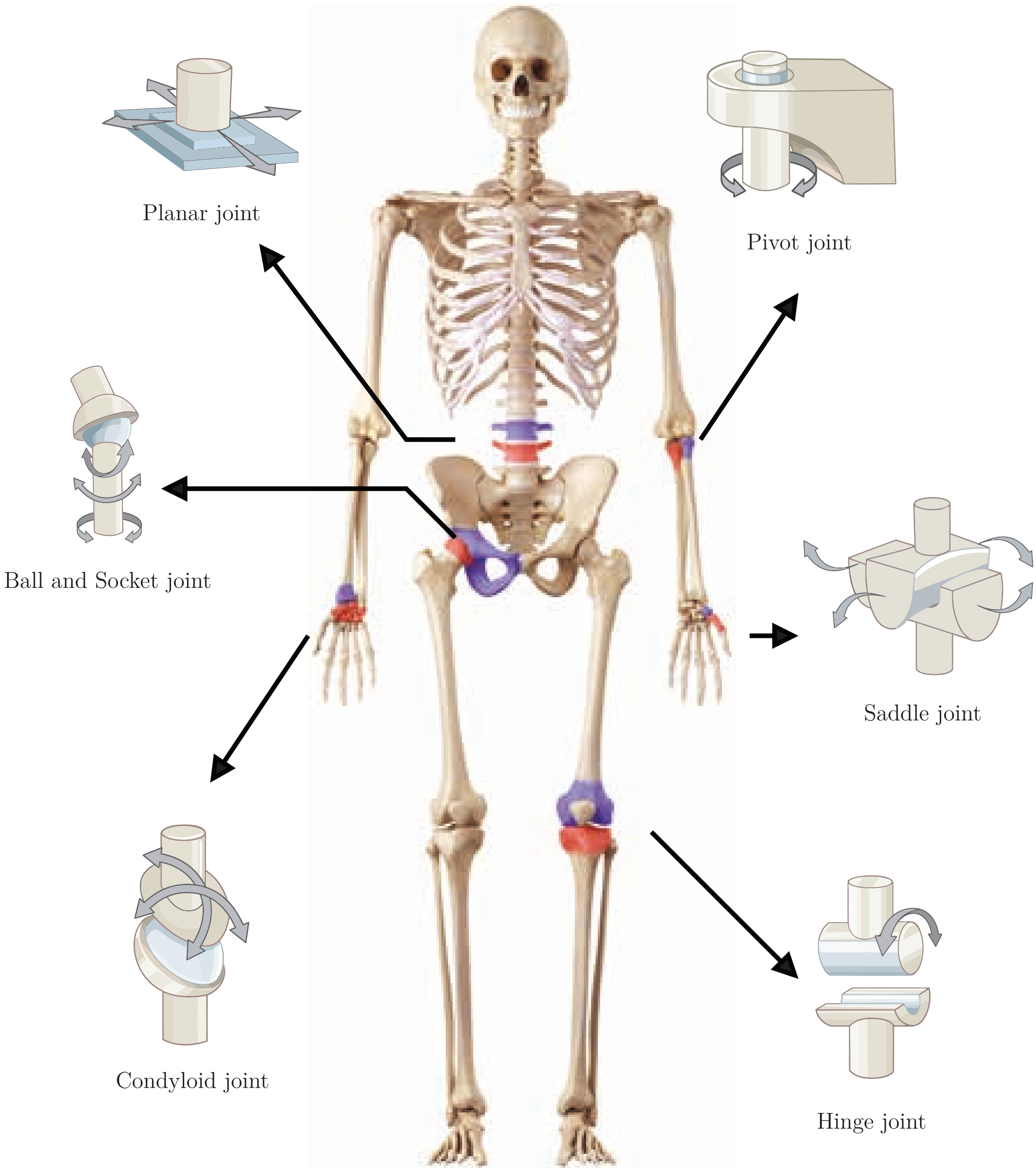

[a]https://cnx.org/contents/FPtK1zmh@11.1:bFtYymxt@5/Synovial-Joints, retrieved on May 24, 2019

[b]https://de.123rf.com/profile_Eraxion, retrieved on May 24, 2019

Figure 2.5: *Mechanical equivalents of some of the synovial joints in the human body*[a]*. Joints adapted from* *The six types of synovial joints allow the body to move in a variety of ways* *by OpenStax, used under* *CC BY* *and skeleton*[b] *from* *medical accurate illustration of the human skeleton* *by* *Sebastian Kaulitzki ©123RF.com*.

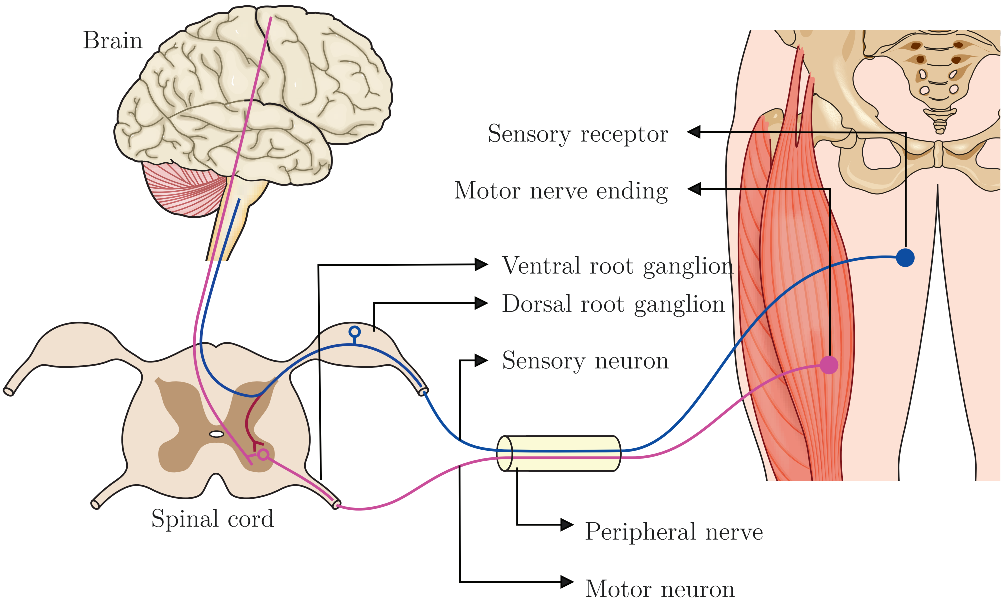

Figure 2.6: *Motor neuron pathway*[4]*. The contraction of skeletal muscles occur as a result of nerve signals from the brain. Source:* Nerve control of muscle *by* Peter Lamb ©123RF.com.

of opposing muscular forces generated by one or more opposing pairs of muscles, called the agonist-antagonist muscle pairs. An agonist muscle performs the desired motion while its antagonist resists this movement, e.g. during knee flexion, the hamstrings play the role of agonist and the quadriceps are the antagonist. The roles of hamstrings and quadriceps are reversed during knee extension. Thus, the resulting muscular force that articulates a bone about a joint is precisely controlled by agonist-antagonist muscle pairs.

Muscular forces are generated due to the contraction of individual muscle fibres in the skeletal muscles. The signals controlling voluntary or involuntary contraction of a specific muscle group originate from the central nervous system, which comprises of the brain and spinal cord. Generally, the brain controls voluntary muscle contractions, and the spinal cord is responsible for involuntary contractions. Motor neuron signals that stimulate voluntary contractions, e.g. flexing the knee, originate from the primary motor cortex (M1) of the brain. These signals are integrated in the spinal cord, which plays the role of mediating the descending signals from the motor cortex with the afferent signals from the sensory organs (cf. Figure 2.6). Motor neurons that innervate the skeletal muscles branch out from the ventral horn of the spinal cord, and the sensory neurons from the peripheral sensory organs enter the dorsal horn of the spinal cord. Upon the reception of activation stimuli from motor neurons, the individual muscle fibres of skeletal muscles contract, which leads to the overall contraction of the muscle bundle.

The architecture of skeletal muscles is shown in Figure 2.7. Each skeletal muscle is wrapped in a sheath of dense connective tissue called the epimysium. The epimysium maintains the structural integrity of the muscle, and also separates muscles from one another, allowing each muscle to contract independently. Within each skeletal muscle are bundles of muscle fibres, called fascicles. Perimysium is the outer sheath of fascicles that bind muscle fibres together, and likewise, every muscle fibre is enclosed within a sheath called endomysium. Anatomically, each individual muscle fibre is composed

[4] https://de.123rf.com/profile_hfsimaging, retrieved on May 24, 2019

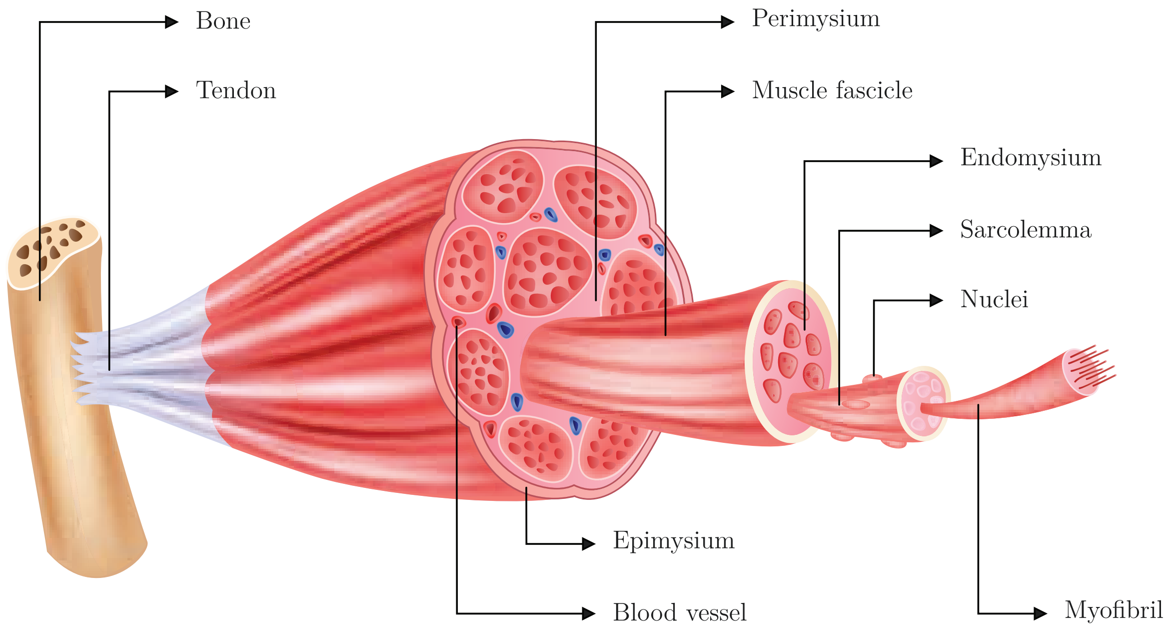

Figure 2.7: *Anatomy of skeletal muscle fibres*[5]. *Source: Vector illustration of Structure Skeletal Muscle Anatomy by Teguh Mujiono ©123RF.com.*

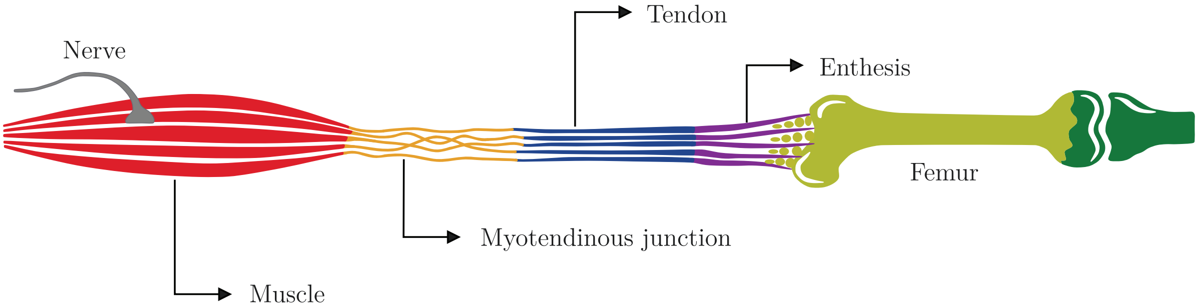

Figure 2.8: *Transition of muscle into tendon, and insertion of tendon into bone. Reproduced with permission from Felsenthal & Zelzer (2017).*

of a series of smaller units called sarcomeres, which contain actin and myosin protein filaments. The sliding filament model explains the contraction of sarcomeres by the sliding of actin and myosin protein filaments. The contraction of individual sarcomeres leads to the contraction of a muscle fibre strand. The contractions of individual fibre strands in a fascicle lead to the contraction of that muscle fascicle, which in turn leads to the contraction of the skeletal muscle. These contractile forces, generated by skeletal muscles, are transmitted to bones through tendons.

Tendons are fibrous connective tissues that connect skeletal muscles to bones. They are mechanically stiffer than skeletal muscles, and gradually transition from skeletal muscles to fibrous cartilage at the myotendinous junction (cf. Figure 2.8). At this junction, the ends of muscle fibres form a serrated border into which the collagen fibres of the tendon penetrate. This junction ensures a smooth transmission of skeletal forces to the stiffer tendon. Similarly, a gradual gradient in the stiffness of tendon is witnessed at the enthesis, i.e. the site of insertion of uncalcified tendon into the calcified bone.

[5]https://www.123rf.com/profile_tigatelu, retrieved on May 24, 2019

Through the aforementioned mechanisms, the forces generated by skeletal muscles are transferred through tendons to the skeletal system. These forces cause bones to articulate about joints in the skeleton, and perform desired actions. This efficient system is disturbed when a portion of the limb is amputated. In the case of a transfemoral amputation, the prosthetic device fitted to a subject must try to replicate the functions of knee and ankle joints. Additionally, the prosthesis must also ensure safe and efficient transfer of external loads to the skeleton, and provide stability when donning the prosthesis. In this regard, the amputation technique also plays an equally important role. The success of post-amputation recovery and rehabilitation depends on the efficient use of the residual musculoskeletal system, which must be realised through the surgical technique. In the following section, some important concepts of amputation surgeries and problems faced by the amputees are discussed.

2.3 Amputation technique

In a conventional transfemoral amputation, skin incisions are drawn out proximal and lateral to the desired level of amputation. Based on the planned distal closure, these incisions result in either symmetric fish mouth or longer anterior skin flap. The skin, subcutaneous fat and muscles are cut with bold positive strokes up to the femur to avoid fraying the cut tissues, and major blood vessels are ligated with sutures at the apex of the cut. The sciatic nerve is pulled distally, ligated, transected, and allowed to retract. This ensures that the nerve is not close to the site of amputation. When the soft tissues have been divided, they are folded back to reveal the site of amputation of the femur. The periosteum of femur is removed above and below the site of incision after which the bone is transected perpendicular to its long axis. The sharp edges of the femur are filed to smoothen the distal end. In some cases, bone wax is applied at the freshly amputated end, and the dissected periosteal tissues are placed over it and sutured to the femur.

Following the amputation of femur, the hip adductor and extensor muscles are cut, while preserving the abductor and flexor muscles. This results in strong abduction and flexion, whereas adduction and extension are weakened. One of the primary goals of the surgery is to try and restore adduction and extension, which is necessary for adequate control of a prosthesis. For this reason, the adductor and medial hamstring muscles are used in a procedure called myodesis, where these muscles are wrapped around the distal end of the femur and sutured to the femur. Finally, after allowing for drain holes, the skin flaps are closed and sutured.

2.4 Post-amputation challenges

After amputation, the mobility of a subject is restored by means of wheelchair, crutches, osseointegrated[6] prostheses or exoprostheses. The use of wheelchairs and crutches restrict mobility, while osseointegrated prostheses might lead to infections, risk of fractures and other complications. As a result, exoprostheses are widely preferred. They require relatively less care, and have lower risk of failure compared to the osseointegrated prostheses. In this thesis, the interaction of stump with exoprostheses is analysed. In an exoprosthesis,

[6]Prostheses that are transcutaneously anchored to the bone in the residual limb.

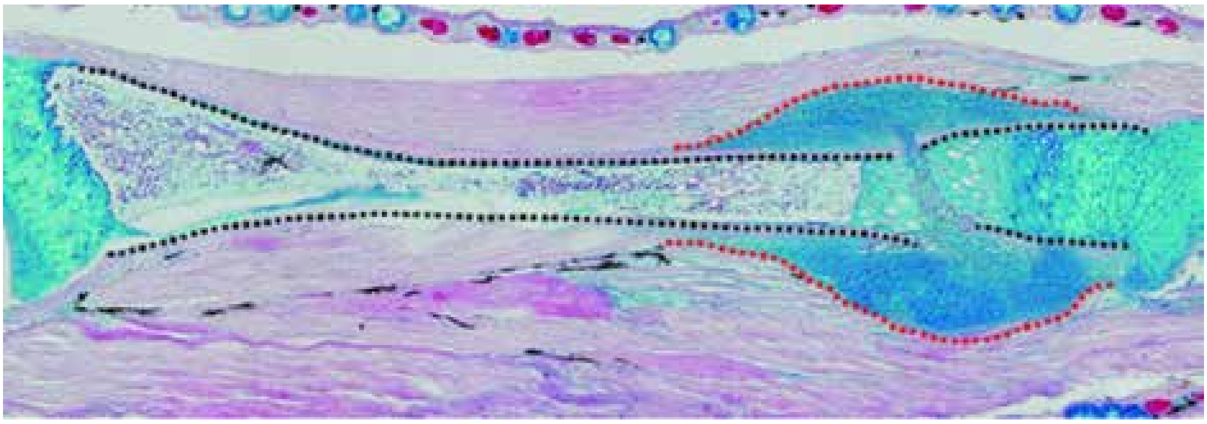

Figure 2.9: *Histology of long bone fracture callus in Xenopus froglets. Soft callus is formed at the fractured end of the bone. The black and red dashed lines indicate bone shafts and outline of the soft callus. Reprinted with permission from* Egawa et al. (2014)*.*

the external loads are transferred from the prosthetic socket, through the soft tissues in the residual limb, into the residual femur. These non-physiological loads acting on the femur cause remodelling of its tissues. In some cases, such bone-remodelling might lead to problems in the residual limb, some of which are discussed below.

The histological changes at the site of amputation in rabbits were documented by Hansen-Leth (1979). In this study, the healing process of the amputated stump in adult rabbits was investigated. Herein, it was discovered that there was increased osteoblastic and osteoclastic activities at the outermost part of the endosteum 3–4 days post-amputation. In some cases, closure of medullary cavity by endosteal callus was followed by atrophy of the cortical bone and dilation of the medullary cavity. By plugging the medullary cavity, periosteal, spongious exostoses developed, which led to the final closure of the medullary cavity. This was followed by an osteoblastic activity around the plugs. Based on microradiography studies on rabbits, Hulth & Olerud (1962) established that bone-remodelling due to fracture is similar to that following an amputation. Figure 2.9 shows the formation of soft callus at the site of fracture in *Xenopus* froglets, which was also observed by Hansen-Leth (1979) in amputees. Sevastikoglou et al. (1969) investigated distal end closure of bones in 47 unilateral amputees (28 transfemoral, 19 transtibial) who complained of local or phantom pain in their residual limbs. In the transfemoral amputees, in all but one subject, the cortical bone of the residual femur was thinner than that of the healthy contralateral femur. A similar trend was found in the transtibial amputees, where the residual cortical tibia was thinner than the healthy contralateral tibia in 17 out of 19 subjects. This was accompanied by an atrophy of the stump in 38 subjects. The combined thinning of the cortical bone and dilation of the medullary cavity leads to the condition where distal end of the bone becomes sharp, painful, and therefore, unsuited for load-beading. Some other painful conditions, which may arise as a result of amputation, are aggressive bone edge, heterotopic ossification, osteomyelitis, cancer, neuroma and phantom pain. The goal of a prosthetist is to identify these problems and accordingly fit an optimal socket.

In the early stages following an amputation, volume of the residual limb fluctuates as scars heal. During this period, a check socket, which accommodates any volume fluctuation, is worn by the amputee. A final socket is designed approximately 3–6 months post amputation, when the volume fluctuations subside. The final sockets are designed either using casting methods or with laser scanners to obtain the residual limb geometry, which are then altered by the prosthetist. The socket shape is altered such that high pressure in sensitive areas of the stump is relieved, while loading other regions of the stump that have higher load-bearing capacity. Further changes to the socket might be necessary depending on the patient's feedback. Since the prosthetic socket is cast or scanned during static loading conditions, it might be necessary to tune the prosthesis for dynamic gait conditions. Furthermore, gait training might also be required to teach the transfemoral amputee to use hip muscles to control the prosthetic knee joint. Gait deviations such as lateral trunk bending, abducted gait, circumduction, vaulting, swing-phase whips, foot rotation at heel strike, foot slap, uneven heel rise, terminal impact, uneven step length and exaggerated lordosis are common among transfemoral amputees. The collective goal of the prosthetist and subject is to correctly design a prosthetic socket, and to fit the prosthetic components in order to eliminate gait abnormalities, and ensure a comfortable prosthesis.

3 Workflow to generate subject-specific residual limb model

This chapter focusses on developing an efficient workflow to generate subject-specific finite element (FE) model from medical scans. The workflow consists of (i) pre-processing the diffusion tensor imaging scans, (ii) generating the finite element (FE) residual limb model, and (iii) enhancing the FE model with skeletal muscle fibres. A general overview of the workflow is provided in Figure 3.1. The workflow is primarily controlled by a MATLAB (v9.4; The MathWorks Inc., Natick, Massachusetts) script, with some sections of the code written in Python (v2.7; Python Software Foundation). In the first stage, the medical scans were pre-processed and prepared for use in a fibre-extraction tool, MedINRIA (v1.9.2, 64 bit; ASCLEPIOS Research Team, France). In the second stage, skeletal muscle fibres were extracted using MedINRIA, with which muscle image stacks were generated. In the third stage, these image stacks were imported into an image segmentation tool, Synopsys Simpleware, which reconstructed the images into 3D models, and also created the FE mesh of residual limb. Finally, the extracted muscle fibre information was encoded into the FE mesh of the residual limb.

3.1 Basics of MRI and DT-MRI imaging

Medical imaging is performed to visualise the internal structure of the human body. Ultrasound, X-Ray projection imaging, Computed Tomography (CT) and Magnetic Resonance Imaging (MRI) are some examples of contemporary medical imaging technologies (cf. Haidekker, 2013). Among these technologies, MRI has gained widespread acceptance and popularity. This is mainly due to its capability to produce geometrically accurate 3D images of the human anatomy without subjecting the patients to any harmful ionising radiation. The MRI scanners generate strong, harmless magnetic fields, which produce net magnetisation in the tissues of the body. The net magnetisation signal from each tissue is localised in 3D space, and mapped into a volumetric image. Since different tissues, such as bones, muscles and fat, have different magnetisation properties, the resulting volumetric image has a good contrast between tissues. By changing the so-called scan sequence parameters, the MRI scanners can produce weighted images, wherein the effect of any one sequence parameter can be studied. Some examples of clinically used sequences are fat suppression, diffusion weighting, angiography and perfusion MRI. Of particular interest to the workflow are diffusion-weighted MRI images in which image contrast is generated based on the movement of water molecules. Diffusion tensor imaging (DT-MRI) is an extension of diffusion-weighted imaging, with which fibre tracks, along which water molecules diffuse, can be tracked. In this section, some basic concepts of MRI and DT-MRI namely (i) working principles of MRI and DT-MRI scanner, (ii) a

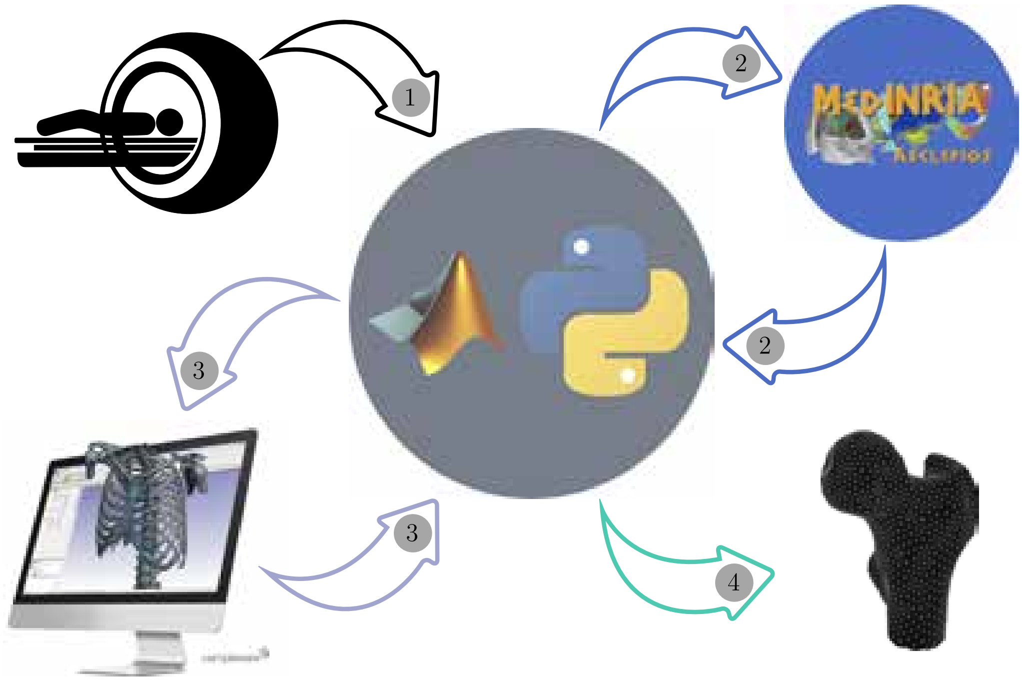

Figure 3.1: *Stages in the proposed workflow to generate an FE mesh of the residual limb from the DT-MRI scans of the subject. In stage 1, the DT-MRI scans are pre-processed with MATLAB. In stage 2, the muscle fibres are tracked with MedINRIA. In stage 3, binary images of muscles generated from the fibres are processed with Simpleware ScanIP and FE mesh of the residual limb is generated, and in stage 4, the tracked fibres are encoded into the FE mesh.*

rudimentary method of extracting diffusion tensors from DT-MRI scans, and (iii) an introduction to medical imaging file formats are introduced.

Magnetic resonance and diffusion-weighted imaging

The human body is primarily made up of water, protein, fat and carbohydrate molecules. In the MRI scanners, hydrogen atoms, which constitute these molecules, are used to generate contrast in images. In the ground state, all precessing hydrogen atoms in our body are randomly oriented, resulting in zero net magnetisation. An MRI scanner has radiofrequency coils both for transmitting, i.e. generating the magnetic field, and for receiving the resulting MR signals. Under the influence of a strong magnetic field, precessing hydrogen atoms align in the direction of the magnetic field, with the precession rate ($42.58\,\mathrm{MHz\,T^{-1}}$) given by Larmor equation (cf. Larmor, 1897). Most of these precessing hydrogen atoms are in a low energy state, while the others are in a high energy state. Atoms in the low energy state are aligned with the applied magnetic field, and those in the high energy state are aligned against the field. As a result, the net longitudinal magnetisation of these hydrogen atoms are aligned with the applied magnetic field. It is not possible to directly detect the net longitudinal magnetisation since it is several orders of magnitude lower than the applied magnetic field. Therefore, a sinusoidal radiofrequency pulse, equal to the Larmor frequency, is applied to determine the magnitude of net magnetisation. This causes two significant changes. Firstly, the net longitudinal magnetisation is cancelled by almost equal amounts of precessing protons in

Tissue	T_1-weighted	T_2-weighted
Skeletal muscle	Grey	Dark grey
Spinal cord	Grey	Light grey
Bone	Very dark	Very dark
Fat (subcutaneous)	Bright	Light
Fat (bone marrow)	Bright	Light
Cerebrospinal fluid	Dark	Bright

Table 3.1: *The contrast produced by T_1- and T_2-weighted MRI scans in selected biological tissues.*

the lower and higher energy states. Secondly, the sinusoidal pulse forces all precessing atoms to precess in phase and perpendicular to the applied magnetic field. This transverse magnetisation of the precessing atoms is picked up by the receiving radiofrequency coils, and transcoded into images.

Upon removing the applied magnetic field, the precessing hydrogen protons repel one another and attain an equilibrium state, resulting in zero net transverse magnetisation. This process is called the T_2- or spin-spin relaxation. Next, those hydrogen protons that were pushed into the high energy state return back to their initial lower energy state, dissipating the absorbed energy. This process is termed the T_1- or spin-lattice relaxation. The T_1 and T_2 relaxation times are characteristic of tissues, which can be studied by changing pulse sequence parameters, namely the repetition time and echo time. Repetition time is the time between subsequent radiofrequency pulses, and echo time is the time between subsequent readings from the receiving coils. T_1 and T_2 relaxation can be better understood with an example. Consider the magnetisation of fat and water molecules. Upon removal of the external magnetic field, fats which contain large chains of hydrocarbons undergo rapid T_2 and T_1 relaxation compared to water molecules. Since water molecules can retain their energy longer and spin in phase, their net transverse magnetisation is higher than those of fat molecules, which is nearly zero. This results in water saturated tissues appearing grey in the scan, as compared to fat, which appears bright. The goal of a radiologist is to effectively modify the pulse sequence parameters such that tissues of interest are adequately contrasted against their surroundings. Image contrast in certain types of tissues produced by T_1- and T_2-weighted images are given in Table 3.1.

Apart from creating image contrasts by modifying pulse sequence parameters, the MRI scanners were enhanced with several other contrasting mechanisms such as diffusion-weighting, perfusion-weighting and functional MRI (cf. Holdsworth & Bammer, 2008). The diffusion-weighted MRI scanners are used to obtain the tissue anisotropy and identify otherwise invisible infarctions; perfusion-weighted scanners for studying blood flow, and functional MRI for studying neural activity. Tissue anisotropy, which is revealed by DT-MRI images, is used in this work for modelling the anatomy of skeletal muscles and other soft tissues in the residual limb.

Diffusion-weighted MRI scanners track the Brownian motion of water molecules in soft tissues. In the absence of obstacles, the diffusion of water molecules is isotropic, which is hampered, e.g. in the presence of skeletal muscle fibres, which force the water molecules to diffuse along the fibres, which are tracked by the DT-MRI scanners. In diffusion-weighted acquisitions, strong, pulsed diffusion 'gradients' are applied, which result in one scan image for each gradient direction. Scans in which diffusion gradient pulses are applied, are called gradient scans, and those in which no gradient pulses are applied, are called baseline scans. In gradient scans, tissue anisotropy is encoded as pixel intensity, and can be extracted using, e.g. the Stejskal-Tanner equation (cf. Mori & Zhang, 2006, Stejskal & Tanner, 1965), which is given by

$$S = P_D(1 - \exp\left(^{-\mathrm{TR}}/_{\mathrm{T}_1}\right)) \exp\left(^{-\mathrm{TE}}/_{\mathrm{T}_2}\right) \exp\left(-bD\right). \tag{3.1}$$

Here, S is the pixel intensity, P_D is the proton density, TR is the repetition time, TE is the echo time, and T_1 and T_2 are the aforementioned relaxation times. The diffusion-related terms are D and b, where D is the diffusion coefficient, and b is a composite factor representing the pulse sequence, gradient strength and other physical constants. In diffusion-weighted imaging, all terms in Equation (3.1), except the weighting factor b and the diffusion coefficient D, are constants. In other words, the pulse sequence is unaltered. This reduces Equation (3.1) to

$$S = S_0 \exp\left(-bD\right), \tag{3.2}$$

where S_0 represents the constant term in Equation (3.1), and is equal to the pixel intensity during a baseline ($b = 0$, or b_0) scan. In order to determine the diffusion coefficient D, the scan volume is subjected to a series of magnetising gradient pulses along pre-defined gradient directions $\boldsymbol{g}$. In theory, at least 6 such gradient scans are required to uniquely determine the diffusion tensor $\mathbf{D}$. The diffusion coefficient D in Equation (3.2) can be rewritten as $D = \boldsymbol{g}_k^{\intercal}\, \mathbf{D}\, \boldsymbol{g}_k$, resulting in the Stejskal-Tanner equation

$$S_k = S_0 \exp\left(-b\, \boldsymbol{g}_k^{\intercal}\, \mathbf{D}\, \boldsymbol{g}_k\right). \tag{3.3}$$

Here, $\boldsymbol{g}_k$ is the k^{th} gradient vector, S_0 is the pixel intensity during the baseline scan, and S_k is the intensity of the same pixel during the diffusion-weighted scan along the k^{th} gradient direction. The extraction of a positive definite, symmetric diffusion tensor $\mathbf{D}$ from 6 gradient scans is illustrated in Figure 3.2. Here, the intensities of the same pixel, across the 6 gradient scans, of the same cross section are shown with which the diffusion tensor $\mathbf{D}$ is reconstructed. While this illustration is primarily intended to help in understanding how diffusion tensors are encoded in the pixels of a diffusion-weighted image, the actual process of extracting these tensors is more involved. An excellent overview on the principles of diffusion tensor imaging is provided by Mori & Zhang (2006).

DICOM and NIfTI formats

The raw medical scans were provided as DICOM[1] data, which is the international standard to transmit, store, retrieve, print, process, and display medical imaging information. Despite DICOM being the standard format, research tools employed to analyse medical scans may sometimes use other formats such as NIFTI[2], Analyze or NRRD[3] (cf. Patel

[1] Digital Imaging and Communications in Medicine
[2] Neuroimaging Informatics Technology Initiative
[3] Nearly Raw Raster Data

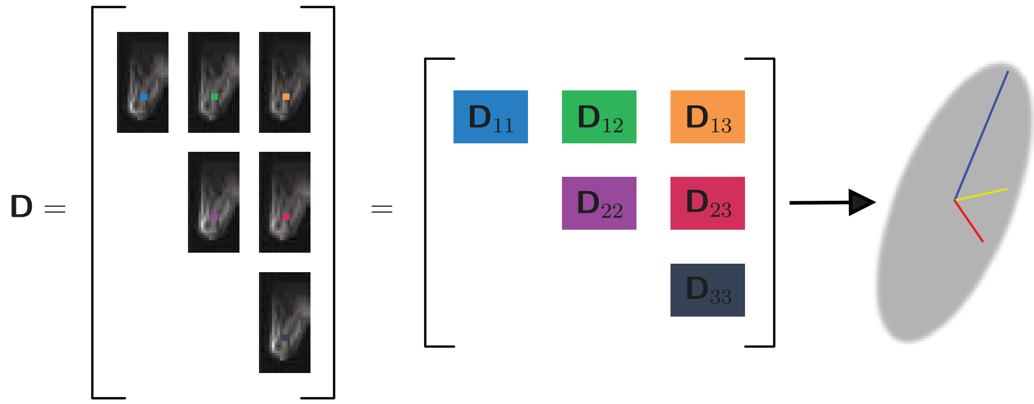

Figure 3.2: *An illustration of a diffusion tensor reconstructed from the pixel intensities of the same pixel across 6 gradient scans. The intensity of the pixel is contrasted against that from a baseline scan to construct the diffusion tensor in that pixel. Shown on the far right is an ellipsoid representing the diffusion tensor whose principal vectors are represented by the three line segments. This illustration was inspired by Le Bihan et al. (2001) and www.diffusion-imaging.com.*

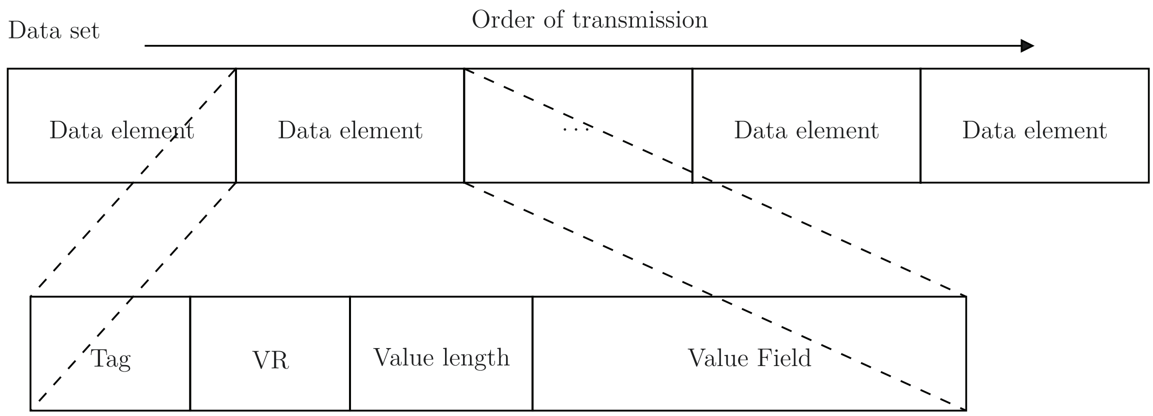

Figure 3.3: *Structure of data elements in a DICOM file. Reproduced from DICOM Standard §PS3.5*

et al., 2010). The reason for using such non-standard data formats is due to the research nature of some imaging software, and are therefore not governed by standards. This means, significant effort is mostly required to transform the data between different software formats. The necessary information (called metadata) to perform any such transformation is available in file headers. The DICOM and NIfTI standards are very comprehensive and continuously evolving. Therefore, only a concise description of each of these file types will now be provided.

The DICOM standard is published by the National Electrical Manufacturers Association (NEMA). A DICOM file is essentially an object consisting of patient, study, series and image models, and can be broadly split into two parts – header and dataset. The header consists of a 128-byte preamble followed by a 4-byte prefix and the binary image data. Information about the patient, exam, series and image are encoded in this 128-byte preamble, and the 4-byte prefix contains the string 'DICM' to indicate that the file is a DICOM file. The metadata in a DICOM object are stored as data elements (see Figure 3.3), where each element has tag, data type, length and value fields. A `tag` identifies

Some standard DICOM attributes	
DICOM attribute	Value
`Width`	532
`Height`	1050
`BitDepth`	12
`SliceThickness`	3
`AcquisitionMatrix`	[0;150;76;0]
`InPlanePhaseEncodingDirection`	'ROW'
`PatientPosition`	'FFS'
`InstanceNumber`	2
`ImagePositionPatient`	[-1.3;-822.7;1708.6]
`ImageOrientationPatient`	[0;1;0;0;0;-1]
`Rows`	1050
`Columns`	532
`PixelSpacing`	[2.986;2.986]
Private DICOM tags	
('`0019`','`100a`')	42
('`0019`','`100e`')	[-0.8630;-0.3572;-0.3572]
('`0051`','`100e`')	'Sag'

Table 3.2: *Attribute names and tags of selected standard and private DICOM elements, and their values that were extracted using MATLAB.*

an attribute, and has the format ('`xxxx`','`yyyy`'), where `xxxx` and `yyyy` are hexadecimal numbers. `Value representation` (VR) describes the data type, e.g. US (unsigned short), FL (floating point single) and IS (integer string), to name a few. The `value length` field contains the length of the attribute, and `value field` contains the data of the attribute. Sample DICOM tags and their values are shown in Table 3.2. DICOM files may have additional tags, called 'private' tags, in addition to those described in the DICOM Standard, which are listed by the medical device manufacturer in a mandatory DICOM Conformance Statement. The private tags in Table 3.2 belong to a Siemens Mangetom Skyra 3 T scanner, and describe the parameters related to the DT-MRI scan, e.g. the DICOM tag ('0019','100e') is the gradient scan direction.

The NIfTI format was developed by the Data Format Working Group to solve the problem of multiple data formats used in functional MRI research. Compared to the DICOM format, NIfTI has fewer tags, and also has simpler data structure. There are two NIfTI formats – NIfTI-1 and NIfTI-2. The NIfTI-2 format is an extension of the NIfTI-1 format, allowing for 64-bit storage, and addresses the storage of large images and matrices. Since NIfTI-2 is simply an extension of the NIfTI-1 format, and is not seen to replace it in the short term, only the NIfTI-1 format is described here. In the NIfTI-1 files, the first 348 bytes are reserved for the metadata, followed by uncompressed image data beginning at byte 352. Some NIfTI tags are listed in Table 3.3. The NIfTI format can hold up to 7-dimensional data. The first element of the array referenced by the `dim` tag, e.g. holds the dimension of this dataset, and the remaining values in this tag

Sample NIfTI tags	
NIfTI tag	Value
`dim`	[4 76 150 42 60 1 1 1]
`bitpix`	16
`pixdim`	[1 2.9867 2.9867 4.5 13 1 0.25 59209]
`sform_code`	1
`srow_x`	[0 0 -4.5 1.3772]
`srow_y`	[-2.9867 0 0 141.75]
`srow_z`	[0 2.9867 0 -80.3897]

Table 3.3: *Selected NIfTI tags-value pairs corresponding to the DICOM attributes in Table 3.2.*

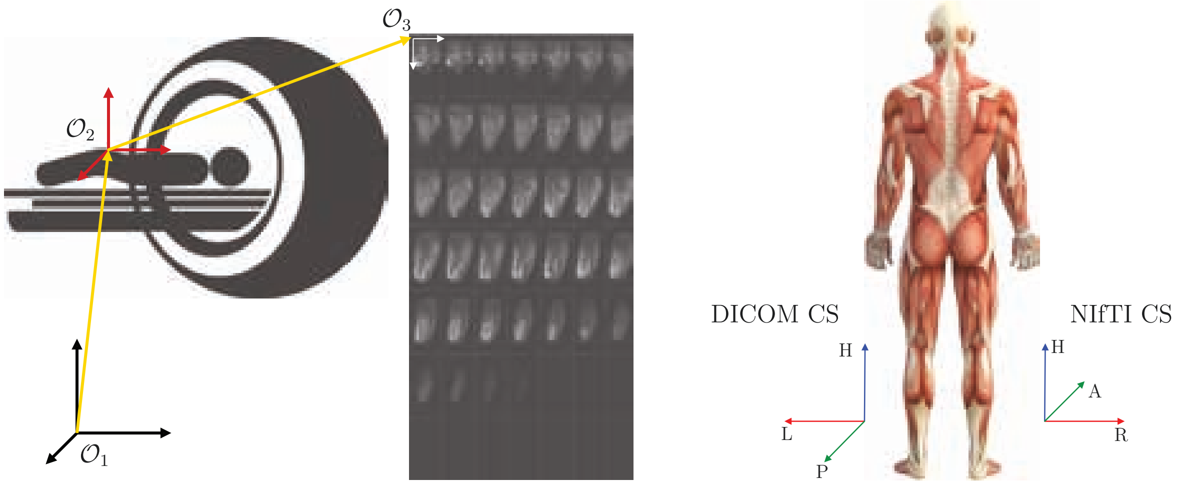

(a) *Coordinate systems in medical imaging* (b) *Anatomical coordinate system*

Figure 3.4: *Coordinate systems in medical imaging applications are illustrated in Figure 3.4(a). The DICOM and NIfTI anatomical coordinate systems, attached to the subject, are shown in Figure 3.4(b). The figure[4] of human musculoskeletal system in Figure 3.4(b) was obtained from Digital illustration of muscular system by Nicolas Fernandez ©123rf.com.*

are dimensions of the image. The `bitpix` tag contains the number of bits in an image voxel, and `pixdim` contains dimensions of the image voxels. The tags `srow_x`, `srow_y` and `srow_z` contain the affine transformation necessary for coordinate transformations. Further details of the NIfTI metadata can be found in Li et al. (2016) and Jenkinson (2007). The binary image data in the DICOM and NIfTI files are represented in their own coordinate systems, namely the DICOM and NIfTI coordinate systems, both of which are attached to the subject. These coordinate systems are described in the following section.

DICOM and NIfTI coordinate system

There are three coordinate systems (CS), which are involved in imaging applications, namely world, anatomical and image (see Figure 3.4(a)). The world or reference CS

$\mathcal{O}_1$ is spatially fixed, relative to the subject. The anatomical CS $\mathcal{O}_2$ is fixed to the subject, and the image CS $\mathcal{O}_3$ is fixed to the first scanned pixel in the image plane. Using the `ImagePositionPatient` and `ImageOrientationPatient` DICOM attributes, the 2D medical scan images are positioned and aligned in the anatomical coordinate system. When the DICOM images are transformed into the NIfTI format, the alignment and position metadata are transcoded into the `sform`, `qform` and `quarternion` NIfTI tags. An elaborate description of the DICOM CS is available in §C7.6.2.1.1 in PS3 of the DICOM Standard; only a minimal description is provided here. The DICOM CS is referred to as the +LPH coordinate system (see Figure 3.4(b)), where the +ve x-axis increases towards the left hand side (mediolateral direction) of the subject, the +ve y-axis increases towards the posterior (anteroposterior direction), and the +ve z-axis increases towards the head (caudocranial direction). The NIfTI CS, on the other hand, is +RAH, i.e. the +ve x-axis increases towards the right hand side of the subject, the +ve y-axis increases towards the anterior, and the +ve z-axis increases towards the head. In the next sections, beginning with medical image scanning, individual steps involved in the workflow will be detailed.

3.2 Data acquisition

The DT-MRI scans of the entire residual limb of a left transfemoral amputee (male, age 44, height 1.67 m, weight 75 kg) were performed at the University Hospital Tübingen, Germany. The MR Examinations were performed on a 3 T MRI whole body scanner (Magnetom Skyra, Siemens Healthcare, Erlangen, Germany), and the volunteer gave written informed consent prior to the examinations. Ethical approval was obtained beforehand (ref: 587/2014BO1).

For signal detection, body array coils of the manufacturer were employed. One coil was positioned below and the other above the thigh stump. A Magnetization Prepared Rapid Acquisition Gradient-Echo sequence (MP-RAGE) sequence was used to obtain high-resolution 3D DICOM data sets of the residual limb with the socket donned, and without the socket. The sequence parameters were: repetition time (TR) 2300 ms, echo time (TE) 3.21 ms, inversion time (TI) 974 ms, readout bandwidth 200 Hz px^{-1}, flip angle (FA) 8°, in-plane resolution 1.1×1.1 mm^2, matrix size 224×448, field of view (FOV) 245×491 mm^2 and slice thickness 1.1 mm, which resulted in 192 sagittal slices. These parameters resulted in an acquisition time of 4 min and 42 s.

For the DT-MRI scans, a 2D Echo Planar Imaging (EPI) sequence with stimulated echo preparation and fat suppression was applied. The sequence parameters were: TR 13 000 ms, TE 36 ms, mixing time (TM) 200 ms, bandwidth 2380 Hz px^{-1}, resolution 3.2×3.2 mm^2, matrix size 76×150, FOV 245×491 mm^2, fractional readout 6/8, slice thickness 3 mm, slice orientation sagittal, 42 slices, 12 diffusion directions, b values 0 and 700 s mm^{-2}, 4 acquisitions for each gradient direction and 12 acquisitions for images with $b = 0\,\mathrm{s\,mm^{-2}}$ (b_0 images). These parameters resulted in an acquisition time of 13 min and 23 s.

[4] https://de.123rf.com/profile_nicolasprimola, accessed on May 24, 2019

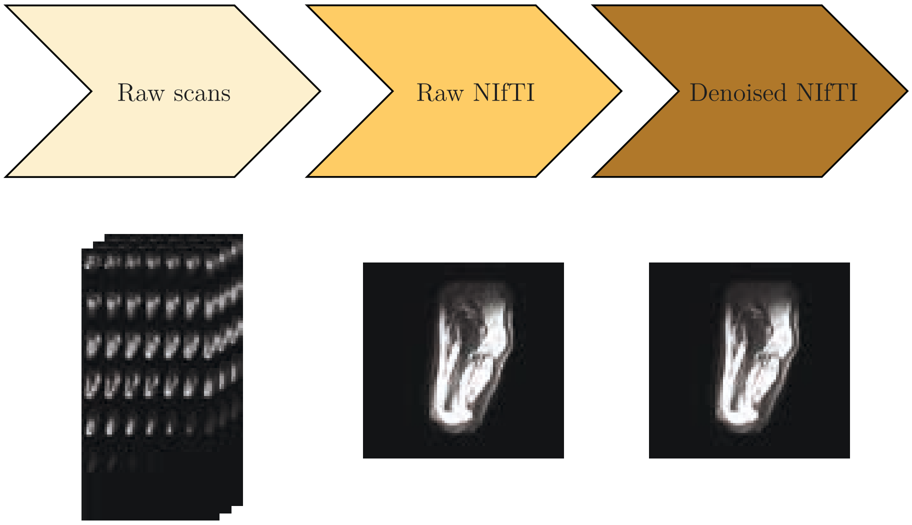

Figure 3.5: *Illustration of the steps involved in pre-processing the DT-MRI scans. The raw, experimental DT-MRI DICOM data is prepared for fibre tractography in MedINRIA by converting them into the NIfTI format, and denoising the resulting data.*

3.3 Extracting muscle fibres using tractography

Fibre tractography is a technique of reconstructing fibre tracts from the diffusion tensors embedded within DT-MRI scans. Several free and commercial tools are available for this purpose, e.g. MedINRIA[5], DIPY[6], MITK Diffusion[7], ExploreDTI[8], Amira[9] and 3D Slicer[10]; a comprehensive list of tools for analysing DT-MRI scans are listed in Soares et al. (2013). Among these tools, MedINRIA was chosen for processing the DT-MRI scans because it offered specific advantages to the proposed workflow, which will be described in due course. The steps involved in preparing the DT-MRI scans for fibre tractography with MedINRIA are (i) conversion of DICOM images into the NIfTI format, and (ii) denoising the resulting data. These steps are illustrated in Figure 3.5, and are detailed below.

3.3.1 Pre-processing DT-MRI scans for fibre tractography

MATLAB and Python scripts formed the backbone of the workflow by orchestrating the tasks of pre- and post-processing medical image data. The first step in preparing the DT-MRI scans for fibre tractography was the conversion of DICOM images into the NIfTI format. Since the DICOM and NIfTI images are in different coordinate systems, conversion from one format to another involves a coordinate transformation. This coordinate transformation was simplified by translating the image such that the first pixel of the DICOM image, which is referenced by the DICOM attribute `ImagePositionPatient`, lay at the global origin of the reference coordinate system $\mathcal{O}_1$. The Pydicom Python package was used for this purpose (cf. Mason, 2018). As a result, the affine transformation that

[5] http://www-sop.inria.fr/asclepios/software/MedINRIA/, accessed on May 24, 2019
[6] http://nipy.org/dipy/, accessed on May 24, 2019
[7] http://www.mitk.org/wiki/DiffusionImaging, accessed on May 24, 2019
[8] http://www.exploredti.com/, accessed on May 24, 2019
[9] https://www.fei.com/software/amira-3d-for-life-sciences/, accessed on May 24, 2019
[10] https://www.slicer.org/, accessed on May 24, 2019

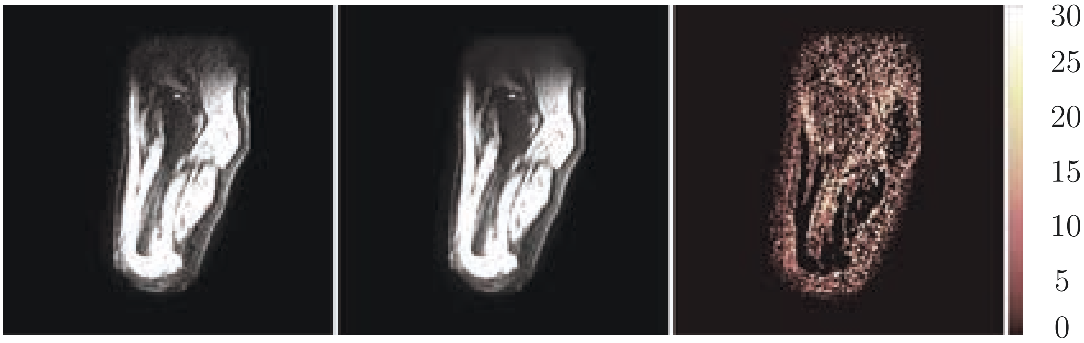

Figure 3.6: *Rician noise, which is inherent in the DT-MRI scans. The raw DT-MRI scan is shown on the left, the denoised scan in the middle, and the Rician noise, which was removed is depicted on the right. The legend shows the intensity of the removed pixels, i.e. Rician noise in the image.*

takes place during the DICOM to NIfTI conversion was reduced to pure rotation. Flipping the images along the stacking direction (in this case, left-right), in the image coordinate system, or 180° rotation about the craniocaudal axis, was sufficient to transform the images between the two coordinate systems (see Figure 3.4(b)). The DICOM to NIfTI conversion was performed using the data conversion tool dcm2niix, which produced the required raw NIfTI files (cf. Li et al., 2016).

Good image contrast is required to successfully segment images. Therefore, the raw NIfTI images were denoised to improve their contrast. Generally, diffusion-weighted images have low signal-to-noise ratio (SNR) due to low signal amplitude and thermal noise (cf. Jones & Basser, 2004). Basu et al. (2006) and Descoteaux et al. (2008) identified the noise to have a Rician distribution. Therefore, the method of overcomplete local principal component analysis by Manjón et al. (2013) was used to remove the noise. The MATLAB toolbox *DWI Denoising Software* was used for this purpose (cf. Coupé & Manjon, 2014). The raw and denoised scans of a cross section of the residual limb, as well as the noise that was removed, are depicted in Figure 3.6. The denoised NIfTI image and diffusion gradients extracted by dicm2niix from the scanning sequence were provided for fibre tractography.

3.3.2 Fibre tractography with MedINRIA

Fibre tractography was performed with the *DTI Track* module in MedINRIA. The tracking parameters were set in DTI Track with a background removal threshold of 50, fractional anisotropy (FA) bounds [0,0], the minimum length of fibres was 10 mm, and fibre sampling rate of 1 fibre per voxel. For the sake of comparison, muscle fibres tracked from both the raw and denoised scan data are shown in Figure 3.7. Fibres of *adductor magnus*, *biceps femoris*, *gluteus maximus*, *gluteus minimus*, *pectineus*, *rectus femoris*, *sartorius*, *semimembranosus*, *semitendinosus*, *vastus lateralis* and *vastus medialis* were clearly visible, and were extracted. Using the *Fibre cropping box* toolbox in MedINRIA, these fibres were manually bundled into separate muscle groups, and exported as `*.fib` ASCII files, and the segmentation of the voxels traversed by each of these muscle groups as `*.inr` binary files. A tensor reader MATLAB toolbox was provided by MedINRIA for processing the `inr` files with which the segmentation of voxels were easily extracted

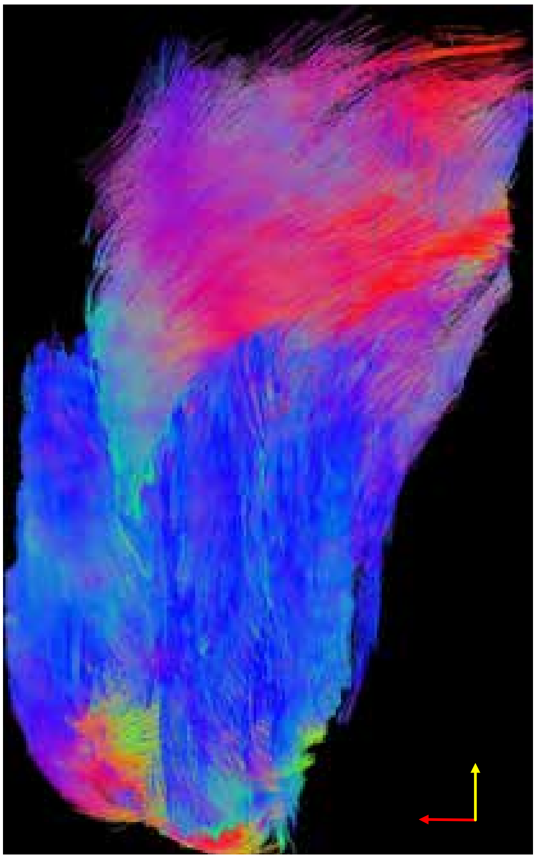

(a) *Fibres from raw NIfTI*

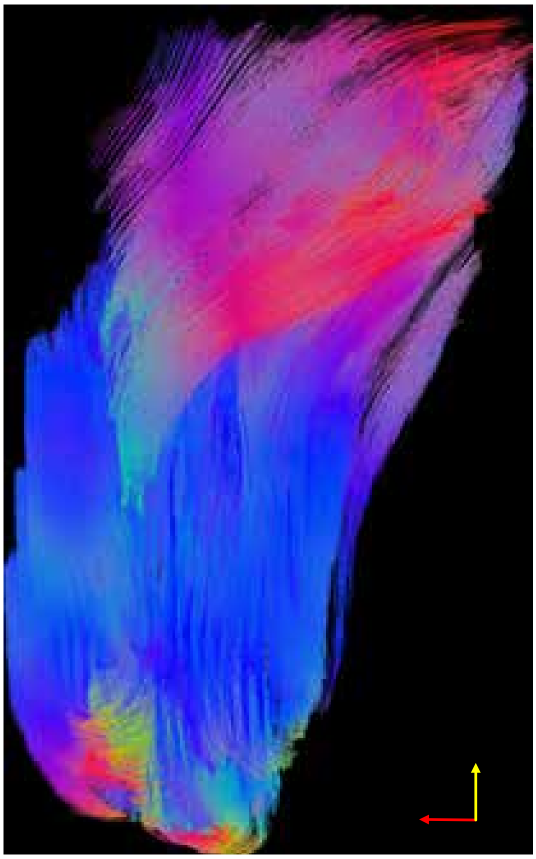

(b) *Fibres from Denoised NIfTI*

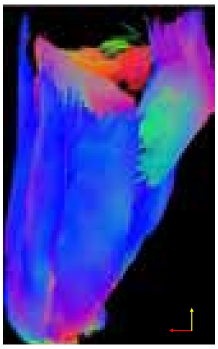

(c) *Left view*

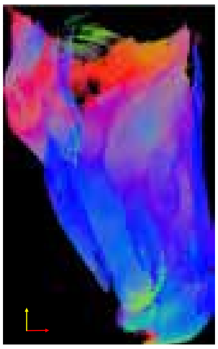

(d) *Right view*

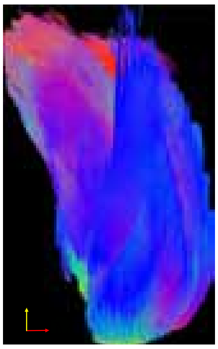

(e) *Anterior view*

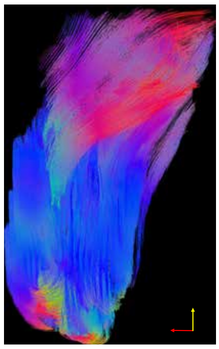

(f) *Posterior view*

Figure 3.7: *Muscle fibres tracked by MedINRIA using the raw and denoised DT-MRI NIfTI images are shown in Figures 3.7(a) and 3.7(b). In Figures 3.7(c) to 3.7(f), the left, right, anterior and posterior views of muscle fibres in the residual limb are shown. The abbreviations* `IS,` `ML` *and* `PA` *stand for inferior-superior, medial-lateral, and posterior-anterior, respectively.*

(cf. Toussaint et al., 2008). The primary reason for choosing MedINRIA over other software lay in the utility of these two files in automating the workflow. Using the MedINRIA tensor reader, each inr file was processed to obtain a segmentation of voxels traversed by the muscle fibre. A binary mask was created from the above segmentation by setting the intensity of image pixels to 0 or 1, depending on whether a fibre passed through it or not. The resulting set of binary masks were morphologically closed using a structuring disk element of size 5 px. This resulted in a stack of binary masks without undesired islands or holes within the masks. A pseudocode for generating binary image stacks of muscles for conventional image processing with Simpleware ScanIP using the voxel segmentation information in inr files is shown in Algorithm 3.1.

Algorithm 3.1: A MATLAB pseudocode to generate binary image stacks of muscles using inr files exported from MedINRIA.

Data: MedINRIA inr file
Result: Binary image stacks of muscles

Make a list of all the binary inr muscle files.
while *not all inr files have been processed* **do**
    Get segmentation mask S of voxels traversed by this muscle.
    Close holes in the mask S using MATLAB's imfill function, which produces the hole-filled mask M.
    Prepare to morphologically close the mask.
        Set threshold size t of structuring element using strel function.
        Perform morphological closing of mask M using imclose function, setting t as the size of structuring element. This produces a morphologically-closed mask C.
    Binarise the morphologically-closed mask C.
end

3.3.3 Generating DICOM images from denoised NIfTI

In the previous section, the binary image stacks of muscles were created for generating their 3D models. To model the femur and remaining soft tissues, i.e. fat and skin, that contain no fibres, DICOM images of the residual limb were required. Since the DT-MRI scans were in the mosaic format, which cannot be used in Simpleware ScanIP to generate 3D models, a baseline denoised NIfTI image was used to create valid 3D DICOM images. The MATLAB Image Processing Toolbox (v10.2) was used to slice the mosaic into 2D DICOM slices. The header for these DICOM images were adapted from the header of the baseline mosaic file. The minimum requirements to create a DICOM file are listed in section A.1.4 in PS3.3 (Information Object Definitions) of the DICOM Standard (see Table 3.4). The three-dimensional model of the residual limb created from the generated DICOM images is shown in Figure 3.8. At this juncture, all the individual components required to generate an FE model of the residual limb were available, i.e. stack of binary images of muscles, DICOM image stack of the residual limb for modelling femur and the remaining soft tissues. The following section describes the process of importing these components into Simpleware ScanIP in order to create an FE mesh of the residual limb.

Mandatory attributes	Optional attributes
StudyDate	PatientAge
StudyTime	PatientSize
PatientID	PatientWeight
StudyID	ExamDate
SeriesNumber	Modality
AccessionNumber	Manufacturer
PhysicianName	Institution
PatientName	SliceThickness
PatientBirthDate	PatientPosition
PatientSex	PatientOrientation
StudyUID	
SeriesInstanceUID	

Table 3.4: *Mandatory and optional DICOM attributes.*

Figure 3.8: *DT-MRI limb model.*

3.4 Generating an FE model of the residual limb

The FE model of the residual limb consisted of the femur, muscle tissues, fat, prosthetic liner and socket. The construction of each of these parts is described below.

Residual limb The DICOM images of the residual limb created in Section 3.3.3 were loaded into Simpleware ScanIP. It was required to import the DICOM images prior to importing any other dataset for two reasons (i) when the DICOMs were imported first, the pixel sizes were consistently and automatically applied to all subsequently loaded image stacks, and (ii) it served to ensure that the image stacks were correctly aligned with each other, and with the medical scan data.

Muscles Binary image stacks of each muscle bundle, which were generated using Algorithm 3.1, were loaded as background in Simpleware ScanIP. The ensuing segmentation in ScanIP resulted in volumetric muscle masks. This is illustrated in Figure 3.9, where segmentation of the binary images of *gluteus maximus*, which are seen stacked up on the left, produced the volumetric muscle model on the right.

Femur and socket The highly diffused spongiosa, and the relatively low water content in the femur resulted in negligible or random diffusion of water in the DT-MRI scans. This made its segmentation difficult. Furthermore, the socket was also invisible in the DT-MRI scans. This was due to absence of water content. For this reason, the femur and socket were segmented from the T_1 MP-RAGE sequences (cf. Section 3.2).

In order to register the T_1 MP-RAGE sequences with the DT-MRI scans, femurs from both these scans were segmented and exported as surface (STL) models. Using an iterative closest point technique, the transformation that correctly positioned and aligned the surface model of femur segmented from T_1 scans (henceforth called the T_1-segmented femur) with that of DT-MRI (henceforth called the DT-MRI-segmented femur), was determined. This transformation was then applied to the

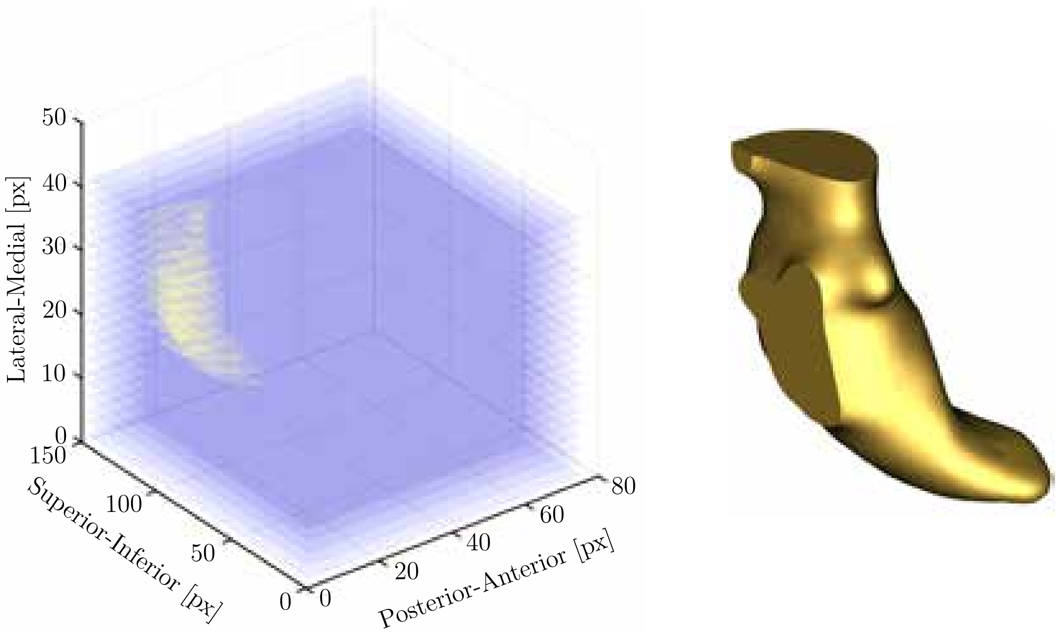

Figure 3.9: *Stacked images of gluteus maximus, created using MATLAB, are shown on the left. This stack of images is loaded as background in Simpleware ScanIP, and segmented to create the volumetric model of the muscle, which is shown on the right.*

T_1-segmented femur and socket, and were imported as CAD models into Simpleware ScanIP using the CAD module.

Fat A mask of the complete residual limb was created from the DT-MRI-DICOMs. A boolean difference of this mask from the union of the muscle and femur masks resulted in the mask for fat tissues.

Liner The liner worn by the subject was 9 mm thick. This liner was modelled by uniformly extending the outer surface of the residual limb in the normal direction towards the exterior by 9 mm.

Simpleware ScanIP offers a Python Application Programming Interface (API), which can interpret Python scripts, and perform actions based on them. In order to simplify the task of loading the DT-MRI-DICOMs (generated in Section 3.3.3) and image stacks of muscles into ScanIP, a Python script was generated by MATLAB, which automated the process of loading the datasets into ScanIP. A snippet of this Python code is shown in Listing 3.1. Firstly, the DICOM images of the residual limb were loaded, followed by the muscle image stacks. It can seen from Figure 3.8 that the residual limb model is coarse, which was a result of modelling the limb from the DT-MRI scans. This coarse model was smoothed using morphological filters (dilation, recursive Gaussian and erosion). All masks were isotropically dilated by 2 px before applying Gaussian filter of size 3 px, followed by an erosion of 1 px. As a result of these operations, volumes of the resulting masks were altered. Table 3.5 lists the volumes of raw and modified ScanIP masks. The difference in volumes of the original and final residual limb along with the liner was 0.1013 %. The

```
from scanip_api import *

# Load DICOM background
App.GetInstance().ImportDicom(DicomSeries([
"d:\dcmSlice001.dcm",
"d:\dcmSlice002.dcm",
 ...,
"d:\dcmSlice042.dcm"])

CommonImportConstraints().SetWindowLevel(0, 0).SetCrop(0, 0, 0, 150, 76,
    ↪ 42).SetPixelType(Doc.Uint16))
App.GetDocument().GetBackgroundByName("DICOM ").Activate()
App.GetDocument().GetBackgroundByName("DICOM ").SetName("DICOM
    ↪ background")
App.GetDocument().CreateMask("DICOM background", Colour(255, 255, 0))

# Activate the current background and the current mask
App.GetDocument().GetBackgroundByName("DICOM background").Activate()
App.GetDocument().GetMaskByName("DICOM background").Activate()

# Load muscle stacks
App.GetDocument().GetActiveMask().PaintWithThreshold([Point3D(75, 38,
    ↪ 21)],Mask.Disk, 300, False, 8, 509,
    ↪ App.GetDocument().GetSliceIndices(Doc.OrientationYZ),
    ↪ Doc.OrientationYZ, True)
App.GetInstance().GetActiveDocument().ImportBackgroundFromStackOfImages
    ↪ ([
"d:\img001.jpg",
"d:\img002.jpg",
 ...,
 "d:\img042.jpg"])
 2.986667, 2.986667, 4.500000,
     ↪ CommonImportConstraints().SetWindowLevel(0, 0).SetCrop(0, 0, 0,
     ↪ 150, 76, 42))

App.GetDocument().CreateMask("muscle", Colour(61, 38, 0))
App.GetDocument().GetBackgroundByName("Stack ").Activate()
App.GetDocument().GetBackgroundByName("Stack ").SetName("muscle")

# Activate the current background and the current mask
App.GetDocument().GetBackgroundByName("muscle").Activate()
App.GetDocument().GetMaskByName("muscle").Activate()

# Similarly, repeat loading the other muscle masks...
```

Listing 3.1: *A sample of the python script used to automate the loading of DICOM files and image stacks into Simpleware ScanIP (v2017.06-SP1)*

Mask	Original mask volume [cm^3]	Morphed mask volume [cm^3]	Normalised volumetric error [%]
Femur	235.0	249.0	0.1266
gluteus maximus	376.0	362.0	0.1266
gluteus minimus	46.0	47.3	0.0118
biceps femoris	84.2	87.1	0.0262
semitendinosus	56.9	59.3	0.0217
semimembranosus	51.7	42.6	0.0823
rectus femoris	153.0	155.0	0.0181
adductor magnus	197.0	193.0	0.0362
pectineus	58.6	68.2	0.0868
vastus lateralis	182.0	178.0	0.0362
vastus medialis	104.0	111.0	0.0633
sartorius	61.0	64.1	0.0280
Skin/Fat	6510.6	6343.4	1.6390
Liner	2939.4	3106.6	1.6390
Total	11 055.4	11 066.6	0.1013

Table 3.5: *Original and smoothed volumes, and the normalised volumetric error in each mask of the residual limb. The* ***mask hierarchy is preserved*** *in this table, i.e. they are listed here in the same order as they were arranged in Simpleware ScanIP.*

normalised volumetric error was computed for each mask m as

$$\begin{aligned} &\overline{\varepsilon}_m = \varepsilon_m w_m, \\ &\text{where} \quad \varepsilon_m = \frac{\left| v_m^i - v_m^f \right|}{v_m^i}, \text{ and } w_m = \frac{v_m^i}{\sum\limits_m v_m^i}. \end{aligned} \tag{3.4}$$

Here, the subscript m denotes the mask, $\overline{\varepsilon}_m$ is the normalised volumetric error, ε_m is the volumetric error fraction of mask m, w_m is the error weighting factor, v_m^i and v_m^f are the initial and final volumes of the mask, i.e. before and after morphological operations. In Simpleware ScanIP, hierarchy of the masks plays a vital role for the resulting model, i.e. when two masks intersect, the mask that is higher up in the list retains its shape, while the intersecting volume is removed from the lower mask. The volumes of the femur, the muscles, the fat and the liner masks along with the volumetric error incurred due to morphological operations in Simpleware ScanIP are listed in Table 3.5.

Using Simpleware ScanIP FE module, an FE mesh of the subject's residual limb that can be read by LS-DYNA (LSTC, Livermore, California) was created. All parts were meshed with linear Lagrange tetrahedral elements. The mesh parameters were: coarseness -35, number of quality optimisation cycles 10, mean Jacobian of 0.5 and minimum of 0.1. The parts were allowed to change during meshing, where the maximum distance that a surface node can be displaced off the original surface was limited to 0.2 mm. Contacts were not defined within the Simpleware FE module, which resulted in common nodes between the tissues of the FE mesh.

```
# vtk DataFile Version 3.0
vtk output
ASCII
DATASET POLYDATA
POINTS 9 float
-121.8 -78.1 145.3 -121.5 -77.6 146.3 -121.1 -77.2 147.3
-120.7 -76.7 148.2 -120.4 -76.3 149.2 -120.0 -75.8 150.2
-119.7 -75.4 151.2 -119.4 -75.0 152.2 -119.1 -74.5 153.1
LINES 3 12
3 0 1 2
2 3 4
4 5 6 7 8
POINT_DATA 9
COLOR_SCALARS scalars 3
0.25098 0 0 0.25098 0 0 0.25098 0 0
0.25098 0 0 0.25098 0 0
0.25098 0 0 0.25098 0 0
0.25098 0 0 0.25098 0 0
```

Listing 3.2: *This snippet shows the contents of a sample MedINRIA `fib` file*

3.5 Mapping fibres to the FE mesh

So far, the process of automating the modelling process was described. The next steps enhance the FE mesh of the residual limb muscles with the respective fibre information. To begin with, the fibres were extracted from the MedINRIA `fib` files, parsed, and were then mapped into the FE mesh of the residual limb. These steps are detailed in the following sections.

3.5.1 Extracting skeletal muscle fibres

In addition to the `inr` files, the `fib` fibre files were also exported for each muscle bundle, in the ASCII `VTK` file format. The contents of a sample `fib` file is shown in Listing 3.2. Point cloud of muscle fibres, connectivity between fibre points, and the colour of fibre strands are defined under the `POINTS`, `LINES`, and `COLOR_SCALARS` keywords. In the file, fibre points are written sequentially, i.e. all the points belonging to a fibre strand are written consecutively before proceeding to the next fibre strand. Using a Python script, the fibre point cloud was extracted, and this structured point cloud was exploited in mapping the fibres to elements of the FE mesh.

A prerequisite to mapping the fibres is their correct position and alignment with the FE mesh. Fibres extracted from NIfTI images were in the NIfTI CS, while the FE mesh generated from DICOM images was in the DICOM CS. Since the FE mesh and muscle fibres were translated to the origin of world coordinate system (cf. Section 3.3.1), their transformation reduced to a case of pure rotation about the craniocaudal axis. However, in some cases, such transformation might not be trivial. Such a condition might occur, e.g. when the optional DICOM attributes `ImagePositionPatient` and `ImageOrientationPatient` are missing, or when software updates, in tools used in the workflow, result in misaligned DT-MRI-DICOMs and muscle fibres. In order to address such possibilities, and ensure robustness of the fibre-mapping method, an iterative closest point (ICP) algorithm was used to ascertain the correct position and orientation of the fibres with the FE mesh. A Python pseudocode for this fibre alignment is provided in Algorithm 3.2, and the code for ICP that is used in the pseudocode is posted in Listing 3.3.

Algorithm 3.2: Pseudocode to align the fibre point cloud with the FE mesh.

Data: Point cloud of fibres $\boldsymbol{p}'_f$, FE nodes of muscles $\boldsymbol{p}'_m$
Result: Fibre point cloud $\boldsymbol{p}_f$ aligned with the FE mesh

`# Get mean-centred point cloud of fibres,` $\tilde{p}_f$

1 $\tilde{\boldsymbol{p}}_f \leftarrow \boldsymbol{p}'_f - \overline{\boldsymbol{p}}_f$ `#` $\overline{p}_f$ `is the mean of` p'_f

`# Get mean-centred FE point cloud of muscles,` $\tilde{p}_m$

2 $\tilde{\boldsymbol{p}}_m \leftarrow \boldsymbol{p}'_m - \overline{\boldsymbol{p}}_m$ `#` $\overline{p}_m$ `is the mean of` p'_m

`# Obtain the transformation` $\boldsymbol{T}$ `that aligns the fibres with the FE mesh`

3 $\boldsymbol{T} \leftarrow$ `ICP`$(\tilde{\boldsymbol{p}}_f, \tilde{\boldsymbol{p}}_m)$

`# Update the fibre point cloud`

4 $\boldsymbol{p}_f \leftarrow \tilde{\boldsymbol{p}}_f \boldsymbol{T} + \overline{\boldsymbol{p}}_f$

5 **return** $\boldsymbol{p}_f$

3.5.2 Mapping skeletal muscle fibres to the FE mesh

The skeletal muscle fibres were not physically modelled and embedded within the FE mesh of the residual limb, but the fibre information was encoded within each element of the FE muscle mesh. LS-DYNA provides a possibility to include fibre directions, i.e. anisotropy, through the `element_solid_ortho` card. The structure of this card is shown in Listing 3.4. Here, the fibre direction is encoded in the vector $\boldsymbol{a}$, and $\boldsymbol{d}$ is any vector in the plane perpendicular to $\boldsymbol{a}$. In order to populate the vector fields $\boldsymbol{a}$ and $\boldsymbol{d}$ for each element, (i) fibre points lying within each element were identified, and (ii) the effective fibre direction of in each element was determined.

The algorithm used to identify the fibre points lying within an element is best explained with an example. Figure 3.10(a) illustrates a triangle $\triangle ABC$ containing two points U and V, whose location with respect to the triangle must be determined, i.e. inside or outside. Let $\boldsymbol{r}_i^P$ be position vectors from a fibre point $P \in \{U, V\}$, to midpoints $i \in \{E, F, G\}$ on the edges of $\triangle ABC$, and let $\boldsymbol{n}_i$ be the normals at the midpoints of each edge pointing away from the centroid of the triangle. Then, a fibre point P is deemed to lie inside the triangle if and only if

$$\boldsymbol{r}_i^P \cdot \boldsymbol{n}_i > 0 \; \forall i \in \{E, F, G\}. \tag{3.5}$$

Once the fibres within each element were known, the effective fibre direction in each of the elements was determined. Again, the steps involved in this process are explained with an example. Consider the shaded triangle in Figure 3.10(b) through which three fibre strands S_1, S_2 and S_3 pass. It can be seen that 8 fibre points ($\{3, 4, 5, 6, 7, 23, 24, 14\}$) lie within the shaded triangle, with which the effective fibre direction in the triangle should be determined. Since continuously indexed fibre points belong to the same fibre strand,

```
def ICP(fibNodes, nodeCoords):
   sourcePoints = vtk.vtkPoints()
   targetPoints = vtk.vtkPoints()
   sourceVertices = vtk.vtkCellArray()
   targetVertices = vtk.vtkCellArray()

   # insert cloud point data into the source and target points
   for fibNode in fibNodes:
      fibNodeList = fibNode.tolist()
      coord = [node for x in fibNodeList for node in x]
      id = sourcePoints.InsertNextPoint(coord[0],coord[1],coord[2])
      sourceVertices.InsertNextCell(1)
      sourceVertices.InsertCellPoint(id)
   for coord in nodeCoords:
      id = targetPoints.InsertNextPoint(coord[0],coord[1],coord[2])
      targetVertices.InsertNextCell(1)
      targetVertices.InsertCellPoint(id)

   source = vtk.vtkPolyData()
   target = vtk.vtkPolyData()
   source.SetPoints(sourcePoints)
   target.SetPoints(targetPoints)
   source.SetVerts(sourceVertices)
   target.SetVerts(targetVertices)

   # Run ICP
   icp = vtk.vtkIterativeClosestPointTransform()
   icp.SetSource(source)
   icp.SetTarget(target)
   icp.GetLandmarkTransform().SetModeToRigidBody()
   icp.SetMaximumNumberOfIterations(20)
   icp.StartByMatchingCentroidsOn()
   icp.Modified()
   icp.Update()

   icpTransformFilter = vtk.vtkTransformPolyDataFilter()
   if vtk.VTK_MAJOR_VERSION <= 5:
      icpTransformFilter.SetInput(source)
   else:
      icpTransformFilter.SetInputData(source)
   icpTransformFilter.SetTransform(icp)
   icpTransformFilter.Update()
   T = np.zeros([4,4])
   for ii in range(4):
      for jj in range(4):
         T[ii,jj] =
             ↪ icp.GetLandmarkTransform().GetMatrix().GetElement(ii,jj)
   return T
```

Listing 3.3: *Python Iterative closest point (ICP) algorithm*

```
1 *ELEMENT_SOLID_ORTHO
2 $#   eid   pid   n1    n2    n3    n4    n5    n6    n7    n8
3
4 $#         a1          a2          a3
5
6 $#         d1          d2          d3
7
8 $#
```

Listing 3.4: *An empty LS-DYNA* `element_solid_ortho` *element card, which contains the directional fibre information within elements. The fibre direction is encoded in vector* $\boldsymbol{a}$ *(line 4), and vector* $\boldsymbol{d}$ *(line 6) is any vector in a plane perpendicular to* $\boldsymbol{a}$*.*

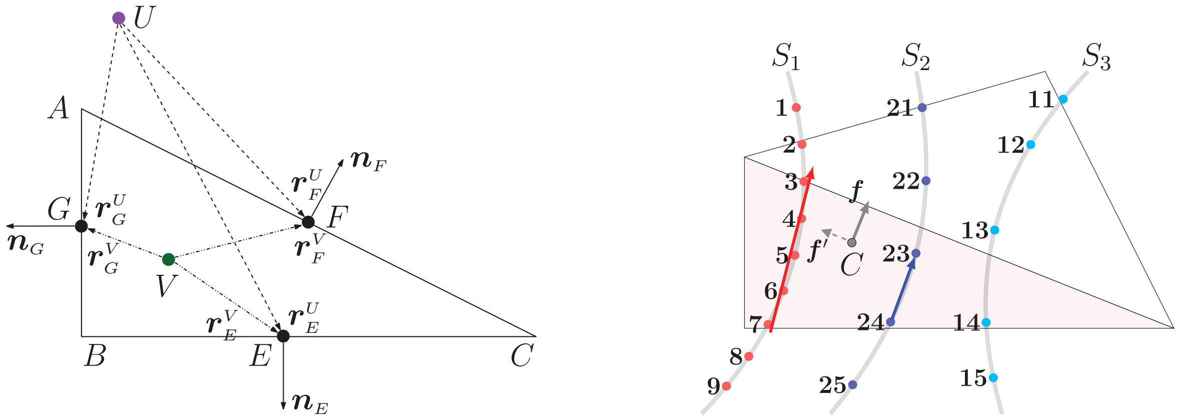

(a) *Determine position of fibre points.* (b) *Effective fibre direction in an element.*

Figure 3.10: *Shown on the left is an illustration of the algorithm that checks if a fibre point lies inside an element. On the right, the effective fibre direction in the shaded element is determined from the fibre points in strands S_1, S_2 and S_3. Trend lines are first fit to fibre points belonging to a given strand, which are then weighted to provide the effective fibre direction in an element.*

they were grouped together into subsets (in this example, into $N = 3$ subsets, namely $\{\{3, 4, 5, 6, 7\}, \{23, 24\}, \{14\}\}$). Ignoring subsets of unit size (in this example, $\{14\}$), trend lines $\tilde{\boldsymbol{f}}_k$ were fit to each subset $k \in \{1, 2, 3, \ldots, N\}$. The effective fibre direction $\boldsymbol{f}$ in the element was computed as $\boldsymbol{f} = w_k \tilde{\boldsymbol{f}}_k$, where w_k was the weight assigned to each fibre subset. In general, if an FE mesh consists of N_e elements, where N_s^j fibre strands traverse the j^{th} element ($j \in N_e$) with its centroid at $\boldsymbol{x}_j$, and $\tilde{\boldsymbol{f}}_s$ was the line of best fit for the strand s with weight w_s, the effective fibre direction in that element, $\boldsymbol{f}(\boldsymbol{x}_j)$, was defined as

$$\boldsymbol{f}(\boldsymbol{x}_j) = \sum_{s=1}^{N_s^j} w_s \tilde{\boldsymbol{f}}_s, \quad \text{with } w_s = \frac{n_s^2}{\sum_{s=1}^{N_s^j} n_s^2}, \tag{3.6}$$

where n_s was the number of fibre points in the fibre strand s. In this manner, the effective fibre direction in all N_e mesh elements was determined. These steps are provided as a pseudocode in Algorithm 3.3.

Algorithm 3.3: Pseudocode to determine the effective fibre direction in an element.

Data: Continuously indexed fibre points $\boldsymbol{p}$, FE mesh
Result: Effective fibre direction $\boldsymbol{f}$ in that element.
1 Determine the set of fibre points P lying within an element.
2 Group consecutively indexed fibre points together into subsets $P = \bigcup_{s=1}^{N} P_s$.
3 Fit linear trend lines to each subset $\tilde{\boldsymbol{f}} = \{\tilde{\boldsymbol{f}}_1, \tilde{\boldsymbol{f}}_2, \ldots, \tilde{\boldsymbol{f}}_N\}$.
4 Determine the weighted, effective trend line for the element $\boldsymbol{f} = \sum_{s=1}^{N} w_s \tilde{\boldsymbol{f}}_s$.

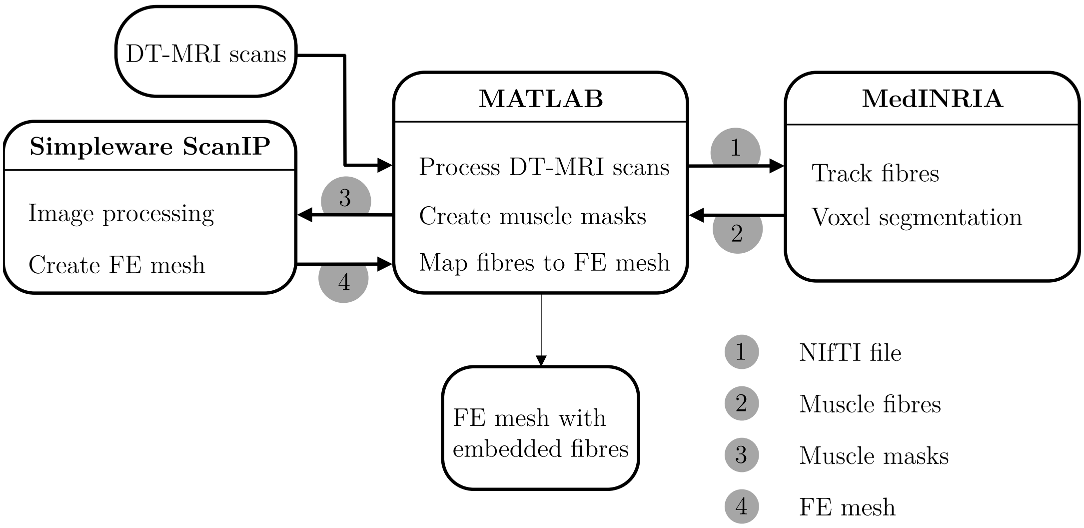

Figure 3.11: *Proposed workflow to generate an FE mesh of the residual limb from the DT-MRI scans of a subject.*

The effective fibre direction in some elements, determined using Algorithm 3.3, were inconsistent with those in their immediate neighbourhood. In some other elements of the mesh, e.g. near the boundary of *gluteus maximus*, no fibres were identified. This is attributed to the partial volume effects, resulting in missing fibre information in some elements. To correct the orientation of fibres, and to enhance the model, the fibre field was smoothed using radial basis interpolation with a Gaussian kernel. The new fibre direction in the j^{th} element with its centroid at $\boldsymbol{x}_j$, $\bar{\boldsymbol{f}}(\boldsymbol{x}_j)$ was defined as

$$\bar{\boldsymbol{f}}(\boldsymbol{x}_j) = \sum_{e=1}^{N_e} \phi \boldsymbol{f}(\boldsymbol{x}_e) \quad \text{with } \phi = \hat{\phi}(\boldsymbol{x}_i, \boldsymbol{x}_e, p) = \exp\left(-p\frac{\|\boldsymbol{x}_j - \boldsymbol{x}_e\|}{L}\right)^2, \tag{3.7}$$

where $\boldsymbol{f}(\boldsymbol{x}_e)$ was the original effective fibre direction in the element with centroid at $\boldsymbol{x}_e$ (cf. Equation (3.6)), ϕ was the Gaussian radial basis function kernel, the scalar parameter p set the number of neighbouring elements that influenced the fibre orientation in the current element (here, $p = 20$), and L was the length of the diagonal of the bounding box formed by mesh elements of the muscle. The above steps were performed for all of the 11 muscles in the residual limb. This resulted in the final FE mesh for our analyses.

3.6 Summary

In this chapter, a workflow was presented that uses DT-MRI scans of a residual limb and efficiently generates the patient-specific FE mesh with minimal human intervention. The DT-MRI scans were first pre-processed with MATLAB to convert DT-MRI-DICOMs to NIfTI, and to improve their signal-to-noise ratio. Using MedINRIA, the fibres in the DT-MRI data were tracked, and the muscle fibres were manually bundled into groups of fibres. Two files were exported for each group – an `inr` file containing the segmentation of voxels traversed by each muscle bundle, and a `fib` file containing the point cloud of fibres. MATLAB parsed these files to generate stacks of binary muscle masks, which Simpleware ScanIP combined to produce a 3D residual limb model. This model was subsequently meshed with the Simpleware FE module. Following the FE mesh generation, MATLAB and Python scripts mapped the fibre information into the FE mesh, and corrected the fibre field such that each muscle finite element contained fibre information and ensured the consistency of the fibre field. Summary of the entire workflow is illustrated in Figure 3.11.

4 Continuum-mechanical model of the residual limb

Chapter 3 described the workflow to generate subject-specific FE models from DT-MRI scans. In addition to FE geometry, material laws, which describe the deformation of soft tissues, are required to determine the internal strains and stresses. Hence, this chapter begins with the fundamentals of continuum mechanics, where the kinematics, balance relations and the concepts of stress and strain are briefly explained for the purpose of understanding the implemented soft tissue material model. After a brief description of the fundamentals of continuum mechanics, a continuum damage model is derived for modelling soft tissue damage. Since Gefen et al. (2008)'s strain-based tissue damage is, to the author's knowledge, the only experimentally-validated model, this model was included in the material model. Finally, details required for implementing this damage model in LS-DYNA are furnished.

4.1 Fundamentals of continuum mechanics

As biological tissues undergo large deformation, the theory of finite elasticity was chosen to address soft tissue deformations. In this section, the basic principles required to understand the implemented continuum-mechanical model is presented. For an in-depth understanding into the theory and other related models, the reader is referred to books on nonlinear continuum mechanics by de Borst et al. (2012), Holzapfel (2000), which form the basis for the following sections.

4.1.1 Kinematics

A continuum body $\mathcal{B}$ is composed of an infinite number of points or particles $\mathcal{P} \in \mathcal{B}$ in the Euclidean space with origin at $\mathcal{O}$ (see Figure 4.1). At any given time t, the body $\mathcal{B}$ and the particles $\mathcal{P} \in \mathcal{B}$ can assume several configurations. The configuration of body $\mathcal{B}$ at $t = 0$ is called its reference configuration, and its configuration at time t is called the current configuration. A linear transformation $\boldsymbol{\chi}$, which uniquely maps the position of the points $\mathcal{P} \in \mathcal{B}$ in the reference configuration $\boldsymbol{X} = \boldsymbol{\chi}_0(\mathcal{P}, t)$ to their current position $\boldsymbol{x}$ at time t, is given by $\boldsymbol{x} = \boldsymbol{\chi}(\boldsymbol{X}, t)$. External forces or tractions applied on the body, which lead to its motion and deformation, act on the surface $(\partial\mathcal{B})_{\boldsymbol{t}}$, and displacements applied on the surface of $\mathcal{B}$ act on $(\partial\mathcal{B})_{\boldsymbol{u}}$. Forces and displacements cannot be applied simultaneously on the same region of the body, i.e. $(\partial\mathcal{B})_{\boldsymbol{u}} \cap (\partial\mathcal{B})_{\boldsymbol{t}} = \emptyset$, and $(\partial\mathcal{B}) = (\partial\mathcal{B})_{\boldsymbol{u}} \cup (\partial\mathcal{B})_{\boldsymbol{t}}$.

The state of $\mathcal{B}$ can be described using the *material* (Lagrangian) or *spatial* (Eulerian) form. In the material description, the focus is on the particle as it moves over time, whereas in the spatial description, the focus is on a given volume of space, as particles move or flow through the control volume. The displacement of the material points from

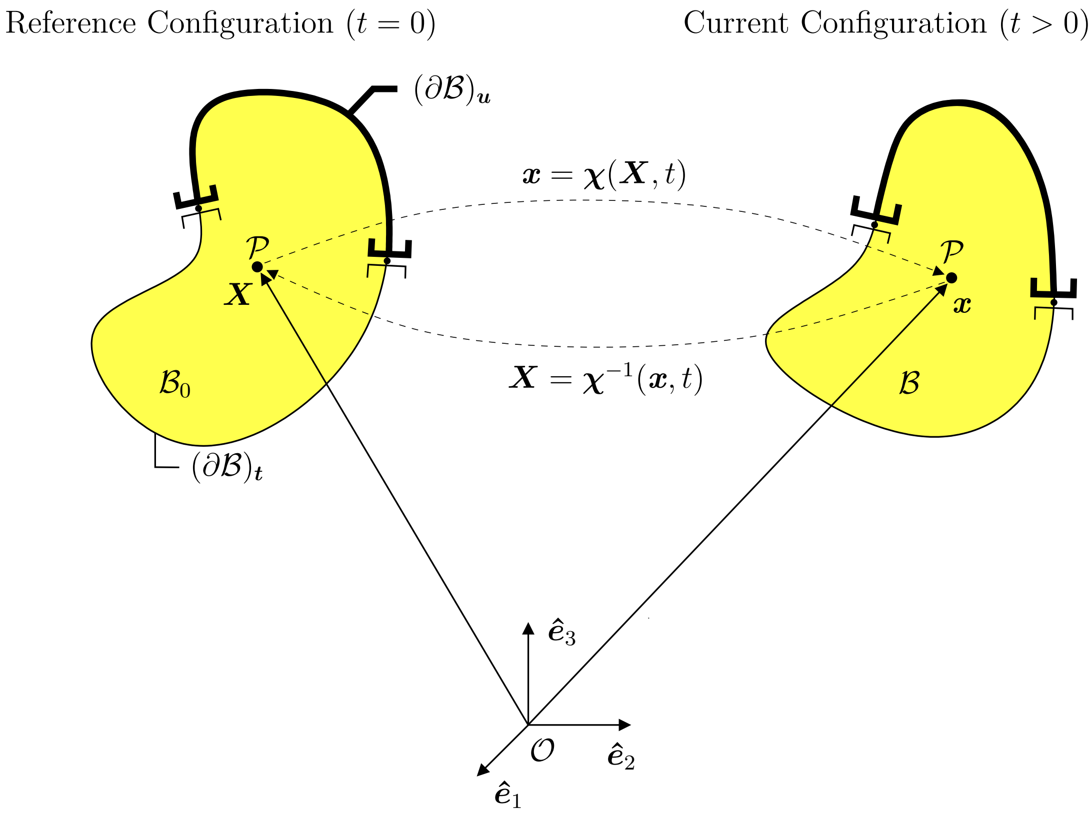

Figure 4.1: *Configuration of body $\mathcal{B}$ undergoing transformation from its reference, undeformed state at time $t = 0$ to its current deformed state at time t.*

the undeformed to the deformed state is given by $\boldsymbol{u}(\boldsymbol{X}, t) = \boldsymbol{x}(\boldsymbol{X}, t) - \boldsymbol{X}$. The velocities ($\boldsymbol{v}$) and accelerations ($\boldsymbol{a}$) of the particle are $\boldsymbol{v}(\boldsymbol{X}, t) = \partial_t\boldsymbol{\chi}(\boldsymbol{X}, t)$ and $\boldsymbol{a}(\boldsymbol{X}, t) = \partial_t\boldsymbol{v}(\boldsymbol{X}, t)$.

The deformation of material points, lines and areas between the reference and the deformed configurations are related through the second-order deformation tensor

$$\mathsf{F} = \partial_{\boldsymbol{X}}\boldsymbol{x}(\boldsymbol{X}, t) = \mathrm{Grad}\,\boldsymbol{x}. \tag{4.1}$$

For the linear transformation map $\boldsymbol{\chi}$ to be invertible, the determinant of the deformation tensor called the *Jacobian*, $J = \det\mathsf{F}$, must be non-zero. The Jacobian also represents the ratio of the volume of the body $\mathcal{B}$ in the actual configuration (v) to its volume in the reference state (V), i.e. $J = {}^{dv}\!/_{dV}$. This implies that when $J > 1$, the volume of $\mathcal{B}$ increases, while $J < 1$ implies that the volume of $\mathcal{B}$ shrinks. The case $J = 0$ implies that the body $\mathcal{B}$ vanishes in the current state. Neither of these cases are applicable for biological tissues, where the volume of tissues is assumed to remain constant between various deformation states, i.e. in the case of biological tissues, $J \overset{!}{=} 1$. However, in this case, the biological tissues are modelled as nearly incompressible materials with $J \approx 1$. If $d\boldsymbol{X}$ and $d\boldsymbol{x}$ are infinitesimally small line elements in the reference and current configurations, dS and ds are infinitesimally small area elements in the reference and current configurations, and dV and dv are infinitesimally small volume elements in the reference and current configurations, the deformation tensor maps the infinitesimal line, area and volume elements between the current and reference states in the following way

$$d\boldsymbol{x} = \mathsf{F}d\boldsymbol{X}, \quad ds = J\mathsf{F}^{-\mathsf{T}}dS, \text{ and } \quad dv = \mathsf{F}dV. \tag{4.2}$$

At this stage, the mathematical foundations relating the configuration of $\mathcal{B}$ in the reference and current states have been established using the deformation tensor $\mathbf{F}$, and the unique and invertible map $\boldsymbol{\chi}$. In the following section, the concepts of stresses and strains, which are essential to understand the deformed state of $\mathcal{B}$ is introduced.

4.1.2 Concept of strains and stresses

Unlike fundamental quantities like displacements and forces that can be experimentally measured, the related strains and stresses are concepts derived from displacements and forces that simplify analyses, but are harder to physically measure. Therefore, numerous definitions of stresses and strains exist in literature, of which only the ones used in this thesis are described.

The deformation tensor $\mathbf{F} = F_{mN}\ \hat{\boldsymbol{e}}_m \otimes \hat{\boldsymbol{e}}_N$ is a two-point tensor, which exists both in the current, and in the reference states. However, it is sometimes convenient to describe the state of $\mathcal{B}$ using tensors that are completely described in either the reference or in its current state. For this purpose, the right Cauchy-Green tensor $\mathbf{C}$ and the left Cauchy-Green tensor $\mathbf{b}$, which relate squares of the line elements in the reference and current states, are defined as

$$\begin{aligned} \|d\boldsymbol{x}\|^2 &= d\boldsymbol{x} \cdot d\boldsymbol{x} = \mathbf{F}d\boldsymbol{X} \cdot \mathbf{F}d\boldsymbol{X} \\ &= d\boldsymbol{X} \cdot \mathbf{F}^{\mathsf{T}}\mathbf{F}d\boldsymbol{X} = d\boldsymbol{X} \cdot \mathbf{C}d\boldsymbol{X}, \text{ and} \\ \|d\boldsymbol{X}\|^2 &= d\boldsymbol{X} \cdot d\boldsymbol{X} = \mathbf{F}^{-1}d\boldsymbol{x} \cdot \mathbf{F}^{-1}d\boldsymbol{x} \\ &= d\boldsymbol{x} \cdot \mathbf{F}^{-\mathsf{T}}\mathbf{F}d\boldsymbol{x} = d\boldsymbol{x} \cdot \mathbf{b}^{-1}d\boldsymbol{x}, \end{aligned} \tag{4.3}$$

where $\mathbf{C} = \mathbf{F}^{\mathsf{T}}\mathbf{F}$ and $\mathbf{b} = \mathbf{F}\mathbf{F}^{\mathsf{T}}$. Both right and left Cauchy-Green tensors are positive definite and symmetric material strain tensors, i.e.

$$\begin{aligned} \mathbf{C} &= \left(\mathbf{F}^{\mathsf{T}}\mathbf{F}\right)^{\mathsf{T}} = \mathbf{C}, \quad \det\mathbf{C} = (\det\mathbf{F})^2 > 0, \text{ and} \\ \mathbf{b} &= \left(\mathbf{F}\mathbf{F}^{\mathsf{T}}\right)^{\mathsf{T}} = \mathbf{b}, \quad \det\mathbf{b} = (\det\mathbf{F})^2 > 0. \end{aligned} \tag{4.4}$$

The Green-Lagrange material strain tensor $\mathbf{E}$ and the Euler-Almansi spatial strain tensor $\mathbf{e}$ are defined using the right and left Cauchy-Green tensors as

$$\begin{aligned} \mathbf{E} &= \frac{1}{2}\left(\mathbf{F}^{\mathsf{T}}\mathbf{F} - \mathbf{I}\right) = \frac{1}{2}\left(\mathbf{C} - \mathbf{I}\right), \text{ and} \\ \mathbf{e} &= \frac{1}{2}\left(\mathbf{I} - \mathbf{b}^{-1}\right). \end{aligned} \tag{4.5}$$

Transformation between the material and spatial quantities can be realised using push-forward $\boldsymbol{\chi}_*(\bullet)$ and pull-back operations $\boldsymbol{\chi}_*^{-1}(\bullet)$. For example, the Euler-Almansi strain tensor, which is the spatial counterpart of the Green-Lagrange material tensor can be obtained by the push-forward of $\mathbf{E}$, i.e.

$$\begin{aligned} \mathbf{e} &= \boldsymbol{\chi}_*(\mathbf{E}) = \mathbf{F}^{-\mathsf{T}}\left[\frac{1}{2}\left(\mathbf{C} - \mathbf{I}\right)\right]\mathbf{F}^{-1} \\ &= \frac{1}{2}\left(\mathbf{F}^{-\mathsf{T}}\mathbf{F}^{\mathsf{T}}\mathbf{F}\mathbf{F}^{-1} - \mathbf{F}^{-\mathsf{T}}\mathbf{F}^{-1}\right) = \frac{1}{2}\left(\mathbf{I} - \mathbf{b}^{-1}\right). \end{aligned} \tag{4.6}$$

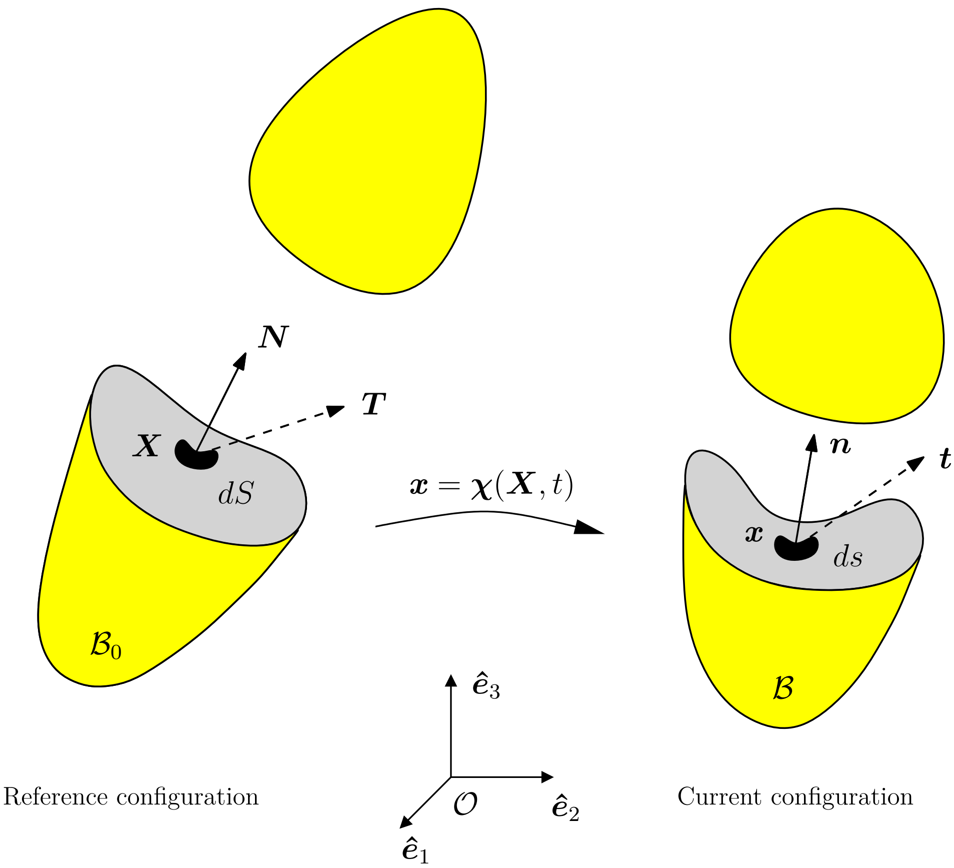

Figure 4.2: *Traction vectors and unit normals to an infinitesimal surface on the cut surface of $\mathcal{B}$ in the initial and current configurations.*

The concept of stress, postulated by Cauchy, plays an important role in continuum-mechanics for understanding the internal state of a material during finite deformation. Stresses arise as a result of particle-particle interactions within the same body, and during interactions with other neighbouring bodies. In the reference state, body $\mathcal{B}$ is in a state of equilibrium, where the internal forces balance each other. However, when the body is cut into two parts by a plane, unbalanced surface forces or tractions act on the free surface. If dS is an infinitesimally small area element on this free surface in the reference configuration, with outward normal $\boldsymbol{N}$, and ds, $\boldsymbol{n}$ are the corresponding quantities in the current configuration, then the infinitesimally small resultant force acting on dS (cf. Figure 4.2) is given by

$$d\boldsymbol{f} = \boldsymbol{t} ds = \boldsymbol{T} dS. \tag{4.7}$$

Cauchy postulated that the traction acting on the area element, lying on the free surface, is a function of its position and outward normal, which is given by

$$\boldsymbol{t} = \boldsymbol{t}(\boldsymbol{x}, \boldsymbol{n}, t), \text{ and } \quad \boldsymbol{T} = \boldsymbol{T}(\boldsymbol{X}, \boldsymbol{N}, t). \tag{4.8}$$

These surface tractions are related to the surface normals at their point of action through unique second-order tensors, namely the symmetric spatial Cauchy stress tensor $\boldsymbol{\sigma}$, and the two-point First Piola-Kirchhoff stress tensor $\mathbf{P}$ such that

$$\boldsymbol{t}(\boldsymbol{x}, \boldsymbol{n}, t) = \boldsymbol{\sigma}(\boldsymbol{x}, t)\boldsymbol{n}, \text{ and } \quad \boldsymbol{T}(\boldsymbol{X}, \boldsymbol{N}, t) = \mathbf{P}(\boldsymbol{X}, t)\boldsymbol{N}. \tag{4.9}$$

Equation (4.9) is called Cauchy's theorem. The second Piola-Kirchhoff stress tensor $\mathbf{S}$ is a symmetric second-order material tensor obtained from the pull-back of the Kirchhoff stress tensor $\boldsymbol{\tau} = J\boldsymbol{\sigma}$,

$$\mathbf{S} = \boldsymbol{\chi}_*^{-1}(\boldsymbol{\tau}) = \mathbf{F}^{-1}\boldsymbol{\tau}\mathbf{F}^{\mathsf{T}}. \tag{4.10}$$

4.1.3 Eigenvalue representation of tensors

In most cases, biological soft tissues, such as skeletal muscles and fat, can be satisfactorily represented by hyperelastic materials, whose state at any given instant of time can be determined from its associated strain energy function. When the strain energy function is purely a function of symmetric tensors such as $\mathbf{C}, \mathbf{b}$, it is invariant under rotation, and may be expressed in terms of invariants of these symmetric tensors. If λ_i ($i \in \{1, 2, 3\}$) are the eigenvalues of $\mathbf{C}$, then characteristic equation of $\mathbf{C}$ is given by

$$\lambda_i^3 - I_1\lambda_i^2 + I_2\lambda_i - I_3 = 0, \tag{4.11}$$

where I_1, I_2, I_3 are the first, second and third invariants of $\mathbf{C}$, respectively. They are defined as

$$\begin{aligned} I_1(\mathbf{C}) &= \mathrm{tr}(\mathbf{C}) = \lambda_1 + \lambda_2 + \lambda_3 \\ I_2(\mathbf{C}) &= \frac{1}{2}\left((\mathrm{tr}(\mathbf{C}))^2 - \mathrm{tr}\left(\mathbf{C}^2\right)\right) = \lambda_1\lambda_2 + \lambda_2\lambda_3 + \lambda_3\lambda_1 \\ I_3(\mathbf{C}) &= \det(\mathbf{C}) = \lambda_1\lambda_2\lambda_3. \end{aligned} \tag{4.12}$$

In this thesis, the biological soft tissues are modelled as hyperelastic materials. The Lagrangian second Piola-Kirchhoff stress, and its energy conjugate, the Green-Lagrange strain $\mathbf{E}$, are adopted to model their behaviour.

4.2 Balance relations

The fundamental balance relations, namely the conservation of mass, momentum and energy, that must be satisfied for any mechanical system at all times, are stated here. Biological tissues considered here are closed systems with no mass transport occurring across the boundary of $\mathcal{B}$. Thermal effects are also not considered here, leading to the analysis of a mechanically and thermally isolated closed system.

4.2.1 Conservation of mass

Biological soft tissues considered here, namely skeletal muscles and fat, are assumed to be homogeneous. Further, they do not undergo mass changes during any transformation $\boldsymbol{\chi}(\boldsymbol{X}, t)$. Therefore, if ρ_0 and ρ are the densities of $\mathcal{B}$ at the reference and current configurations, then the local form of mass balance is given by $\rho_0 dV = \rho dv$. If m is the mass of $\mathcal{B}$, then the global mass balance is given by

$$\begin{aligned} m &= \int_{\mathcal{B}_0} \rho_0 dV = \int_{\mathcal{B}} \rho dv = \mathrm{const} > 0, \text{and therefore} \\ \dot{m} &= \frac{\mathrm{D}}{\mathrm{Dt}} \int_{\mathcal{B}_0} \rho_0 dV = \frac{\mathrm{D}}{\mathrm{Dt}} \int_{\mathcal{B}} \rho dv = 0. \end{aligned} \tag{4.13}$$

4.2.2 Conservation of momentum

Similar to the classical Newtonian mechanics, the balance of linear momentum $\boldsymbol{L}(t)$ of particles $\mathcal{P} \in \mathcal{B}$ with velocities $\boldsymbol{V}(\boldsymbol{X}, t)$ and $\boldsymbol{v}(\boldsymbol{x}, t)$ in the reference and current configurations is given by

$$\boldsymbol{L} = \int\limits_{\mathcal{B}_0} \rho_0 \boldsymbol{V} dV = \int\limits_{\mathcal{B}} \rho \boldsymbol{v} dv. \tag{4.14}$$

The external force $\boldsymbol{f}$ acting on $\mathcal{B}$ can be obtained from the rate of change of linear momentum, i.e.

$$\boldsymbol{f}(t) = \dot{\boldsymbol{L}}(t) = \int\limits_{\mathcal{B}_0} \rho_0 \dot{\boldsymbol{V}} dV = \int\limits_{\mathcal{B}} \rho \dot{\boldsymbol{v}} dv. \tag{4.15}$$

This external force $\boldsymbol{f}$ can also be described in terms of the surface tractions $\boldsymbol{t}$ (cf. Section 4.1.2) and body forces $\boldsymbol{b}$ (Note: The body force vector $\boldsymbol{b}$ is different from the left Cauchy Green tensor $\mathbf{b}$ that was introduced in Section 4.1.2). Substituting Equation (4.7) into Equation (4.15), and integrating the infinitesimal surface force $d\boldsymbol{f}$ over the traction boundary, the external force is given by

$$\boldsymbol{f}(t) = \int\limits_{\mathcal{B}} \rho \dot{\boldsymbol{v}} dv = \int\limits_{(\partial\mathcal{B})_t} \boldsymbol{t} ds + \int\limits_{\mathcal{B}} \boldsymbol{b} dv. \tag{4.16}$$

Applying Gauss' divergence theorem to the surface traction $\boldsymbol{t}$ in Equation (4.9) results in a volumetric representation of the surface traction, which is given by

$$\int\limits_{(\partial\mathcal{B})_t} \boldsymbol{t} ds = \int\limits_{(\partial\mathcal{B})_t} \boldsymbol{\sigma} \boldsymbol{n} ds = \int\limits_{(\partial\mathcal{B})_t} \boldsymbol{\sigma} d\boldsymbol{s} = \int\limits_{\mathcal{B}} \operatorname{div} \boldsymbol{\sigma} dv. \tag{4.17}$$

Substituting Equations (4.16) and (4.17) into Equation (4.15), we obtain the important Cauchy's first equation of motion, which is given by

$$\int\limits_{\mathcal{B}} (\operatorname{div} \boldsymbol{\sigma} + \boldsymbol{b} - \rho \dot{\boldsymbol{v}}) \, dv = \mathbf{0}. \tag{4.18}$$

The angular momentum $\boldsymbol{J}(t)$ of the particles $\mathcal{P} \in \mathcal{B}$ with respect to an arbitrary fixed point whose position vector is given by $\boldsymbol{x}_0$ is given by

$$\boldsymbol{J}(t) = \int\limits_{\mathcal{B}} \boldsymbol{r} \times \boldsymbol{L}(t) = \int\limits_{\mathcal{B}_0} \boldsymbol{r} \times \rho_0 \boldsymbol{V} dV = \int\limits_{\mathcal{B}} \boldsymbol{r} \times \rho \boldsymbol{v} dv, \tag{4.19}$$

where $\boldsymbol{r} = \boldsymbol{x} - \boldsymbol{x}_0$ is the position vector of $\mathcal{P}$ from the origin of the coordinate system $\mathcal{O}$, with respect to which the angular momentum $\boldsymbol{J}$ is computed. The rate change of angular momentum $\boldsymbol{M}(t)$ of $\mathcal{B}$ is

$$\boldsymbol{M}(t) = \dot{\boldsymbol{J}}(t) = \int\limits_{\mathcal{B}} \boldsymbol{r} \times \dot{\boldsymbol{L}}(t) = \int\limits_{\mathcal{B}_0} \boldsymbol{r} \times \rho_0 \dot{\boldsymbol{V}} dV = \int\limits_{\mathcal{B}} \boldsymbol{r} \times \rho \dot{\boldsymbol{v}} dv. \tag{4.20}$$

On substituting Equation (4.16) in Equation (4.20), one obtains

$$\boldsymbol{M} = \int_{(\partial\mathcal{B})_t} \boldsymbol{r} \times \boldsymbol{t} ds + \int_{\mathcal{B}} \boldsymbol{r} \times \boldsymbol{b} dv = \int_{\mathcal{B}} \boldsymbol{r} \times \rho \dot{\boldsymbol{v}} dv. \tag{4.21}$$

The most important consequence of the balance of angular momentum is the symmetry of Cauchy stress tensor. Expressing Equation (4.21) in index notation, and applying the Gauss divergence theorem yields

$$\begin{aligned} \int_{\mathcal{B}} \partial_{x_m} \left(\mathcal{E}_{ijk}\sigma_{km}r_j\right) dv + \int_{\mathcal{B}} \mathcal{E}_{ijk} r_j b_k dv &= \int_{\mathcal{B}} \mathcal{E}_{ijk} r_j \rho \dot{v}_k dv \\ \int_{\mathcal{B}} \mathcal{E}_{ijk} \left(\sigma_{km}\delta_{jm} + r_j \partial_{x_m}\sigma_{km}\right) dv + \int_{\mathcal{B}} \mathcal{E}_{ijk} r_j b_k dv &= \int_{\mathcal{B}} \mathcal{E}_{ijk} r_j \rho \dot{v}_k dv. \end{aligned} \tag{4.22}$$

On rearranging the terms in Equation (4.22), the balance of angular momentum yields

$$\int_{\mathcal{B}} \mathcal{E}_{ijk}\sigma_{kj} dv = \int_{\mathcal{B}} \mathcal{E}_{ijk} r_j \left(-\partial_{x_m}\sigma_{km} - b_k + \rho\dot{v}_k\right) dv, \tag{4.23}$$

where the term in parenthesis on the right hand side of Equation (4.23) is the Cauchy's first equation of motion obtained from the balance of linear momentum (cf. Equation (4.18)). Substituting Equation (4.18) in Equation (4.23) results in

$$\int_{\mathcal{B}} \mathcal{E}_{ijk}\sigma_{kj} dv = 0 \quad \text{and therefore,} \quad \mathcal{E}_{ijk}\sigma_{kj} \overset{!}{=} 0. \tag{4.24}$$

Using the property of Ricci permutation tensor, where $\boldsymbol{\mathcal{E}}\boldsymbol{\mathcal{E}} = 2\mathbf{I}$, on multiplying both sides of Equation (4.24) with $\mathcal{E}_{imn}$, one obtains

$$\begin{aligned} \mathcal{E}_{imn}\mathcal{E}_{ijk}\sigma_{kj} &= 0 \\ \left(\delta_{jm}\delta_{kn} - \delta_{mk}\delta_{nj}\right)\sigma_{kj} &= 0, \quad \text{and therefore,} \\ \sigma_{mn} &= \sigma_{nm}. \end{aligned} \tag{4.25}$$

This shows the symmetry of the Cauchy stress tensor.

4.3 Balance of mechanical energy

Since only isothermal processes are considered here, the balance of mechanical energy is a natural consequence of the Cauchy's first equation of motion and need not be additionally satisfied. The balance of mechanical energy, in the spatial description, is provided here for the sake of completeness.

Scalar product of the linear momentum balance (cf. Equation (4.18)) by the velocity $\boldsymbol{v}$ of particles in $\mathcal{B}$ arising from any motion $\boldsymbol{\chi}(\boldsymbol{X}, t)$ yields

$$\int_{\mathcal{B}} \left(\operatorname{div}\boldsymbol{\sigma} \cdot \boldsymbol{v} + \boldsymbol{b} \cdot \boldsymbol{v} - \rho\dot{\boldsymbol{v}} \cdot \boldsymbol{v}\right) dv = \mathbf{0}. \tag{4.26}$$

Through the application of divergence theorem,

$$\operatorname{div}\left(\boldsymbol{\sigma}^{\mathsf{T}}\boldsymbol{v}\right) = \operatorname{div}\boldsymbol{\sigma}\cdot\boldsymbol{v} + \boldsymbol{\sigma} : \operatorname{grad}\boldsymbol{v}. \tag{4.27}$$

Therefore, Equation (4.26) can be rewritten as

$$\int_{\mathcal{B}} \left(\operatorname{div}\left(\boldsymbol{\sigma}^{\mathsf{T}}\boldsymbol{v}\right) - \boldsymbol{\sigma} : \operatorname{grad}\boldsymbol{v} + \boldsymbol{b}\cdot\boldsymbol{v} - \rho\dot{\boldsymbol{v}}\cdot\boldsymbol{v}\right) dv = \mathbf{0}. \tag{4.28}$$

Re-arranging the terms in Equation (4.28), one obtains

$$\int_{\mathcal{B}} \left(\rho\dot{\boldsymbol{v}}\cdot\boldsymbol{v}\right) dv = \int_{\mathcal{B}} \left(\operatorname{div}\left(\boldsymbol{\sigma}^{\mathsf{T}}\boldsymbol{v}\right) - \boldsymbol{\sigma} : \operatorname{grad}\boldsymbol{v} + \boldsymbol{b}\cdot\boldsymbol{v}\right) dv, \tag{4.29}$$

where $\mathbf{v} = \operatorname{grad}\boldsymbol{v}$ is the material velocity gradient. By applying Gaussian integral theorem and Cauchy's postulate (cf. Equation (4.17)), the divergence term in Equation (4.26) can be expressed as,

$$\int_{\mathcal{B}} \operatorname{div}\left(\boldsymbol{\sigma}^{\mathsf{T}}\boldsymbol{v}\right) dv = \int_{(\partial\mathcal{B})_t} \boldsymbol{\sigma}^{\mathsf{T}}\boldsymbol{v}\cdot d\boldsymbol{s} = \int_{(\partial\mathcal{B})_t} \boldsymbol{v}\cdot\boldsymbol{\sigma} d\boldsymbol{s} = \int_{(\partial\mathcal{B})_t} \boldsymbol{v}\cdot\boldsymbol{t} ds. \tag{4.30}$$

Inserting the above expression into Equation (4.29),

$$\int_{\mathcal{B}} \left(\rho\dot{\boldsymbol{v}}\cdot\boldsymbol{v}\right) dv = \int_{(\partial\mathcal{B})_t} \boldsymbol{t}\cdot\boldsymbol{v} ds - \int_{\mathcal{B}} \left(\boldsymbol{\sigma} : \operatorname{grad}\boldsymbol{v} + \boldsymbol{b}\cdot\boldsymbol{v}\right) dv, \tag{4.31}$$

which can be re-arranged into the well-known expression for the balance of mechanical energy,

$$\int_{\mathcal{B}} \left(\rho\dot{\boldsymbol{v}}\cdot\boldsymbol{v} + \boldsymbol{\sigma} : \operatorname{grad}\boldsymbol{v}\right) dv = \int_{(\partial\mathcal{B})_t} \boldsymbol{t}\cdot\boldsymbol{v} ds + \int_{\mathcal{B}} \boldsymbol{b}\cdot\boldsymbol{v} dv. \tag{4.32}$$

Since Cauchy stress tensor is symmetric, the material velocity gradient $\mathbf{v}$ can be reduced to its symmetric form, which is the rate of deformation tensor $\mathbf{d} = {}^1\!/_2\left(\mathbf{v} + \mathbf{v}^{\mathsf{T}}\right)$. An alternate expression for Equation (4.32) is

$$\frac{\mathrm{D}}{\mathrm{Dt}}\mathcal{K}(t) + \mathcal{P}_{\text{int}}(t) = \mathcal{P}_{\text{ext}}(t), \tag{4.33}$$

where

$$\begin{aligned}
\mathcal{K}(t) &= \int_{\mathcal{B}} \frac{1}{2}\rho\boldsymbol{v}^2 dv, \\
\mathcal{P}_{\text{int}}(t) &= \int_{\mathcal{B}} \boldsymbol{\sigma} : \mathbf{d} dv, \text{ and} \\
\mathcal{P}_{\text{ext}}(t) &= \int_{(\partial\mathcal{B})_t} \boldsymbol{t}\cdot\boldsymbol{v} ds + \int_{\mathcal{B}} \boldsymbol{b}\cdot\boldsymbol{v} dv.
\end{aligned} \tag{4.34}$$

4.4 Thermodynamic balance laws

Thermodynamics of irreversible processes provides a convenient framework to describe the mechanics of materials undergoing an irreversible process such as damage. In this framework, heat is assumed to be any form of energy which is transferred between two systems, or a system and its surroundings. In thermodynamics, this energy (heat) is assumed to be heat transfer. Similar to the mechanical power $\mathcal{P}$ (cf. Equation (4.34)), the thermal power in a system $\mathcal{Q}$ is given, in the spatial description, by

$$\mathcal{Q}(t) = \int_{\mathcal{B}} r dv - \int_{(\partial\mathcal{B})_t} \boldsymbol{q} \cdot \boldsymbol{n} ds, \tag{4.35}$$

where r is the heat source per unit volume of $\mathcal{B}$, and $\boldsymbol{q}$ is the heat efflux per unit area on the surface of $\mathcal{B}$ along the direction given by $\boldsymbol{n}$. Upon accounting for thermal energy in the system, the global balance of mechanical energy in Equation (4.33) becomes

$$\frac{\mathrm{D}}{\mathrm{Dt}}\mathcal{K}(t) + \frac{\mathrm{D}}{\mathrm{Dt}}\mathcal{E}(t) = \mathcal{P}_{\text{ext}}(t) + \mathcal{Q}(t), \tag{4.36}$$

or in the local form with Equations (4.33) to (4.35) as

$$\dot{e} = \boldsymbol{\sigma} : \mathbf{d} - \operatorname{div} \boldsymbol{q} + r, \tag{4.37}$$

where $\mathcal{E}(t) = \int_{\mathcal{B}} e(\boldsymbol{x}, t) dv$ is the sum of all internal energy e in the system. Equation (4.36) is the first law of thermodynamics, and governs the balance of energy in a system during thermodynamic process, but not the direction of energy transfer. The second law of thermodynamics governs the direction of energy transfer in a thermodynamic process by introducing the concept of entropy. Entropy S is a measure of randomness and disorder in a thermodynamic system, which can never be retrieved for performing useful work. It is defined, in the spatial description, as

$$S(t) = \int_{\mathcal{B}} \xi(\boldsymbol{x}, t) dv, \tag{4.38}$$

where ξ is the entropy per unit volume at a spatial point. The second law of thermodynamics states that any given point in time, the sum of entropy influx and supply cannot be greater than the rate of entropy creation, i.e.

$$\frac{\mathrm{D}}{\mathrm{Dt}}S(t) \geqslant \int_{\mathcal{B}} \tilde{r} dv - \int_{(\partial\mathcal{B})_t} \tilde{\boldsymbol{q}} \cdot \boldsymbol{n} ds. \tag{4.39}$$

Here, $\tilde{r}$ and $\tilde{\boldsymbol{q}}$ are the entropy source and efflux terms. According to Clausius, the entropy source and efflux are related to the absolute temperature $\theta(\boldsymbol{x}, t)$ of particles in $\mathcal{B}$ as $\tilde{r} = {}^{r}/_{\theta}$ and $\tilde{\boldsymbol{q}} = {}^{\boldsymbol{q}}/_{\theta}$. On substituting these terms in Equation (4.39), one obtains the global form of Clausius-Duhem inequality

$$\begin{aligned}
\int_{\mathcal{B}} \dot{\xi} dv &\geqslant \int_{\mathcal{B}} \frac{r}{\theta} dv - \int_{(\partial\mathcal{B})_t} \frac{\boldsymbol{q}}{\theta} \cdot \boldsymbol{n} ds \\
&\geqslant \int_{\mathcal{B}} \frac{r}{\theta} dv - \int_{\mathcal{B}} \operatorname{div}\left(\frac{\boldsymbol{q}}{\theta}\right) dv \\
&\geqslant \int_{\mathcal{B}} \frac{r}{\theta} dv - \int_{\mathcal{B}} \frac{1}{\theta} \operatorname{div} \boldsymbol{q} - \frac{1}{\theta^2} \boldsymbol{q} \cdot \operatorname{grad} \theta dv,
\end{aligned} \tag{4.40}$$

or the local form,

$$\dot{\xi} \geqslant \frac{r}{\theta} - \frac{1}{\theta}\,\mathrm{div}\,\boldsymbol{q} + \frac{1}{\theta^2}\boldsymbol{q} \cdot \mathrm{grad}\,\theta. \tag{4.41}$$

Upon substituting the local form of first law of thermodynamics, i.e. Equation (4.37) in Equation (4.41), an alternate version of the local form of Clausius-Duhem is obtained as

$$\boldsymbol{\sigma} : \mathbf{d} - \dot{e} + \dot{\xi}\theta - \frac{1}{\theta}\boldsymbol{q} \cdot \mathrm{grad}\,\theta \geqslant 0. \tag{4.42}$$

The term $-{}^{\boldsymbol{q}}/_{\theta} \cdot \mathrm{grad}\,\theta$ in Equation (4.42) is non-negative since $\theta \geqslant 0$ and $\boldsymbol{q} \cdot \mathrm{grad}\,\theta \leqslant 0$ (classical heat conduction inequality). This results in a stronger form of the Clausius-Duhem inequality, called the Clausius-Planck inequality, and is given by

$$\mathcal{D} = \boldsymbol{\sigma} : \mathbf{d} - \dot{e} + \dot{\xi}\theta \geqslant 0, \tag{4.43}$$

where $\mathcal{D} \geqslant 0$ is the local entropy production. The non-negativity of internal dissipation $\mathcal{D}$ places an important constraint in the direction of energy transfer, and in the evolution of irreversible processes.

4.5 Skeletal muscle model

In this section, a 3D continuum-mechanical model describing the behaviour of active and passive biological tissues in the residual limb is introduced. All soft tissues in the residual limb are modelled as nearly incompressible ($J \approx 1$), hyperelastic materials. The skeletal muscles are modelled as transversely isotropic due to the embedded fibres in the muscle matrix (see Section 3.5). A reversible, isothermal process allows the existence of a strain energy function Ψ governing the stress-strain relationship of the hyperelastic soft tissues. A unique additive decomposition of Ψ into volumetric (Ψ_{vol}) and isochoric (Ψ_{ich}) components is given by

$$\Psi(\mathbf{C}, \mathbf{M}, \alpha) = \Psi_{\mathrm{vol}}(J) + \Psi_{\mathrm{ich}}(\bar{\mathbf{C}}, \mathbf{M}, \alpha), \tag{4.44}$$

where $\mathbf{C}$ is the right Cauchy-Green tensor, $\bar{\mathbf{C}} = J^{-2/3}\mathbf{C}$ is the isochoric part of $\mathbf{C}$, $\mathbf{M} = \boldsymbol{a}_0 \otimes \boldsymbol{a}_0$ is the structural tensor with fibres along $\boldsymbol{a}_0$, and $\alpha \in [0, 1]$ is the muscle activation level. The strain energy function in Equation (4.44) can be additively split into individual contributions from the fibres and soft tissue matrix as

$$\Psi(\mathbf{C}, \mathbf{M}, \alpha) = \Psi^{\mathrm{m}}_{\mathrm{vol}}(J) + \Psi^{\mathrm{m}}_{\mathrm{ich}}(\bar{\mathbf{C}}) + (1 - \omega)\left(\Psi^{\mathrm{fp}}_{\mathrm{ich}}(\bar{\mathbf{C}}, \mathbf{M}) + \alpha\Psi^{\mathrm{fa}}_{\mathrm{ich}}(\bar{\mathbf{C}}, \mathbf{M})\right). \tag{4.45}$$

Here, $\Psi^{\mathrm{m}}_{\mathrm{vol}}$ and $\Psi^{\mathrm{m}}_{\mathrm{ich}}$ are the volumetric and isochoric components of the strain energy in soft tissue matrix. $\Psi^{\mathrm{fp}}_{\mathrm{ich}}$ and $\Psi^{\mathrm{fa}}_{\mathrm{ich}}$ are the isochoric strain energies in the passive and active fibres, respectively. The soft tissue model is also intended to be applicable for isotropic soft tissues. Therefore, a binary variable $\omega \in \{0, 1\}$ is introduced, which controls the inclusion ($\omega = 0$) or exclusion ($\omega = 1$) of anisotropy components. For the sake of clarity, the arguments will be omitted henceforth, and will be re-introduced when the context demands it. The rate form of Equation (4.45) is

$$\dot{\Psi} = \left[\mathbf{S}^{\mathrm{m}}_{\mathrm{vol}} + \mathbf{S}^{\mathrm{m}}_{\mathrm{ich}} + (1 - \omega)\left(\mathbf{S}^{\mathrm{fp}}_{\mathrm{ich}} + \alpha\mathbf{S}^{\mathrm{fa}}_{\mathrm{ich}}\right)\right] : \dot{\mathbf{E}}, \tag{4.46}$$

where $\mathbf{S}^{\text{m}}_{\text{vol}}$, $\mathbf{S}^{\text{m}}_{\text{ich}}$, $\mathbf{S}^{\text{fp}}_{\text{ich}}$, $\mathbf{S}^{\text{fa}}_{\text{ich}}$ are the volumetric and isochoric components of the second Piola-Kirchhoff stresses $\mathbf{S} = 2\partial_{\mathbf{C}}\Psi$ in the soft tissue matrix and fibres. $\mathbf{E}$ is the Green-Lagrange strain tensor. The Clausius-Planck inequality (cf. Equation (4.43)) for an isothermal process states that the internal dissipation at any particle $\mathcal{P} \in \mathcal{B}$ should be non-negative at any given instant of time, i.e.

$$\mathbf{S} : \dot{\mathbf{E}} - \dot{\Psi} \geqslant 0. \tag{4.47}$$

Substituting the expression for $\dot{\Psi}$ in Equation (4.46) in Equation (4.47) yields

$$\left[\mathbf{S} - \mathbf{S}^{\text{m}}_{\text{vol}} - \mathbf{S}^{\text{m}}_{\text{ich}} - (1-\omega)\left(\mathbf{S}^{\text{fp}}_{\text{ich}} + \alpha\mathbf{S}^{\text{fa}}_{\text{ich}}\right)\right] : \dot{\mathbf{E}} \geqslant 0, \tag{4.48}$$

from which the second Piola-Kirchhoff stress are recovered using the Coleman-Noll procedure, i.e.

$$\mathbf{S} = \mathbf{S}^{\text{m}}_{\text{vol}} + \mathbf{S}^{\text{m}}_{\text{ich}} + (1-\omega)\left(\mathbf{S}^{\text{fp}}_{\text{ich}} + \alpha\mathbf{S}^{\text{fa}}_{\text{ich}}\right). \tag{4.49}$$

The strain energy functions for the volumetric and isochoric parts of the soft tissues and skeletal muscle fibres in Equation (4.45) are obtained from Röhrle et al. (2017), which are

$$\begin{aligned}
\Psi^{\text{m}}_{\text{vol}} &= \frac{1}{2}\kappa\left(J-1\right)^2,\\
\Psi^{\text{m}}_{\text{ich}} &= c_1\left(\bar{I}_1 - 3\right) + c_2\left(\bar{I}_2 - 3\right),\\
\Psi^{\text{fp}}_{\text{ich}} &= \frac{c_3}{c_4}\left(I_4^{c_4/2} - 1\right) - \frac{c_3}{2}\ln\left(I_4\right), \text{ and}\\
\Psi^{\text{fa}}_{\text{ich}} &= \begin{cases} -\dfrac{\sigma_{\max}}{\nu_{\text{asc}}}\left(\lambda_{\text{opt}}\Delta W_{\text{asc}}\right)^{-1/\nu_{\text{asc}}} \displaystyle\int_{\frac{\lambda^{\nu_{\text{asc}}}}{\lambda_{\text{opt}}\Delta W_{\text{asc}}}}^{\infty} \lambda^{(1/\nu_{\text{asc}}-1)}\exp\left(-\lambda\right)d\lambda, & \text{if } \lambda \leqslant \lambda_{\text{opt}}\\
-\dfrac{\sigma_{\max}}{\nu_{\text{dsc}}}\left(\lambda_{\text{opt}}\Delta W_{\text{dsc}}\right)^{-1/\nu_{\text{dsc}}} \displaystyle\int_{\frac{\lambda^{\nu_{\text{dsc}}}}{\lambda_{\text{opt}}\Delta W_{\text{dsc}}}}^{\infty} \lambda^{(1/\nu_{\text{dsc}}-1)}\exp\left(-\lambda\right)d\lambda, & \text{if } \lambda > \lambda_{\text{opt}},\end{cases}
\end{aligned} \tag{4.50}$$

where κ is the bulk modulus, c_1 and c_2 are the Mooney-Rivlin material constants of the isotropic matrix, and c_3 and c_4 are material constants affecting passive fibre stretch. $\bar{I}_1, \bar{I}_2$, and $\bar{I}_3$ are the invariants of $\bar{\mathbf{C}}$. $\sigma^{\max}_{\text{iso}}$ is the magnitude of maximum contractile stress generated by a muscle fibre, which occurs at the optimum fibre stretch λ_{opt}. The parameters $\Delta W_{\text{asc}}, \Delta W_{\text{des}}, \nu_{\text{asc}}$ and ν_{des} affect the magnitude of active contractile stress generated by muscle fibres. The expressions for second Piola-Kirchhoff stress tensors for the matrix and fibre strain energies given in Equation (4.50) are

$$
\begin{aligned}
\mathbf{S}^{\mathrm{m}}_{\mathrm{vol}} &= \kappa J\,(J-1)\,\mathbf{C}^{-1} \\
\mathbf{S}^{\mathrm{m}}_{\mathrm{ich}} &= 2\left[\left(c_1 J^{-2/3} + c_2 I_1 J^{-4/3}\right)\mathbf{I} - c_2 J^{-4/3}\mathbf{C} - \left(\frac{1}{3}c_1 I_1 J^{-2/3} + \frac{2}{3}c_2 I_2 J^{-4/3}\right)\mathbf{C}^{-1}\right] \\
\mathbf{S}^{\mathrm{fp}}_{\mathrm{ich}} &= \begin{cases} \dfrac{1}{\lambda^2}c_3\left(\lambda^{c_4}-1\right)\mathbf{M} & \text{if } \lambda \geqslant 1 \\ \mathbf{0} & \text{otherwise, and} \end{cases} \\
\mathbf{S}^{\mathrm{fa}}_{\mathrm{ich}} &= \begin{cases} \dfrac{\sigma^{\max}_{\mathrm{iso}}}{\lambda^2}\exp\left(-\left|\dfrac{\lambda/\lambda_{\mathrm{opt}}-1}{\Delta W_{\mathrm{asc}}}\right|^{\nu_{\mathrm{asc}}}\right)\mathbf{M} & \text{if } \lambda \leqslant \lambda_{\mathrm{opt}} \\ \dfrac{\sigma^{\max}_{\mathrm{iso}}}{\lambda^2}\exp\left(-\left|\dfrac{\lambda/\lambda_{\mathrm{opt}}-1}{\Delta W_{\mathrm{des}}}\right|^{\nu_{\mathrm{des}}}\right)\mathbf{M} & \text{if } \lambda > \lambda_{\mathrm{opt}}. \end{cases}
\end{aligned}
\tag{4.51}
$$

Before proceeding further, the damage occurring in soft tissues as a result of excessive strains must be accounted for. The details of the implemented damage model are provided in the following section.

4.5.1 Soft tissue damage model

Damage occurring in the soft tissues and fibres due to excessive strains is modelled with a rate-independent finite strain damage model within the framework of nonlinear continuum damage mechanics. Following Peña (2014), soft tissue damage is hypothesised to occur independently in the matrix and fibres. As a result, the strain energy characterising the deformation of soft tissues (cf. Equation (4.45)) is modified to model damage, i.e.

$$
\Psi(\mathbf{C},\mathbf{M},\zeta^{\mathrm{m}},\zeta^{\mathrm{f}},\alpha) = \Psi_{\mathrm{vol}}(J) + \Psi_{\mathrm{ich}}(\bar{\mathbf{C}},\mathbf{M},\zeta^{\mathrm{m}},\zeta^{\mathrm{f}},\alpha), \tag{4.52}
$$

where ζ^{m} and ζ^{f} are internal damage parameters capturing stress softening in the ground matrix and fibres, respectively. According to Simo (1987), stress softening affects only the isochoric strain energy function. Further, damage is not assumed to Therefore, the isochoric strain energy term in Equation (4.52) can be expressed with the internal damage parameters as

$$
\begin{aligned}
\Psi(\mathbf{C},\mathbf{M},\zeta^{\mathrm{m}},\zeta^{\mathrm{f}},\alpha) = \Psi^{\mathrm{m}}_{\mathrm{vol}}(J) + (1-\zeta^{\mathrm{m}})\Psi^{\mathrm{m}}_{\mathrm{ich}}(\bar{\mathbf{C}}) +& \\
(1-\omega)\left((1-\zeta^{\mathrm{f}})\Psi^{\mathrm{fp}}_{\mathrm{ich}}(\bar{\mathbf{C}},\mathbf{M}) + \alpha\Psi^{\mathrm{fa}}_{\mathrm{ich}}(\bar{\mathbf{C}},\mathbf{M})\right)&.
\end{aligned}
\tag{4.53}
$$

Here, $(1-\zeta^{\mathrm{m}})$ and $(1-\zeta^{\mathrm{f}})$ are damage reduction factors such that $0 \leqslant \zeta^{\mathrm{m}},\zeta^{\mathrm{f}} < 1$. Expressions for the second Piola-Kirchhoff stresses are obtained in the same fashion as in the damage-free case (cf. Equations (4.46) to (4.49)), i.e. the rate form of Equation (4.53) is

$$
\begin{aligned}
\dot{\Psi} = \left[\mathbf{S}^{\mathrm{m}}_{\mathrm{vol}} + (1-\zeta^{\mathrm{m}})\mathbf{S}^{\mathrm{m}}_{\mathrm{ich}} + (1-\omega)\left((1-\zeta^{\mathrm{f}})\mathbf{S}^{\mathrm{fp}}_{\mathrm{ich}} + \alpha\mathbf{S}^{\mathrm{fa}}_{\mathrm{ich}}\right)\right] : \dot{\mathbf{E}}& \\
+ \Psi^{\mathrm{m}}_{\mathrm{ich}}\dot{\zeta}^{\mathrm{m}} + \Psi^{\mathrm{fp}}_{\mathrm{ich}}\dot{\zeta}^{\mathrm{f}}&.
\end{aligned}
\tag{4.54}
$$

From the Clausius-Planck inequality (cf. Equation (4.47)), the internal dissipation at any given instant of time must be non-negative, i.e. $\mathbf{S}:\dot{\mathbf{E}} - \dot{\Psi} \geqslant 0$. Substituting Equation (4.54) for $\dot{\Psi}$, one obtains

$$\Big[\mathbf{S} - \mathbf{S}^{\mathrm{m}}_{\mathrm{vol}} - (1-\zeta^{\mathrm{m}})\mathbf{S}^{\mathrm{m}}_{\mathrm{ich}} - (1-\omega)\left((1-\zeta^{\mathrm{f}})\mathbf{S}^{\mathrm{fp}}_{\mathrm{ich}} + \alpha\mathbf{S}^{\mathrm{fa}}_{\mathrm{ich}}\right)\Big] : \dot{\mathbf{E}} - \Psi^{\mathrm{m}}_{\mathrm{ich}}\dot{\zeta^{\mathrm{m}}} - \Psi^{\mathrm{fp}}_{\mathrm{ich}}\dot{\zeta^{\mathrm{f}}} \geqslant 0. \quad (4.55)$$

from which the second Piola-Kirchhoff stress are recovered using the Coleman-Noll procedure as

$$\mathbf{S} = \mathbf{S}^{\mathrm{m}}_{\mathrm{vol}} + (1-\zeta^{\mathrm{m}})\mathbf{S}^{\mathrm{m}}_{\mathrm{ich}} + (1-\omega)\left((1-\zeta^{\mathrm{f}})\mathbf{S}^{\mathrm{fp}}_{\mathrm{ich}} + \alpha\mathbf{S}^{\mathrm{fa}}_{\mathrm{ich}}\right). \quad (4.56)$$

Here, $\mathbf{S}^{\mathrm{m}}_{\mathrm{vol}}$, $\mathbf{S}^{\mathrm{m}}_{\mathrm{ich}}$, $\mathbf{S}^{\mathrm{fp}}_{\mathrm{ich}}$, $\mathbf{S}^{\mathrm{fa}}_{\mathrm{ich}}$ are the damage-free components of the second Piola-Kirchhoff stress, which were derived earlier (cf. Equation (4.51)). The dissipative inequalities in Equation (4.55) are given by

$$\begin{aligned} f^{\mathrm{m}}\dot{\zeta^{\mathrm{m}}} &\geqslant 0, \text{ where } f^{\mathrm{m}} = -\Psi^{\mathrm{m}}_{\mathrm{ich}}, \text{ and} \\ f^{\mathrm{f}}\dot{\zeta^{\mathrm{f}}} &\geqslant 0, \text{ where } f^{\mathrm{f}} = -\Psi^{\mathrm{fp}}_{\mathrm{ich}}. \end{aligned} \quad (4.57)$$

Here, f^{m} and f^{f} are the thermodynamic forces driving damage in the ground matrix and in the fibres, respectively, and the evolution of f is the effective stress power $\dot{f} = \mathbf{S} : \dot{\mathbf{E}}$. According to Miehe (1995) and Peña (2014), the phenomenological damage parameters ζ^{m} and ζ^{f} can be additively split into discontinuous and continuous damage

$$\zeta^{\mathrm{m}} = \zeta^{\mathrm{m}}_{\mathrm{d}} + \zeta^{\mathrm{m}}_{\mathrm{c}}, \quad \zeta^{\mathrm{f}} = \zeta^{\mathrm{f}}_{\mathrm{d}} + \zeta^{\mathrm{f}}_{\mathrm{c}}, \quad (4.58)$$

where $\zeta^{\bullet}_{\mathrm{d}}$ and $\zeta^{\bullet}_{\mathrm{c}}$ are the discontinuous and continuous damage variables in the matrix and fibres ($\bullet \in \{\mathrm{m}, \mathrm{f}\}$), respectively. Expressions for the discontinuous and continuous damage variables in matrix and fibres of fibred biological tissues, adopted from Peña (2014), are

$$\begin{aligned} \zeta^{\mathrm{m}}_{\mathrm{d}} &= \frac{\zeta^{\mathrm{m}}_{\mathrm{d},\infty}}{1+\exp\left[-\mu^{\mathrm{m}}\left(\varphi^{\mathrm{m}} - \gamma^{\mathrm{m}}\right)\right]}, \quad \zeta^{\mathrm{m}}_{\mathrm{c}} = \zeta^{\mathrm{m}}_{\mathrm{c},\infty}\left[1 - \exp\left(-\eta^{\mathrm{m}}\beta^{\mathrm{m}}\right)\right], \text{ and} \\ \zeta^{\mathrm{f}}_{\mathrm{d}} &= \frac{\zeta^{\mathrm{f}}_{\mathrm{d},\infty}}{1+\exp\left[-\mu^{\mathrm{f}}\left(\varphi^{\mathrm{f}} - \gamma^{\mathrm{f}}\right)\right]}, \quad \zeta^{\mathrm{f}}_{\mathrm{c}} = \zeta^{\mathrm{f}}_{\mathrm{c},\infty}\left[1 - \exp\left(-\eta^{\mathrm{f}}\beta^{\mathrm{f}}\right)\right]. \end{aligned} \quad (4.59)$$

Here, $\zeta^{\bullet}_{\mathrm{d},\infty}$ is the maximum permitted discontinuous damage, $\mu^{\bullet}$ affects the discontinuous damage growth rate, $\varphi^{\bullet} = \sqrt{2\Psi^{\bullet}_{\mathrm{ich}}}$ is an internal state variable accounting for the discontinuous damage energy in the system at time t, and the initiation of discontinuous damage is offset by the parameter $\gamma^{\bullet}$. Likewise, $\zeta^{\bullet}_{\mathrm{c},\infty}$ is the maximum permitted continuous damage, $\eta^{\bullet}$ affects the growth rate of continuous damage, and $\beta^{\bullet}$ is an internal state variable accounting for the continuously accumulated damage in the system. The parameters $\zeta^{\bullet}_{\mathrm{d},\infty}, \mu^{\bullet}, \eta^{\bullet}$ and $\gamma^{\bullet}$ are material constants, which are determined from experiments. The influence of the damage growth factors $\mu^{\bullet}, \eta^{\bullet}$, and the influence of discontinuous damage offset parameter $\gamma^{\bullet}$ in the evolution of discontinuous and continuous damage are plotted in Figures 4.3 to 4.5. The discontinuous damage variable $\zeta^{\bullet}_{\mathrm{d}}$ is the maximum thermodynamic force or effective strain energy reached in the interval $[0, t]$ (cf. Miehe (1995)), and is given by

$$\zeta^{\mathrm{m}}_{\mathrm{d}}(t) = \max_{s\in[0,t]} \Psi^{\mathrm{m}}_{\mathrm{ich}}, \quad \zeta^{\mathrm{f}}_{\mathrm{d}}(t) = \max_{s\in[0,t]} \Psi^{\mathrm{fp}}_{\mathrm{ich}}. \quad (4.60)$$

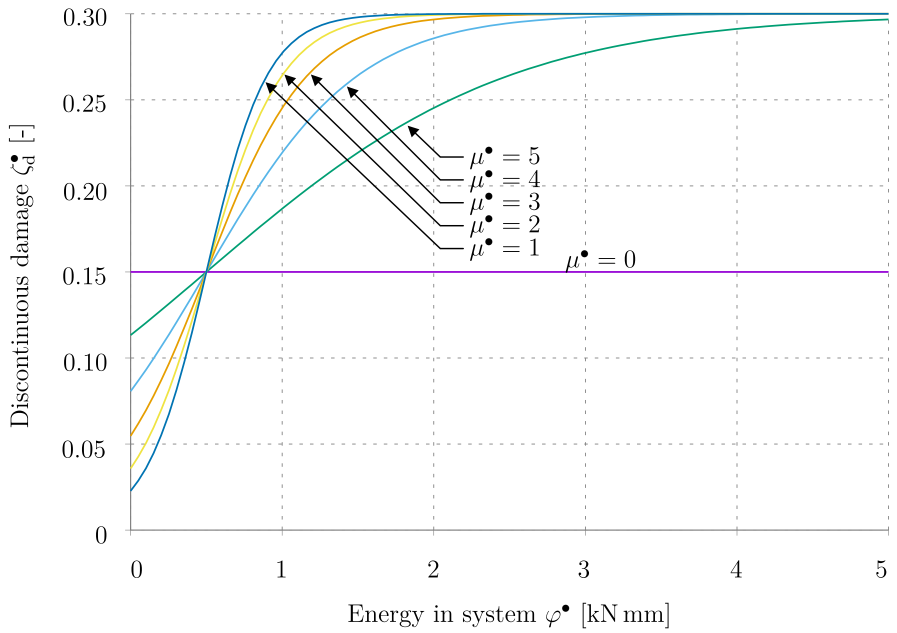

Figure 4.3: *Plot of phenomenological discontinuous damage $\zeta_{\mathrm{d}}^{\bullet}$ against accumulated damaged energy $\varphi^{\bullet}$, in the matrix/fibres, for different values of discontinuous damage growth rates $\mu^{\bullet}$ ($\bullet \in \{\mathrm{m}, \mathrm{f}\}$). Here, the discontinuous damage saturation parameter $\zeta_{\mathrm{d},\infty}^{\bullet} = 0.3$.*

The evolution of Equation (4.60) is given by

$$\dot{\zeta}_{\mathrm{d}}^{\mathrm{m}} = \begin{cases} \dot{f}^{\mathrm{m}} = \mathbf{S}_{\mathrm{ich}}^{\mathrm{m}} : \dot{\mathbf{E}} & \text{if } (f^{\mathrm{m}} - \zeta_{\mathrm{d}}^{\mathrm{m}}) = 0 \text{ and } \dot{f}^{\mathrm{m}} > 0 \\ 0 & \text{otherwise,} \end{cases}$$

and (4.61)

$$\dot{\zeta}_{\mathrm{d}}^{\mathrm{f}} = \begin{cases} \dot{f}^{\mathrm{f}} = \mathbf{S}_{\mathrm{ich}}^{\mathrm{fp}} : \dot{\mathbf{E}} & \text{if } (f^{\mathrm{f}} - \zeta_{\mathrm{d}}^{\mathrm{f}}) = 0 \text{ and } \dot{f}^{\mathrm{f}} > 0 \\ 0 & \text{otherwise.} \end{cases}$$

Continuous damage in the matrix and fibres is assumed to be governed by the the arclength of the damage force

$$\zeta_{\mathrm{c}}^{\mathrm{m}}(t) = \int_0^t \left| \dot{f}^{\mathrm{m}}(s) \right| ds, \quad \zeta_{\mathrm{c}}^{\mathrm{f}}(t) = \int_0^t \left| \dot{f}^{\mathrm{f}}(s) \right| ds, \tag{4.62}$$

whose evolution is

$$\dot{\zeta}_{\mathrm{c}}^{\mathrm{m}} = \left| \dot{f}^{\mathrm{m}} \right| = \operatorname{sgn} \dot{\Psi}_{\mathrm{ich}}^{\mathrm{m}}, \text{ and } \quad \dot{\zeta}_{\mathrm{c}}^{\mathrm{f}} = \left| \dot{f}^{\mathrm{f}} \right| = \operatorname{sgn} \dot{\Psi}_{\mathrm{ich}}^{\mathrm{fp}}. \tag{4.63}$$

This concludes the damage formulation in matrix and fibres.

For implicit analyses in LS-DYNA, fourth-order spatial tangent modulus $\mathfrak{B}$, obtained by the push-forward operation of the fourth-order material tangent $\mathfrak{C} = 2\partial_{\mathbf{C}}\mathbf{S}$, i.e. $\mathfrak{B} = \boldsymbol{\chi}_{*}(\mathfrak{C})$, is required. The material tangent $\mathfrak{C}$ is

$$\mathfrak{C} = \mathfrak{C}_{\mathrm{vol}}^{\mathrm{m}} + \mathfrak{C}_{\mathrm{ich}}^{\mathrm{m}} + (1 - \omega) \left(\mathfrak{C}_{\mathrm{ich}}^{\mathrm{fp}} + \mathfrak{C}_{\mathrm{ich}}^{\mathrm{fa}} \right), \tag{4.64}$$

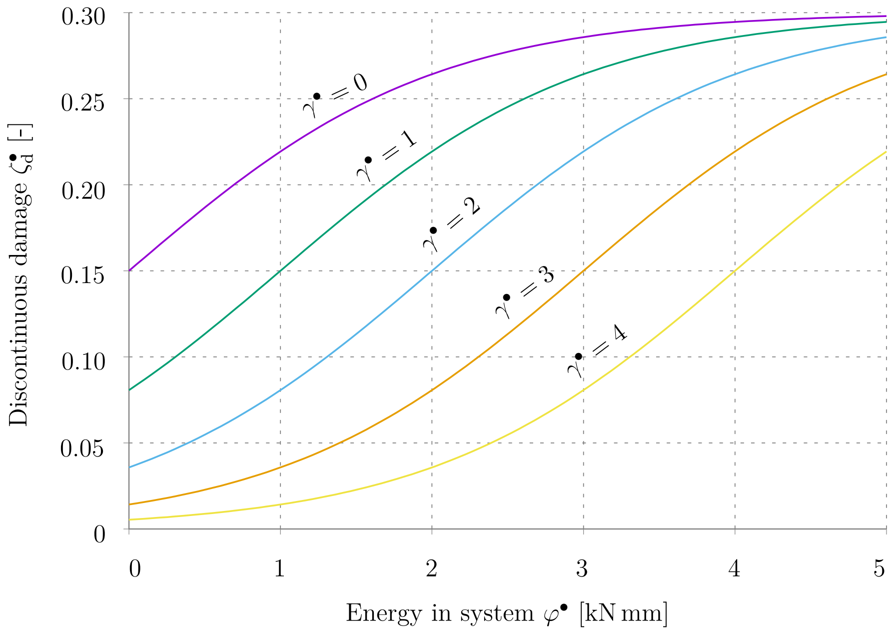

Figure 4.4: *Plot of phenomenological discontinuous damage $\zeta_d^\bullet$ against accumulated damaged energy $\varphi^\bullet$, in the matrix/fibres, for different values of discontinuous damage offset $\gamma^\bullet$ ($\bullet \in \{\mathrm{m}, \mathrm{f}\}$). Here, the discontinuous damage saturation parameter $\zeta_{d,\infty}^\bullet = 0.3$.*

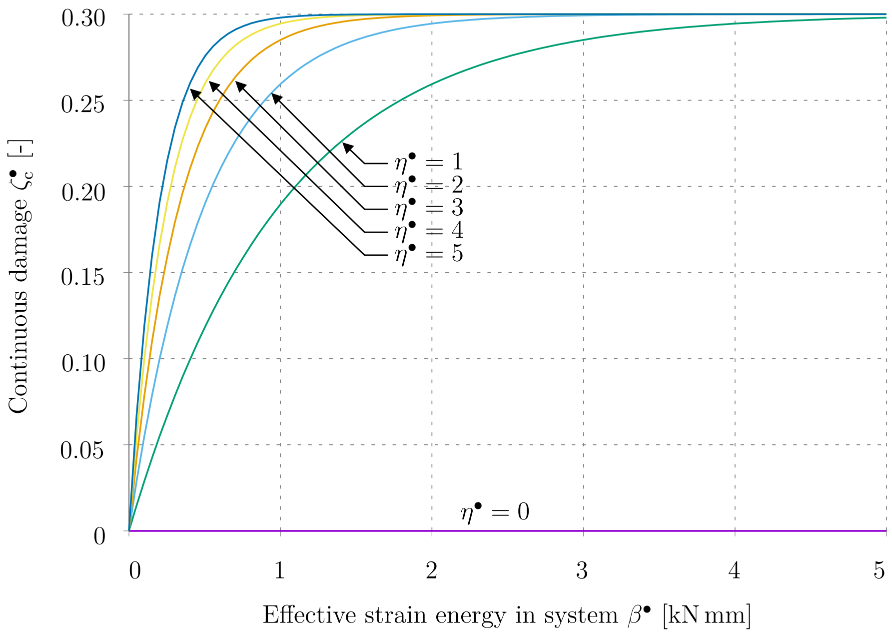

Figure 4.5: *Plot of phenomenological continuous damage $\zeta_c^\bullet$ with the accumulated damaged energy $\beta^\bullet$, in the matrix/fibres, for different values of continuous damage growth factor $\eta^\bullet$ ($\bullet \in \{\mathrm{m}, \mathrm{f}\}$). Here, the continuous damage saturation parameter $\zeta_{c,\infty}^\bullet = 0.3$.*

where individual components of the material tangent are

$$
\begin{aligned}
\mathfrak{C}^{\mathrm{m}}_{\mathrm{vol}} &= 2\partial_{\mathbf{C}}\mathbf{S}^{\mathrm{m}}_{\mathrm{vol}} = \kappa\left[\left(2J^2-J\right)\left(\mathbf{C}^{-1}\otimes\mathbf{C}^{-1}\right)+2\left(J^2-J\right)\partial_{\mathbf{C}}\mathbf{C}^{-1}\right]\\
\mathfrak{C}^{\mathrm{m}}_{\mathrm{ich}} &= 2\partial_{\mathbf{C}}\left[\left(1-\zeta^{\mathrm{m}}\right)\mathbf{S}^{\mathrm{m}}_{\mathrm{ich}}\right] = \left(1-\zeta^{\mathrm{m}}\right)\left(2\partial_{\mathbf{C}}\mathbf{S}^{\mathrm{m}}_{\mathrm{ich}}\right)+2\partial_{\mathbf{C}}\left(1-\zeta^{\mathrm{m}}\right)\otimes\mathbf{S}^{\mathrm{m}}_{\mathrm{ich}}\\
&= \left(1-\zeta^{\mathrm{m}}\right)\mathfrak{C}^{\mathrm{m1}}_{\mathrm{ich}}+\mathfrak{C}^{\mathrm{m2}}_{\mathrm{ich}}\\
\mathfrak{C}^{\mathrm{fp}}_{\mathrm{ich}} &= 2\partial_{\mathbf{C}}\left(1-\zeta^{\mathrm{f}}\right)\mathbf{S}^{\mathrm{fp}}_{\mathrm{ich}} = \left(1-\zeta^{\mathrm{f}}\right)\left(2\partial_{\mathbf{C}}\mathbf{S}^{\mathrm{fp}}_{\mathrm{ich}}\right)+2\partial_{\mathbf{C}}\left(1-\zeta^{\mathrm{f}}\right)\otimes\mathbf{S}^{\mathrm{fp}}_{\mathrm{ich}}\\
&= \left(1-\zeta^{\mathrm{f}}\right)\mathfrak{C}^{\mathrm{f1}}_{\mathrm{ich}}+\mathfrak{C}^{\mathrm{f2}}_{\mathrm{ich}} \qquad (4.65)\\
\mathfrak{C}^{\mathrm{fa}}_{\mathrm{ich}} &= 2\alpha\partial_{\mathbf{C}}\mathbf{S}^{\mathrm{fa}}_{\mathrm{ich}}\\
&= \begin{cases} -\alpha\sigma^{\max}_{\mathrm{iso}}\exp\left(-\left|p\right|^{\nu_{\mathrm{asc}}}\right)\left[2\lambda^{-4}+\dfrac{p\lambda^{-3}\nu_{\mathrm{asc}}\left|p\right|^{\nu_{\mathrm{asc}}-2}}{\Delta W_{\mathrm{asc}}\lambda_{\mathrm{opt}}}\right]\mathbf{M}\otimes\mathbf{M}, & \text{if } \lambda\leqslant\lambda_{\mathrm{opt}}\\ -\alpha\sigma^{\max}_{\mathrm{iso}}\exp\left(-\left|q\right|^{\nu_{\mathrm{dsc}}}\right)\left[2\lambda^{-4}+\dfrac{q\lambda^{-3}\nu_{\mathrm{dsc}}\left|q\right|^{\nu_{\mathrm{dsc}}-2}}{\Delta W_{\mathrm{dsc}}\lambda_{\mathrm{opt}}}\right]\mathbf{M}\otimes\mathbf{M}, & \text{if } \lambda>\lambda_{\mathrm{opt}}. \end{cases}
\end{aligned}
$$

The placeholder variables $\mathfrak{C}^{\mathrm{m1}}_{\mathrm{ich}}, \mathfrak{C}^{\mathrm{m2}}_{\mathrm{ich}}, \mathfrak{C}^{\mathrm{f1}}_{\mathrm{ich}}, \mathfrak{C}^{\mathrm{f2}}_{\mathrm{ich}}, p$ and q used in Equation (4.65) are

$$
\begin{aligned}
\mathfrak{C}^{\mathrm{m1}}_{\mathrm{ich}} &= 2\partial_{\mathbf{C}}\mathbf{S}^{\mathrm{m}}_{\mathrm{ich}}\\
&= \left(-\frac{4}{3}c_1J^{-2/3}-\frac{8}{3}c_2J^{-4/3}I_1\right)\left(\mathbf{I}\otimes\mathbf{C}^{-1}\right)+\left(4c_2J^{-4/3}\right)\left(\mathbf{I}\otimes\mathbf{I}\right)\\
&+\left(\frac{8}{3}c_2J^{-4/3}\right)\left(\mathbf{C}\otimes\mathbf{C}^{-1}\right)+\left(-4c_2J^{-4/3}\right)\mathfrak{I}\\
&+\left(-\frac{4}{3}c_1J^{-2/3}-\frac{8}{3}c_2I_1J^{-4/3}\right)\left(\mathbf{C}^{-1}\otimes\mathbf{I}\right)+\left(\frac{8}{3}c_2J^{-4/3}\right)\left(\mathbf{C}^{-1}\otimes\mathbf{C}\right)\\
&+\left(\frac{4}{9}c_1I_1J^{-2/3}+\frac{16}{9}c_2I_2J^{-4/3}\right)\left(\mathbf{C}^{-1}\otimes\mathbf{C}^{-1}\right)\\
&+\left(-\frac{4}{3}c_1I_1J^{-2/3}-\frac{8}{3}c_2I_2J^{-4/3}\right)\partial_{\mathbf{C}}\mathbf{C}^{-1},
\end{aligned}
$$

$$
\begin{aligned}
\mathfrak{C}^{\mathrm{m2}}_{\mathrm{ich}} &= 2\partial_{\mathbf{C}}\left(1-\zeta^{\mathrm{m}}\right)\otimes\mathbf{S}^{\mathrm{m}}_{\mathrm{ich}}\\
&= \left[\frac{\zeta^{\mathrm{m}}_{\mathrm{d},\infty}\mu^{\mathrm{m}}\exp\left(-\mu^{\mathrm{m}}\left(\varphi^{\mathrm{m}}-\gamma^{\mathrm{m}}\right)\right)}{2\varphi^{\mathrm{m}}\left(1+\exp\left(-\mu^{\mathrm{m}}\left(\varphi^{\mathrm{m}}-\gamma^{\mathrm{m}}\right)\right)\right)}+\zeta^{\mathrm{m}}_{\mathrm{c},\infty}\eta^{\mathrm{m}}\exp\left(-\eta^{\mathrm{m}}\beta^{\mathrm{m}}\right)\right]\mathbf{S}^{\mathrm{m}}_{\mathrm{ich}}\otimes\mathbf{S}^{\mathrm{m}}_{\mathrm{ich}},
\end{aligned}
$$

$$
\begin{aligned}
\mathfrak{C}^{\mathrm{f1}}_{\mathrm{ich}} &= 2\partial_{\mathbf{C}}\mathbf{S}^{\mathrm{fp}}_{\mathrm{ich}}\\
&= c_3\left[\left(c_4-2\right)\lambda^{\left(c_4-4\right)}+2\lambda^{-4}\right]\mathbf{M}\otimes\mathbf{M}, \text{ and}
\end{aligned}
$$

$$
\begin{aligned}
\mathfrak{C}^{\mathrm{f2}}_{\mathrm{ich}} &= 2\partial_{\mathbf{C}}\left(1-\zeta^{\mathrm{f}}\right)\otimes\mathbf{S}^{\mathrm{fp}}_{\mathrm{ich}}\\
&= \left[\frac{\zeta^{\mathrm{f}}_{\mathrm{d},\infty}\mu^{\mathrm{f}}\exp\left(-\mu^{\mathrm{f}}\left(\varphi^{\mathrm{f}}-\gamma^{\mathrm{f}}\right)\right)}{2\varphi^{\mathrm{f}}\left(1+\exp\left(-\mu^{\mathrm{f}}\left(\varphi^{\mathrm{f}}-\gamma^{\mathrm{f}}\right)\right)\right)}+\zeta^{\mathrm{f}}_{\mathrm{c},\infty}\eta^{\mathrm{f}}\exp\left(-\eta^{\mathrm{f}}\beta^{\mathrm{f}}\right)\right]\mathbf{S}^{\mathrm{fp}}_{\mathrm{ich}}\otimes\mathbf{S}^{\mathrm{fp}}_{\mathrm{ich}},
\end{aligned}
$$

with

$$p = \left(\frac{\lambda/\lambda_{\text{opt}} - 1}{\Delta W_{\text{asc}}} \right),$$
$$q = \left(\frac{\lambda/\lambda_{\text{opt}} - 1}{\Delta W_{\text{dsc}}} \right),$$

where

$$\begin{aligned}
\mathbf{I} \otimes \mathbf{C}^{-1} &= \delta_{ij} \mathsf{C}_{kl}^{-1} \left(\hat{\boldsymbol{e}}_i \otimes \hat{\boldsymbol{e}}_j \otimes \hat{\boldsymbol{e}}_k \otimes \hat{\boldsymbol{e}}_l \right) \\
\mathbf{I} \otimes \mathbf{I} &= \delta_{ij} \delta_{kl} \\
\mathbf{C} \otimes \mathbf{C}^{-1} &= \mathsf{C}_{ij} \mathsf{C}_{kl}^{-1} \\
\mathfrak{I} &= \frac{1}{2} \left(\delta_{ik} \delta_{jl} + \delta_{il} \delta_{jk} \right) \\
\mathbf{C}^{-1} \otimes \mathbf{I} &= \mathsf{C}_{ij}^{-1} \delta_{kl} \\
\mathbf{C}^{-1} \otimes \mathbf{C} &= \mathsf{C}_{ij}^{-1} \mathsf{C}_{kl} \\
\mathbf{C}^{-1} \otimes \mathbf{C}^{-1} &= \mathsf{C}_{ij}^{-1} \mathsf{C}_{kl}^{-1} \\
\partial_{\mathsf{c}} \mathbf{C}^{-1} &= \frac{1}{2} \left(-\mathsf{C}_{ik}^{-1} \mathsf{C}_{jl}^{-1} - \mathsf{C}_{il}^{-1} \mathsf{C}_{jk}^{-1} \right).
\end{aligned}$$

4.6 Strain-time cell-death model

Through extensive experiments on bio-artificial muscles (tissue-engineered constructs), Gefen et al. (2008) obtained a sigmoid-type cell death function to predict deep tissue injury based on tissue strains, which is given by

$$\varepsilon_{\text{eff}} = \frac{K}{1 + \exp\left[\mathring{\alpha} \left(t - t_0 \right) \right]} + C. \tag{4.66}$$

Here, $K, \mathring{\alpha}, t_0$ and C were empirically determined constants. Gefen et al. fitted the curve for two tissue-engineered specimens, whose parameters are listed in Table 4.1, and are plotted in Figure 4.6. For all values of effective tissue strains ε_{eff}, bounded by the sigmoid threshold curves and axes, the tissue specimens were deemed undamaged. Since this was an experimentally-validated cell-death model (also experimentally verified by Linder-Ganz et al. (2006) on rats), it was additionally implemented in the LS-DYNA material model, which flagged an element as damaged if the effective strain exceeded a prescribed threshold. An internal state variable ϑ was set to either 1 or 0, depending on whether the element was damaged or not, respectively. Parameters of specimen 1, listed in Table 4.1, were used for the FE analyses of residual limb. An algorithmic procedure of building the continuum damage model is provided in Algorithm 4.1. The procedure develops the spatial tangent modulus $\mathfrak{B}$, which is required by implicit solvers in LS-DYNA. The user material model was implemented in LS-DYNA by adding a user-material subroutine in the `dyn21.f` interface file.

The implemented material model was tested on a plate with dimensions $30 \times 30 \times 3$ mm^3, and with a hole at the centre of the xy-face with radius 5 mm (cf. Figure 4.7). The $x = 0$ face of the plate was constrained in all degrees of freedom, and was attached to a rigid

Parameters	Specimen 1	Specimen 2
K [-]	0.131	0.268
t_0 [min]	162	163
$\mathring{\alpha}$ [min^{-1}]	0.04	0.035
C [-]	0.439	0.332

Table 4.1: *Parameters of model fit from two tissue-engineered specimens (cf. Gefen et al., 2008).*

Algorithm 4.1: Algorithmic procedure for implementing the continuum damage model in LS-DYNA.

Update internal variables: Initialise and/or update strain energies in matrix and fibres $\varphi^{\mathrm{m}}, \varphi^{\mathrm{f}}, \beta^{\mathrm{m}}$, and β^{f}, maximum strain energies in the matrix and fibres $\max \Psi^{\mathrm{m}}_{\mathrm{ich}}, \max \Psi^{\mathrm{fp}}_{\mathrm{ich}}$, damage in matrix and fibres $\zeta^{\mathrm{m}}_{\mathrm{d}}, \zeta^{\mathrm{f}}_{\mathrm{d}}, \zeta^{\mathrm{m}}_{\mathrm{c}}, \zeta^{\mathrm{f}}_{\mathrm{c}}$, and element damage flag ϑ.

Compute damage-free stresses: Compute right Cauchy-Green tensor C from deformation tensor F at time $(t)_{\mathrm{n+1}}$, and determine the damage-free second Piola-Kirchhoff stresses in Equation (4.51).

Determine continuous damage in matrix and fibres:

- $(\beta^{\bullet})_{\mathrm{n+1}} = (\beta^{\bullet})_{\mathrm{n}} + \left|(\Psi^{\bullet}_{\mathrm{ich}})_{\mathrm{n+1}} - (\Psi^{\bullet}_{\mathrm{ich}})_{\mathrm{n}}\right|$
- $(\zeta^{\bullet}_{\mathrm{c}})_{\mathrm{n+1}} = \zeta^{\bullet}_{\mathrm{c},\infty}\left[1 - \exp\left(-\eta^{\bullet}\,(\beta^{\bullet})_{\mathrm{n+1}}\right)\right]$

Determine discontinuous damage in matrix and fibres:

- $(\varphi^{\bullet})_{\mathrm{n+1}} = \sqrt{2\,(\Psi^{\bullet}_{\mathrm{ich}})_{\mathrm{n+1}}}$
- **if** $(\varphi^{\bullet})_{\mathrm{n+1}} > \max\limits_{s\in[0,t]} \Psi^{\bullet}_{\mathrm{ich}}$ **then**
  - $(\zeta^{\bullet}_{\mathrm{d}})_{\mathrm{n+1}} = \dfrac{\zeta^{\mathrm{m}}_{\mathrm{d},\infty}}{1 + \exp\left[-\mu^{\bullet}\left((\varphi^{\bullet})_{\mathrm{n+1}} - \gamma^{\bullet}\right)\right]}$
- **else**
  - $(\zeta^{\bullet}_{\mathrm{d}})_{\mathrm{n+1}} = (\zeta^{\bullet}_{\mathrm{d}})_{\mathrm{n}}$
- **end**

Determine material tangent modulus: Update the material tangent modulus $(\mathfrak{C})_{\mathrm{n+1}}$ using Equation (4.65).

Obtain the spatial tangent modulus: Obtain the spatial tangent modulus $(\mathfrak{B})_{\mathrm{n+1}}$ through the push-forward of $(\mathfrak{C})_{\mathrm{n+1}}$, i.e. $(\mathfrak{B}_{ijkl})_{\mathrm{n+1}} = (\mathsf{F}_{iM})_{\mathrm{n+1}}\,(\mathsf{F}_{jN})_{\mathrm{n+1}}\,(\mathsf{F}_{kO})_{\mathrm{n+1}}\,(\mathsf{F}_{lP})_{\mathrm{n+1}}\,(\mathfrak{C}_{MNOP})_{\mathrm{n+1}}$.

Flag damaged elements based on Gefen et al.'s model:

- Compute effective Green strain $\varepsilon_{\mathrm{eff}}$ in the material as $\varepsilon_{\mathrm{eff}} = \sqrt{2/3\,\mathsf{E}_{ij}\mathsf{E}_{ij}}$.
- Compute the critical strain $\varepsilon_{\mathrm{crit}} = \dfrac{K}{1 + \exp\left[\mathring{\alpha}\,(t - t_0)\right]} + C$.
- **if** $\varepsilon_{\mathrm{eff}} > \varepsilon_{\mathrm{crit}}$ ***or*** $\vartheta == 1$ **then**
  - Set $\vartheta = 1$
- **else**
  - Set $\vartheta = 0$
- **end**

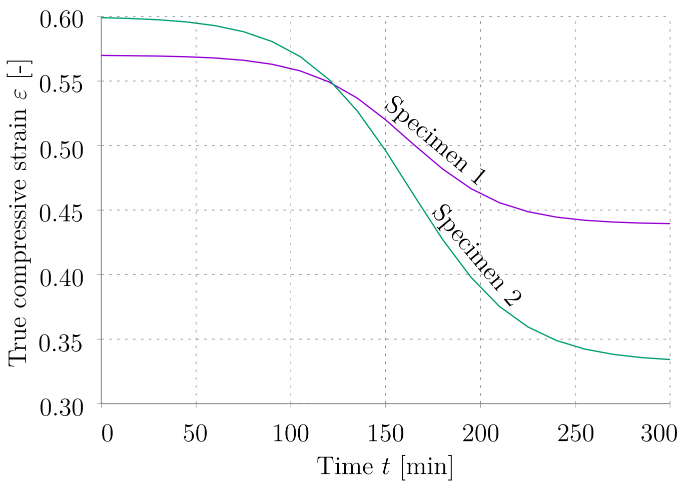

Figure 4.6: *Strain-based threshold plot to determine cell damage. The parameters used to plot the sigmoid thresholds for the two specimens are listed in Table 4.1. Reproduced from Gefen et al. (2008).*

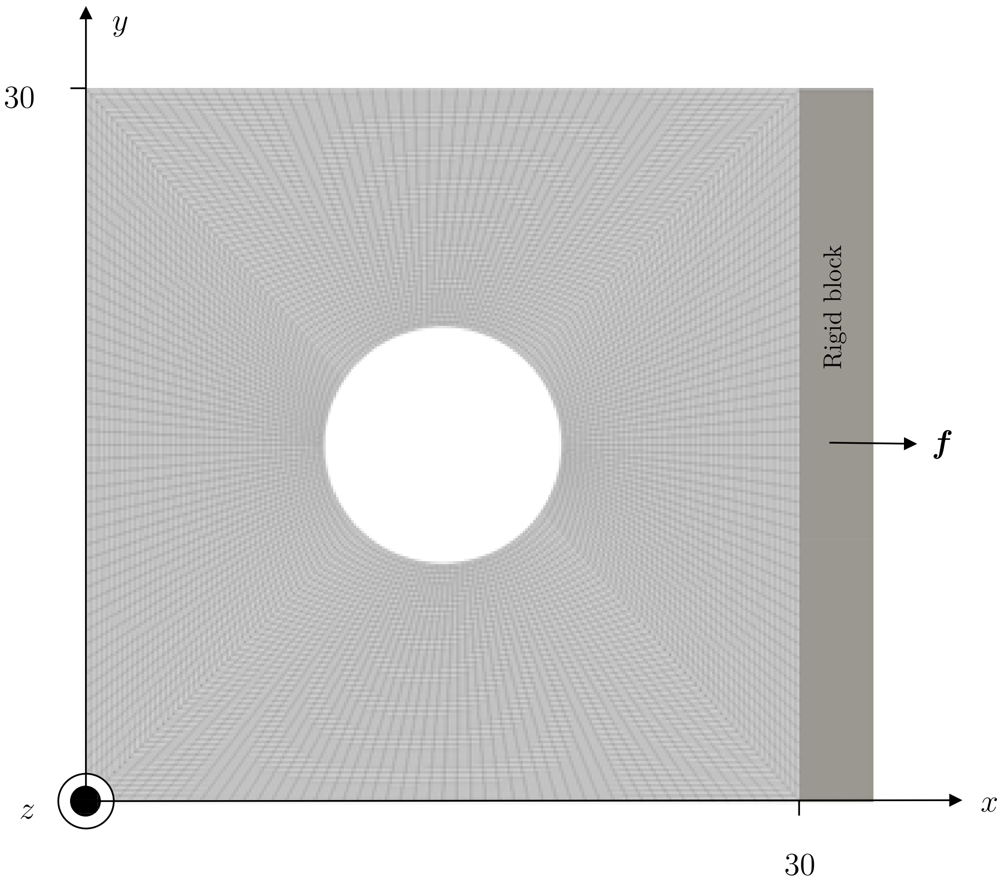

Figure 4.7: *Boundary conditions applied to a three-dimensional plate with a hole at its centre. The plate was fixed in all degrees of freedom at the $x = 0$ surface, while being subjected to a tensile load $\boldsymbol{f}$ at the $x = 30$ face. The load was applied on a rigid block, which was tied to the nodes of the plate at the contact surface.*

Model	Material Parameter	Contribution	Value
Muscle (Ramasamy et al., 2018)	c_1^{m}	Isotropic	2.5×10^{-6} MPa
	c_2^{m}	Isotropic	6×10^{-3} MPa
	c_3^{m}	Anisotropic (passive)	1×10^{-3} MPa
	c_4^{m}	Anisotropic (passive)	6 [-]
	$\sigma_{\mathrm{iso}}^{\mathrm{max}}$	Anisotropic (active)	0.1 MPa
	ΔW_{asc}	Anisotropic (active)	0.15 [-]
	ΔW_{dsc}	Anisotropic (active)	0.16 [-]
	ν_{asc}	Anisotropic (active)	2 [-]
	ν_{dsc}	Anisotropic (active)	4 [-]
	λ_{opt}	Anisotropic (active)	1.3 [-]
	ω^{m}	-	0
	α^{m}	-	0
Skin/Fat (Ramasamy et al., 2018)	c_1^{s}	Isotropic	2.5×10^{-6} MPa
	c_2^{s}	Isotropic	6×10^{-3} MPa
	ω^{s}	-	1
Liner (Łagan & Liber-Kneć, 2018)	c_1^{l}	Isotropic	0.33 MPa
	c_2^{l}	Isotropic	0.01 MPa
Femur (Zhang et al., 2013)	ρ	-	1×10^{-3} g mm^{-3}
	E	-	1.5×10^{4} MPa
	ν	-	0.27
Socket (Zhang et al., 2013)	ρ	-	1×10^{-3} g mm^{-3}
	E	-	1.0×10^{4} MPa
	ν	-	0.30

Table 4.2: *Parameters of the damage-free continuum mechanical model.*

Model	Material Parameter	Value
Continuum damage (Peña, 2014)	$\zeta_{\mathrm{d},\infty}^{\bullet}$, $\zeta_{\mathrm{c},\infty}^{\bullet}$	0.3 [-]
	$\mu^{\bullet}$	1.0 N^{-1} mm^{-1}
	$\eta^{\bullet}$	2.0 N^{-1} mm^{-1}
	$\gamma^{\bullet}$	0.5 N mm
Strain-time cell-death (Gefen et al., 2008)	K	0.131 [-]
	t_0	9.72×10^{6} ms
	$\mathring{\alpha}$	5.83×10^{-8} ms^{-1}
	C	0.439 [-]

Table 4.3: *Parameters of the continuum damage model, and the strain-time cell-death model.*

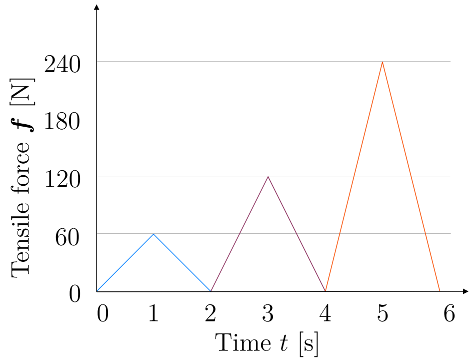

(a) *Neumann boundary condition*

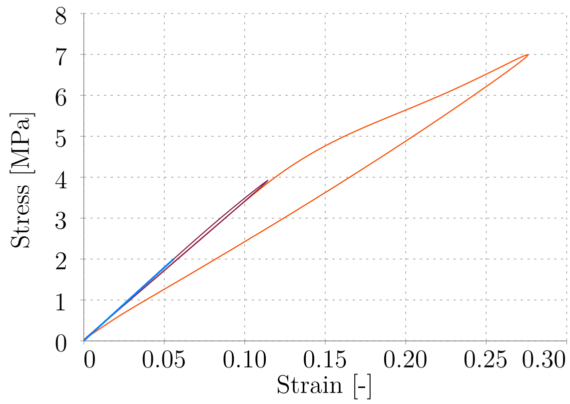

(b) *Stress-strain response*

Figure 4.8: *The force applied on the rigid block (cf. Figure 4.8(a)), and the stress-strain response of an element in the plate adjacent to rigid block (cf. Figure 4.8(b)). In the initial loading cycle, the material exhibits a linear response. In the second, there is negligible softening of the material, while in the third loading cycle, there is significant damage in the material at the zones shown in Figure 4.9.*

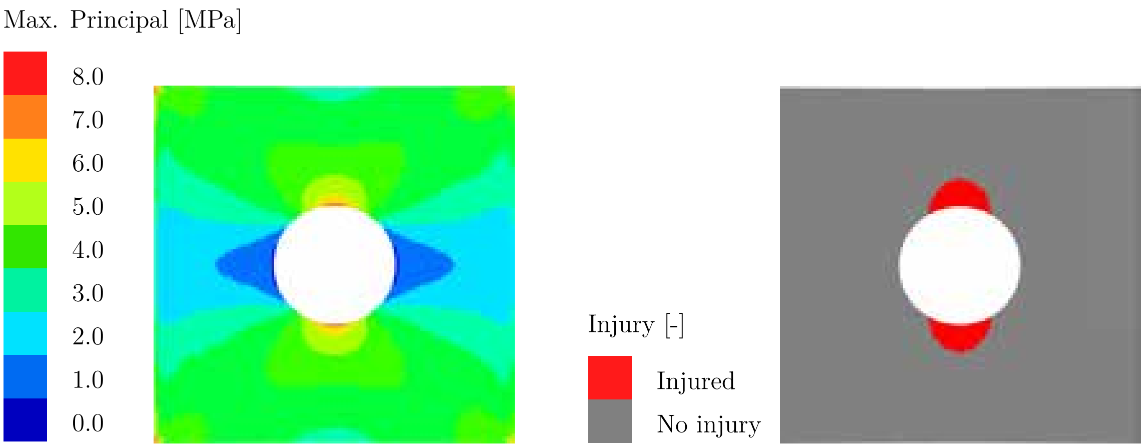

Figure 4.9: *The maximum principal stress and damaged elements at the end of the prescribed cyclic tensile loading (cf. Figure 4.7).*

block on the $x = 30$ face using `tied_nodes_to_surface` contact boundary condition. Neumann boundary conditions, which were applied on the rigid body along the +ve x-axis are shown in Figure 4.8(a), and the resulting stress-strain distribution, in the element located at $(30, 30, 3)$, is plotted in Figure 4.8(b). The stress distribution in the plate and damaged elements, at the end of $t = 6$ s, are shown in red in Figure 4.9.

The bulk and shear moduli of all soft tissues were assumed to be $\kappa = 10$ MPa and $\iota = 0.8$ MPa, respectively. The material parameters for the damage-free continuum mechanical model, and the damage parameters for the strain-time cell-death and continuum damage models are provided in Tables 4.2 and 4.3, respectively.

5 Result: Subject-specific residual limb model

In this chapter, the FE residual limb model, which was obtained as a result of applying the proposed workflow on the DT-MRI scans, is presented. To showcase the necessity and importance of high-fidelity residual limb models, comparisons between the proposed and the state-of-the-art model are required. For this purpose, an additional stump model representing the state-of-the-art model is generated. Since the original socket worn by the subject was probably well-fitting, a volumetrically smaller socket representing a misfitting socket is generated for studying deep tissue injuries. The design of additional models, boundary conditions, and results of the analyses will now be described.

5.1 Quantifying error in fibre tractography

The accuracy of fibre tractography in MedINRIA plays an important role in determining the accuracy of models created using the proposed workflow. In this regard, some fibre tracts were manually generated using the `Fiberfox` module in MITK Diffusion[1] (v2014.10.02, German Cancer Research Center, Heidelberg, Germany). Furthermore, the `Fiberfox` module also generated the diffusion tensor images corresponding to the fibre tracts, with which fibre tractography was performed in MedINRIA. The quality of fibre tractography algorithm in MedINRIA was determined by comparing the orientations of the original and MedINRIA-estimated fibres. For this purpose, 4 types of fibres were modelled in `Fiberfox`: (i) convergent, (ii) fusiform, (iii) bipennate, and (iv) intersecting fibres (cf. Figure 5.1(a)). The `Fiberfox` parameters used to create the fibres, from which diffusion tensor images were generated, are provided in Table 5.1. Strong magnetic fields, number of diffusion gradients, noise, b-values and spatial resolution are known to affect tractography with diffusion tensor images (cf. Hoefnagels et al., 2017, Mukherjee et al., 2008). The influence of the above factors on fibre tractography were determined from tractography studies on the human brain, which is volumetrically smaller compared to the residual limb. Therefore, in order to determine any potential influence of scan volume on fibre tractography, three different volumetric samples $V_{\mathrm{im}} \in \{30 \times 30 \times 30\,\mathrm{px}^3, 40 \times 40 \times 40\,\mathrm{px}^3, 50 \times 50 \times 50\,\mathrm{px}^3\}$ of the above-mentioned fibres were created in `Fiberfox`.

Following fibre tractography with MedINRIA, the accuracy of tracked fibres was determined by calculating the differences in alignment of fibres between the known MITK-fibres and the MedINRIA-estimated fibres. The results are plotted on radial histograms for all three volumetric samples in Figures 5.1(c) to 5.1(e). The mean percentage of MedINRIA-fibres that were perfectly aligned with the MITK-fibres, for each of the 4 fibre

[1] http://www.mitk.org/wiki/DiffusionImaging, accessed on May 24, 2019

	MITK Fiberfox modules	
Parameter	Fibre Definition	Signal Generation
Fibre distribution	Uniform	
Number of fibres	100	
Fibre sampling	1	
Tension	0	
Continuity	0	
Bias	0	
Image dimensions [px]		V_{im}
Image spacing [px]		$3 \times 3 \times 3$
Gradient directions		12
b-value [$\mathrm{s\,mm^{-2}}$]		1000
Signal scale		100
Echo time, TE [ms]		100
Line readout time		1
$\mathrm{T_{inhom}}$ relaxation [ms]		50
Fibre radius		0
Intra-axonal compartment		
$\mathrm{T_2}$-relaxation [ms]		110
d_1 [$\mathrm{mm^2\,s^{-1}}$]		0.001
d_2 [$\mathrm{mm^2\,s^{-1}}$]		2.5×10^{-4}
d_3 [$\mathrm{mm^2\,s^{-1}}$]		2.5×10^{-4}
FA [-]		0.707 107
Extra-axonal compartment		
$\mathrm{T_2}$-relaxation [ms]		80
d [$\mathrm{mm^2\,s^{-1}}$]		0.001

Table 5.1: *Parameters used to generate artificial diffusion tensor images with MITK* `Fiberfox` *module. The fibres were generated in three sample volumes,* $V_{\mathrm{im}} \in \{30 \times 30 \times 30\,\mathrm{px}^3, 40 \times 40 \times 40\,\mathrm{px}^3, 50 \times 50 \times 50\,\mathrm{px}^3\}$

types, are 90%, 95%, 96% and 81%, respectively. The colours in the radial histogram (cf. Figure 5.1(b)) were rendered with 20% transparency in order to show the underlying radial histograms. As a result of overlaying the transparent colours one upon another in the plots, the colours in the plot differ from those in the legend.

5.2 Residual limb-liner-socket model

The duration of the overall modelling process, from segmenting the DT-MRI scans to creating the FE model of the residual limb with tissue anisotropy, was about 20 minutes. The individual parts of the residual limb model obtained as a result of applying the proposed workflow (cf. Chapter 3) to the DT-MRI data are shown in Figure 5.2. In Figure 5.2(a), the geometries of femur and skeletal muscles within the residual limb are shown by suppressing the opacity of the outer skin and the liner. The residual limb and the prosthetic liner worn over it are shown in Figure 5.2(b). The original socket worn by the subject is shown in Figure 5.2(c). The FE mesh consisting of linear Lagrange tetrahedral elements (cf. Section 3.4), is shown in Figure 5.3. In Figure 5.3(a), the FE meshes of femur and skeletal muscles are overlaid with the mesh of the skin/fat layer. The FE meshes of liner and socket are shown in Figures 5.3(b) and 5.3(c), respectively. The femur consists of 5416 elements, the muscles of 35 257 elements, the skin/fat of 97 503 elements, the liner of 51 791 elements, and the socket of 327 865 elements.

The direction of skeletal muscle fibres in the complete residual limb, after correcting for missing and misaligned fibres, is depicted in Figure 5.4(c). In Figures 5.4(a) and 5.4(b), the fibres in *gluteus maximus* before and after correcting the fibre field are illustrated.

5.3 Additional residual limb and socket models

As previously mentioned, two additional models were created for investigating the necessity of the highly detailed residual limb model, and for the analysis of deep tissue injury. The residual limb model seen in literature, which was required for comparison with the proposed detailed limb model, was created by fusing all muscle masks in Simpleware ScanIP. The resulting model, representing the state-of-the-art stump model, will be referred to as the fused-muscle model, while the proposed detailed model will be referred to as the individual-muscle model. An FE mesh of the fused-muscle model was generated using the same mesh parameters, which were employed for generating the FE mesh of the individual-muscle residual limb model. The resulting fused-muscle residual limb model is shown in Figure 5.5(a). In Figure 5.5(b), the fused-muscle model is shown in grey, and is overlaid upon the FE mesh of individual-muscle model. The number of linear Lagrange tetrahedral elements in the fused muscle was 477 989.

In order to understand the effect of donning a misfitting socket on the evolution of deep tissue injury, the original prosthetic socket was isometrically down-scaled by 10%. This scaling factor has no underlying basis, and was randomly chosen. The original and misfitting (scaled) sockets are shown in Figure 5.5(c), where the outer grey-shaded socket is the original socket, the inner meshed socket is the misfitting socket.

The interaction between the various stump and the socket models will be analysed using four case studies, namely (i) the individual-muscle model with original socket (IM-OS), (ii) the fused-muscle model with the original socket (FM-OS), (iii) the individual-muscle model with smaller, misfitting socket (IM-MS), and (iv) the fused-muscle model with the misfitting socket (FM-MS).

In case (i), the IM model will be fitted with the original model of the socket to analyse the soft tissue damage and the state of stress/strain in the stump. This analysis will serve as the baseline against which the effects of a misfitting socket and the current state-of-the-art models will be compared.

In case (ii), the state-of-the-art FM model will be fitted with the original socket model. This analysis serves to highlight the changes in the soft tissue damage and stress/strain state of the tissues in the stump when compared against case (i).

Since it is expected that the original socket optimally fits the stump, soft tissue damage might be negligible. Therefore, in cases (iii) and (iv), the influence of stump models on soft tissue damage were analysed by repeating cases (i) and (ii) with the misfitting socket

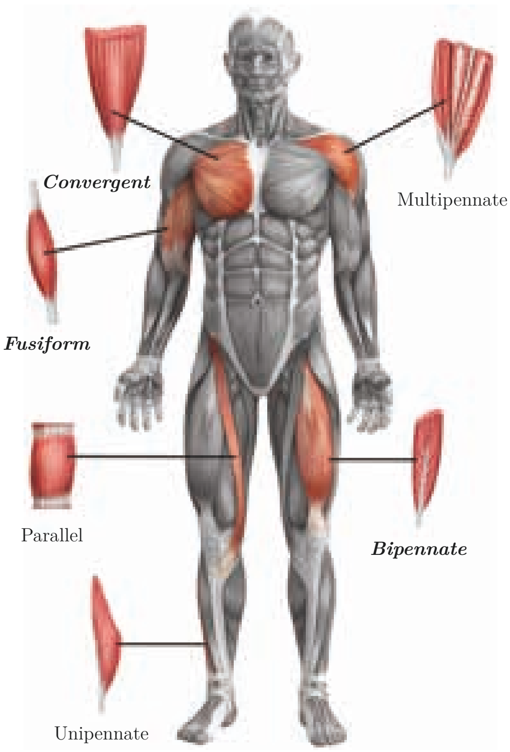

(a) *Types of muscle fibre pennation*

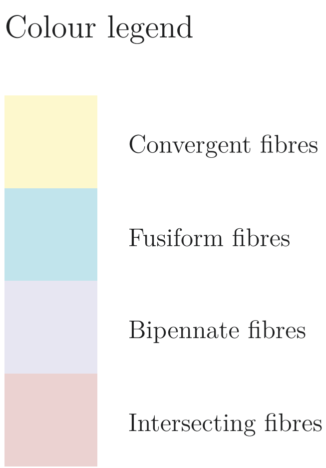

(b) *Legend*

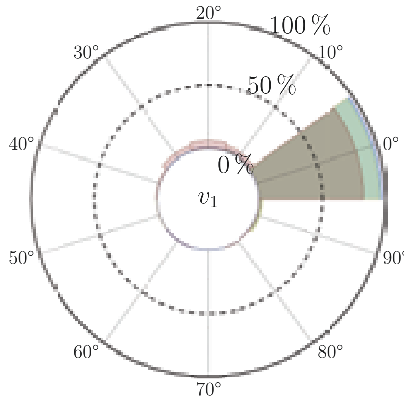

(c) *Volume* $(30 \times 30 \times 30)\,\mathrm{px}^3$

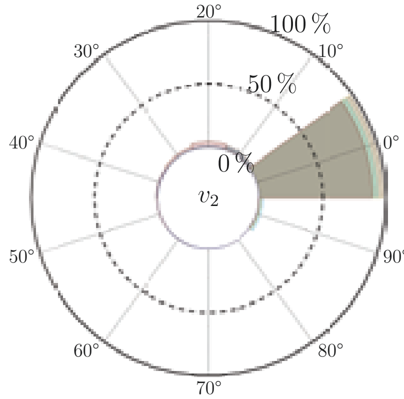

(d) *Volume* $(40 \times 40 \times 40)\,\mathrm{px}^3$

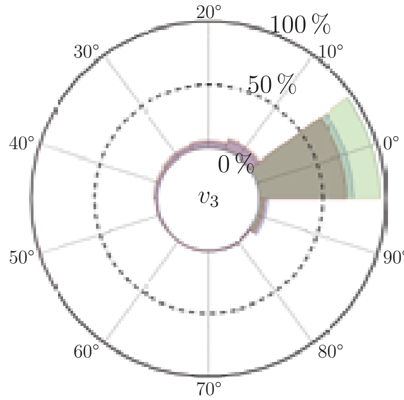

(e) *Volume* $(50 \times 50 \times 50)\,\mathrm{px}^3$

Figure 5.1: *The difference in alignment between MITK-generated fibres, and MedINRIA-tracked fibres are plotted in the radial histograms for different sample volumes* v_1, v_2 *and* v_3*. The colours in the radial plots contain an alpha layer to show the magnitude of errors of different fibre types. As a result of alpha overlays, the colours in the legend do not match those in the plots. Some types of muscle fibre pennations are shown in Figure 5.1(a), which was adapted from Digital illustration of muscular system*[a] *by Nicolas Fernandez ©123rf.com*

[a] https://www.123rf.com/profile_nicolasprimola, accessed on May 24, 2019

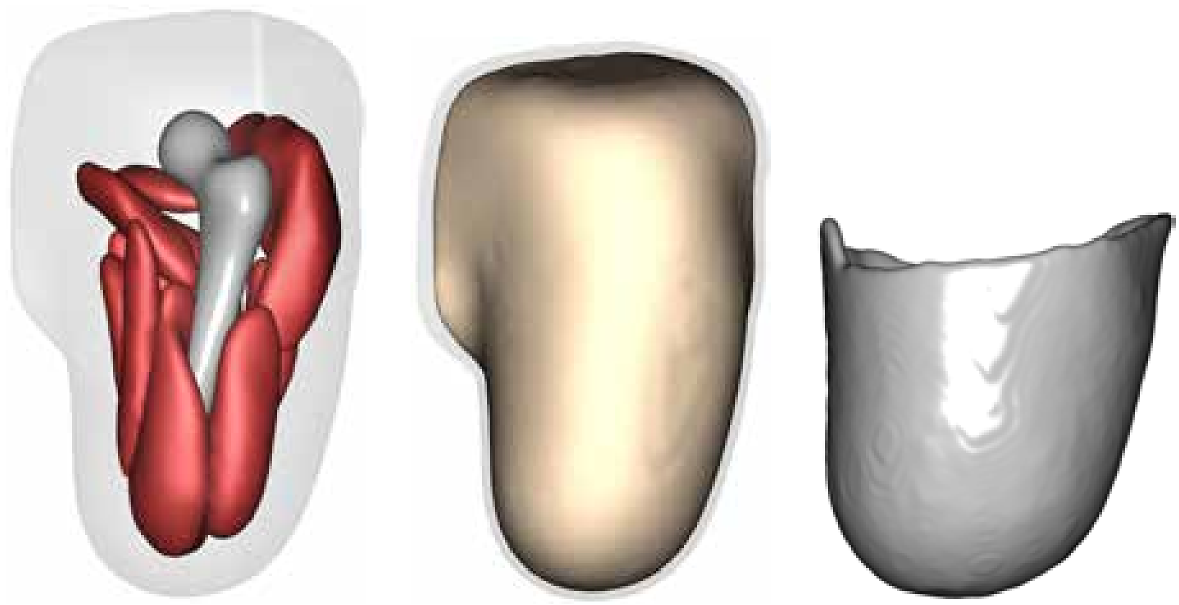

(a) Femur and muscles (b) Skin and translucent liner (c) Prosthetic socket

Figure 5.2: *Residual limb-liner-socket model created with Simpleware ScanIP. The opacity of liner and fat layers have been reduced in Figure 5.2(a) to reveal the underlying bone and muscle geometries. In Figure 5.2(b), the liner worn over skin is shown in light grey, and the model of the original socket worn by the subject is displayed in Figure 5.2(c).*

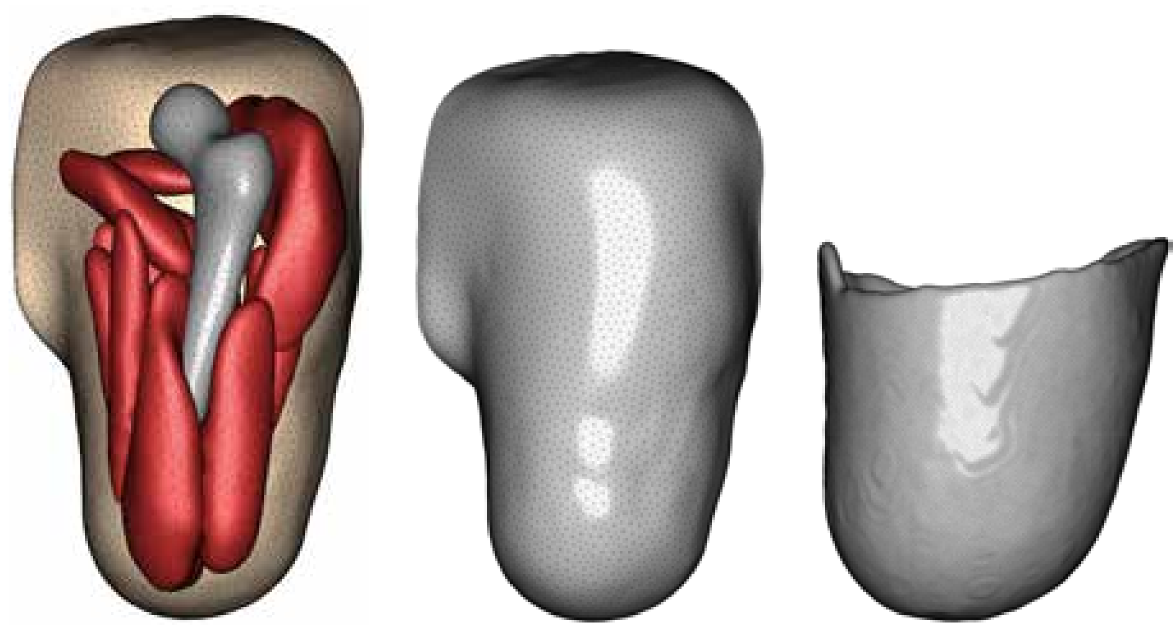

(a) Femur, muscles and skin (b) Liner (c) Socket

Figure 5.3: *The FE mesh of residual limb, liner and socket are presented in Figures 5.3(a) to 5.3(c), respectively. In Figure 5.3(a), the FE mesh of femur and skeletal muscles are overlaid on that of skin.*

(a) *Fibres before correction*

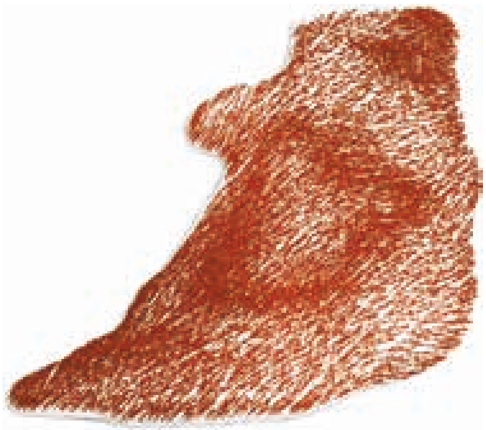

(b) *Fibres after correction*

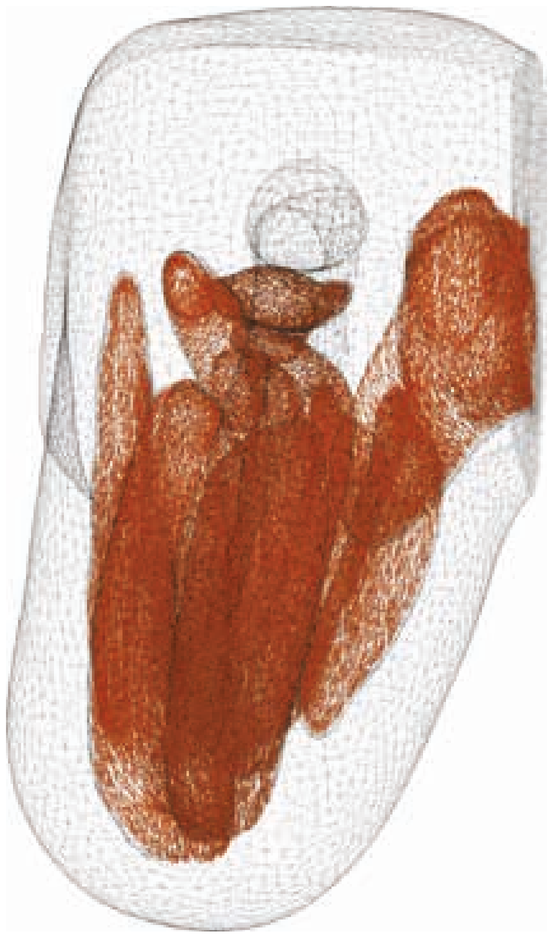

(c) *Corrected fibres in the residual limb.*

Figure 5.4: *Fibres in gluteus maximus, before and after correcting the fibre field, are shown in Figures 5.4(a) and 5.4(b), and the corrected fibre field in the complete residual limb is depicted in Figure 5.4(c).*

model. A detailed description of the above analyses, boundary conditions and results of the analyses are provided in Chapter 7.

5.4 Discussion

The core of the proposed modelling-simulation-analysis workflow is the efficient generation of detailed and accurate patient-specific FE models of residual limbs from DT-MRI scans with minimal human effort. On comparing the MITK- and MedINRIA-generated fibre tracts, there was more than 90 % accuracy in tracking the fusiform, bipennate and convergent fibre types, and the intersecting-type fibres were tracked with 85 % accuracy. This accuracy of MedINRIA's fibre tracking algorithm was considered acceptable, and the residual limb models generated using the workflow were also considered accurate for the purposes of FE analyses.

Model generation was based on the fibres extracted from DT-MRI scans, i.e. the muscle and other soft tissue masks that were imported into Simpleware ScanIP, were

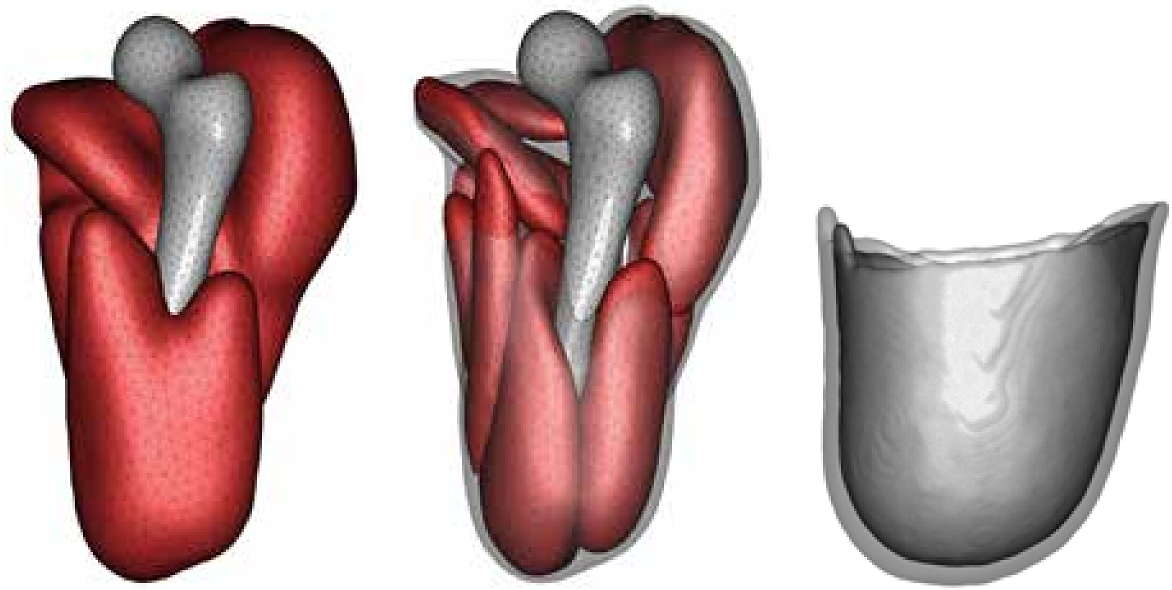

(a) *FE mesh of fused muscles* (b) *FM overlaid on IM* (c) *OS overlaid on MS*

Figure 5.5: *Additional residual limb and socket models created for deep tissue injury analyses, and for analysing the necessity of the individual-muscle residual limb model. The fused-muscle (FM) residual limb model is shown in Figure 5.5(a), which is overlaid on the individual-muscle (IM) model in Figure 5.5(b). The isotropically down-scaled socket (MS) is overlaid on the original socket (OS) in Figure 5.5(c).*

created from the tracked fibres. However, the process of extracting these fibres was done manually, and was therefore subjected to some degree of human-related error. For example, the influence of parameters set in MedINRIA's DTI Track module, in the resulting fibre distribution, and in the muscle masks that were generated, is not known. It is expected that changes in these parameters might affect the volume of muscle masks but not the resulting fibre orientations. Another potential source of error is due to the manual grouping of muscle fibres into bundles in MedINRIA. This can lead to some fibres being simultaneously grouped into two muscle bundles, and therefore result in overlapping muscle masks in Simpleware ScanIP, where the stacking order of these masks plays a vital role in determining the resulting model and FE mesh. In case of overlapping volumes, the masks at the top of the stack overwrite the volume of intersecting masks below them. Hence, different models can result from different mask hierarchies. Moreover, the morphological operations in ScanIP, which are essential to obtain a smooth and kink-free FE mesh, alter the resulting volume and geometry of the residual limb. However, utmost care was taken in performing these morphological operations such that the total normalised volume of the muscle masks did not vary by more than 0.1013 %. In contrast to the proposed approach, Choi & Blemker (2013) proposed to solve a Laplace equation to generate divergence-free vector fields, which represented the muscle fibre architecture. This approach was verified against DT-MRI data by Handsfield et al. (2017). However, in order to use this approach, one must know the muscle geometry beforehand, the regions of muscle insertions to the bone, and must additionally perform fluid simulations. Further, when the geometry of the muscles and their insertions into bones are unknown, such as in amputees, this method cannot be easily applied.

In some cases, despite the muscle masks being generated from the corresponding muscle fibres, not all elements of the FE mesh generated from these masks contained fibre information. This can be attributed to one or more reasons. For example, morphological close operations done in MATLAB, while creating the binary muscle masks, tend to increase the volume of masks (cf. Algorithm 3.1). In this study, the structuring element was a disk of size $t = 5\,\text{px}$. The volumes of the *gluteus maximus* masks, before and after morphological closing operation, were 2075.46 px and 2111.55 px, respectively. Similarly, morphological operations in Simpleware ScanIP, which were primarily performed to smooth the surface of masks, also changed the volume of masks. Another possibility, which might cause some elements to lack muscle fibres might be due to a rather fine finite element mesh. In this case, the total number of tracked fibre points might be lesser than the total number of elements in the FE mesh. As a result, those elements containing lesser than 2 fibre points will not contain any anisotropy information. In addition to missing fibres, sometimes, insufficient fibres points within an element, or rather coarse FE mesh might result in inconsistent fibre directions, in some elements of the mesh. These issues were addressed through the implemented fibre-correction algorithm, which fills in the missing fibre information and also corrects inconsistent fibre orientations within each muscle. However, this correction is done at the cost of smoothing the fibre orientation field over the entire muscle domain, which might, sometimes, lead to over-smoothing. The extent of any such over-smoothing must be verified by comparing the smoothed fibre field with that of the non-smoothed, original fibre field. Human error in manual bundling of muscle fibres can result in the actual geometry of muscles being altered as they are automatically constructed from the fibre fields. This can be witnessed, e.g. in Figure 5.4(a), where a small protrusion can be seen on the left side of *gluteus maximus*. Naturally, the fibres in such regions of a muscle may not match the fibre field in the rest of the muscle volume. A potential scope for improving the fibre-correction algorithm is to ensure that no fibre point appears in two or more muscles, i.e. to ensure the mutual exclusivity of the fibre field. Another possibility is to model the Gaussian kernel size p, which is currently assumed to be constant, as a function of mesh density. The value of p should be inversely proportional to the mesh density, i.e. a dense mesh will have a smaller value of p than a coarse mesh. For the proposed model, these errors are expected to play a very minor role since the majority of muscle fibres in the model tend to have distinct lines of action, where relatively negligible inconsistencies and error in fibre orientations do not contribute to large differences in the direction and magnitude of the generated muscle force.

The fused muscles, which were generated for the sake of comparison with the individual-muscle model, were created by fusing the individual muscle masks that were created with the workflow. This resulted in the state-of-the-art bone-fat-muscle complex similar to that of Portnoy et al. (2008), which did not model muscle anisotropy. Therefore, to be consistent, the fused-muscle model was also created without any fibre information.

Another limitation in modelling the residual limb is the fact that tendons cannot be currently extracted from the DT-MRI images. Tendons are responsible for transferring the forces generated by skeletal muscles to the skeleton, and also play an important role in maintaining pre-stresses in the muscles. However, due to the inherent limitations of the DT-MRI scans, tendons cannot be tracked. To do so, scanners with large magnetic field strength, and extremely high pixel resolution are necessary (cf. Gupta et al., 2010, Karampinos et al., 2012). In Gupta et al. (2010), excised rabbit tendons were tracked using DT-MRI with in-plane pixel resolution of 200 µm, in a 11.74 T scanner. Scanning with such high resolution is not feasible for humans due to the extremely high scan duration. As a result, models created with the proposed workflow lack tendons, and therefore, pre-stresses in muscles, which is not a limitation of the proposed methodology but rather of the current scanner technology. Tendons may, however, be laboriously hand-segmented from T_1- or T_2-weighted MRI scans, and imported into the limb model.

Despite these limitations, having good knowledge in anatomy for grouping the muscle fibres is helpful in resolving most fibre-bundling-related problems in MedINRIA. It remains to be verified in future experiments, if higher resolution DT-MRI scans will mitigate partial volume effects to such an extent that the boundaries between muscle fibres are distinctly visible, leading to easier classification, which result in mutually exclusive fibre bundles. If not, an alternative would be to overlay the muscle masks over T_1- or T_2-weighted MRI scans, and correct the mask boundaries before creating the model. It is common for surgical amputations to result in extensive modifications of the limb musculature, which results in a unique residual limb anatomy in each patient. In such cases, conventional segmentation of the residual limb with MRI or CT scans, with the intention of creating a detailed limb model, is rather difficult. With the proposed technique, the anatomy of this new musculature is evident from its fibre distribution with which individual muscles of the residual limb can be easily modelled. This ease of use of the proposed workflow is obvious, given the relatively short time (about 20 min) that is required to model the highly detailed patient-specific FE mesh of the stump.

With the proposed workflow, a highly detailed residual limb of the subject was created from the DT-MRI scans in a quasi-automated manner. While the workflow was largely automated, minimal human intervention is required to bundle muscle fibres from fibre tractography. With advancements in the field of machine learning, it might be possible to automate this step, provided large training data is available. However, it remains to be seen if such an automation is possible in the case of amputees, where the anatomy of residual limb changes drastically from one amputee to another. The other situation requiring human intervention is in the creation of FE mesh. With enough experience, it might be possible to gauge the mesh parameters from the size of the residual limb, and sizes of individual muscles. Hence, there still exists some scope for the proposed workflow to be completely automated. Since the model generation module is separate from the FE mesh generation and fibre-mapping modules, each module can be independently upgraded and extended.

6 Case study: Muscle activation and liner donning

In Chapter 5, the novel residual limb model with skeletal muscle fibre information, generated using the proposed workflow, was presented. Unlike the state-of-the-art stump models, the availability of skeletal muscle fibre information in the proposed model permits forward simulation of muscle contraction in the stump. The liner, which was modelled in Section 3.4, was extended normally outward from the surface of the stump. But in reality, the liner is worn over the residual limb like a sock, which compresses the soft tissues in the limb. Although donning the liner pre-stresses the soft tissues in the stump, the effect of liner compression has not been researched. Therefore, the second case study was to examine the stresses on the liner and on the skin surface following a realistic, dynamic liner donning simulation. In this chapter, the effect of pre-stresses introduced by donning a prosthetic liner, and the necessity of muscle fibres in stump models are demonstrated with FE simulations.

All FE simulations, in this and in the following chapters, were performed with double precision, shared memory parallel (SMP) LS-DYNA (R7.1.2, revision 95028) executable, which was compiled with the user material model developed in Chapter 4. All analyses were solved using the implicit David-Fletcher-Powell (DFP) quasi-Newton non-linear iterative solver on a Linux workstation having 16 physical cores (2x Intel Xeon(R) CPU E5-2687W, 3.10 GHz) and 96 GB DDR3-1600 RAM.

6.1 Muscle activation

Locomotion occurs due to contraction of skeletal muscles. A distinctive feature of the proposed residual limb model is the fibre-enhanced skeletal muscles with which muscle contraction can be simulated by providing activation signals $0 \leq \alpha \leq 1$ (cf. Section 4.5). In this study, the displacement of femur due to the contraction of *gluteus maximus* is investigated. For this study, the pelvis, femur and *gluteus maximus* were modelled (see Figure 6.1). Since the pelvis was not available from the medical scans, a generic CAD model of the pelvis was obtained from GrabCAD[1], and was scaled to accommodate the femoral head at the acetabulum. Based on recommendations from the International Society of Biomechanics (ISB), joint coordinate systems were defined on the femoral head and acetabulum, which were then aligned to form the hip joint (cf. Wu et al., 2002). In skeletal muscles, active and passive stresses are generated along their fibre directions. Therefore, to understand the importance of obtaining correct muscle fibre directions, three additional models of the *gluteus maximus* were generated in which the fibre orientation was (i) randomised, (ii) rotated 20°, and (iii) rotated 40° about the craniocaudal axis.

[1] https://grabcad.com/library/human-pelvis-bone-1, accessed on May 24, 2019

Material Parameter	Contribution	New Value
c_1	Isotropic	4.5 MPa
c_2	Isotropic	2.0 MPa
c_3	Anisotropic	2.0 MPa
c_4	Anisotropic	20.0 MPa
κ	Bulk modulus	50 MPa
ι	Shear modulus	2.0 MPa

Table 6.1: *Altered soft tissue material parameters for the analysis of muscle activation (cf. Table 4.2).*

Muscle activation simulations were performed with the 3 models to study the effect of changes in muscle fibre orientation on the displacement of femur.

6.1.1 Boundary conditions

The *gluteus maximus*, which was modelled with the proposed workflow, did not extend until the femur. Therefore, using Simpleware ScanIP, the *gluteus maximus* was artificially extended to butt against the femur, and was meshed using the Simpleware FE module with the same mesh parameters defined in Section 3.4. No contacts were defined in Simpleware ScanIP, which resulted in common nodes between the femur and *gluteus maximus*. The model consisted of 22 024 linear Lagrange tetrahedral elements in femur, and 36 573 linear Lagrange tetrahedral elements in the *gluteus maximus*. The pelvis was meshed with 163 961 mixed linear Lagrange quadrilateral and triangular shell elements. The pelvis was rigidly fixed in all degrees of freedom, and a spherical joint was defined between the femoral head and acetabulum of the pelvis in LS-DYNA. Muscle contraction was simulated over a period of $t = 10\,\mathrm{s}$. This was achieved by linearly increasing the activation parameter α from 0 to 1 in $t = 3\,\mathrm{s}$, and holding it constant until the end of the simulation.

6.1.2 Material parameter

Material parameters of the skeletal muscles, which are listed in Table 4.2, were obtained from existing literature. These material parameters were soft, leading to numerical convergence problems. For this reason, the passive material parameters (c_1, c_2, c_3, c_4) governing the deformation of soft tissues (both muscle and fat), were stiffened. Further, the bulk and shear moduli were also stiffened, and the new values are listed in Table 6.1. The pelvis was modelled with the same material as that of femur, and the material parameters for *gluteus maximus* were the same as those listed in Table 4.2, updated with the passive material parameters listed in Table 6.1.

6.1.3 Results

The results of activating the *gluteus maximus*, with original fibre orientation, are shown in Figure 6.1. In Figure 6.1(a), both the initial and final positions of the femur are

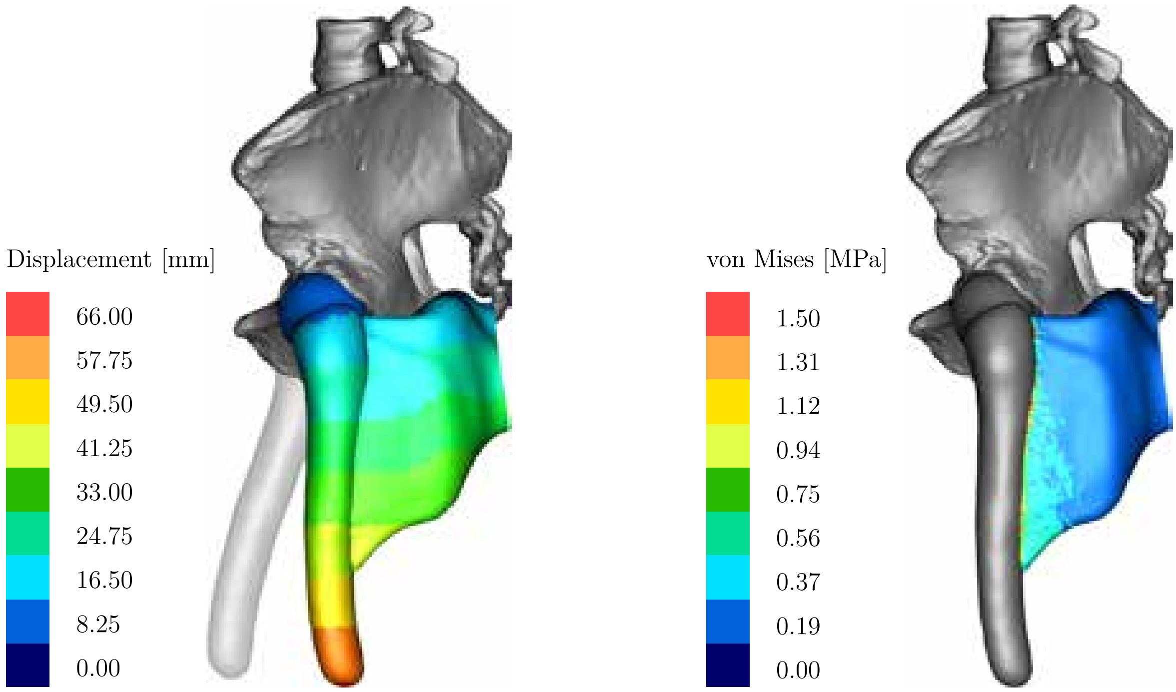

(a) *Displacement of femur and gluteus.* (b) *Stresses in gluteus maximus*

Figure 6.1: *Displacement of the femur and stresses produced in gluteus maximus upon its activation are shown in Figures 6.1(a) and 6.1(b), respectively. Displacement of the femur in Figure 6.1(a) is overlaid upon the initial state of the femur at $t = 0\,\mathrm{s}$.*

shown. The maximum in-plane (sagittal) displacement of the femur was 66 mm, and the maximum von Mises stress in the *gluteus maximus* at this state was 3.25 MPa at the femur-muscle interface. The stress fringe is capped at 1.5 MPa for better illustrating the stress distribution.

The effect of changes in fibre orientation on the resulting displacement of femur was analysed by activating the additional 3 models of *gluteus maximus* under the same boundary conditions (see Section 6.1.1). The displacement of the distal end of the femur in the original muscle-femur complex, and in the additional 3 cases, is plotted in Figure 6.2. It is observed that while the original muscle fibres produced 66 mm displacement at the distal tip of the femur, changes of 20° and 40° in the orientation of the fibres resulted in 60.02 mm and 20.02 mm displacement at the distal tip of the femur, respectively. Randomly oriented muscle fibres resulted in negligible displacement (0.93 mm) of the femur.

6.2 Liner donning

Prosthetic liners play an important role in maintaining the vacuum that attaches the prosthetic socket to the residual limb, in managing the stump volume, and in shielding the limb from high shear forces at the limb-socket interface (cf. Gholizadeh et al., 2016). Thickness and material of the liner play an important role in minimising the stresses at the stump-socket interface, and thereby maximising comfort (cf. Cagle et al., 2017). In this case study, an FE analysis of dynamic prosthetic liner donning was performed, from

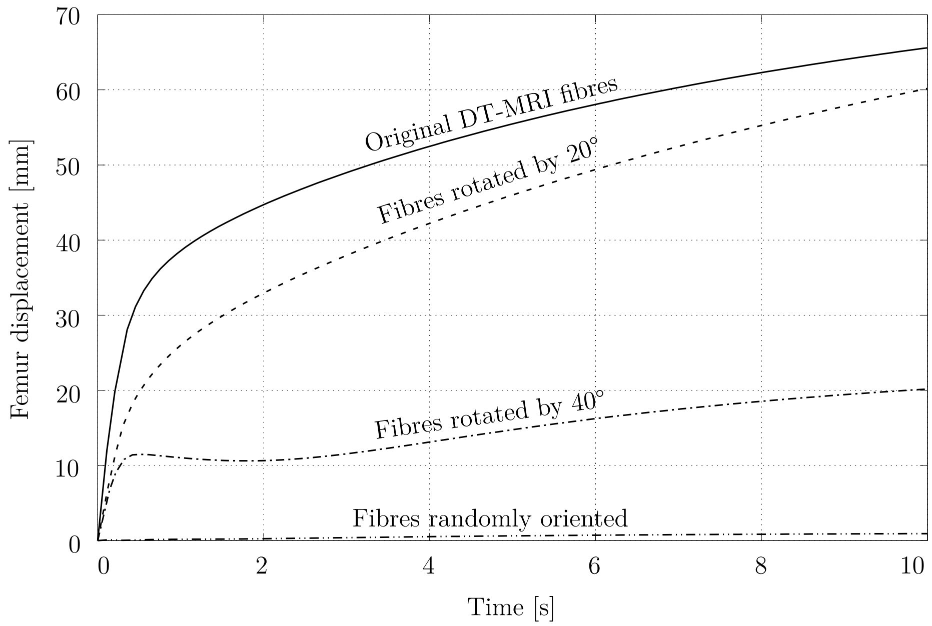

Figure 6.2: *Displacement of the distal tip of femur for the original fibre orientation in gluteus maximus, and for the 3 cases, where the muscle fibres were (i) randomised, (ii) rotated by* 20°, *and (iii) rotated by* 40° *about the craniocaudal axis.*

which post-donning stresses on the liner, and strains on the stump, were obtained.

The prosthetic liner model was generated in SolidWorks (v.2015, Dassault Systèmes) by revolving the cross section of the liner about its central axis (cf. Figure 6.3(a)). The mid surface of the solid liner was extracted and meshed with 50 692 linear Lagrange triangular shell elements using ANSA Pre-Processor (v17.1.4, BETA CAE Systems, Thessaloniki, Greece). The liner was assumed to have a uniform cross section of thickness 3 mm, i.e. all shell elements were modelled with uniform thickness of 3 mm as fully integrated shell elements (`ELFORM` 16) in LS-DYNA.

6.2.1 Boundary conditions

The prosthetic liner was aligned with the residual limb such that the revolute axis of the liner coincided with the anatomical axis of the femur. In the initial state, the liner was positioned such that the distance between its proximal flat surface and distal tip of the residual limb was 5.46 mm (see Figure 6.3(b)). A local coordinate system $(\boldsymbol{x}', \boldsymbol{y}', \boldsymbol{z}')$ was defined for the limb-liner complex with its origin at the centroid of liner nodes. Here, $\boldsymbol{z}'$ was the anatomical axis of the femur, and the local x- and y-axes was any pair of orthogonal axes normal to $\boldsymbol{z}'$. Translation and rotation of the liner nodes along the distal open end of the liner were constrained in and about $\boldsymbol{z}'$. The residual limb was permitted to translate only along $\boldsymbol{z}'$, while translation in the other 5 degrees of freedom were constrained. Dirichlet boundary conditions were prescribed to the femur along $\boldsymbol{z}'$ such that in $t = 5$ s, the femur translated by $|\boldsymbol{d}| = 240$ mm. Contact between the liner and residual limb was assumed to be frictionless, and was modelled with the `automatic_single_surface_mortar` contact card in LS-DYNA. The material parameters of the stump used in the liner-donning simulation were identical to those used in the muscle activation studies. The material parameters of the liner are listed in Table 4.2.

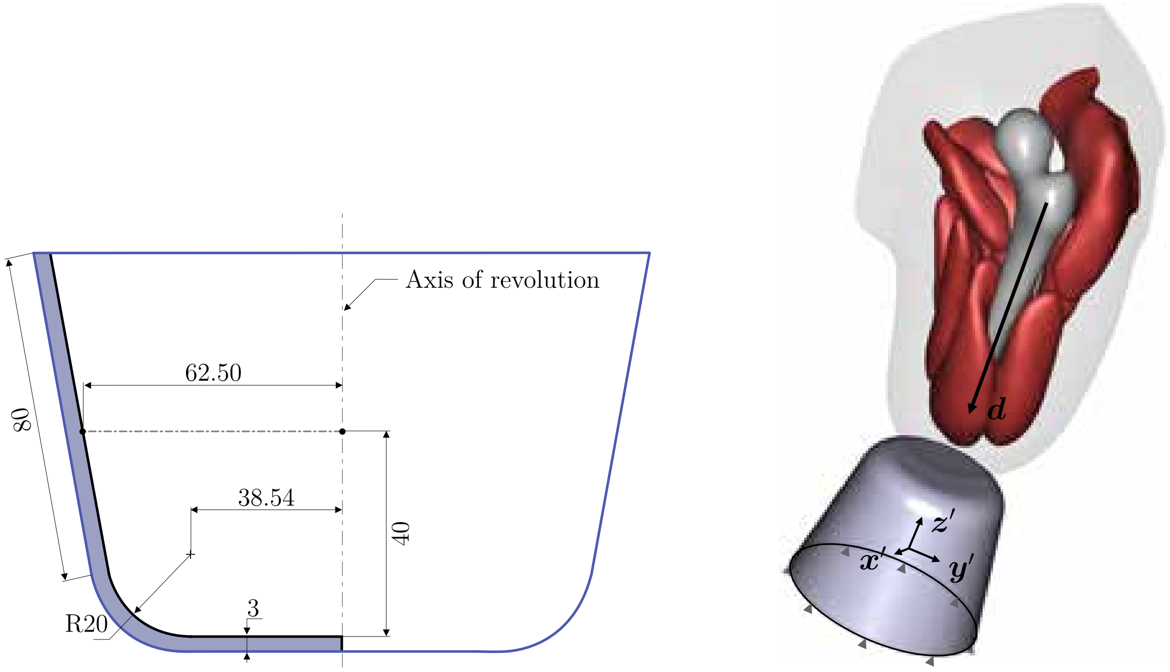

(a) *Cross section of liner (all dimensions in* mm*).* (b) *BC for FE analysis*

Figure 6.3: *The cross section and complete model of the liner are illustrated in Figure 6.3(a). In Figure 6.3(b), the boundary conditions (BC) applied on the liner and residual limb are shown. The distal free end of the liner, whose translation and rotation about the z' axis was constrained, is illustrated with small triangles.*

6.2.2 Results

The stresses developed in the liner, as a result of applying the boundary conditions described in Section 6.2.1, are shown in Figure 6.4. The maximum von Mises stress in the liner was 3.78 MPa. The von Mises stress legend is capped at 2.0 MPa to better illustrate the stress distribution. The compressive strains developed on the surface of the skin and in the skeletal muscles are shown in Figure 6.5. The fringes in Figure 6.5 were capped at 0.7 % and 5 % for illustrating the strains on the skin and in the muscles, respectively. The dynamic liner donning simulation resulted in 0.4 % volume-normalised compressive strain, where the volume-normalised strain $\tilde{\varepsilon}$ is computed as

$$\tilde{\varepsilon} = \frac{1}{V}\sum_{e=1}^{N_e} \varepsilon_e v_e. \tag{6.1}$$

Here, V is the total volume of the body, N_e is the number of elements in the body, and ε_e is the compressive strain in the e^{th} element of the body. Maximum compressive strain of 0.816 % corresponding to a von Mises stress of 317.91 kPa was observed on the surface of the residual limb. Further, maximum strain of 11.64 % corresponding to a von Mises stress of 3.32 MPa was witnessed in the deep tissues.

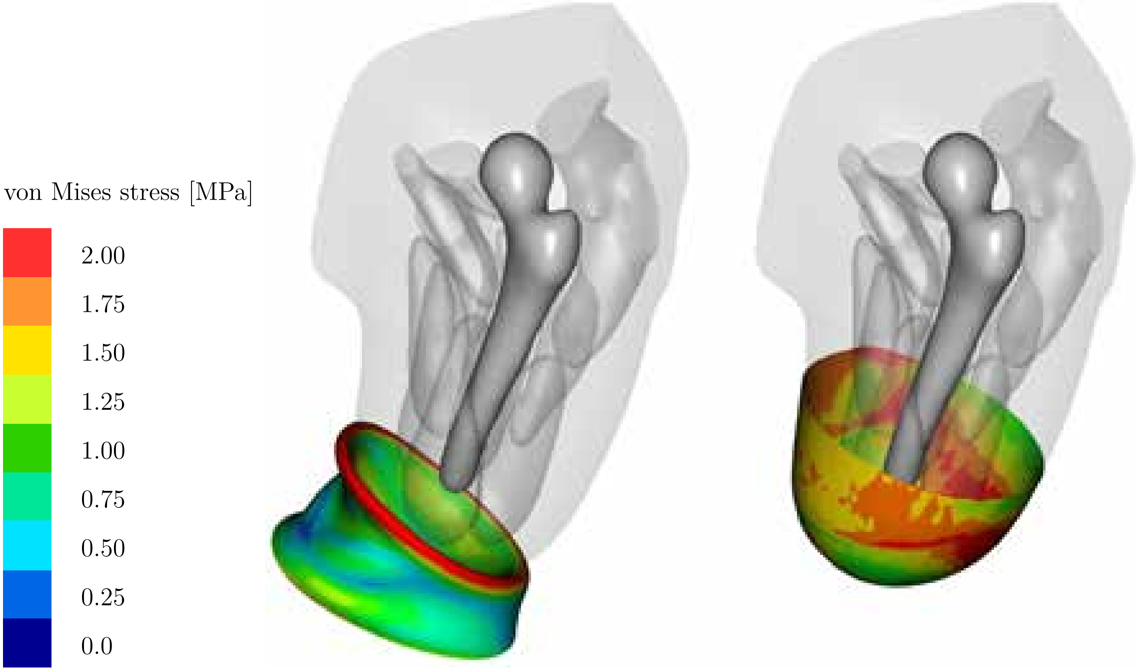

Figure 6.4: *The von Mises stresses developed in the liner during an intermediate state ($t = 2.42\,\mathrm{s}$), and at the final donned state ($t = 5\,\mathrm{s}$).*

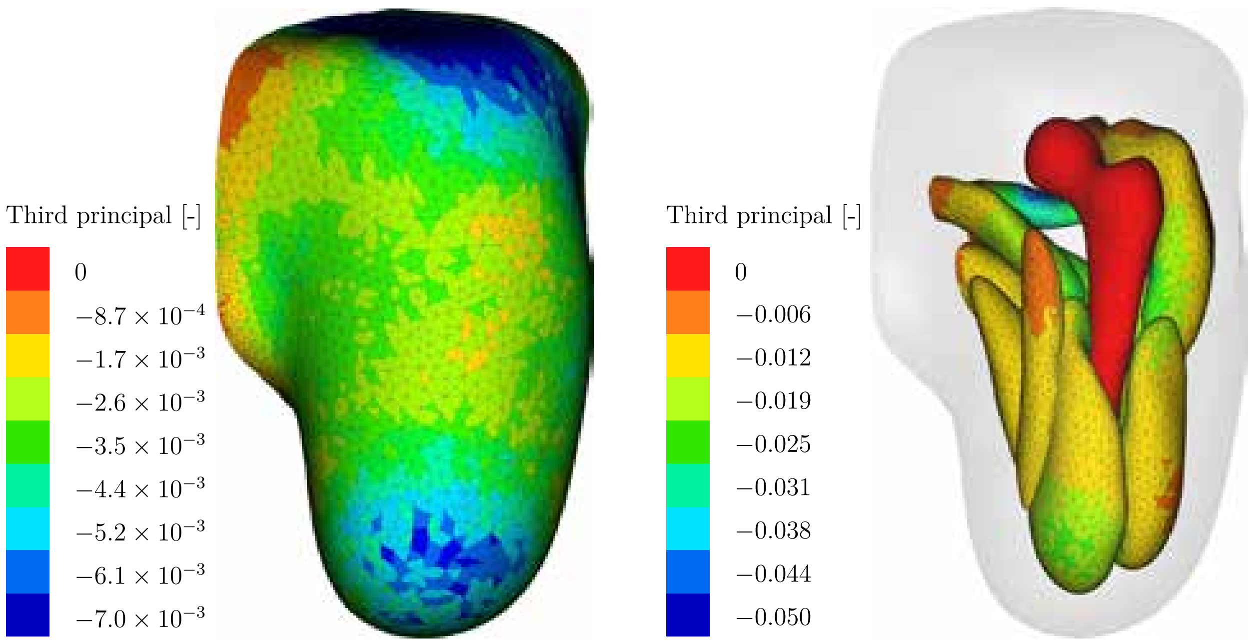

(a) *Strains on skin surface* (b) *Strains in skeletal muscle*

Figure 6.5: *Third principal strains on the surface of the skin, and in the skeletal muscles at the end of liner donning simulation ($t = 5\,\mathrm{s}$).*

6.3 Discussion

Skeletal muscle fibres play an important role in determining the movement of the skeletal structure to which they are attached. This was illustrated in a case study, where the fibres of *gluteus maximus* were rotated by 20° and 40° about the caudocranial axis. Upon activation, the displacement of femur in the sagittal plane decreased by 9.06 % and 69.67 %, respectively, when compared to the activation of *gluteus maximus* containing the original DT-MRI fibres. This is because the fibres of the *gluteus maximus* arise from the posterior gluteal line of the inner upper ilium, and a large portion of it inserts into the iliotibial band of the fascia lata, i.e. in an obliquely downward and lateral direction. In the sagittal plane, these fibres are oriented along the anteroposterior direction, but a rotation about the craniocaudal axis aligns them at an angle to this plane, which results in the observed decreased displacement of the femur. Skeletal muscle fibres are not only useful for forward simulations, but also play an important role in generating passive stress in muscles due to stretch. Therefore, the inclusion or exclusion of muscle fibres will significantly influence the overall stress generated in skeletal muscles.

The liner is primarily subjected to bending loads during the donning process, making shell elements the ideal choice to model the liner. However, as mentioned in the beginning of this chapter and in Section 3.4, the liner was modelled as an extension of the skin with solid elements. The reason for choosing solid elements over shells is that the liner is sandwiched between the socket and stump, and is subjected to high compressive and shear forces in the socket-donned state. Under such high compressive forces, the liner modelled with shell elements underwent excessive penetration and an eventual loss of contact with the skin and socket. In this case study, a realistic liner donning simulation was presented to illustrate the ability of the model to predict both the surface and deep tissue compressive stresses/strains exerted by the liner on the residual limb.

The use of realistic constitutive laws is, as in any other subject-specific computational model, both a challenge and a source of error. Here, the damage-free soft tissue parameters of the continuum-mechanical model were adapted from Röhrle et al. (2017), where the skeletal muscle parameters were optimised for healthy upper limb muscles. However, unlike healthy muscles, amputated muscles are incapable of generating normal muscular force. The primary reasons for the reduced capacity to generate normal muscular force are the reduced physiological cross-sectional area and altered insertion points of transected muscles, among other factors. Therefore, the soft tissue parameters of the stump were adapted from the healthy parameter set by simply weakening them (see Ramasamy et al. (2018)). The correctness of such a set is not guaranteed, especially when dealing with subject-specific models. Extensive experimental methods, which currently are active topics of research (cf. Sengeh et al., 2016), are required to accurately determine the correct parameter set for the stump.

The muscle activations chosen for simulating the contraction of *gluteus maximus* were not obtained from sEMG experiments, and therefore, were not physiologically-motivated. Obtaining sEMG recordings in amputees is rather difficult due to socket-stump environment, which does not permit easy placement of EMG sensors. The EMG sensors are sensitive to external pressure, which might lead to spurious recordings, and difficulty in filtering the EMG signals. In such cases, EMG signals can be simulated by solving extracellular bidomain equations (see Mordhorst et al. (2017)). The simulated EMG signals can be used to study the effect of skeletal muscle activations, both with the proposed model and with multiscale continuum-mechanical models (see Fernandez et al. (2016)). To date, skeletal muscle activations are widely studied using multibody simulations with 1D muscle models. Unlike 1D Hill-type muscle models, 3D continuum-mechanical models are capable of capturing the complex lines of action of the generated muscle forces. For example, Röhrle & Pullan (2007) compared the forces predicted by a 1D model of a human *masseter* with its 3D continuum-mechanical model to show that the forces predicted by the 1D model was error-prone. Another example that illustrates the superiority of fibre-enhanced 3D models over 1D models is that of the human tongue. The human tongue is highly dextrous owing to a complex interlaced fibre distribution (see Wang et al. (2013)). The physiological retraction modes of the tongue can be easily modelled by accounting for its fibre distribution, which might be complicated to represent using 1D models.

The material parameters listed in Table 4.2 were soft for the muscle activation studies. Using these parameters resulted in non-physiological deformation of the soft tissues and stability problems in the FE simulations. Such stability problems are commonly encountered when modelling biological tissues. Material parameter identification of biological tissues, which do not cause stability problems in FE simulations, is tricky. For example, in order to mitigate convergence problems, Sprenger (2015) increased the Mooney-Rivlin parameter c_1 100-fold despite fitting the Mooney-Rivlin parameters from experiments. Hendriks et al. (2006) used suction experiments to characterise the mechanical behaviour of skin but large differences in the fitted parameters of skin layers caused convergence problems in their FE simulations. Iivarinen et al. (2013) estimated the elastic moduli of human skin tissue from suction experiments to be in the range 948 to 1364 kPa, but also acknowledged that the range of Young's modulus in other literature data varied from 0.008 to 540 MPa. From the sensitivity study of the passive material parameters, i.e. c_1, c_1, c_3 and c_4, it was seen that the parameters c_1 and c_2 played an important role in compression and shear, while c_3 and c_4 played a significant role in tension. Since all the above modes of deformation are expected during muscle activation and dynamic interaction of the soft tissues with the socket, and because tissue experiments were outside the scope of this study, these material parameters were stiffened with the motive to improve the stability and convergence of the FE simulations during dynamic gait analysis.

7 Case study: Bipedal stance

The deformed state of soft tissues in the stump as a result of applying bipedal stance boundary conditions on the residual limb is widely studied by many researchers. By performing a similar bipedal stance analysis with the detailed residual limb model under similar boundary conditions, it might be possible to compare the stresses obtained from this model with those reported in the literature. A reliable comparison between the detailed and state-of-the-art models is only possible when both models are subjected to identical boundary conditions. For this reason, the state-of-the-art residual limb model, which was modelled in Section 5.3 with fused-muscles, and the individual-muscle model were analysed with the same boundary conditions. In addition to the analysis of stresses, the evolution of deep tissue injury during bipedal stance with both original and misfitting sockets was also analysed.

7.1 Transfemoral prosthesis

A 4-bar polycentric transfemoral knee joint, along with the rest of the prosthesis, namely pylon, socket adaptor and foot was obtained from GrabCAD[1], and attached to the prosthetic socket (see Figure 7.1). Figure 7.1 shows the complete transfemoral prosthesis on the left, and a close-up view of the knee joint on the right. The knee joint complex is composed of four links, which are constrained by four joints (illustrated as red crosses in Figure 7.1) that allow the knee joint complex to only flex and extend in the sagittal plane. Revolute joint constraints were defined at Joints 2 and 4, between Links A and B, and B and D, respectively. With these joint constraints, the resulting knee complex behaves like a double pendulum. By defining spherical joint constraints at Joints 1 and 3, Link C constrains the relative motion between Links A and D, resulting in the desired knee complex with one degree of freedom. Further details on joint dynamics in LS-DYNA is available in the LS-DYNA theory manual (cf. Hallquist, 2006).

The knee joint was locked for the analysis of bipedal stance, i.e. there was no relative motion between the four bars of the knee mechanism. All parts of the prosthesis and the femur were modelled as rigid bodies. Beginning with the foot upwards, each component of the prosthesis was rigidly constrained to the body above it, i.e. the foot was constrained to the pylon, the pylon to knee joint, and the knee joint to prosthetic socket. As a result, the complete prosthesis behaved as a single rigid body. These constraints were defined using the `constrained_rigid_bodies` card in LS-DYNA.

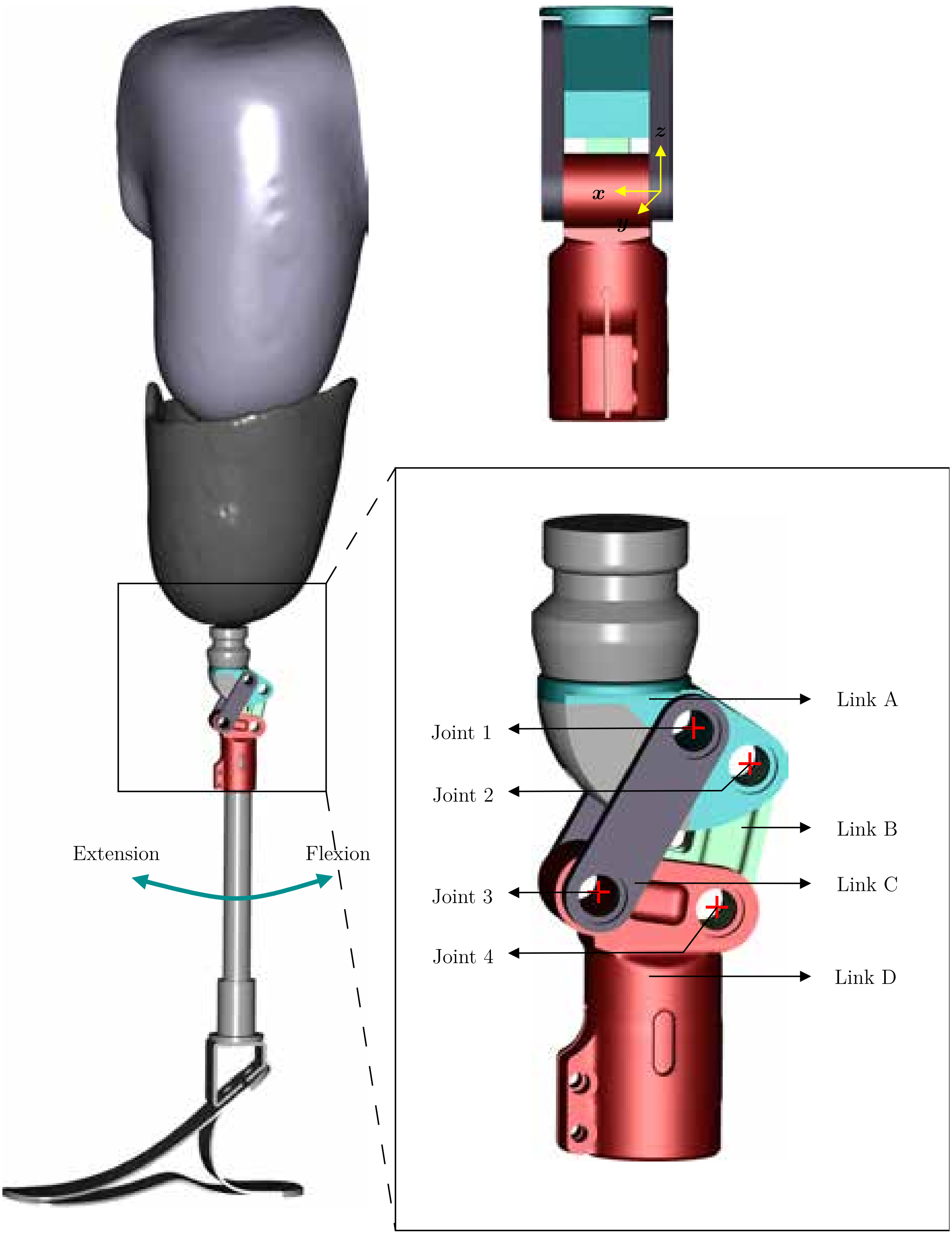

Figure 7.1: *Four-bar polycentric knee joint mechanism used in the transfemoral prosthesis.*

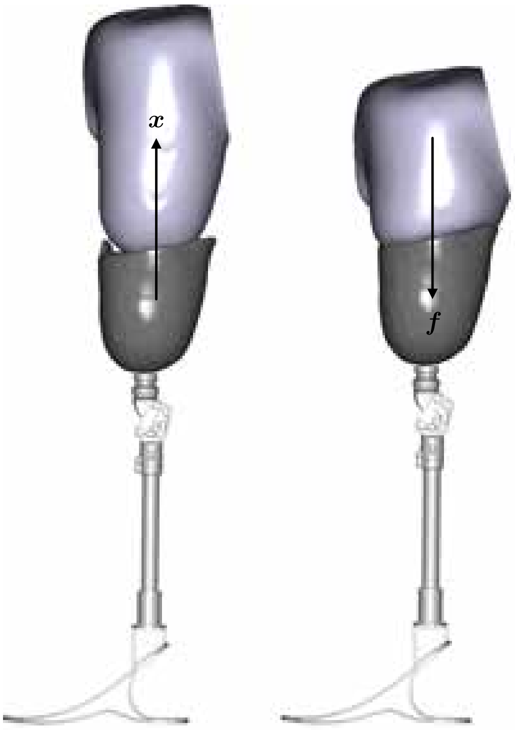

(a) *Illustration of BC for bipedal stance*

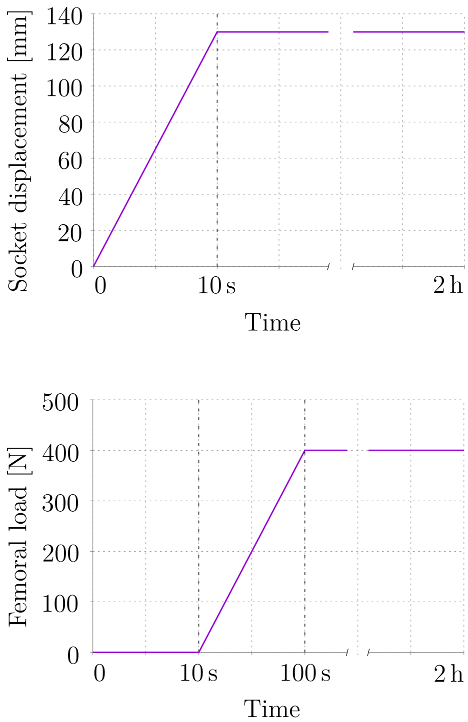

(b) *BC on socket and femur.*

Figure 7.2: *Boundary conditions (BC) on socket and femur during the two stages of bipedal stance simulation. In the first stage, the socket along with the prosthesis was translated by* $|\boldsymbol{x}| = 130\,\text{mm}$ *in* $10\,\text{s}$*, which simulated socket donning. During this period, i.e.* $0 \leq t \leq 10\,\text{s}$*, the femur was constrained in all degrees of freedom (DoF). In the second stage, the socket was constrained in all DoF, while femoral load was ramped from* $0\,\text{N}$ *to* $400\,\text{N}$ *between* $10\,\text{s}$ *and* $100\,\text{s}$*, and held constant thereafter until the end of the simulation, i.e.* $2\,\text{h}$*.*

7.2 Boundary conditions

In the initial state, the socket and residual limb-liner complex were separated by a distance of $|\boldsymbol{x}| = 130\,\text{mm}$ along the craniocaudal direction (see Figure 7.2(a)). The femur was constrained in all degrees of freedom (DoF), and the displacement of the socket was restricted to the craniocaudal direction (1 DoF). A frictionless surface-to-surface mortar contact was defined between the outer surface of the liner and inner surface of the socket. The dynamic FE analysis of bipedal stance was performed in two stages: (i) socket donning, and (ii) femoral load over a period of $2\,\text{h}$.

During the first stage ($0 \leq t \leq 10\,\text{s}$), the socket was translated toward the residual limb by $|\boldsymbol{x}| = 130\,\text{mm}$, while the femur remained stationary. In the second stage ($10\,\text{s} < t \leq 2\,\text{h}$), the boundary conditions were modified such that the spatial position of the socket (in the donned state) was fixed, and the displacement of femur along the craniocaudal axis was permitted. A femoral load of $|\boldsymbol{f}| = 400\,\text{N}$, which is approximately half the subject's body weight, was linearly ramped during $10 < t \leq 100\,\text{s}$, and held constant for $2\,\text{h}$ (see Figure 7.2(b)) (cf. Gefen et al., 2008). This duration ($2\,\text{h}$) was selected to be long enough to study strain-time dependent cell death. A birth-death switch was used to shift from

[1] https://grabcad.com/library/prosthetic-leg-6

Dirichlet to Neumann boundary condition between the two stages.

7.3 Mesh convergence

Before performing the bipedal stance analysis, a mesh convergence study, with the experimental setup described in Section 7.2, was performed. Seven stump models with varying mesh densities were obtained by adjusting the mesh coarseness slider between −35 and −5 in the Simpleware FE module. The selection criteria was based on convergence of volume-normalised stresses in the residuum, with which the optimal mesh was selected. The volume-normalised stress $\tilde{\boldsymbol{\sigma}}$ is computed by

$$\tilde{\boldsymbol{\sigma}} = \frac{1}{V}\sum_{e=1}^{N_e} \boldsymbol{\sigma}_e^{\mathrm{VM}} v_e, \tag{7.1}$$

where $\boldsymbol{\sigma}_e^{\mathrm{VM}} = \sqrt{3/2}\ \boldsymbol{\sigma}_{\mathrm{ich}}$ is the von Mises stress in an element of volume v_e, and $\boldsymbol{\sigma}_{\mathrm{ich}} = \boldsymbol{\sigma} - 1/3(\mathrm{tr}\,(\boldsymbol{\sigma})) - \mathbf{I}$ is the isochoric Cauchy stress tensor (cf. Section 4.1.2). The total volume of the residual limb is V, and N_e is the total number of elements in the residuum. The mesh convergence plot and the mesh densities of the residual limb model are shown in Figure 7.3. From the figure, it is evident that the normalised stress is decreasing with increasing mesh density, in a negligible fashion, i.e. by less than 1.5 %. As a result, the FE model created with the coarseness factor of −35, resulting in a mesh with 517 832 elements, was chosen for this study.

7.4 Sensitivity study

Sensitivities of the passive material parameters (c_1, c_2, c_3, c_4) were studied on a unit cube subjected to 1 % uniaxial tensile and compressive strains, and 5.7° simple shear. A sequential optimisation metamodel was designed in LS-OPT (v5.1, LSTC, Livermore, California) with 50 000 global sensitivity points. Table 7.1 lists the initial and range of parameter values chosen for the sensitivity study. A radial basis function network with a space-filling model was chosen to discretise the design space, and the number of simulation points was set to 90. A metamodel was created by collating the tension, compression and shear stages. Default termination conditions were used, and the response of the metamodel was studied for the applied boundary conditions. Figure 7.4 shows the sensitivities of passive parameters in tension, compression and shear. The parameters c_1 and c_2 is seen to have a large influence on the resulting stresses in compression and shear, while c_3 and c_4 highly influence the tensile stresses.

7.5 Results

The bipedal stance simulation was performed for four scenarios, namely (i) the individual-muscle model with original socket (IM-OS), (ii) the fused-muscle model with the original socket (FM-OS), (iii) the individual-muscle model with smaller, misfitting socket (IM-MS), and (iv) the fused-muscle model with the misfitting socket (FM-MS). All simulations were performed with the boundary conditions described in Section 7.2. The von

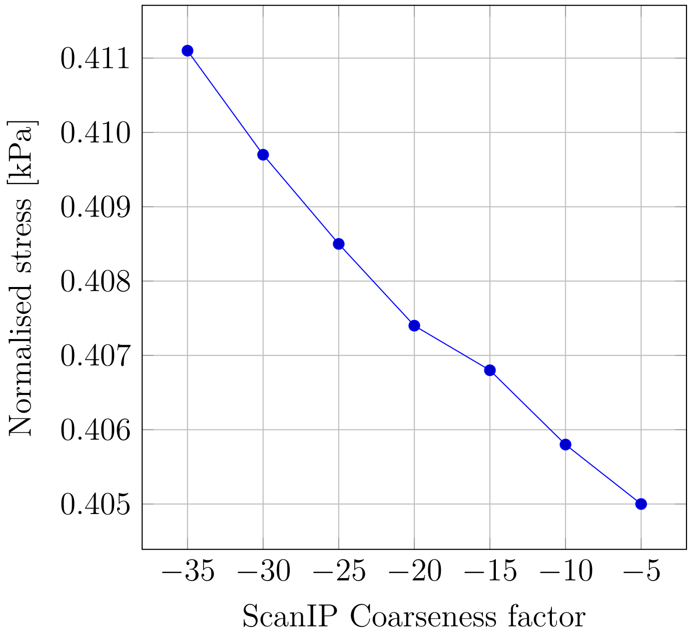

Coarseness factor	Number of elements
−35	517 832
−30	545 581
−25	583 766
−20	658 033
−15	779 300
−10	1 177 396
−5	2 879 958

Figure 7.3: *Convergence of the normalised von Mises Stresses of the residual limb model with decreasing ScanIP coarseness factor. On the right, the number of linear Lagrange tetrahedral elements in the FE model of residual limb is tabulated against the ScanIP coarseness factors. The decrease in normalised stress is negligible upon increasing the mesh density. Therefore, the FE mesh created with a coarseness factor of −35 was considered optimal for this study.*

Parameter	Starting	Minimum	Maximum
c_1 [MPa]	2.5×10^{-6}	1.0×10^{-8}	1.0×10^{-4}
c_2 [MPa]	6.0×10^{-3}	1.0×10^{-5}	1.0×10^{-1}
c_3 [MPa]	1.0×10^{-3}	1.0×10^{-5}	1.0×10^{-1}
c_4 [-]	6	1	50

Table 7.1: *Starting and range of parameter values chosen for the sensitivity analysis of material parameters.*

Mises stresses and tissue damage in the skeletal muscles, at the end of the bipedal stance simulation ($t = 2\,\mathrm{h}$), are shown in Figure 7.5. The peak stresses in the above four cases, in order, were 21.09 kPa, 10.83 kPa, 51.60 kPa, and 16.88 kPa, respectively. Similarly, the volume-normalised (cf. Equation (7.1)) von Mises stresses for the four analyses, were 4.2 kPa, 4.1 kPa, 6.6 kPa, and 6.0 kPa, respectively.

The deep tissue injury occurring in skeletal muscles at the end of bipedal stance simulation is reported in Figures 7.5(e) to 7.5(h). The volume percentage of damaged tissues with respect to the total, undamaged volume of the tissues is plotted over the duration of the entire stance simulation in Figure 7.6. The original sockets produced no tissue damage in the bipedal stance analyses, whereas the misfitting sockets produced 12.85 % and 21.98 % damage in the fused- and individual-muscle models, respectively.

The interface stresses generated on the skin/fat layer after the 2 h bipedal stance simulation, when the fused- and individual-muscle models were fitted with the original

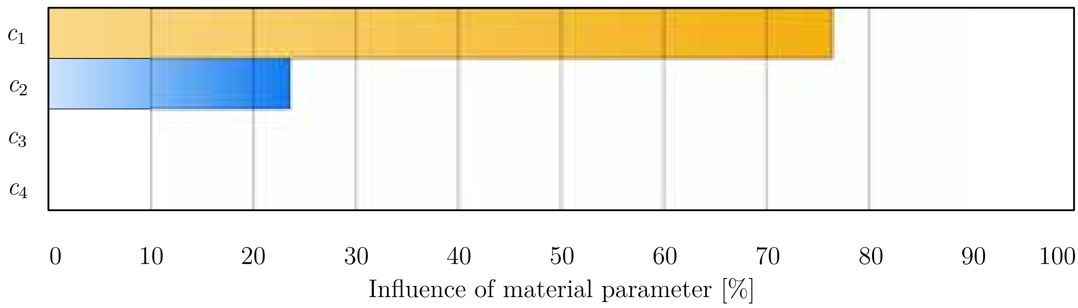

(a) *Compression*

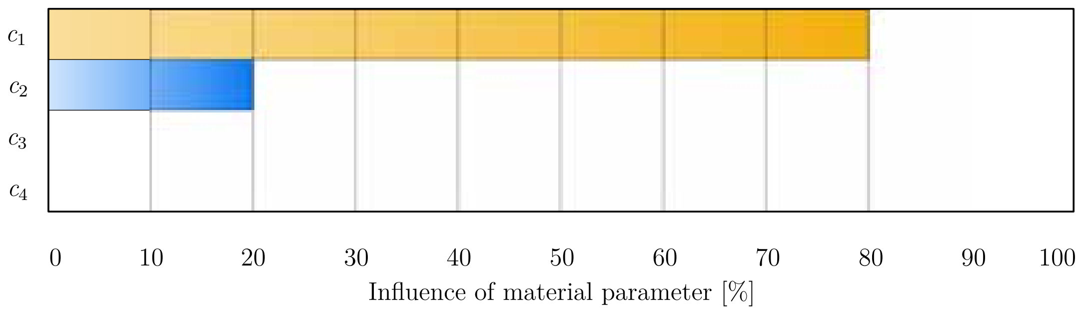

(b) *Shear*

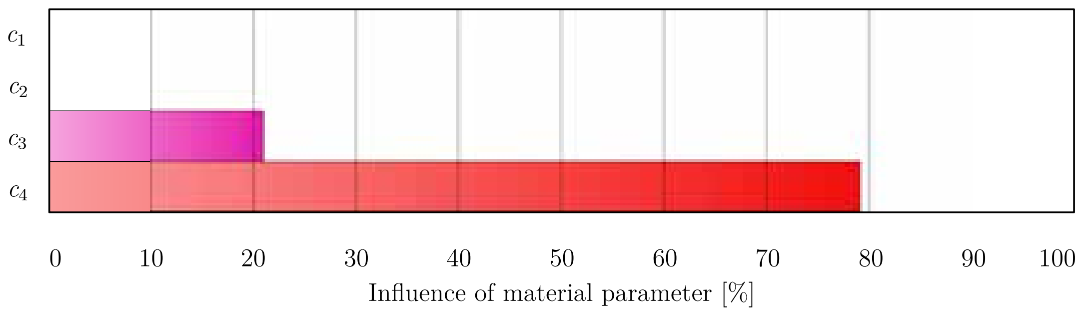

(c) *Tension*

Figure 7.4: *Sensitivity of material parameters to uniaxial tension, compression and simple shear. The parameters c_1 and c_2 can be seen to have high influence on resulting stresses in compression and shear, while c_3 and c_4 influence the tensile stresses.*

and misfitting sockets, are shown in Figure 7.7. The mean and standard deviation of the interface stresses in the FM-OS and IM-OS scenarios were 4.7 ± 0.8 kPa and 4.6 ± 0.7 kPa, respectively. Similarly, the interface stresses in the FM-MS and IM-MS cases were 6.1 ± 1.5 kPa and 6.4 ± 1.6 kPa, respectively. The peak stresses in the two models with the original socket were 14.6 kPa and 15.8 kPa, respectively, which were observed in the proximal anterior and posterior regions of the residual limb.

7.6 Discussion

The models of residual limb and prosthetic socket were generated from DT-MRI and T_1-MRI scans, respectively. This was due to the fact that the socket, which lacked water content, was invisible in the DT-MRI scans and therefore could not be segmented.

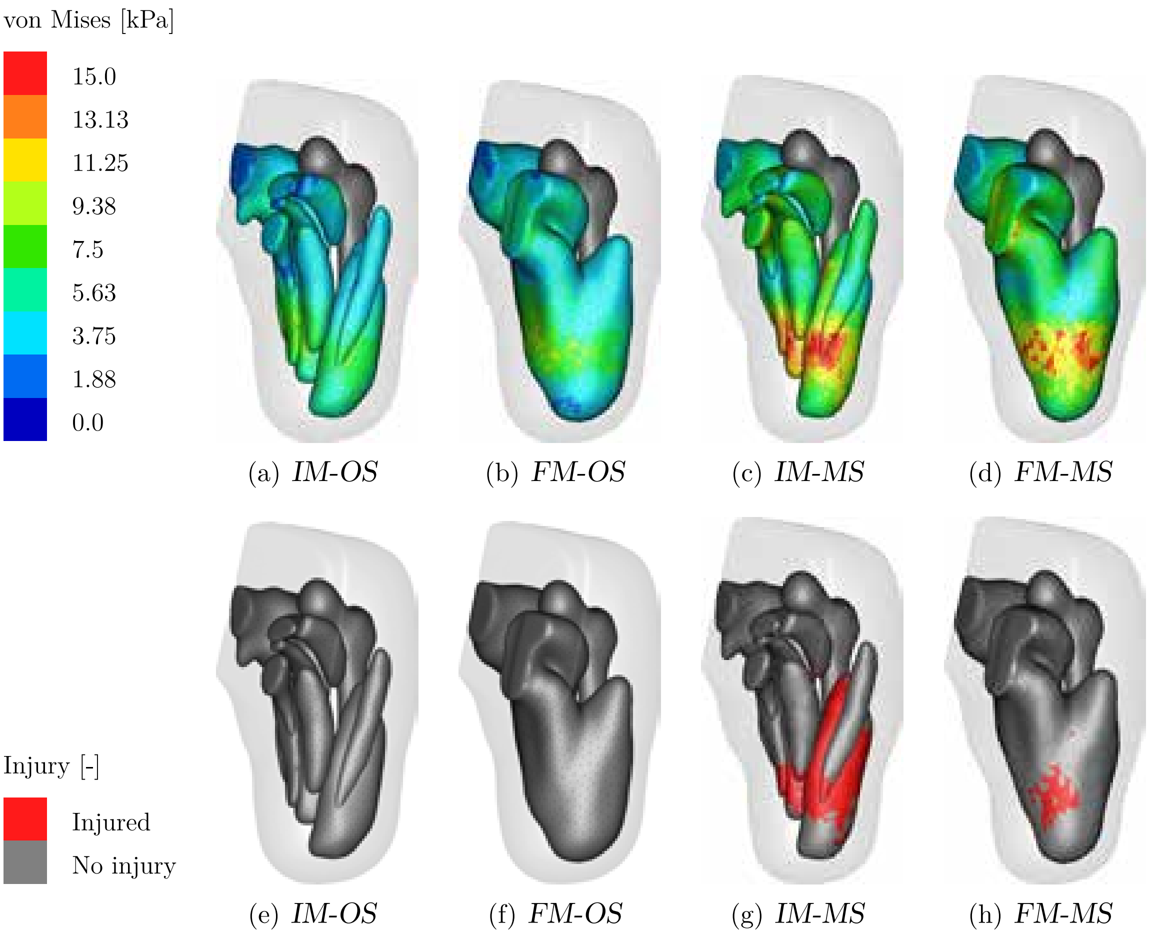

Figure 7.5: *Results of the FE analysis (in the anterior-medial viewing direction) for the four cases described in Section 7.5. Figures 7.5(a) to 7.5(d) show the von Mises stresses in the individual-muscle (IM) and fused-muscle (FM) residual limb models when bipedal stance was analysed with the original socket (OS) and misfitting socket (MS). The stress legend was capped at* 15 kPa *for better illustrating the stress zones. Figures 7.5(e) to 7.5(h) show the regions of potential deep tissue injury at the end of the bipedal stance analysis (at* $t = 2\,\mathrm{h}$*).*

The correct alignment between the residual limb and socket was achieved by manually segmenting and aligning the femur in both models. This manual segmentation of the femur in Simpleware ScanIP is trivial and quick due to large differences in the pixel intensities of the bone and surrounding soft tissues. Following this alignment procedure, the initial position of the socket for the socket donning simulation was chosen such that the stump and the socket were not in initial contact. The duration of this simulation was assumed to be 10 s, which was not experimentally-motivated. The duration for bipedal stance was chosen to be 2 h, which was motivated by the strain-based cell necrosis study by Gefen et al. (2008), where tolerance of engineered tissues to compressive strains decreased significantly between 1 and 3 h upon loading.

The differences between the individual- and fused-muscle models are immediately clear upon comparing the magnitude and distribution of stresses in the muscles during bipedal stance. A three-fold difference in the peak stresses is present between the two models, with the peak stresses in the individual- and fused-muscle models with misfitting sockets

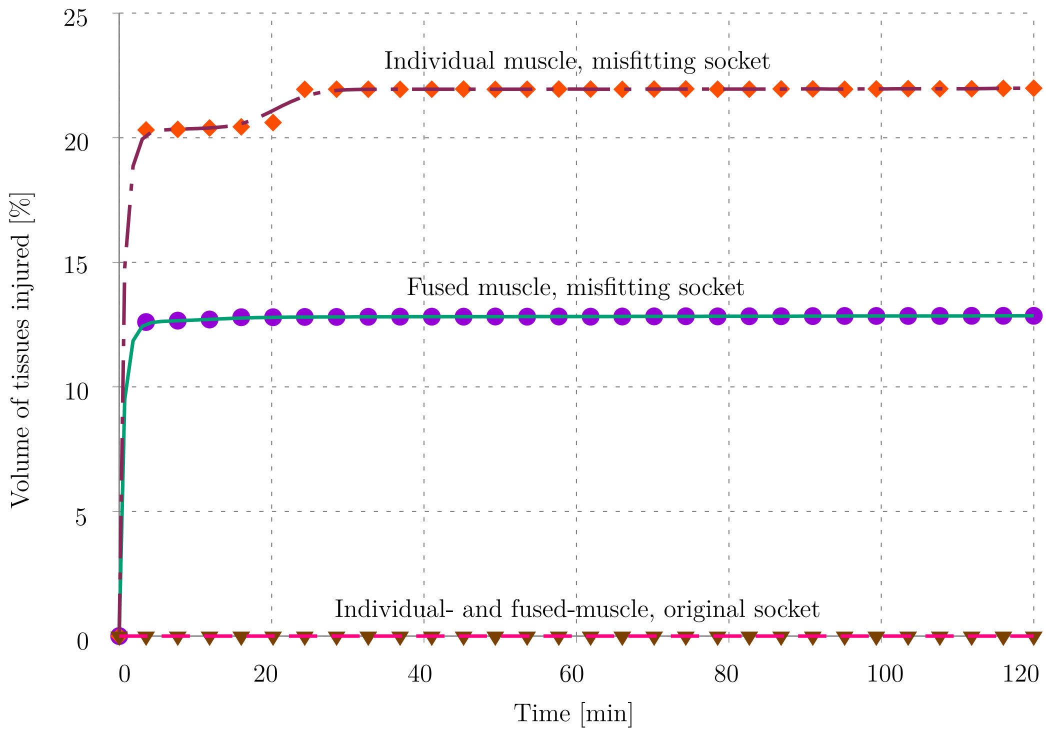

Figure 7.6: *The plot shows the volume of muscle tissues that was affected by deep tissue injury as a percentage of total muscle volume in the residual limb during bipedal stance. The evolution of tissue damage for all cases is plotted here.*

being 51.6 kPa and 16.88 kPa, respectively. This large difference may be attributed to the contribution of passive fibre stiffness to the global stiffness matrix in the individual-muscle model, which is absent in the fused-muscle model. With regard to the stress distribution, the stresses in the fused-muscle model are easily spread over the single muscle volume, resulting in lower magnitude and larger spread of the stresses, while stress concentrations are seen at the interfaces between muscles in the individual-muscle model. In contrary to the large stress differences in the deep tissues of the residual limb, the difference in the mean interface stresses between the fused- and individual-muscle models with the original socket resulted in only a small difference, i.e. 4.1 kPa in the fused-muscle model and 4.2 kPa in the individual-muscle model. The magnitude of the mean interface stresses in both these models are similar to those obtained by Lacroix & Patiño (2011). Hence, the study of interface stresses, while necessary, is not sufficient to ensure the good health of deep tissues in the stump. In the above results, the magnitude and distribution of stress in the soft tissues corresponded to those of strains, and therefore, only stresses were reported here in order to be consistent with the rest of the literature. In all bipedal stance scenarios, the strains in the stump corresponded to the stresses. In order to be consistent with results presented in literature, only the stresses were reported here. As expected, the bipedal stance simulation of the stump fitted with the original socket predicted negligible tissue damage. However, the volume of tissues in the fused-muscle model that was predicted to have been damaged was 1.71 times less than that predicted to be damaged in the individual-muscle model. Therefore, using fused-muscle model in deep tissue injury studies might undermine the true extent of tissue damage.

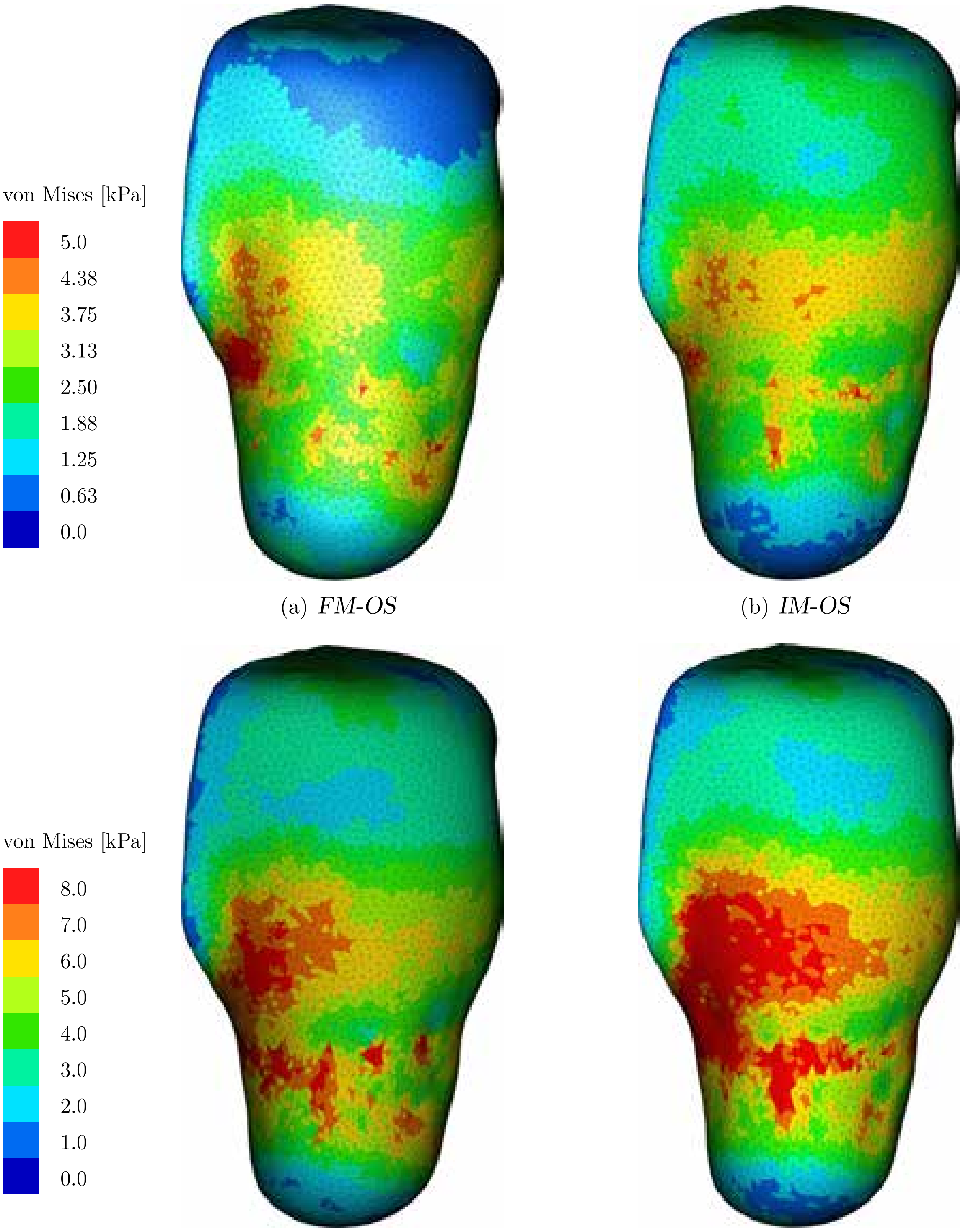

(a) *FM-OS* (b) *IM-OS*

(c) *FM-MS* (d) *IM-MS*

Figure 7.7: *Interface stresses (viewed in the anterio-posterior direction) on the skin in the fused- and individual-muscle models at the end of 2 h bipedal stance analysis, when donned with the original and misfitting sockets. For the sake of clarity, the liner and socket are hidden to show the stresses on the skin. Each stress legend is common to the models on their right, and were capped at 5 kPa (analysis with original socket) and at 8 kPa (analysis with misfitting socket) to better illustrate the stress zones.*

8 Case study: Gait analysis

In Chapter 7, the state-of-the-art and the detailed stump models were compared in FE analyses of bipedal stance. The results revealed the potential inaccuracies of the state-of-the-art stump models, both in predicting the stresses and deep tissue injuries in the stump. In this chapter, the stance analysis will be extended to a dynamic FE gait analysis of a limb-socket-prosthesis system. Loads on the residual limb are influenced by dynamic alignment of various prosthetic components, and by the impact forces during heel-strike and toe-off (cf. Kobayashi et al., 2015). Despite the importance of gait studies on fitting prosthetic sockets, there are no comprehensive FE simulations that study the dynamic interaction between the stump and a complete transfemoral prosthesis using boundary conditions from motion capture data. Here, the previous analysis of bipedal stance is extended by adapting an above-knee amputee gait stride that takes into account a detailed limb model including all components of an above-knee prosthesis.

8.1 Boundary conditions

In addition to the stump-socket model used in the bipedal stance simulations, a kinematic knee joint and floor models are necessary to perform a dynamic FE analysis. Furthermore, pre-processing of kinematic boundary conditions obtained from gait analysis is necessary.

8.1.1 Polycentric knee joint

The transfemoral prosthesis (Figure 7.1), which was used in the bipedal stance analysis, is also used in analysing the dynamic socket-stump interaction during gait. However, the immobilisation constraints on the knee joint must be removed. The geometric construction of the 4-bar knee joint complex prevents extension beyond the natural extended position as shown in Figure 7.1. However, the knee joint is flaccid in flexion. Therefore, in order to try and emulate the normal behaviour of the prosthesis during gait, the knee joints in LS-DYNA were modelled with torsional stiffness about their local x-axis using the `constrained_joint_stiffness_generalized` card (cf. Figure 7.1). The moment-angle and damping moment versus rate of rotation parameters required for defining the joint stiffness are provided in Table 8.1.

8.1.2 Motion capture

Reflective markers were placed on the subject's prosthesis, which were tracked using Qualisys motion capture systems (Qualisys AB, Göteborg Sweden). The subject walked with self-selected, normal pace, and the marker positions between heel-strike and toe-off of the prosthetic limb, i.e. one gait stride, were obtained. A rigid body was defined from 3 non-collinear markers placed on the prosthetic socket from which its rotations and

Angle [rad]	Torsional moment [kN mm]
0	0
0.1047	1.3×10^6
0.3840	1.9×10^6

Rate of rotation [rad ms^{-1}]	Damping moment [kN mm]
0	0
8.725×10^{-4}	1.2×10^3

Table 8.1: *Torsional joint stiffness and damping parameters used for stiffening the knee joint in flexion.*

translations were extracted. The motion of the femur was not recorded at the time of performing the experiments. Therefore, for the FE simulations, the motion of the socket in the Qualisys coordinate system was used as the Dirichlet boundary conditions on the femur.

The Dirichlet boundary conditions on the femur are applicable only when the position and alignment of the physical socket in Qualisys and FE model of the socket in the LS-DYNA coordinate systems match. Since the socket was modelled from medical scans, registration of the Qualisys and LS-DYNA sockets was performed by virtually placing the 3 non-collinear markers, which were used to define the socket rigid body in Qualisys, on the FE mesh of the socket. Finally, the transformation matrix obtained as a result of this registration process was applied to the Dirichlet boundary conditions, i.e. to the rotations and translations of the socket. Noise in the motion of the socket was smoothed by fitting a spline to the curves using the `splinefit` toolbox in MATLAB (cf. Lundgren, 2017). Smoothing the raw curves from experimental data is required in order to prevent unintended sharp accelerations in the FE analysis. The raw and smoothed curves are shown in Figure 8.1.

The original duration of the gait stride was 1.94 s. For the FE gait simulation, this duration was upsampled to 50 s, and the Dirichlet boundary conditions on the femur were interpolated accordingly. The entire duration of the gait simulation was 60 s, and was performed in two stages: (i) socket donning in the first 10 s, and (ii) kinematic gait during the next 50 s. The boundary conditions during the first stage, i.e. socket donning, were identical to those during the first stage of bipedal stance (cf. Section 7.2). At the end of socket donning phase, frictionless sliding contact between the liner and socket was switched to a tied contact (`contact_tied_nodes_to_surface`) using birth/death definitions in the contact cards. The tied contact shall resemble the vacuum suspension technique, which was used to attach the transfemoral prosthesis to the residual limb. Furthermore, during the second stage, all translational and rotational constraints on the prosthesis and femur were removed, and the transformed and interpolated Dirichlet boundary conditions were applied on the femur.

8.1.3 Floor model

Modelling the floor is essential to obtain the ground reaction forces resulting from contact between the floor and prosthesis during gait. Moreover, these contact forces determine the internal stresses and deep tissue injury in the residual limb. In order to model the floor, the socket was rigidly constrained (using the `constrained_rigid_bodies` card) to move with the femur. A rigid body simulation of the bone-socket-prosthesis complex was

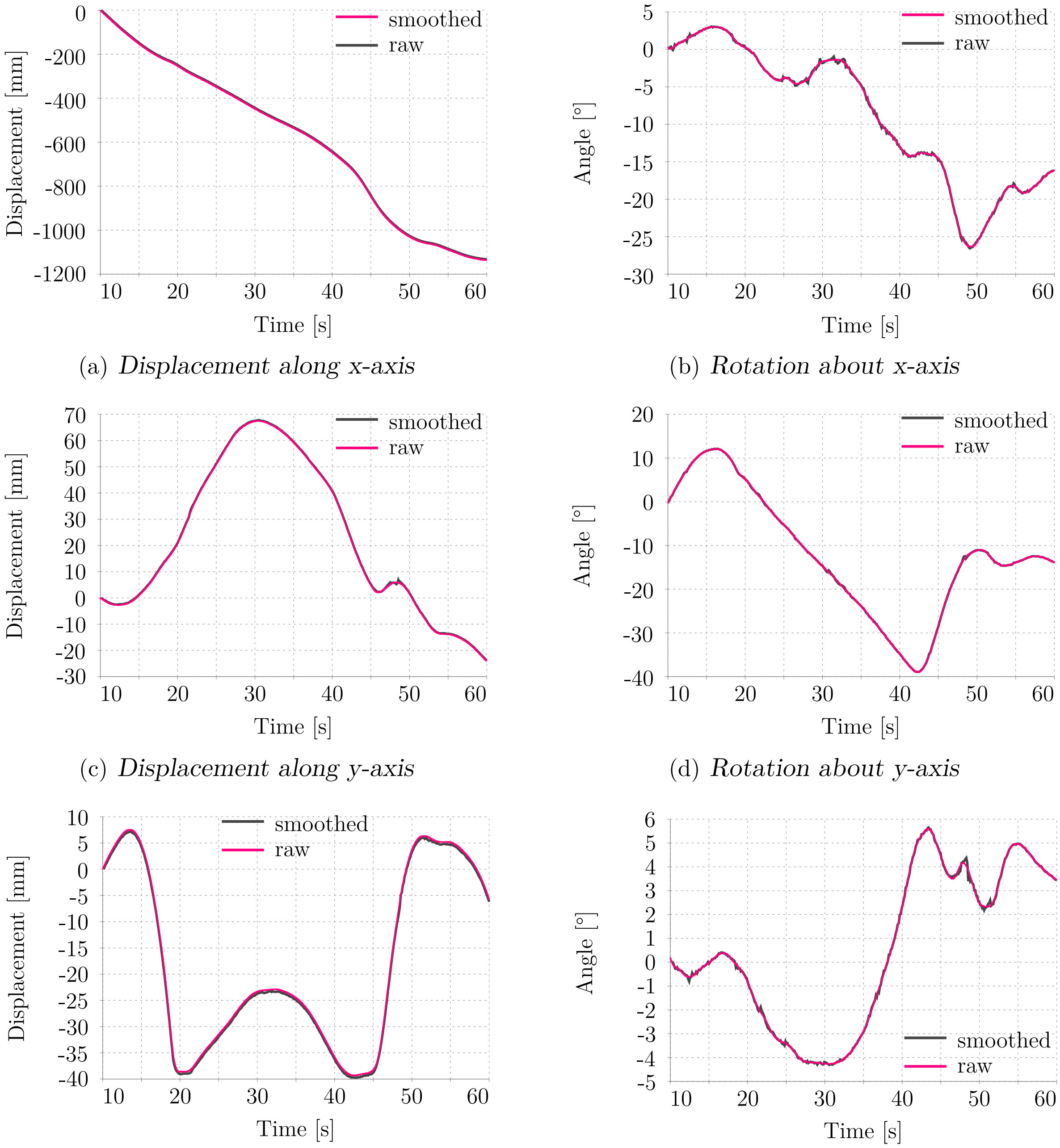

(a) *Displacement along x-axis*
(b) *Rotation about x-axis*
(c) *Displacement along y-axis*
(d) *Rotation about y-axis*
(e) *Displacement along z-axis*
(f) *Rotation about z-axis*

Figure 8.1: *Raw experimental and smoothed Dirichlet boundary conditions applied on the femur.*

performed by applying Dirichlet boundary conditions on the femur. Heel-strike and toe-off events were determined from Qualisys force-plate recordings. When the force recorded by the force plate exceeded a pre-defined threshold (in this case, 30 N), the event was flagged as heel-strike. Similarly, following heel-strike, when the force dropped below the threshold (30 N), the event was flagged as toe-off. The instantaneous nodal coordinates of the heel and toe nodes of the FE prosthetic foot during heel-strike and toe-off were used to fit a plane, which formed the top contact surface of the floor. This plane was extruded by 20 mm in the inferior direction to form a solid model of the floor. The floor was meshed with 436 635 linear Lagrange tetrahedral elements, and the contact between the prosthetic foot and floor was modelled with `automatic_single_surface` contact in LS-DYNA.

8.2 Results

The FE gait analysis was performed with the boundary conditions listed in Section 8.1 on the individual-muscle (IM) residual limb model with the original socket (OS). The stresses developed in the skeletal muscles, and on the surface of residual limb at the end of the simulation ($t = 60\,\text{s}$) are shown in Figure 8.2. The maximum interface stress on the residual limb when fitted with the original socket was 16.94 MPa. The maximum stress in the skeletal muscles when fitted with the original socket was 147.1 MPa.

Figures 8.2(c) and 8.2(d) show the potential sites, where deep tissue injury could develop during the dynamic interaction between the stump and the original socket. The volume of skeletal muscles injured at the end of socket donning stage was 0.24 % when the residual limb was fitted with the original socket. This value rose to 1.85 % during heel-strike, and remained almost constant during the stance phase before rising to 2.83 % during toe-off. Relative motion between femur and the original socket was obtained by projecting a distal node of the femur onto a plane at the centroid of the socket and normal to the first principal axis of the socket. The relative motion between the projected femur node and the centroid of the socket is representative of the relative motion between the femur and socket during gait, and is plotted in Figure 8.4. The maximum relative displacement between the femur and original socket were observed during heel-strike and toe-off, which were 10.59 mm and 16.06 mm, respectively.

8.3 Discussion

The kinematic boundary conditions for gait were obtained from motion capture. Herein, the motion of socket was applied as Dirichlet boundary conditions on the femur. While this may not be true, the experimental set-up did not include sensors to capture the motion of femur during gait. It is possible to record the motion of the femur using ultrasound sensors (cf. Chong & Röhrle, 2016). Further, by synchronising the sensors with Qualisys, it might be possible to directly obtain the motion of femur in the Qualisys reference frame. The complete gait occurred in 1.94 s but were extrapolated to 50 s in the FE simulations to reduce dynamic effects. As discussed previously, the soft tissue parameters of the residual limb were weak and resulted in excessive deformation in the tissues of the stump, causing stability and convergence problems. Therefore, in addition

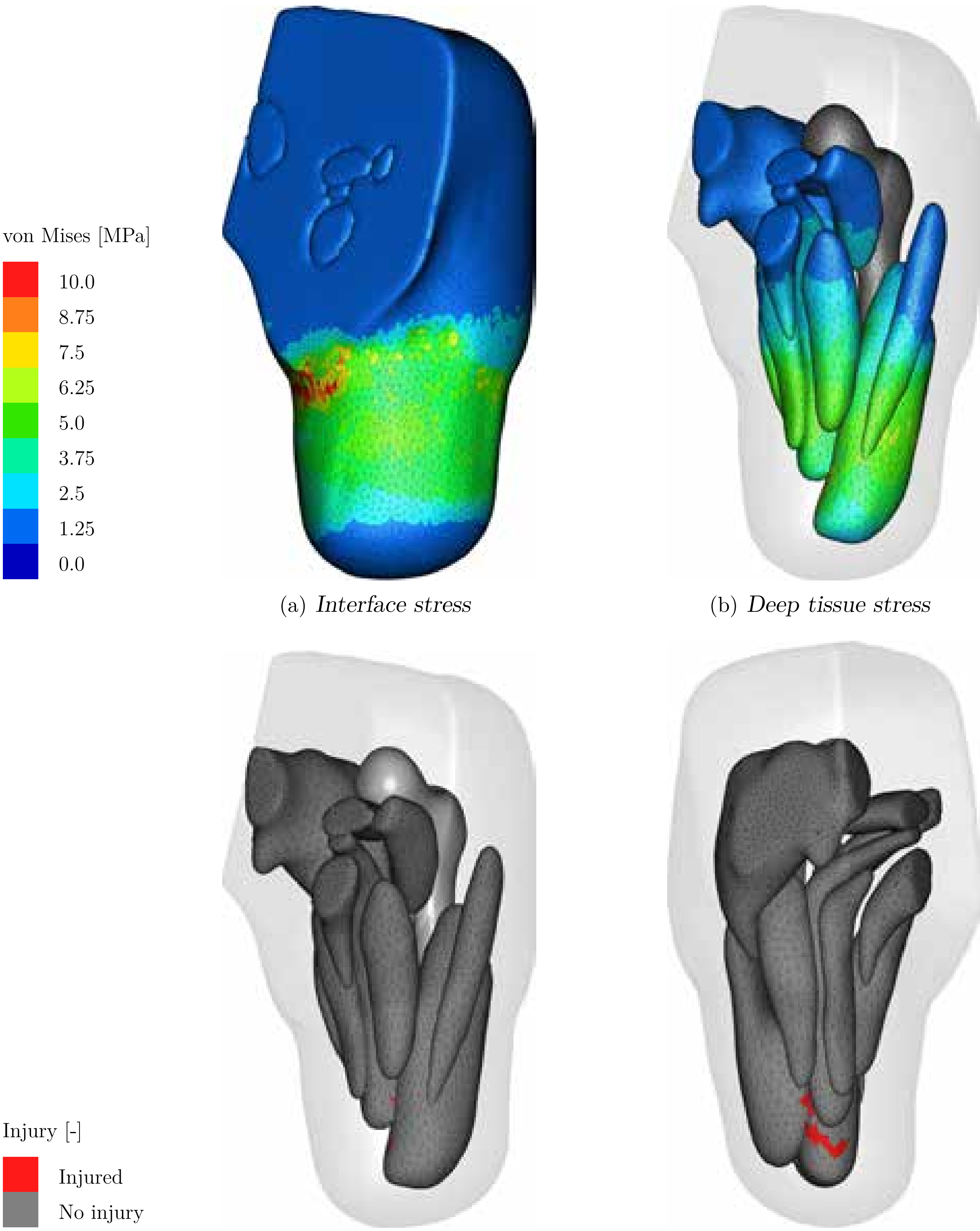

(a) *Interface stress* (b) *Deep tissue stress*

(c) *Muscle injury* (d) *Muscle injury*

Figure 8.2: *The von Mises stresses developed on the surface of the skin and in the muscles, at the end of the gait simulation, are shown in Figures 8.2(a) and 8.2(b). The stress legend in both cases are capped at 10 MPa to better illustrate the stress distribution. The regions of potential soft tissue damage are depicted in Figures 8.2(c) and 8.2(d).*

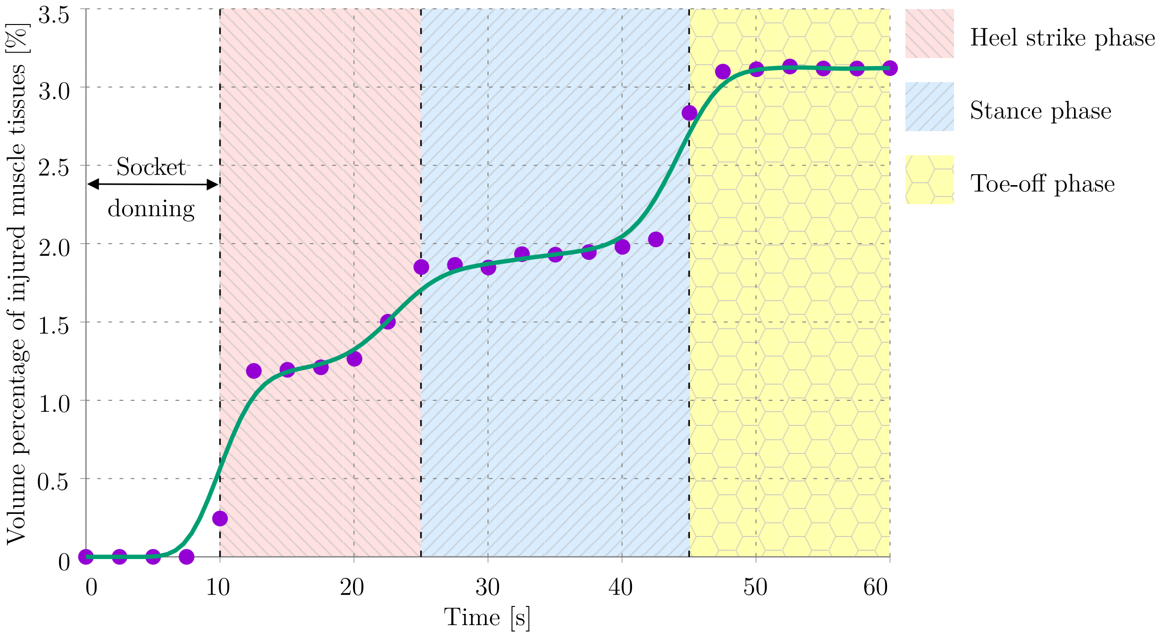

Figure 8.3: *Evolution of deep tissue injury in skeletal muscles over the complete gait phase with the original socket.*

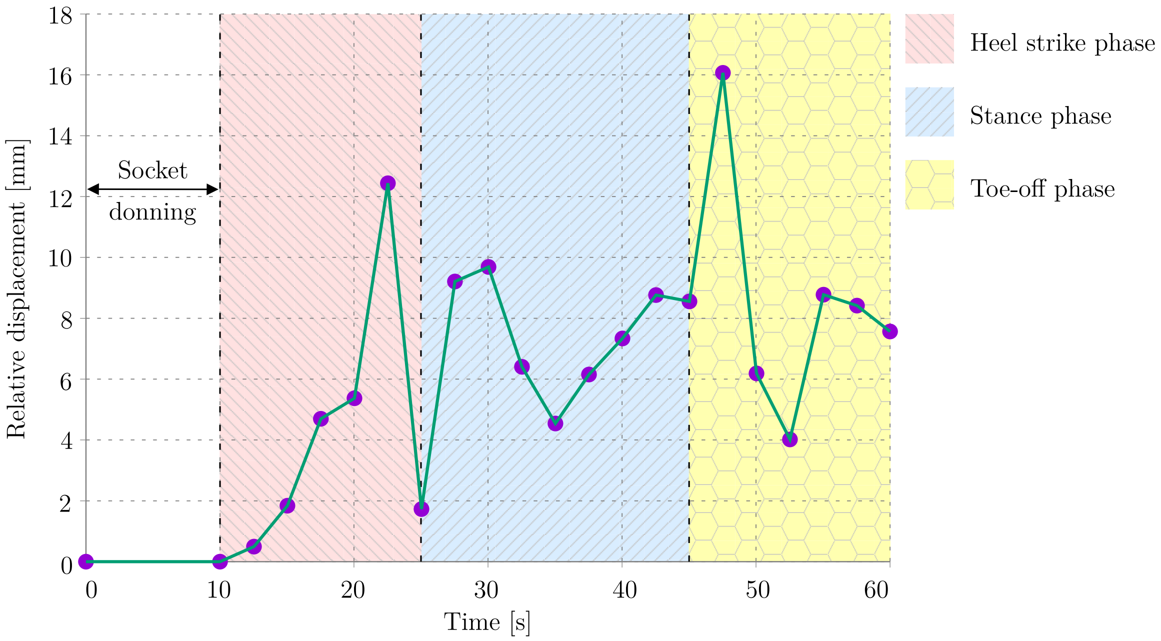

Figure 8.4: *Relative motion between the original socket and femur during gait is plotted over the complete gait phase.*

to stiffening the material parameters, duration of the FE simulation was also increased to minimise accelerations in the stump-prosthesis system. From the dynamic FE gait simulation, maximum relative motion between the socket and femur was observed to be 10.59 mm during heel-strike, and 16.06 mm during toe-off. This relative motion can, in addition to deep tissue stresses and injury, serve as a measure of dynamic socket-fit.

Modelling the floor was essential to account for the soft tissue deformation due to contact between the prosthesis and the ground, which was also evident from the increase in soft tissue damage during heel-strike and toe-off. The floor can be modelled in one of several methods, apart from that described in this thesis. For example, the simplest method would be to place reflective markers on the floor to which a plane can be fit. Another technique would be to use the metadata from the force plates connected to Qualisys. A force plate provides the spatial position of its corners in the Qualisys coordinate system, and the normal distance from the surface of the floor. With this information, it is possible to estimate the surface of the floor. One caveat to these approaches is that all components of the prosthesis must be registered in the Qualisys coordinate system in order to ensure proper contact with the floor. Further, each component in the FE model of the prosthesis must be modelled to scale. If it is required to study the interaction of different prosthetic devices with the stump, the above standard approaches might be cumbersome. The greatest advantage of using the proposed approach is its general applicability and ease of use when testing different prosthetic devices.

The stiffness of polycentric knee joint in the transfemoral prosthesis was obtained through trial-and-error simulations by assuming torsional stiffness and damping at the joints, and by applying a force on link D along the local y-axis, while holding link A fixed (cf. Figure 7.1). These values were optimised such that for the dynamic gait conditions, the knee joint was neither rigid nor flaccid. While stiffness parameters of the knee joint model was neither based on experiments nor product catalogues, the inclusion of such a polycentric knee joint was meant to showcase the modelling approach to simulate realistic prosthetic systems in this comprehensive modelling-simulation-analysis workflow.

As a result of upsampling the original stride duration from 1.94 s to 50 s, the dynamic effects of gait were substantially reduced. Otherwise, the simulations failed to converge in the presence of large dynamic effects. The material parameters listed in Table 4.2 were fitted to healthy muscles in the upper limb, which were not subjected to compressive forces such as those experienced in the residual limb. Therefore, it is very likely that the isotropic Mooney-Rivlin parameters have to be fit to correctly represent the loads in the stump, which may then truly enable dynamic FE simulations.

The evolution of injury in gait analysis shows that tissue damage occurs primarily during heel-strike and toe-off phases. While FE analysis with the original socket showed no damage during bipedal stance simulations, tissue damage during gait rose to 3.12 % at the end of the simulation. As discussed earlier, the inclusion of the injury model by Gefen et al. (2008), whose parameters were based on experiments on engineered tissue samples, could have resulted in the observed tissue damage values. However, disregarding the absolute values, the proposed technique, along with the novel workflow provides a convenient scientific setup to assess socket fits, and when appropriate tissue material models have been developed, or when parameters are fit to the proposed material model, this workflow can be used to assist the prosthetist in developing well-fitting, scientifically sound socket designs.

An alternative to motion capture-based FE gait analysis is the forward simulation of stump. For instance, muscle activations in the stump can be optimised such that they produce the experimentally observed stump kinematics. Several open source and commercial software are available for forward simulations. Using OpenSim[1] and Anybody Technology[2] software platforms, skeletal muscle activations for a given motion can be determined through optimisation strategies. Transtibial amputee models containing 1D Hill-type muscles are already available for use in OpenSim (cf. LaPrè et al., 2018). Muscle activations, which are determined from these tools can be used to drive forward simulations of the 3D continuum-mechanical stump models from which the physiological loaded state of internal tissues in the stump can be determined. Internal soft tissue stresses and injury determined through forward simulations are more realistic since they are closer to the natural mechanism of human motion. Further, forward models pave way for FE simulations with active prosthetic devices, which are controlled through muscle contractions.

[1] https://simtk.org/frs/index.php?group_id=91, accessed on May 24, 2019
[2] https://www.anybodytech.com/, accessed on May 24, 2019

9 Summary and outlook

9.1 Summary

The aim of this thesis was to develop a modelling-simulation-analysis workflow for analysing the stump-socket interaction in transfemoral amputees. The proposed workflow generated a detailed patient-specific stump geometry from the DT-MRI scans with minimal human effort. The workflow also automated the generation of the FE mesh of the stump, and mapped the skeletal muscle fibre information to the FE mesh. The resulting FE model of the stump was novel, in which individual muscles, fat and bone were efficiently segmented from the DT-MRI scans. The entire process of generating the FE mesh of the stump, from start to finish, was approximately 20 min.

Another objective of the thesis was to model the heterogeneous soft tissue material, and to predict potential regions of deep tissue injury in the stump. The large deformations occurring in biological soft tissues were modelled with the finite strain theory, in a continuum-mechanical framework. The soft tissue material response was additively split into an isotropic response of the matrix and a transversely isotropic response of the muscle fibres. The contraction of skeletal muscles was modelled using a scalar parameter, and the mechanism of soft tissue injury was formulated using continuum damage mechanics using the concept of internal variables.

Four FE case studies were performed with the detailed model, namely (i) liner donning, (ii) forward simulation of *gluteus maximus*, (iii) bipedal stance, and (iv) gait with complete transfemoral prosthesis. The motive behind these FE analyses were to showcase the necessity of detailed stump models in the field of prosthetics. Forward simulations with the stump models are facilitated by the muscle fibre information in the stump model. Prosthetic liners are largely ignored in stump-socket analyses. The strains on the stump and stresses in the liner, at the end of a liner donning simulation, might provide useful hints for choosing an appropriate liner for a given amputee. In the bipedal stance simulations, stresses and deep tissue injury occurring in the state-of-the-art stump model and the proposed detailed model were compared. The results of the FE analyses revealed that the state-of-the-art models underestimate both stresses and soft tissue damage in the subcutaneous tissues of the stump. Finally, one dynamic gait stride was simulated with the complete transfemoral prosthesis, featuring a kinematic four-bar knee joint. Three diagnostic reports on the state of soft tissues in the stump were presented in this work, namely (i) internal and interface soft tissue stresses, (ii) volume-normalised deep tissue injury, and (iii) relative displacement between femur and socket.

9.2 Outlook

According to a report by the World Health Organisation, "technology diffusion in medicine is a complex, non-linear and dynamic process. There are obstacles to the introduction of any innovative method, procedure or piece of equipment, regardless of whether it takes place in a developing or developed country" (cf. World Health Organization, 2010). This is currently the problem with innovations in prosthetic devices as well. Despite several advancements in myoelectric control of prosthetic devices, the basic requirement, i.e. a comfortable socket, still remains unsatisfied. As motivated in the beginning of this thesis, the work presented here is only a first step in assisting the scientific community towards generating comfortable sockets. The diagnostic reports presented in this work must be collated into a meaningful scalar parameter, which is indicative of socket comfort.

Computational models, especially the finite element method, provide the safety and liberty of simulating potentially dangerous or ethically unacceptable scenarios. To obtain useful results, the models, materials and boundary conditions must represent the real world conditions to which they will be subjected. Therefore, the relevant physics involved in such simulations must be accounted for. For instance, when a prosthetic socket is developed for use in a hot and humid environment, in addition to the mechanical interaction between the socket and stump, the effects of temperature, humidity and friction or slip conditions must be considered. Lately, the materials chosen for simulating the mechanical behaviour of the stump have been largely nonlinear. This trend must be extended to model other geometrically nonlinearities as well. Several research groups, around the world, have advanced tissue models, which could be incorporated within the scope of prosthetic technologies. At the University of Stuttgart, the Continuum Biomechanics research group[1] of Prof. Oliver Röhrle has developed multiscale methods for bridging cellular mechanics to the macroscopically observed muscle contractions. More recent simulations involve compartmentalising skeletal muscle bundles, and stimulating the contraction of individual compartments. Prof. Dan Bader is a part of the Health Sciences team at the University of Southampton. His research[2] focusses on skin health, *in vivo* models to examine real-time cell death using computational and experimental methods, and the biomechanics of soft tissue health at different hierarchical levels. Prof. Cees Oomens at the Department of Biomedical Engineering[3] at the Technical University of Eindhoven and Prof. Dan Bader collaborate on developing detailed soft tissue damage models based on animal and human studies, and by using tissue engineered constructs. Here, a major field of study is the aetiology of pressure ulcers. Dr. Silvia Blemker, an Associate Professor of Biomedical Engineering at the University of Virginia, focusses on developing *in silico* methods from *in vivo* experiments to gain new insights into the form, function, biology, and diseases of muscles. Prof. Can Yücesoy, director of the Institute of Biomedical Engineering[4] at the Boğaziçi University, focusses on the biomechanics of musculoskeletal system using computational and experimental methods, on myofascial force transmission in skeletal muscles, and in the application of *in vivo* MRI analyses to detect strains along muscle fibres. At the MIT Media Lab[5], Prof. Hugh Herr heads the Biomechatronics group, where several

[1] http://www.mechbau.uni-stuttgart.de/ls2/jrg/, accessed on May 24, 2019
[2] https://www.southampton.ac.uk/ifls/about/staff/dan_bader.page, accessed on May 24, 2019
[3] https://www.tue.nl/en/research/researchers/cees-oomens/, accessed on May 24, 2019
[4] https://bme.boun.edu.tr/, accessed on May 24, 2019
[5] https://www.media.mit.edu/people/hherr/overview/, accessed on May 24, 2019

prosthetic-centric topics are researched, e.g. bionic joints, neural interfaces for prosthetics, exoskeletons and automated computational design of subject-specific prosthetic devices.

The above-listed research groups are by no means a comprehensive list of people involved in the field of soft tissue biomechanics. Clearly, the advanced computational models developed by these groups can be used in the field of prosthetics. For example, to solve the issue of socket comfort, the work presented in this thesis can be used as an initial prototype. This model can be further improved upon by modelling tendons along with the connective tissues of the extracellular matrix proposed by Yucesoy & Huijing (2012). By placing surface EMG sensors on the stump, synergistic muscle activations acquired during a gait cycle can be factorised into individual motor modules (cf. Cappellini et al., 2006), and can be used to simulate the activation of individual motor units (cf. Röhrle et al., 2012). With such a model, forward simulation of the muscles in the stump, along with ground reaction forces acquired during motion capture, can provide realistic boundary conditions for the FE analyses. Material models such as the one proposed here, multiscale and multiphysics models require proper tuning of the material parameters for each individual subject, before accurate predictions on the state of soft tissue stresses or strains can be made. The multipin indenter experiment by Sengeh et al. (2016) is a first step towards obtaining patient-specific material parameters in a clinical set-up. The soft tissue parameters identified with this method is representative of the homogeneous soft tissues in the stump. Further advancements are required to fit parameters to each tissue group in the stump. By simulating the socket-stump complex with real world loading conditions, one can obtain accurate predictions about the loads on the tissues in the stump. Using shape and topology optimisation techniques, an initial socket shape conceived by the prosthetist can be modified such that the final socket shape is comfortable to the subject. Further, multi-criteria optimisation function can be formulated such that subcutaneous strains close to the bones and socket are minimised, deep tissue injury is eliminated, and the relative displacement between the femur and socket is reduced.

It is of little use to the prosthetists and amputees if scientific research does not meet the requirements for clinical adoption. For computational tools to be clinically usable, they must be simple, intuitive, real time and reliable. Complex FE analyses often involve geometrical, material and contact-related nonlinearities. Further, complex stump geometries might consist of a large number of elements, which require expensive computing power, time and expertise to setup the model. At the time of writing the thesis, most commercial FE tools perform numerical calculations on the CPU. However, newer FE software, which are accelerated by Graphics Processing Unit (GPU) might pave the path for real time simulations. High Performance Computing (HPC) is also a viable alternative to GPU-computing for virtual testing of several prosthetic socket designs. For example, Bradley et al. (2018) have shown the possibility of simulating detailed biomechanical models on HPC systems with good scalability. Any number of factors might cause a simulation to terminate in an error, e.g. numerical inaccuracies, wrong boundary conditions and incorrect fitting of material parameters. Since clinicians, very likely, cannot determine and fix these errors, a possible solution could be web-based engineering services, where engineers can create the FE models from medical images that reside within the servers of a prosthetic clinic. Prosthetists can be trained to digitally rectify socket shapes, which can then be used in the FE simulations. Prosthetic socket comfort remains an unsolved problem since its inception. Only an interdisciplinary effort between medical professionals and engineers can lead to a fruitful solution to this problem.

Appendix A: Search Strategy

In the following sections, scientific methods and advancements in the multidisciplinary field of prosthetics are summarised for each decade. Such an overview of the field provides not only a bigger picture but also point out those areas that need more scientific focus and rigour. For this purpose, the PubMed database was searched for topics, i.e. keywords related to the development of transfemoral prosthetics. These topics, and the PubMed search queries were the following ones:

Transfemoral prosthesis Articles related to amputation that resulted in the use of transfemoral, or above-knee prostheses were shortlisted. Osseointegrated prostheses were excluded from the study. The purpose of this search was to obtain those articles that might discuss advancements in transfemoral prosthetic socket design, amputation techniques, knee mechanisms, methods to understand gait pathologies in transfemoral amputees, and problems that might be faced by transfemoral amputees.

```
( (transfemoral prosthesis OR above-knee prosthesis) AND
(amputee OR amputation) ) NOT
(osseointegrated OR bone-anchored) AND
("1941"[Date - Publication] : "2018"[Date - Publication])
```

Finite element analysis Articles related to lower limb amputees (both transtibial and transfemoral), where the finite element (FE) method was employed for the analysis or betterment of prosthetic devices. Again, bone-anchored prostheses were excluded from the search. The purpose of this search was to examine the application of FE analyses in the field of prosthetics, and to identify new opportunities for its applicability.

```
( (lower limb amputees OR residual limb OR residuum) AND
(prosthetics OR prosthesis) AND
(simulation OR finite element analysis) ) NOT
(osseointegrated OR bone-anchored) AND
("1941"[Date - Publication] : "2018"[Date - Publication])
```

Medical imaging Articles related to medical imaging, where the residual limb was scanned using medical scanners for the purpose of use in FE analyses were shortlisted. The purpose of this search was to understand the extent to which medical images were being used to model patient-specific geometries of residual limbs, i.e. to gauge the accuracy of the FE models.

```
(residual limb OR residuum) AND
(medical imaging OR imaging OR diffusion tensor) AND
(simulation OR finite element analysis) AND
("1941"[Date - Publication] : "2018"[Date - Publication])
```

Appendix B: Glossary

abduction a movement in the coronal plane that moves a limb laterally away from the body. 20

adduction a movement in the coronal plane that brings a limb closer towards the body. 20

aetiology the cause, set of causes, or manner of causation of a disease or condition. 2

amputation removal of a portion of a limb by trauma, medical illness, or surgery. 1

anthropometry the scientific study of the measurements and proportions of the human body. 7

callus bony healing tissue which forms around the ends of broken bone. 27

cartilage a firm but soft connective tissue. 17

circumduction combination of flexion, extension, adduction and abduction. 28

distal situated away from the centre of the body or from the point of attachment. 17

extension a movement in the sagittal plane that increases the angle between two segments. 20

flexion a movement in the sagittal plane that decreases the angle between two segments. 20

foot slap foot progresses too quickly from heel strike to foot flat, creating a slapping noise. 28

gait a person's manner of walking. 2

histology the study of the microscopic structure of tissues. 17

histopathology the study of changes in tissues caused by disease. 8

lateral the side of the body or a body part that is farther from the middle or center of the body. 20

ligament a tough, flexible fibrous connective tissue which connects two bones or cartilages or holds together a joint. 17

ligation the surgical procedure of tying a ligature tightly around a blood vessel or other duct or tube in the body. 26

lordosis normal inward curvature of the lumbar and cervical regions of the human spine. 28

mask a collection of voxels that defines a region of interest in the image data. 38

medial the side of the body or a body part that is closer to the middle or center of the body. 20

myodesis a surgical procedure in which a transected muscle is sutured to bone in order to stabilise the limb. 7

physiology Branch of biology that deals with the normal functions of living organisms and their parts. 21

precession precession is defined as the change in the rotational axis of a rotating body. 30

proximal situated nearer to the centre of the body or the point of attachment. 17

pylon a component that connects the transfemoral knee to the foot-ankle prosthesis. 4

rotation rotation towards or away from the centre of the body. 20

step rate number of steps per minute, where one step is the distance between the heel contact point of one foot and that of the other foot. 7

step width the distance between the centre lines of the two feet, perpendicular to the plane of walking. 7

stride length distance between the successive heel contact points of the same foot. 7

stump a residual limb or stump is the part of limb that remains attached to the body after amputation. 1

swing-phase whip lateral or medial movement of the heel at toe-off. 28

tendon a flexible but inelastic cord of strong fibrous collagen tissue attaching a muscle to a bone. 20

vaulting compensatory mechanism used by transfemoral amputees to assist toe clearance during the prosthetic swing phase. 28

word cloud a visual representation of text data, whose font sizes and thicknesses are determined by the frequency of their occurrence. 10

Bibliography

Aeyels, B.; Peeraer, L.; Vander Sloten, J. & van der Perre, G.: Development of an above-knee prosthesis equipped with a microcomputer-controlled knee joint: first test results. *Journal of biomedical engineering* **14** (1992), 199–202, ISSN 0141-5425.

Allende, M. F.; Levy, S. W. & Barnes, G. H.: Epidermoid cysts in amputees. *Acta dermato-venereologica* **43** (1963), 56–67, ISSN 0001-5555.

Andersen, M. S.; Damsgaard, M.; Rasmussen, J.; Ramsey, D. K. & Benoit, D. L.: A linear soft tissue artefact model for human movement analysis: proof of concept using in vivo data. *Gait & posture* **35** (2012), 606–611, ISSN 0966-6362.

Appoldt, F. A.; Bennett, L. & Contini, R.: Tangential pressure measurements in above-knee suction sockets. *Bulletin of prosthetics research* **10** (1970), 70–86, ISSN 0007-506X.

Asrael, W. & Leckitner, M. D.: Assistive device for applying above-knee suction socket. *Archives of physical medicine and rehabilitation* **45** (1964), 243–244, ISSN 0003-9993.

Bader, D. L. & Worsley, P. R.: Technologies to monitor the health of loaded skin tissues. *Biomedical engineering online* **17** (2018), 40.

Balzani, D.; Brinkhues, S. & Holzapfel, G. A.: Constitutive framework for the modeling of damage in collagenous soft tissues with application to arterial walls. *Computer Methods in Applied Mechanics and Engineering* **213-216** (2012), 139–151, ISSN 00457825.

Basu, S.; Fletcher, T. & Whitaker, R.: Rician noise removal in diffusion tensor MRI. *Medical image computing and computer-assisted intervention : MICCAI ... International Conference on Medical Image Computing and Computer-Assisted Intervention* **9** (2006), 117–125.

Beil, T. L.; Street, G. M. & Covey, S. J.: Interface pressures during ambulation using suction and vacuum-assisted prosthetic sockets. *Journal of rehabilitation research and development* **39** (2002), 693–700, ISSN 0748-7711.

Blemker, S. S.; Asakawa, D. S.; Gold, G. E. & Delp, S. L.: Image-based musculoskeletal modeling: applications advances and future opportunities. *Journal of magnetic resonance imaging : JMRI* **25** (2007), 441–451, ISSN 1053-1807.

Blemker, S. S.; Pinsky, P. M. & Delp, S. L.: A 3D model of muscle reveals the causes of nonuniform strains in the biceps brachii. *Journal of biomechanics* **38** (2005), 657–665, ISSN 0021-9290.

Boone, D. A.; Kobayashi, T.; Chou, T. G.; Arabian, A. K.; Coleman, K. L.; Orendurff, M. S. & Zhang, M.: Perception of socket alignment perturbations in amputees with transtibial prostheses. *Journal of rehabilitation research and development* **49** (2012), 843–853, ISSN 0748-7711.

de Borst, R.; Crisfield, M. A.; Remmers, J. J. C. & Verhoosel, C. V.: *Non-Linear Finite Element Analysis of Solids and Structures*. John Wiley & Sons, Ltd, Chichester, UK 2012, ISBN 9781118375938.

Bradley, C. P.; Emamy, N.; Ertl, T.; Göddeke, D.; Hessenthaler, A.; Klotz, T.; Krämer, A.; Krone, M.; Maier, B.; Mehl, M.; Rau, T. & Röhrle, O.: Enabling Detailed Biophysics-Based Skeletal Muscle Models on HPC Systems. *Frontiers in physiology* **9** (2018), 816.

Brodbeck, J. A.: Experiment with the suction socket for above-knee amputees. *Bulletin of the U.S. Army Medical Department. United States. Army. Medical Department* **7** (1947), 408–411, ISSN 0096-9443.

Cagle, J. C.; Reinhall, P. G.; Allyn, K. J.; McLean, J.; Hinrichs, P.; Hafner, B. J. & Sanders, J. E.: A finite element model to assess transtibial prosthetic sockets with elastomeric liners. *Medical & biological engineering & computing* (2017), ISSN 0140-0118.

Canty, T. J. & Ware, R. M.: Suction socket for above knee prosthesis. *United States naval medical bulletin* **49** (1949), 216–233.

Cappellini, G.; Ivanenko, Y. P.; Poppele, R. E. & Lacquaniti, F.: Motor patterns in human walking and running. *Journal of neurophysiology* **95** (2006), 3426–3437, ISSN 0022-3077.

Cappozzo, A.; Leo, T. & Cortesi, S. S.: A polycentric knee-ankle mechanism for above-knee prostheses. *Journal of biomechanics* **13** (1980), 231–239, ISSN 0021-9290.

Chi, S.-W.; Hodgson, J.; Chen, J.-S.; Edgerton, V. R.; Shin, D. D.; Roiz, R. A. & Sinha, S.: Finite Element Modeling Reveals Complex Strain Mechanics in the Aponeuroses of Contracting Skeletal Muscle. *Journal of biomechanics* **43** (2010), 1243–1250, ISSN 0021-9290.

Choi, H. F. & Blemker, S. S.: Skeletal muscle fascicle arrangements can be reconstructed using a Laplacian vector field simulation. *PloS one* **8** (2013), e77576.

Chong, S.-Y.; Dorow, B.; Ramasamy, E.; Dennerlein, F. & Röhrle, O.: The use of collision detection to infer multi-camera calibration quality. *Frontiers in bioengineering and biotechnology* **3** (2015), 1–6, ISSN 2296-4185.

Chong, S.-Y. & Röhrle, O.: Exploring the Use of Non-Image-Based Ultrasound to Detect the Position of the Residual Femur within a Stump. *PloS one* **11** (2016), e0164583.

Colombo, G.; Facoetti, G. & Rizzi, C.: A digital patient for computer-aided prosthesis design. *Interface focus* **3** (2013), 20120082, ISSN 2042-8898.

Commean, P. K.; Smith, K. E. & Vannier, M. W.: Lower extremity residual limb slippage within the prosthesis. *Archives of physical medicine and rehabilitation* **78** (1997), 476–485, ISSN 0003-9993.

Convery, P. & Murray, K. D.: Ultrasound study of the motion of the residual femur within a trans-femoral socket during gait. *Prosthetics and orthotics international* **24** (2000), 226–232, ISSN 0309-3646.

Coupé, P. & Manjon, J. V.: MATLAB Toolbox: DWI Denoising Software (2014).

Descoteaux, M.; Wiest-Daesslé, N.; Prima, S.; Barillot, C. & Deriche, R.: Impact of Rician Adapted Non-Local Means Filtering on HARDI. In Metaxas, D. N. (ed.): *Medical image computing and computer-assisted intervention - MICCAI 2008*. Springer, Berlin 2008, vol. 5242 of *Lecture notes in computer science, 0302-9743*, ISBN 978-3-540-85989-5, pp. 122–130.

Detrembleur, C.; Vanmarsenille, J.-M.; de Cuyper, F. & Dierick, F.: Relationship between energy cost gait speed vertical displacement of centre of body mass and efficiency of pendulum-like mechanism in unilateral amputee gait. *Gait & posture* **21** (2005), 333–340, ISSN 0966-6362.

Dickinson, A. S.; Steer, J. W. & Worsley, P. R.: Finite element analysis of the amputated lower limb: A systematic review and recommendations. *Medical engineering & physics* **43** (2017), 1–18, ISSN 1350-4533.

Dillingham, T. R.; Pezzin, L. E.; MacKenzie, E. J. & Burgess, A. R.: Use and satisfaction with prosthetic devices among persons with trauma-related amputations: a long-term outcome study. *American journal of physical medicine & rehabilitation* **80** (2001), 563–571.

Dou, P.; Jia, X.; Suo, S.; Wang, R. & Zhang, M.: Pressure distribution at the stump/-socket interface in transtibial amputees during walking on stairs slope and non-flat road. *Clinical biomechanics (Bristol, Avon)* **21** (2006), 1067–1073, ISSN 0268-0033.

Downie, W. W.; Leatham, P. A.; Rhind, V. M.; Wright, V.; Branco, J. A. & Anderson, J. A.: Studies with pain rating scales. *Annals of the rheumatic diseases* **37** (1978), 378–381, ISSN 0003-4967.

Dumas, R.; Branemark, R. & Frossard, L.: Gait Analysis of Transfemoral Amputees: Errors in Inverse Dynamics Are Substantial and Depend on Prosthetic Design. *IEEE transactions on neural systems and rehabilitation engineering : a publication of the IEEE Engineering in Medicine and Biology Society* **25** (2017), 679–685, ISSN 1534-4320.

Dumbleton, T.; Buis, A. W. P.; McFadyen, A.; McHugh, B. F.; McKay, G.; Murray, K. D. & Sexton, S.: Dynamic interface pressure distributions of two transtibial prosthetic socket concepts. *Journal of rehabilitation research and development* **46** (2009), 405–415, ISSN 0748-7711.

Durandau, G.; Farina, D. & Sartori, M.: Robust Real-Time Musculoskeletal Modeling Driven by Electromyograms. *IEEE transactions on bio-medical engineering* **65** (2018), 556–564.

Dyck, W. R.; Onyshko, S.; Hobson, D. A.; Winter, D. A. & Quanbury, A. O.: A voluntarily controlled electrohydraulic above-knee prosthesis. *Bulletin of prosthetics research* (1975), 169–186, ISSN 0007-506X.

E. Sayers: A General Introduction to the E-utilities: In: EntrezProgramming Utilities Help (2010).

Edsberg, L. E.; Black, J. M.; Goldberg, M.; McNichol, L.; Moore, L. & Sieggreen, M.: Revised National Pressure Ulcer Advisory Panel Pressure Injury Staging System: Revised Pressure Injury Staging System. *Journal of Wound, Ostomy, and Continence Nursing* **43** (2016), 585–597, ISSN 1071-5754.

Egawa, S.; Miura, S.; Yokoyama, H.; Endo, T. & Tamura, K.: Growth and differentiation of a long bone in limb development repair and regeneration. *Development, growth & differentiation* **56** (2014), 410–424.

Ehret, A. E.; Böl, M. & Itskov, M.: A continuum constitutive model for the active behaviour of skeletal muscle. *Journal of the Mechanics and Physics of Solids* **59** (2011), 625–636, ISSN 00225096.

Ehret, A. E. & Itskov, M.: Modeling of anisotropic softening phenomena: Application to soft biological tissues. *International Journal of Plasticity* **25** (2009), 901–919, ISSN 07496419.

Felsenthal, N. & Zelzer, E.: Mechanical regulation of musculoskeletal system development. *Development (Cambridge, England)* **144** (2017), 4271–4283.

Fernandez, J.; Zhang, J.; Heidlauf, T.; Sartori, M.; Besier, T.; Röhrle, O. & Lloyd, D.: Multiscale musculoskeletal modelling data-model fusion and electromyography-informed modelling. *Interface focus* **6** (2016), 20150084, ISSN 2042-8898.

Fernandez, J. W. & Pandy, M. G.: Integrating modelling and experiments to assess dynamic musculoskeletal function in humans. *Experimental physiology* **91** (2006), 371–382, ISSN 0958-0670.

Fernie, G.; Holden, J. & Soto, M.: Biofeedback training of knee control in the above-knee amputee. *American journal of physical medicine* **57** (1978), 161–166, ISSN 0002-9491.

Ferreira, J. P. S.; Parente, M. P. L.; Jabareen, M. & Jorge, R. M. N.: A general framework for the numerical implementation of anisotropic hyperelastic material models including non-local damage. *Biomechanics and modeling in mechanobiology* **16** (2017), 1119–1140.

Flowers, W. C. & Mann, R. W.: An electrohydraulic knee-torque controller for a prosthesis simulator. *Journal of biomechanical engineering* **99** (1977), 3–8, ISSN 0148-0731.

Forten, L.: The vacuum-suction above knee leg. *The OALMA journal* **1** (1947), 5–9.

Frillici, F. S. & Rotini, F.: Prosthesis Socket Design through Shape Optimization. *Computer-Aided Design and Applications* **10** (2013), 863–876.

Froeling, M.; Oudeman, J.; Strijkers, G. J.; Maas, M.; Drost, M. R.; Nicolay, K. & Nederveen, A. J.: Muscle changes detected with diffusion-tensor imaging after long-distance running. *Radiology* **274** (2015), 548–562, ISSN 0033-8419.

Gefen, A.; Gefen, N.; Linder-Ganz, E. & Margulies, S. S.: In vivo muscle stiffening under bone compression promotes deep pressure sores. *Journal of biomechanical engineering* **127** (2005), 512–524, ISSN 0148-0731.

Gefen, A.; van Nierop, B.; Bader, D. L. & Oomens, C. W.: Strain-time cell-death threshold for skeletal muscle in a tissue-engineered model system for deep tissue injury. *Journal of biomechanics* **41** (2008), 2003–2012, ISSN 0021-9290.

Geng, B.; Dong, J.; Jensen, W.; Dosen, S.; Farina, D. & Kamavuako, E. N.: Psychophysical Evaluation of Subdermal Electrical Stimulation in Relation to Prosthesis Sensory Feedback. *IEEE transactions on neural systems and rehabilitation engineering : a publication of the IEEE Engineering in Medicine and Biology Society* **26** (2018), 709–715, ISSN 1534-4320.

Gholizadeh, H.; Abu Osman, N. A.; Eshraghi, A. & Ali, S.: Transfemoral prosthesis suspension systems: A systematic review of the literature. *American journal of physical medicine & rehabilitation* **93** (2014), 809–823.

Gholizadeh, H.; Abu Osman, N. A.; Eshraghi, A.; Arifin, N. & Chung, T. Y.: A comparison of pressure distributions between two types of sockets in a bulbous stump. *Prosthetics and orthotics international* **40** (2016), 509–516, ISSN 0309-3646.

Gottschalk, F.: Transfemoral amputation. Biomechanics and surgery. *Clinical orthopaedics and related research* (1999), 15–22, ISSN 0009-921X.

Gottschalk, F. A. & Stills, M.: The biomechanics of trans-femoral amputation. *Prosthetics and orthotics international* **18** (1994), 12–17, ISSN 0309-3646.

Gupta, A.; Li, W.; Stebbins, G. T.; Magin, R. L. & Wang, V. M.: High resolution diffusion tensor MRI of rabbit tendons and ligaments at 11.7 T. *Proceedings of the International Society for Magnetic Resonance in Medicine (ISMRM)(Stockholm)* **885** (2010).

Ha, K. H.; Varol, H. A. & Goldfarb, M.: Volitional control of a prosthetic knee using surface electromyography. *IEEE transactions on bio-medical engineering* **58** (2011), 144–151.

Haidekker, M. A.: *Medical Imaging Technology*. Springer New York, New York, NY 2013, ISBN 978-1-4614-7072-4.

Hale, S. A.: Analysis of the swing phase dynamics and muscular effort of the above-knee amputee for varying prosthetic shank loads. *Prosthetics and orthotics international* **14** (1990), 125–135, ISSN 0309-3646.

Hall, J. E.: *Guyton and Hall textbook of medical physiology*. Elsevier, Philadelphia, PA 2016, ISBN 1455770051.

Hallquist, J. O.: *LS-DYNA Theory Manual*. Livermore Software Technology Corporation, Livermore, California 2006, r:8234 edn., ISBN 0-9778540-0-0.

Handsfield, G. G.; Bolsterlee, B.; Inouye, J. M.; Herbert, R. D.; Besier, T. F. & Fernandez, J. W.: Determining skeletal muscle architecture with Laplacian simulations: a comparison with diffusion tensor imaging. *Biomechanics and modeling in mechanobiology* **16** (2017), 1845–1855.

Hanger, H. B.: Above-knee Socket Shape and Clinical Considerations (1964).

Hansen-Leth, C.: Bone Vascularization and Bone Healing in the Amputation Stump: An Experimental Study. *Acta Orthopaedica Scandinavica* **50** (1979), 39–47, ISSN 0001-6470.

Hanspal, R. S.; Fisher, K. & Nieveen, R.: Prosthetic socket fit comfort score. *Disability and rehabilitation* **25** (2003), 1278–1280, ISSN 0963-8288.

He, P.; Xue, K. & Murka, P.: 3-D imaging of residual limbs using ultrasound. *Journal of rehabilitation research and development* **34** (1997), 269–278, ISSN 0748-7711.

Hefferman, G. M.; Zhang, F.; Nunnery, M. J. & Huang, H.: Integration of surface electromyographic sensors with the transfemoral amputee socket: a comparison of four differing configurations. *Prosthetics and orthotics international* **39** (2015), 166–173, ISSN 0309-3646.

Hendershot, B. D.; Shojaei, I.; Acasio, J. C.; Dearth, C. L. & Bazrgari, B.: Walking speed differentially alters spinal loads in persons with traumatic lower limb amputation. *Journal of biomechanics* **70** (2018), 249–254, ISSN 0021-9290.

Hendershot, B. D. & Wolf, E. J.: Three-dimensional joint reaction forces and moments at the low back during over-ground walking in persons with unilateral lower-extremity amputation. *Clinical biomechanics (Bristol, Avon)* **29** (2014), 235–242, ISSN 0268-0033.

Hendershot, B. D. & Wolf, E. J.: Persons with unilateral transfemoral amputation have altered lumbosacral kinetics during sitting and standing movements. *Gait & posture* **42** (2015), 204–209, ISSN 0966-6362.

Hendriks, F. M.; Brokken, D.; Oomens, C. W. J.; Bader, D. L. & Baaijens, F. P. T.: The relative contributions of different skin layers to the mechanical behavior of human skin in vivo using suction experiments. *Medical engineering & physics* **28** (2006), 259–266, ISSN 1350-4533.

Hershler, C. & Milner, M.: Angle-angle diagrams in above-knee amputee and cerebral palsy gait. *American journal of physical medicine* **59** (1980), 165–183, ISSN 0002-9491.

Hoefnagels, F. W. A.; de Witt Hamer, P. C.; Pouwels, P. J. W.; Barkhof, F. & Vandertop, W. P.: Impact of Gradient Number and Voxel Size on Diffusion Tensor Imaging Tractography for Resective Brain Surgery. *World neurosurgery* **105** (2017), 923–934.e2.

Holdsworth, S. J. & Bammer, R.: Magnetic resonance imaging techniques: fMRI DWI and PWI. *Seminars in neurology* **28** (2008), 395–406, ISSN 0271-8235.

Holzapfel, G. A.: *Nonlinear solid mechanics: A continuum approach for engineering*. Wiley, Chichester and New York 2000, ISBN 0471823198.

Hughes, J. & Jacobs, N.: Normal human locomotion. *Prosthetics and orthotics international* **3** (1979), 4–12, ISSN 0309-3646.

Hulth, A. & Olerud, S.: Studies on amputation stumps in rabbits. *The Journal of bone and joint surgery. British volume* **44-B** (1962), 431–435, ISSN 0301-620X.

Iivarinen, J. T.; Korhonen, R. K.; Julkunen, P. & Jurvelin, J. S.: Experimental and computational analysis of soft tissue mechanical response under negative pressure in forearm. *Skin research and technology : official journal of International Society for Bioengineering and the Skin (ISBS) [and] International Society for Digital Imaging of Skin (ISDIS) [and] International Society for Skin Imaging (ISSI)* **19** (2013), e356–65.

Ishai, G. & Bar, A.: Computer simulation for the prediction of stump loading in above-knee amputees. *Medical & biological engineering & computing* **21** (1983), 186–190, ISSN 0140-0118.

Jaegers, S. M.; Arendzen, J. H. & de Jongh, H. J.: Prosthetic gait of unilateral transfemoral amputees: a kinematic study. *Archives of physical medicine and rehabilitation* **76** (1995), 736–743, ISSN 0003-9993.

Jaegers, S. M.; Arendzen, J. H. & de Jongh, H. J.: An electromyographic study of the hip muscles of transfemoral amputees in walking. *Clinical orthopaedics and related research* (1996), 119–128, ISSN 0009-921X.

Jenkinson, M.: NIfTI-1 Data Format – Neuroimaging Informatics Technology Initiative: Nifti.nimh.nih.gov (2007).

Jia, X.; Zhang, M. & Lee, W. C. C.: Load transfer mechanics between trans-tibial prosthetic socket and residual limb–dynamic effects. *Journal of biomechanics* **37** (2004), 1371–1377, ISSN 0021-9290.

Jones, D. K. & Basser, P. J.: Squashing peanuts and smashing pumpkins: how noise distorts diffusion-weighted MR data. *Magnetic resonance in medicine* **52** (2004), 979–993, ISSN 0740-3194.

Karajan, N.; Röhrle, O.; Ehlers, W. & Schmitt, S.: Linking continuous and discrete intervertebral disc models through homogenisation. *Biomechanics and modeling in mechanobiology* **12** (2013), 453–466.

Karampinos, D. C.; Banerjee, S.; King, K. F.; Link, T. M. & Majumdar, S.: Considerations in high-resolution skeletal muscle diffusion tensor imaging using single-shot echo planar imaging with stimulated-echo preparation and sensitivity encoding. *NMR in biomedicine* **25** (2012), 766–778.

Karmarkar, A. M.; Collins, D. M.; Wichman, T.; Franklin, A.; Fitzgerald, S. G. .; Dicianno, B. E.; Pasquina, P. F. & Cooper, R. A.: Prosthesis and wheelchair use in veterans with lower-limb amputation. *Journal of rehabilitation research and development* **46** (2009), 567, ISSN 0748-7711.

Kay, H. W.; Cody, K. A. & Kramer, H. E.: Total contact above-knee socket studies (1966).

Kent, J. & Franklyn-Miller, A.: Biomechanical models in the study of lower limb amputee kinematics: A review. *Prosthetics and orthotics international* **35** (2011), 124–139, ISSN 0309-3646.

Klein, R. W.: The limb-fitting team artificial arms and techniques of above-knee fitting. *The Medical journal of Australia* **1** (1959), 839–842, ISSN 0025-729X.

Klotz, R.; Colobert, B.; Botino, M. & Permentiers, I.: Influence of different types of sockets on the range of motion of the hip joint by the transfemoral amputee. *Annals of physical and rehabilitation medicine* **54** (2011), 399–410.

Kobayashi, T.; Orendurff, M. S. & Boone, D. A.: Dynamic alignment of transtibial prostheses through visualization of socket reaction moments. *Prosthetics and orthotics international* **39** (2015), 512–516, ISSN 0309-3646.

Krouskop, T. A.; Muilenberg, A. L.; Doughtery, D. R. & Winningham, D. J.: Computer-aided design of a prosthetic socket for an above-knee amputee. *Journal of rehabilitation research and development* **24** (1987), 31–38, ISSN 0748-7711.

Lacroix, D. & Patiño, J. F. R.: Finite element analysis of donning procedure of a prosthetic transfemoral socket. *Annals of biomedical engineering* **39** (2011), 2972–2983, ISSN 0090-6964.

Łagan, S. & Liber-Kneć, A.: The determination of mechanical properties of prosthetic liners through experimental and constitutive modelling approaches. *Czasopismo Techniczne* **3** (2018), 197–209, ISSN 2353737X.

LaPrè, A. K.; Price, M. A.; Wedge, R. D.; Umberger, B. R. & Sup, F. C.: Approach for gait analysis in persons with limb loss including residuum and prosthesis socket dynamics. *International journal for numerical methods in biomedical engineering* **34** (2018), e2936.

Larmor, J.: LXIII. On the theory of the magnetic influence on spectra; and on the radiation from moving ions. *The London, Edinburgh, and Dublin Philosophical Magazine and Journal of Science* **44** (1897), 503–512, ISSN 1941-5982.

Le Bihan, D.; Mangin, J. F.; Poupon, C.; Clark, C. A.; Pappata, S.; Molko, N. & Chabriat, H.: Diffusion tensor imaging: concepts and applications. *Journal of magnetic resonance imaging : JMRI* **13** (2001), 534–546, ISSN 1053-1807.

Leavitt, L. A.; Zuniga, E. N.; Calvert, J. C.; Canzoneri, J. & Peterson, C. R.: Gait analysis and tissue-socket interface pressures in above-knee amputees. *Southern medical journal* **65** (1972), 1197–1207, ISSN 0038-4348.

Lee, W. C. C.; Zhang, M.; Jia, X. & Cheung, J. T. M.: Finite element modeling of the contact interface between trans-tibial residual limb and prosthetic socket. *Medical engineering & physics* **26** (2004), 655–662, ISSN 1350-4533.

Legro, M. W.; Reiber, G.; del Aguila, M.; Ajax, M. J.; Boone, D. A.; Larsen, J. A.; Smith, D. G. & Sangeorzan, B.: Issues of importance reported by persons with lower limb amputations and prostheses. *Journal of rehabilitation research and development* **36** (1999), 155–163, ISSN 0748-7711.

Li, X.; Morgan, P. S.; Ashburner, J.; Smith, J. & Rorden, C.: The first step for neuroimaging data analysis: DICOM to NIfTI conversion. *Journal of neuroscience methods* **264** (2016), 47–56.

Linder-Ganz, E.; Engelberg, S.; Scheinowitz, M. & Gefen, A.: Pressure-time cell death threshold for albino rat skeletal muscles as related to pressure sore biomechanics. *Journal of biomechanics* **39** (2006), 2725–2732, ISSN 0021-9290.

Linder-Ganz, E. & Gefen, A.: Mechanical compression-induced pressure sores in rat hindlimb: muscle stiffness histology and computational models. *Journal of Applied Physiology* **96** (2004), 2034–2049, ISSN 8750-7587.

Linder-Ganz, E.; Shabshin, N.; Itzchak, Y. & Gefen, A.: Assessment of mechanical conditions in sub-dermal tissues during sitting: a combined experimental-MRI and finite element approach. *Journal of biomechanics* **40** (2007), 1443–1454, ISSN 0021-9290.

Lundgren, J.: MATLAB Toolbox: Splinefit (2017).

Mak, A. F.; Zhang, M. & Boone, D. A.: State-of-the-art research in lower-limb prosthetic biomechanics-socket interface: a review. *Journal of rehabilitation research and development* **38** (2001), 161–174, ISSN 0748-7711.

Malinauskas, M.; Krouskop, T. A. & Barry, P. A.: Noninvasive measurement of the stiffness of tissue in the above-knee amputation limb. *Journal of rehabilitation research and development* **26** (1989), 45–52, ISSN 0748-7711.

Manjón, J. V.; Coupé, P.; Concha, L.; Buades, A.; Collins, D. L. & Robles, M.: Diffusion weighted image denoising using overcomplete local PCA. *PloS one* **8** (2013), e73021.

Mason, D.: Pydicom (2018).

Miehe, C.: Discontinuous and continuous damage evolution in Ogden-type large-strain elastic materials. *European journal of mechanics. A. Solids* **14** (1995), 697–720.

Mordhorst, M.; Strecker, T.; Wirtz, D.; Heidlauf, T. & Röhrle, O.: POD-DEIM reduction of computational EMG models. *Journal of Computational Science* **19** (2017), 86–96, ISSN 18777503.

Mori, S. & Zhang, J.: Principles of diffusion tensor imaging and its applications to basic neuroscience research. *Neuron* **51** (2006), 527–539, ISSN 0896-6273.

Mukherjee, P.; Chung, S. W.; Berman, J. I.; Hess, C. P. & Henry, R. G.: Diffusion tensor MR imaging and fiber tractography: technical considerations. *AJNR. American journal of neuroradiology* **29** (2008), 843–852.

Murray, M. P.; Sepic, S. B.; Gardner, G. M. & Mollinger, L. A.: Gait patterns of above-knee amputees using constant-friction knee components. *Bulletin of prosthetics research* **10-34** (1980), 35–45, ISSN 0007-506X.

Netter, F. H.: *Atlas of human anatomy*. Netter Basic Science, Saunders/Elsevier, Philadelphia, PA 2014, ISBN 1455758841.

Neumann, E. S.: Measurement of socket discomfort: Part I: Pressure Sensation. *Journal of Prosthetics and Orthotics* **13** (2001), 99–110.

Nola, G. T. & Vistnes, L. M.: Differential response of skin and muscle in the experimental production of pressure sores. *Plastic and reconstructive surgery* **66** (1980), 728–733, ISSN 0032-1052.

Oberg, K. & Lanshammar, H.: An investigation of kinematic and kinetic variables for the description of prosthetic gait using the ENOCH system. *Prosthetics and orthotics international* **6** (1982), 43–47, ISSN 0309-3646.

Odegard, G. M.; Donahue, T. L. H.; Morrow, D. A. & Kaufman, K. R.: Constitutive modeling of skeletal muscle tissue with an explicit strain-energy function. *Journal of biomechanical engineering* **130** (2008), 061017, ISSN 0148-0731.

Oomens, C. W. J.; Loerakker, S. & Bader, D. L.: The importance of internal strain as opposed to interface pressure in the prevention of pressure related deep tissue injury. *Journal of tissue viability* **19** (2010), 35–42, ISSN 0965-206X.

Patel, V.; Dinov, I. D.; van Horn, J. D.; Thompson, P. M. & Toga, A. W.: LONI MiND: Metadata in NIfTI for DWI. *NeuroImage* **51** (2010), 665–676, ISSN 10538119.

Peery, J. T.; Klute, G. K.; Blevins, J. J. & Ledoux, W. R.: A three-dimensional finite element model of the transibial residual limb and prosthetic socket to predict skin temperatures. *IEEE transactions on neural systems and rehabilitation engineering : a publication of the IEEE Engineering in Medicine and Biology Society* **14** (2006), 336–343, ISSN 1534-4320.

Peña, E.: A rate dependent directional damage model for fibred materials: application to soft biological tissues. *Computational Mechanics* **48** (2011), 407–420, ISSN 0178-7675.

Peña, E.: Computational aspects of the numerical modelling of softening damage and permanent set in soft biological tissues. *Computers & Structures* **130** (2014), 57–72, ISSN 00457949.

Peña, E.; Peña, J. A. & Doblaré, M.: On the Mullins effect and hysteresis of fibered biological materials: A comparison between continuous and discontinuous damage models. *International Journal of Solids and Structures* **46** (2009), 1727–1735, ISSN 00207683.

Popović, D.; Oğuztöreli, M. N. & Stein, R. B.: Optimal control for the active above-knee prosthesis. *Annals of biomedical engineering* **19** (1991), 131–150, ISSN 0090-6964.

Popović, D.; Oğuztöreli, M. N. & Stein, R. B.: Optimal control for an above-knee prosthesis with two degrees of freedom. *Journal of biomechanics* **28** (1995), 89–98, ISSN 0021-9290.

Portnoy, S.; Siev-Ner, I.; Shabshin, N. & Gefen, A.: Effects of sitting postures on risks for deep tissue injury in the residuum of a transtibial prosthetic-user: a biomechanical case study. *Computer methods in biomechanics and biomedical engineering* **14** (2011), 1009–1019.

Portnoy, S.; Siev-Ner, I.; Shabshin, N.; Kristal, A.; Yizhar, Z. & Gefen, A.: Patient-specific analyses of deep tissue loads post transtibial amputation in residual limbs of multiple prosthetic users. *Journal of biomechanics* **42** (2009a), 2686–2693, ISSN 0021-9290.

Portnoy, S.; Siev-Ner, I.; Yizhar, Z.; Kristal, A.; Shabshin, N. & Gefen, A.: Surgical and morphological factors that affect internal mechanical loads in soft tissues of the transtibial residuum. *Annals of biomedical engineering* **37** (2009b), 2583–2605, ISSN 0090-6964.

Portnoy, S.; Yarnitzky, G.; Yizhar, Z.; Kristal, A.; Oppenheim, U.; Siev-Ner, I. & Gefen, A.: Real-time patient-specific finite element analysis of internal stresses in the soft tissues of a residual limb: a new tool for prosthetic fitting. *Annals of biomedical engineering* **35** (2007), 120–135, ISSN 0090-6964.

Portnoy, S.; Yizhar, Z.; Shabshin, N.; Itzchak, Y.; Kristal, A.; Dotan-Marom, Y.; Siev-Ner, I. & Gefen, A.: Internal mechanical conditions in the soft tissues of a residual limb of a trans-tibial amputee. *Journal of biomechanics* **41** (2008), 1897–1909, ISSN 0021-9290.

Pritham, C. H.: Biomechanics and shape of the above-knee socket considered in light of the ischial containment concept. *Prosthetics and orthotics international* **14** (1990), 9–21, ISSN 0309-3646.

Radcliffe, C. W.: Functional considerations in the fitting of above-knee prostheses. *Artificial limbs* **2** (1955), 35–60, ISSN 0004-3729.

Radcliffe, C. W.; JOHNSON, N. C. & Foort, J.: Some experience with prosthetic problems of above-knee amputees. *Artificial limbs* **4** (1957), 41–75, ISSN 0004-3729.

Ramasamy, E.; Avci, O.; Dorow, B.; Chong, S.-Y.; Gizzi, L.; Steidle, G.; Schick, F. & Röhrle, O.: An Efficient Modelling-Simulation-Analysis Workflow to Investigate Stump-Socket Interaction Using Patient-Specific Three-Dimensional Continuum-Mechanical Finite Element Residual Limb Models. *Frontiers in Bioengineering and Biotechnology* **6** (2018), 1–17.

Ramírez, J. F. & Vélez, J. A.: Incidence of the boundary condition between bone and soft tissue in a finite element model of a transfemoral amputee. *Prosthetics and orthotics international* **36** (2012), 405–414, ISSN 0309-3646.

Redhead, R. G.: Total surface bearing self suspending above-knee sockets. *Prosthetics and orthotics international* **3** (1979), 126–136, ISSN 0309-3646.

Reynolds, D. P. & Lord, M.: Interface load analysis for computer-aided design of below-knee prosthetic sockets. *Medical & biological engineering & computing* **30** (1992), 419–426, ISSN 0140-0118.

Röhrle, O.: Simulating the Electro-Mechanical Behavior of Skeletal Muscles. *Computing in Science & Engineering* **12** (2010), 48–58, ISSN 1521-9615.

Röhrle, O.; Davidson, J. B. & Pullan, A. J.: Bridging Scales: A Three-Dimensional Electromechanical Finite Element Model of Skeletal Muscle. *SIAM Journal on Scientific Computing* **30** (2008), 2882–2904, ISSN 1064-8275.

Röhrle, O.; Davidson, J. B. & Pullan, A. J.: A physiologically based multi-scale model of skeletal muscle structure and function. *Frontiers in physiology* **3** (2012), 358.

Röhrle, O.; Köstler, H. & Loch, M.: Segmentation of Skeletal Muscle Fibres for Applications in Computational Skeletal Muscle Mechanics. In Wittek, A.; Nielsen, P. M. F. & Miller, K. (eds.): *Computational biomechanics for medicine*. Springer, New York 2011, ISBN 978-1-4419-9618-3, pp. 107–117.

Röhrle, O. & Pullan, A. J.: Three-dimensional finite element modelling of muscle forces during mastication. *Journal of biomechanics* **40** (2007), 3363–3372, ISSN 0021-9290.

Röhrle, O.; Sprenger, M. & Schmitt, S.: A two-muscle continuum-mechanical forward simulation of the upper limb. *Biomechanics and modeling in mechanobiology* **16** (2017), 743–762.

Russell Esposito, E.; Aldridge Whitehead, J. M. & Wilken, J. M.: Sound limb loading in individuals with unilateral transfemoral amputation across a range of walking velocities. *Clinical biomechanics (Bristol, Avon)* **30** (2015), 1049–1055, ISSN 0268-0033.

Sanders, J. E.: Interface mechanics in external prosthetics: review of interface stress measurement techniques. *Medical & biological engineering & computing* **33** (1995), 509–516, ISSN 0140-0118.

Scheys, L.; Jonkers, I.; Loeckx, D.; Maes, F.; Spaepen, A. & Suetens, P.: Image Based Musculoskeletal Modeling Allows Personalized Biomechanical Analysis of Gait. In Hutchison, D.; Kanade, T.; Kittler, J.; Kleinberg, J. M.; Mattern, F.; Mitchell, J. C.; Naor, M.; Nierstrasz, O.; Pandu Rangan, C.; Steffen, B.; Sudan, M.; Terzopoulos, D.; Tygar, D.; Vardi, M. Y.; Weikum, G.; Harders, M. & Székely, G. (eds.): *Biomedical Simulation*. Springer Berlin Heidelberg, Berlin, Heidelberg 2006, vol. 4072 of *Lecture Notes in Computer Science*, ISBN 978-3-540-36009-4, pp. 58–66.

Sengeh, D. M. & Herr, H.: A Variable-Impedance Prosthetic Socket for a Transtibial Amputee Designed from Magnetic Resonance Imaging Data. *JPO Journal of Prosthetics and Orthotics* **25** (2013), 129–137, ISSN 1040-8800.

Sengeh, D. M.; Moerman, K. M.; Petron, A. & Herr, H.: Multi-material 3-D viscoelastic model of a transtibial residuum from in-vivo indentation and MRI data. *Journal of the mechanical behavior of biomedical materials* **59** (2016), 379–392.

Sevastikoglou, J. A.; Eriksson, U. & Larsson, S.-E.: Skeletal Changes of the Amputation Stump and the Femur on the Amputated Side: A Clinical Investigation. *Acta Orthopaedica Scandinavica* **40** (1969), 624–633, ISSN 0001-6470.

Shojaei, I.; Hendershot, B. D.; Wolf, E. J. & Bazrgari, B.: Persons with unilateral transfemoral amputation experience larger spinal loads during level-ground walking compared to able-bodied individuals. *Clinical biomechanics (Bristol, Avon)* **32** (2016), 157–163, ISSN 0268-0033.

Shorten, P. R.; O'Callaghan, P.; Davidson, J. B. & Soboleva, T. K.: A mathematical model of fatigue in skeletal muscle force contraction. *Journal of muscle research and cell motility* **28** (2007), 293–313, ISSN 0142-4319.

Silver-Thorn, M. B. & Childress, D. S.: Parametric analysis using the finite element method to investigate prosthetic interface stresses for persons with trans-tibial amputation. *Journal of rehabilitation research and development* **33** (1996), 227–238, ISSN 0748-7711.

Silver-Thorn, M. B. & Childress, D. S.: Generic geometric finite element analysis of the transtibial residual limb and prosthetic socket. *Journal of rehabilitation research and development* **34** (1997), 171–186, ISSN 0748-7711.

Silver-Thorn, M. B.; Steege, J. W. & Childress, D. S.: A review of prosthetic interface stress investigations. *Journal of rehabilitation research and development* **33** (1996), 253–266, ISSN 0748-7711.

Simo, J. C.: On a fully three-dimensional finite-strain viscoelastic damage model: Formulation and computational aspects. *Computer Methods in Applied Mechanics and Engineering* **60** (1987), 153–173, ISSN 00457825.

Smith, K. E.; Commean, P. K. & Vannier, M. W.: Residual-limb shape change: three-dimensional CT scan measurement and depiction in vivo. *Radiology* **200** (1996), 843–850, ISSN 0033-8419.

Soares, J. M.; Marques, P.; Alves, V. & Sousa, N.: A hitchhikers guide to diffusion tensor imaging. *Frontiers in neuroscience* **7** (2013), 31, ISSN 1662-4548.

Sondik, E. J.; Anderson, J. R.; Madans, J. H.; Curtin, L. R.; Williams, D. P.; Hunter, E. L.; Zinn, D. L. & Rothwell, C. J.: *Vital and Health Statistics: Current Estimates from the National Health Interview Survey*. Tech. Rep. 200, U.S. Department of Health and Human Services, Hyattsville, Maryland 1999.

Sprenger, M.: *A 3D continuum-mechanical model for forward-dynamics simulations of the upper limb*. Dissertation, Universität Stuttgart, Stuttgart (2015).

Steege, J. W.; Schnur D. S.; Vorhis R. L. & Rovick, J. S. (eds.): *Finite element analysis as a method of pressure prediction at the below-knee socket interface*, 1987.

Stein, J. L. & Flowers, W. C.: Stance phase control of above-knee prostheses: knee control versus SACH foot design. *Journal of biomechanics* **20** (1987), 19–28, ISSN 0021-9290.

Stejskal, E. O. & Tanner, J. E.: Spin Diffusion Measurements: Spin Echoes in the Presence of a Time–Dependent Field Gradient. *The Journal of Chemical Physics* **42** (1965), 288–292, ISSN 0021-9606.

Taylor, J. S.: Above-knee prosthetic alignment. *Prosthetics and orthotics international* **3** (1979a), 82–84, ISSN 0309-3646.

Taylor, J. S.: Modular assembly above-knee prostheses. *Prosthetics and orthotics international* **3** (1979b), 144–146, ISSN 0309-3646.

Taylor, L. M.; Edwards, J. M. & Porter, J. M.: Present status of reversed vein bypass grafting: five-year results of a modern series. *Journal of vascular surgery* **11** (1990), 193–205; discussion 205–6, ISSN 0741-5214.

Taylor, L. M.; Phinney, E. S. & Porter, J. M.: Present status of reversed vein bypass for lower extremity revascularization. *Journal of vascular surgery* **3** (1986), 288–297, ISSN 0741-5214.

Thorndike, A.: End results in suction socket prosthesis for above-knee amputees. *American journal of surgery* **89** (1955), 919–923, ISSN 0002-9610.

Torres-Moreno, R.; Foort, J.; Morrison, J. B. & Saunders, C. G.: A reference shape library for computer aided socket design in above-knee prostheses. *Prosthetics and orthotics international* **13** (1989), 130–139, ISSN 0309-3646.

Toussaint, N.; Souplet, J. C. & Fillard, P.: MedINRIA: Matlab Tensor Reader/Writer. Internet (2008).

Tözeren, A.: *Human body dynamics: Classical mechanics and human movement*. Springer, New York 2000, ISBN 0387988017.

Tsai, C. S. & Mansour, J. M.: Swing phase simulation and design of above knee prostheses. *Journal of biomechanical engineering* **108** (1986), 65–72, ISSN 0148-0731.

Underwood, H. A.; Tokuno, C. D. & Eng, J. J.: A comparison of two prosthetic feet on the multi-joint and multi-plane kinetic gait compensations in individuals with a unilateral trans-tibial amputation. *Clinical biomechanics (Bristol, Avon)* **19** (2004), 609–616, ISSN 0268-0033.

Valentin, J.; Sprenger, M.; Pflüger, D. & Röhrle, O.: Gradient-based optimization with B-splines on sparse grids for solving forward-dynamics simulations of three-dimensional continuum-mechanical musculoskeletal system models. *International journal for numerical methods in biomedical engineering* **34** (2018), e2965.

Vogl, T. J.; Then, C.; Naguib, N. N. N.; Nour-Eldin, N.-E. A.; Larson, M.; Zangos, S. & Silber, G.: Mechanical soft tissue property validation in tissue engineering using magnetic resonance imaging experimental research. *Academic radiology* **17** (2010), 1486–1491.

Volokh, K. Y.: Prediction of arterial failure based on a microstructural bi-layer fiber-matrix model with softening. *Journal of biomechanics* **41** (2008), 447–453, ISSN 0021-9290.

Waffenschmidt, T.; Polindara, C.; Menzel, A. & Blanco, S.: A gradient-enhanced large-deformation continuum damage model for fibre-reinforced materials. *Computer Methods in Applied Mechanics and Engineering* **268** (2014), 801–842, ISSN 00457825.

Wang, Y. K.; Nash, M. P.; Pullan, A. J.; Kieser, J. A. & Röhrle, O.: Model-based identification of motion sensor placement for tracking retraction and elongation of the tongue. *Biomechanics and modeling in mechanobiology* **12** (2013), 383–399.

Wilson, A. B.: Recent advances in above-knee prosthetics. *Artificial limbs* **12** (1968), 1–27, ISSN 0004-3729.

World Health Organization: *Barriers to innovation in the field of medical devices: background paper 6*. Tech. rep., World Health Organization 2010.

Wu, G.; Siegler, S.; Allard, P.; Kirtley, C.; Leardini, A.; Rosenbaum, D.; Whittle, M.; D'Lima, D. D.; Cristofolini, L.; Witte, H.; Schmid, O. & Stokes, I.: ISB recommendation on definitions of joint coordinate system of various joints for the reporting of human joint motion—part I: ankle hip and spine. *Journal of biomechanics* **35** (2002), 543–548, ISSN 0021-9290.

Yaman, A.; Ozturk, C.; Huijing, P. A. & Yucesoy, C. A.: Magnetic resonance imaging assessment of mechanical interactions between human lower leg muscles in vivo. *Journal of biomechanical engineering* **135** (2013), 91003, ISSN 0148-0731.

Yucesoy, C. A. & Huijing, P. A.: Specifically tailored use of the finite element method to study muscular mechanics within the context of fascial integrity: the linked fiber-matrix mesh model. *International Journal for Multiscale Computational Engineering* **10** (2012), 155–170, ISSN 1543-1649.

Yucesoy, C. A.; Koopman, B. H. F. J. M.; Huijing, P. A. & Grootenboer, H. J.: Three-dimensional finite element modeling of skeletal muscle using a two-domain approach: linked fiber-matrix mesh model. *Journal of biomechanics* **35** (2002), 1253–1262, ISSN 0021-9290.

Zachariah, S. G. & Sanders, J. E.: Interface mechanics in lower-limb external prosthetics: a review of finite element models. *IEEE transactions on rehabilitation engineering : a publication of the IEEE Engineering in Medicine and Biology Society* **4** (1996), 288–302, ISSN 1063-6528.

Zahedi, M. S.; Spence, W. D.; Solomonidis, S. E. & Paul, J. P.: Alignment of lower-limb prostheses. *Journal of rehabilitation research and development* **23** (1986), 2–19, ISSN 0748-7711.

Zarrugh, M. Y. & Radcliffe, C. W.: Simulation of swing phase dynamics in above-knee prostheses. *Journal of biomechanics* (1976), 283–292, ISSN 0021-9290.

Zhang, L.; Zhu, M.; Shen, L. & Zheng, F.: Finite element analysis of the contact interface between trans-femoral stump and prosthetic socket. *Conference proceedings : ... Annual International Conference of the IEEE Engineering in Medicine and Biology Society. IEEE Engineering in Medicine and Biology Society. Annual Conference* **2013** (2013), 1270–1273, ISSN 1557-170X.

Zhang, M.; Lord, M.; Turner-Smith, A. R. & Roberts, V. C.: Development of a non-linear finite element modelling of the below-knee prosthetic socket interface. *Medical engineering & physics* **17** (1995), 559–566, ISSN 1350-4533.

Zhang, M. & Mak, A. F.: A finite element analysis of the load transfer between an above-knee residual limb and its prosthetic socket–roles of interface friction and distal-end boundary conditions. *IEEE transactions on rehabilitation engineering : a publication of the IEEE Engineering in Medicine and Biology Society* **4** (1996), 337–346, ISSN 1063-6528.

Zhang, M.; Mak, A. F. & Roberts, V. C.: Finite element modelling of a residual lower-limb in a prosthetic socket: a survey of the development in the first decade. *Medical engineering & physics* **20** (1998), 360–373, ISSN 1350-4533.

Zhang, M. & Roberts, C.: Comparison of computational analysis with clinical measurement of stresses on below-knee residual limb in a prosthetic socket. *Medical engineering & physics* **22** (2000), 607–612, ISSN 1350-4533.

Curriculum Vitæ

Personal data

Name:	Ellankavi Ramasamy
Date of birth:	November 4, 1985
Place of birth:	Chennai, India
Nationality:	Indian
Marital status:	Married

Education

02/2011:	Degree: Master of Science
10/2008 – 12/2010:	University of Stuttgart, Germany
04/2008:	Degree: Bachelors in Mechanical Engineering
07/2003 – 04/2008:	P.S.G College of Technology, Coimbatore
03/2001 – 03/2003:	High school, S.B.I.O.A School & Junior College, Chennai

Work experience

01/2012 – 03/2019:	Research Assistant, Department of Biomechatronic Systems, Fraunhofer IPA
02/2010 – 03/2011:	Student assistant at the Biomechanics Group, Institute of Applied Mechanics, University of Stuttgart
06/2009 – 03/2011:	Student assistant at the Institute of Material Science, Material Testing and Strength of Materials (IMWF), University of Stuttgart

Released report series

CBM-01 Thomas Heidlauf: *Chemo-Electro-Mechanical Modelling of the Neuromuscular System*, September 2015

CBM-02 Michael Sprenger: *A 3D Continuum-Mechanical Model for Forward-Dynamics Simulations of the Upper Limb*, October 2015

CBM-03 Ellankavi Ramasamy: *A Modelling-Simulation-Analysis Workflow for Investigating Socket-Stump Interaction*, April 2019